The Impact of Radiation Damage on Electron Multiplying CCD Technology for the WFIRST Coronagraph

Thesis

The Impact of Radiation Damage on Electron Multiplying CCD Technology for the WFIRST Coronagraph

Thesis submitted for the degree of

Doctor of Philosophy

at The Open University

by

Nathan Bush

Centre for Electronic Imaging

Faculty of Science Technology Engineering and Mathematics

The Open University

September 2017

The Impact of Radiation Damage on Electron Multiplying CCD Technology for the WFIRST Coronagraph

Nathan Bush

Abstract

This thesis follows an investigation into the effects of radiation damage on the e2v CCD201-20; the detector baselined for use in the WFIRST coronagraph imaging and spectroscopy camera systems (hereafter, WFIRST CGI). The CCD201 is an EM-CCD, a variant of traditional CCD technology that is well suited for operation in light starved conditions. Despite successful implementation on many ground-based instruments, the technology has yet to be used within a space environment and therefore has low technological maturity compared to the standard CCD counterpart. Improvement of the technological maturity rested upon in-depth investigations into the effect of radiation damage on the CCD201, which in turn could be used to estimate the End Of Life (EOL) performance of the instrument and de-risk the utilisation of EM-CCDs for the mission. An in-depth radiation campaign was completed whereby multiple CCD201s were irradiated to multiple fluence levels at both room temperature and the nominal operating temperature of the mission (165 K). Performance was measured prior to and following each irradiation, including measurements of low-signal Charge Transfer Inefficiency (CTI), dark current and Clock Induced Charge (CIC). Significant performance differences were noted between the room temperature and cryogenic irradiation case, indicating that cryogenic irradiations are instrumental to accurate EOL performance estimates. CTI was identified as the key limitation to CGI science performance, and so attention then turned to amelioration strategies focused on improving performance in the presence of radiation damage, including trap pumping and narrow-channel modelling. The results presented in this thesis have helped lead to the adoption of the CCD201-20 for the WFIRST mission, have provided key insight into the differences between room temperature and cryogenic irradiations, have advanced the “trap pumping” technique for use on EM-CCDs and presented the properties on the dominant traps that impact CTI for radiation damaged CCDs. The findings are not only useful for the WFIRST CGI, but for any future space mission that will utilise EM-CCD technology in an environment where radiation has the potential to degrade science performance.

Declaration

I hereby declare that no part of this thesis has been previously submitted to this or any other university as part of the requirement for a higher degree. The work described herein was conducted solely by the undersigned except for those colleagues and other workers acknowledged in the text.

Nathan Bush

22nd September 2017

Dedication

This thesis is dedicated to my friends, family, colleagues and loved ones who have provided steadfast support throughout my education. Without them, this work would not have been possible.

Acknowledgements

I would like to acknowledge current and past members of the CEI for their professional support and guidance throughout my PhD. Particular thanks go to my supervisory team; David Hall, Konstantin Stefanov and Andrew Holland. Additional thanks go to David Hall, Matthew Soman, Neil Murray, Jason Gow and Ben Dryer who provided consistent support throughout my entire PhD, often dedicating large portions of their own time to help troubleshoot equipment issues and provide advice and support. Finally, I'd like to thank David Burt and Doug Jordan from e2v who often provided in-depth technical insight into many results that significantly helped the analysis effort and provided future avenues for further research.

List of acronyms

ADU	Analogue-to-Digital Unit
BI	Back Illuminated
BOL	Beginning of Life
CCD	Charge Coupled Device
CDS	Correlated Double Sampling
CIC	Clock Induced Charge
CGI	Coronagraph Instrument
COTS	Commercial “Off-The-Shelf”
CTE	Charge Transfer Efficiency
CTI	Charge Transfer Inefficiency
DLTS	Deep-Level Transient Spectroscopy
DN	Digital Number
EM-CCD	Electron Multiplying Charge Coupled Device
ENF	Excess Noise Factor
EPER	Extended Pixel Edge Response
EOL	End of Life
FI	Front Illuminated
FOV	Field of View
FPR	First Pixel Response
FWC	Full-Well Capacity
FWHM	Full Width Half Maximum
GEO	Geostationary Orbit
HLC	Hybrid Lyot Coronagraph
HR	High Responsivity
HST	Hubble Space Telescope
IMO	Inverted Mode Operation
LEO	Low Earth Orbit
LET	Linear Energy Transfer
LS	Large Signal
MOS	Metal Oxide Semiconductor
MOSFET	Metal Oxide Semiconductor Field Effect Transistor
NIEL	Non-Ionising Energy Loss

NIMO	Non-Inverted Mode Operation
NRO	National Reconnaissance Office
PSF	Point Spread Function
PTC	Photon Transfer Curve
Rϕ2HV	Rϕ2 High Voltage
RTS	Random Telegraph Signal
SEGR	Single Event Gate Rupture
SPC	Shaped Pupil Coronagraph
SRIM	Stopping and Range of Ions in Matter
TRL	Technology Readiness Level
WFI	Wide Field Imager
WFIRST	Wide Field Infra-Red Survey Telescope

Publications

The results from the work in this thesis are partly contained within the following publications:

1. **Bush, Nathan**; Hall, David; Holland, Andrew; Burgon, Ross; Murray, Neil; Gow, Jason; Jordan, Douglas; Demers, Richard; Harding, Leon K.; Nemati, Bijan; Hoenk, Michael; Michaels, Darren and Peddada, Pavani (2016). Cryogenic irradiation of an EMCCD for the WFIRST coronagraph: preliminary performance analysis. In: *High Energy, Optical, and Infrared Detectors for Astronomy VII*, Society of Photo-Optical Instrumentation Engineers (SPIE), article no. 99150A.

2. Hall, David; Wood, Daniel; **Bush, Nathan**; Murray, Neil; Gow, Jason; Skottfelt, Jesper and Holland, Andrew (2016). Mapping radiation-induced defects in CCDs through space and time. In: *High Energy, Optical, and Infrared Detectors for Astronomy VII*, SPIE Digital Library, article no. 99150I.

3. Harding, Leon K.; Demers, Richard T.; Hoenk, Michael; Peddada, Pavani; Nemati, Bijan; Cherng, Michael; Michaels, Darren; Neat, Leo S.; Loc, Anthony; **Bush, Nathan**; Hall, David; Murray, Neil; Gow, Jason; Burgon, Ross; Holland, Andrew; Reinheimer, Alice; Jorden, Paul R. and Jordan, Douglas (2015). Technology advancement of the CCD201-20 EMCCD for the WFIRST coronagraph instrument: sensor characterization and radiation damage. *Journal of Astronomical Telescopes, Instruments, and Systems*, 2(1) 011007.

4. Harding, Leon K.; Demers, Richard T.; Hoenk, Michael; Peddada, Pavani; Nemati, Bijan; Cherng, Michael; Michaels, Darren; Loc, Anthony; **Bush, Nathan**; Hall, David; Murray, Neil; Gow, Jason; Burgon, Ross; Holland, Andrew; Reinheimer, Alice; Jorden, Paul R. and Jordan, Douglas (2015). Electron multiplication CCD detector technology advancement for the WFIRST-AFTA coronagraph. In: *Techniques and Instrumentation for Detection of Exoplanets VII* (Shaklan, Stuart ed.), Proceedings of SPIE, SPIE Press, article no. 96050F.

5. **Bush, Nathan**; Hall, David; Holland, Andrew; Burgon, Ross; Murray, Neil; Gow, Jason; Soman, Matthew; Jordan, Doug; Demers, Richard; Harding, Leon K.; Hoenk, Michael; Michaels, Darren; Nemati, Bijan and Peddada, Pavani (2015). The impact of radiation damage on photon counting with an EMCCD for the WFIRST-AFTA coronagraph. In: *Proceedings of SPIE*, Society of Photo-Optical Instrumentation Engineers (SPIE), 9605, article no. 96050E.

6. Hall, David J.; **Bush, Nathan**; Murray, Neil; Gow, Jason; Clarke, Andrew; Burgon, Ross and Holland, Andrew (2015). Challenges in photon-starved space astronomy in a harsh radiation environment using CCDs. In: *Proceedings of SPIE*, Society of Photo-Optical Instrumentation Engineers (SPIE), 9602, article no. 96020U.

7. **Bush, Nathan.**; Stefanov, Konstantin.; Hall, David.; Jordan, Doug. and Holland, Andrew. (2014). Simulations of charge transfer in Electron Multiplying Charge Coupled Devices. *Journal of Instrumentation*, 9(12), article no. C12042.

Technical Notes

The results from the work in this thesis are partly contained within the following technical notes, delivered to JPL and e2v:

1. Open-e2v TN: Investigation into the Trailing Charge exhibited by the CCD251 Bush, Nathan

2. Open-JPL-TN 3.1: WFIRST AFTA-C: Preliminary Performance Analysis after Radiation Damage. Test Readiness Review Document Bush, Nathan

3. Open-JPL-TN 4.1: WFIRST AFTA-C: Preliminary Performance Analysis after Radiation Damage. Pre-and Post-Radiation Analysis. Bush, Nathan

4. Open-JPL-TN 5.1: WFIRST AFTA-C: Phase II Final Report. Pre- and Post- Cryogenic-Radiation Analysis. Bush, Nathan

5. Open-JPL-TN 6.0 WFIRST Radiation Damage Study. Phase III trap pumping Results. Bush, Nathan

6. Open-JPL-TN 7.0 WFIRST Radiation Damage Study. Phase III Charge Storage Modelling Bush, Nathan

7. Open-JPL-TN 8.0 WFIRST Radiation Damage Study. Image Pixel Narrow Channel Modelling Clarke, Andy with support from Bush, Nathan

8. Open-JPL-TN 9.0 WFIRST Radiation Damage Study. Register Pixel Narrow Channel Modelling Clarke, Andy and Bush, Nathan

Table of Contents

1 The past, present and future of CCD technology 1

1.1 Thesis outline 6

2 The Wide Field Infra-Red Survey Telescope (WFIRST) 8

2.1 The demands of modern exoplanet science 8

2.2 WFIRST 12

2.3 The WFIRST Coronagraph Instrument (CGI) 14

2.3.1 The Shaped Pupil Coronagraph (SPC) 15

2.3.2 The Hybrid Lyot Coronagraph (HLC) 16

2.3.3 The CGI camera systems 18

2.4 Detector selection 18

2.5 Chapter summary: EM-CCDs for exoplanet science 22

3 The CCD 23

3.1 Overview 23

3.2 Charge generation 24

3.3 Charge collection 27

3.4 Charge storage 31

3.5 Charge transfer 35

3.5.1 Carrier drift 36

3.5.2 Carrier diffusion 41

3.5.3 High field transport 43

3.6 The CCD output circuit 44

3.7 Noise sources for CCDs 46

3.7.1 Shot noise 46

3.7.2 Dark current 47

3.7.3 Clock Induced Charge (CIC) 49

3.7.4 Read noise 50

3.8 CCD design variations 52

3.9 Summary of CCD technology in relation to the CGI 53

4 The EM-CCD 54

4.1 Structure of the CCD201-20 EM-CCD 54

4.2 The Electron Multiplication (EM) register 56

4.3 Noise sources for EM-CCDs 59

4.3.1 Effective read noise 59

4.3.2 The Excess Noise Factor (ENF) 60
4.3.3 Photon counting mode 62
4.4 Dark current and CIC 64
4.4.1 EM-CCD noise sources for the CGI 65
4.5 Additional performance considerations 66
4.5.1 Surface CTI of the EM register 67
4.5.2 EM-CCD ageing 69
4.5.3 EM register “glow” 71
4.6 Summary: BOL performance considerations for EM-CCDs 74
5 Radiation damage effects on CCD-based technologies 75
5.1 The near-Earth space environment 76
5.2 Orbit selection for WFIRST 79
5.3 WFIRST radiation environment 80
5.4 Proton damage effects in CCDs 85
5.5 Ionising effects 86
5.6 Non-ionising effects 87
5.7 Charge trapping sites relevant to CCD technology 88
5.8 Past studies of radiation damage on EM-CCDs 93
5.9 Cryogenic irradiations 94
5.10 Summary of radiation damage considerations for the WFIRST CGI 97
6 The WFIRST CGI radiation damage campaign 98
6.1 Campaign overview 98
6.2 Detectors for study and timeline for testing 100
6.3 The WFIRST room temperature irradiations 103
6.3.1 Facility 103
6.3.2 Shielding 104
6.3.3 Beam profile and dosimetry 107
6.4 The WFIRST cryogenic irradiations 109
6.4.1 Facility 109
6.4.2 Beam profile and dosimetry 109
6.4.3 Consideration of the final fluence (cumulative 7.5×10^{9} protons/cm^{2}) 109
6.5 Differences between the cryogenic and room temperature irradiations 110
6.5.1 Impact of beam energy 110
6.5.2 Biased vs unbiased irradiations 111
6.6 Experimental setup 111

6.6.1 Characterisation at the Open University 111
6.6.2 Characterisation at the Harwell facility 113
6.7 Test procedures and operating conditions 117
6.7.1 Methods for CTI measurement 117
6.7.2 Methods for dark signal measurement 119
6.8 Defect identification through “trap pumping” 120
6.9 Summary 126
7 Activation and isothermal annealing 127
7.1 Transient signals caused by charged particles 127
7.2 Thermal dark signal 128
7.2.1 Isothermal annealing of trapping sites 129
7.3 Summary 137
8 The impact of CTI on CGI performance 138
8.1 Extended Pixel Edge Response (EPER) 141
8.1.1 Parallel EPER 141
8.1.2 Serial EPER 147
8.2 First Pixel Response (FPR) 149
8.3 Fe^{55} CTI 152
8.4 Conclusions from CTI measurements and impact on the CGI 157
9 The impact of dark signal on CGI performance 159
9.1 Thermal dark signal 159
9.1.1 Pre-irradiation measurements 159
9.1.2 Post-irradiation measurements 161
9.1.3 Hot pixels 163
9.2 Parallel Clock Induced Charge (CIC) 165
9.2.1 Simulation of CIC generation 165
9.2.2 Device-device variation 166
9.2.3 Impact of clock voltage and operating mode 168
9.2.4 Impact of clock delay 169
9.2.5 Impact of temperature 171
9.2.6 Impact of irradiation 172
9.3 Summary of radiation study results 178
10 Defect identification in the CCD201-20 180
10.1 Implementing trap pumping for the CCD201-20 180
10.2 CCD201 trap pumping schemes 185

10.3 Experimental implementation 190
10.4 Results from trap pumping 192
10.4.1 General trends 192
10.4.2 The double acceptor state of the silicon divacancy (VV^{--}) 197
10.4.3 The “unknown” trap species 203
10.4.4 The single acceptor state of the silicon divacancy (VV^{-}) 206
10.4.5 The phosphorus vacancy complex (Si-E/PV) 210
10.4.6 The Si-A centre 215
10.4.7 Other defects 217
10.5 Summary of results and implications for the WFIRST CGI 217
11 Charge storage modelling in the CCD201-20 222
11.1 Introduction 222
11.2 Signal volume theory 222
11.2.1 CGI operating modes 224
11.3 Signal volume results for the CCD201 227
11.3.1 Models and experimental method 227
11.3.2 Image pixel results 231
11.3.3 Register pixel results 233
11.4 Implications for the CGI 235
11.5 Narrow channel modelling 237
11.5.1 Non-uniform charge density profiles 237
11.5.2 Narrow channel structures 239
11.5.3 Narrow channel image pixel 240
11.5.4 Narrow channel serial pixel 246
11.6 Conclusions from charge storage modelling for the CGI 251
12 Conclusions and future work 252
13 Bibliography 257

1 The past, present and future of CCD technology

The adoption of the Charge Coupled Device (CCD) for astronomical observations has changed our view of the Universe considerably. Once thought to be only useful primarily as a device for temporary data storage, the potential of the CCD was soon noted and presented to scientists at the Jet Propulsion Laboratory (JPL) who required an imaging technology for the Large Space Telescope (LST) (Boyle & Smith, 1970, Janesick, 2001). Complications with array size, cooling requirements and signal loss were successfully addressed in the development process. The implementation of mature devices onto ground based observatories cemented the CCD as the successor to photographic film for astronomical imaging, and development of space qualified devices soon followed (Janesick, 2001).

LST was renamed the Hubble Space Telescope (HST) and was the first telescope to adopt CCDs for space-based astronomical observations, shown in Figure 1.1. CCDs were used on 2 of the 4 original instruments to observe from the near infra-red to the UV (Jenkner, 1990). The achievements of Hubble are numerous and ground-breaking. Through observations of Cepheid variable stars, Hubble helped estimate the age of the Universe at approximately 13.7 billion years old (Freedman *et al.*, 2001). Black holes, once purely theoretical, were discovered by Hubble and are now thought to be at the centre of the majority of galaxies (Macchetto *et al.*, 1997). The observation of distant supernovae confirmed that the expansion of the Universe is accelerating with an as yet unknown cause, termed "Dark Energy" (Riess *et al.*, 2001). The discovery of organic molecules outside of the solar system was attributed to Hubble observations (Cardelli *et al.*, 1996), and a wealth of information on other astrophysical topics was returned that revolutionised the landscape of modern space science.

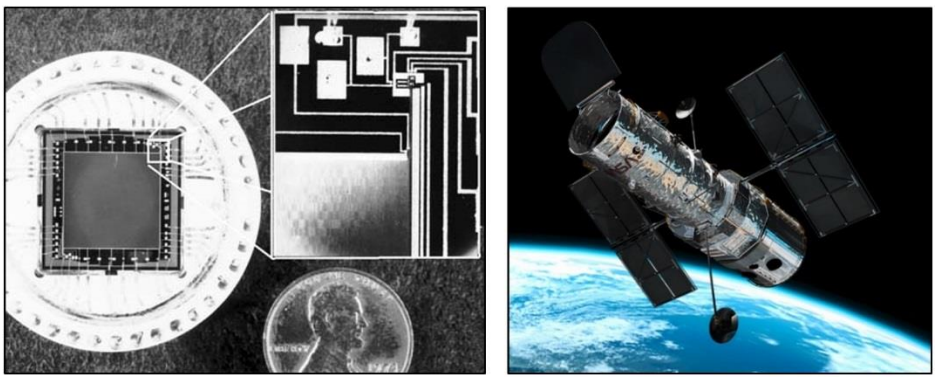

Figure 1.1 *Left: The Texas Instruments 800×800 pixel CCD developed for use in the Wide Field and Planetary Camera 1 (WFPC-1) of the Hubble Space Telescope (HST). A magnified view of the readout circuitry is also shown. Right: HST (Image Credit: NASA).*

The early success of CCDs on Hubble lead to the adoption of devices on the next generation of space observatories. Chandra, the National Aeronautics and Space Administration's (NASA's) X-ray observatory, utilised a focal plane of 10 CCDs for the Advanced CCD imaging Spectrometer (ACIS), launched as one of two instruments in 1999 (Garmire *et al.*, 2003). Chandra has provided a wealth of information on X-ray sources within the Universe and supported important discoveries concerning the behaviour and distribution of dark matter, X-ray generation from black holes and an additional measurement of the Hubble constant (Bonamente *et al.*, 2006).

The Cassini spacecraft used CCD based instruments to image Saturn, its moons and ring system (Smith *et al.*, 1981). The NASA Solar Dynamics Observatory (SDO) uses CCD technology to continually monitor solar activity and understand the influence of solar radiation on Earth and near Earth space (Pesnell, 2015). NASA's Kepler mission, launched in 2009, used the CCD focal plane array shown in Figure 1.2 to conduct a large-scale survey for extrasolar planets. The sensitivity of the CCD camera system permitted detection of the first Earth analogue planets and the mission has since catalogued over a thousand extrasolar planets in total (Batalha *et al.*, 2013).

The European Space Agency's (ESA's) Gaia satellite launched in 2013 with the largest focal array of CCDs ever built at the time, with 106 CCDs comprising of almost 10^9 pixels (Laborie *et al.*, 2007). Gaia will provide a three-dimensional map of our Galaxy by surveying a billion stars and provide information on the origin and evolution of the Milky Way. Instruments aboard ESA's Rosetta mission to comet 67P used CCD technology to image the surface topology of the comet to a level of detail never achieved before (Basilevsky *et al.*, 2015).

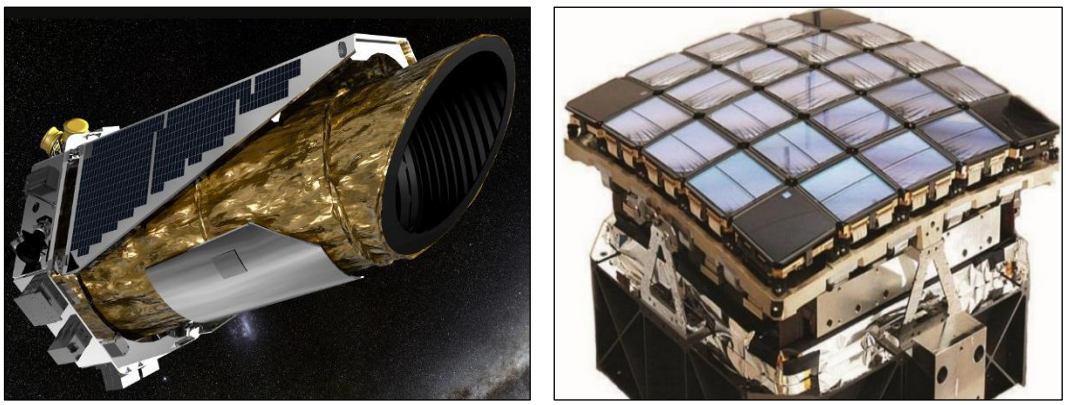

Figure 1.2*: Left: Kepler Space Telescope. Right: The Kepler focal plane array that consists of forty-two scientific CCDs. The array is bowed to account for natural field curvature introduced by the telescope optics. Kepler launched in 2009 as a dedicated "planet hunting" telescope. It has since catalogued over a thousand extrasolar planets. (Image Credit: NASA).*

CCD based instruments have therefore been instrumental to answering some of the fundamental science questions concerning the formation and evolution of galaxies, stars, planets and even the origins of life. However, as more discoveries are made, more questions arise to be answered. Both NASA and ESA have recently outlined their plans for the next decade of astronomical research based upon the results from current and previous science missions.

ESA's "Cosmic Visions" programme for the years 2015-2025 outlined the four main topics that future space missions should aim to address, including the conditions for the emergence of life, the science that drives our solar system, the fundamental physical laws of the Universe and the constitution of Dark Matter and Dark Energy (ESA Cosmic Vision Proposal, 2005).

Of the six missions selected as part of the Cosmic Visions programme, three are baselined to use state of the art scientific CCDs. The CHaractiersing ExOPlanets Satellite (CHEOPS) will be the first mission dedicated to searching for exoplanetary transits by performing ultra-high precision photometry (Beaudoin *et al.*, 1996). The PLAnetary Transits and Oscillations of stars mission (PLATO) will find and study a large number of extrasolar planetary systems with emphasis on the properties of terrestrial planets in the habitable zone around solar like stars (Catala *et al.*, 2009). Euclid is a mission to map the geometry of the dark Universe. The observatory will investigate the evolution of cosmic structures by measuring shape distortion of galaxies and clusters due to weak gravitational lensing (Laureijs *et al.*, 2010). The Visible Imager (VIS) instrument will use a total of 36 CCDs for the focal plane, an example device is shown in Figure 1.3.

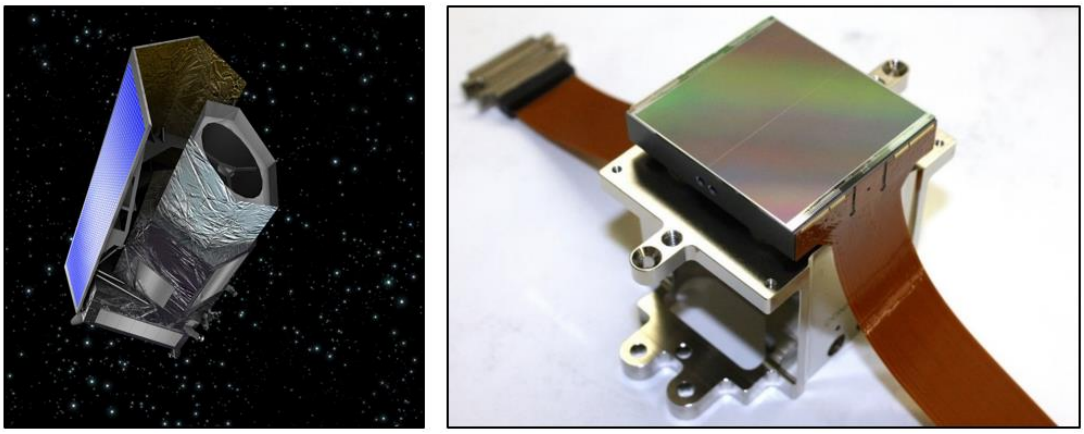

Figure 1.3*: Left: Euclid observatory. Right: Euclid Visible Imager (VIS) CCD273-84. The devices are 4k × 4k pixels in size (approximately 25 cm^2). They are a variant of a similar technology that was flown on the Solar Dynamics Observatory (SDO) with modifications to improve tolerance to radiation. Image Credit: ESA.*

A similar long-term science plan was outlined by NASA with the 2010 decadal survey. The priority science objectives included searching for the first stars, galaxies and black-holes that formed in the Universe, seeking nearby habitable planets and advancing understanding of the fundamental physics of the Universe (Spergel *et al.*, 2015).

The top recommended space based mission to fulfil these objectives was the Wide Field Infra-Red Survey Telescope (WFIRST) that will use a variant of CCD technology in an on-board Coronagraph Instrument (CGI) to perform direct observations of exoplanets and debris discs (Spergel *et al.*, 2013). The top recommended ground-based observatory was the Large Synoptic Survey Telescope (LSST), a telescope that will continually survey the night sky searching for moving and changing objects ranging from recent supernovae to nearby asteroids. The LSST focal plane consists of 189 CCD sensors, with 3.2 gigapixels at a total diameter of approximately 64 cm (Ivezic *et al.*, 2008).

CCD technology is therefore still being selected for use in large scale missions and will continue to have a role in ground-breaking scientific discoveries for many years to come. There are, however, challenges the technology faces in order to meet ever-increasing performance requirements. Operation within the space environment subjects the detectors to radiation which damages the device and degrades signal to noise performance (Hopkinson *et al.,* 1996). The effects of radiation damage were known at the time of the HST launch, however, it did not seriously impact science performance. Post-processing algorithms were also developed that were able to correct up to 97% of the effects of charge loss due to radiation damage. An example of such a correction is presented in the work of Massey *et al.* (2009) and illustrated in Figure 1.4.

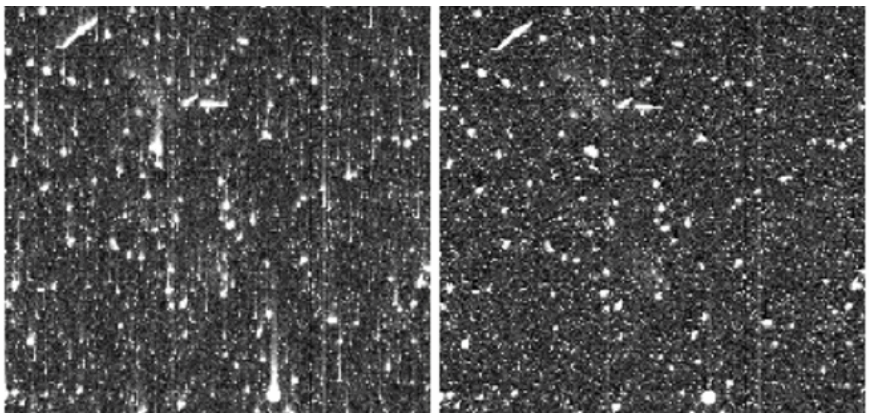

Figure 1.4*: Image degradation caused by radiation damage in an HST image. The signal intensity is shown in logarithmic scale to highlight the effect of the damage. The left panel shows "tails" along the direction of transfer due to the capture and release of signal from radiation-induced trapping sites. The corrected image is shown on the right panel. The charge tails have been removed through use of the properties of the trapping species responsible for the tails.*

For current and future missions, such as Gaia and Euclid, the effects of radiation damage are a much greater concern. Euclid, for example, will measure the distortion of light sources due to the effects of weak gravitational lensing. The main challenge for the mission is that radiation induced damage will distort the appearance of galaxies in a similar manner to that expected due to the weak lensing phenomena. The effects of radiation damage must therefore be corrected to an order of magnitude higher precision than implemented on HST. Such a correction requires detailed characterisation of the exact type of damage that has taken place within the silicon lattice (Hall *et al.*, 2012).

As the signal flux continues to decrease, the impact of radiation damage becomes more prominent. The WFIRST CGI is the most sensitive optical instrument to-date and is designed to directly image extrasolar planets and debris disks. Signal levels from planets of interest will rarely be above the single electron level, representing the ultimate limit of imaging performance. Each of the two coronagraph camera systems are baselined to use an Electron Multiplying Charge Coupled Device (EM-CCD), a variant of CCD technology capable of single photon imaging and so perfectly suited to the coronagraph application. The EM-CCD was predicted to provide the highest planet yield compared to competing technologies so long as noise sources can be appropriately mitigated, however, the impact of radiation damage is predicted to be severe (Harding *et al.*, 2016). In the single photon regime, a single silicon defect has the potential to continuously hide the planet signal and significantly diminish the planet yield.

For WFIRST, the characterisation of radiation induced damage is therefore more important than ever before. Small discrepancies in the type and magnitude of the damage have been shown to change the predicted instrument lifetime by a number of years (Bush *et al.*, 2016). The temperature at which the irradiation is performed, illumination pattern and operating mode all have a substantial impact on the effective science performance of the instrument. Understanding these phenomena in greater detail requires the development and implementation of techniques that, until this point, had only been theorised for use in large scale missions. If successful, however, these techniques have the potential to provide information that allows correction to such high order that the effects of radiation damage are much less of a concern. The long-term future of CCD technology at present therefore appears promising, so long as our understanding of radiation damage processes allows us to meet the increasing performance requirements of the next generation of space-missions.

1.1 Thesis outline

The WFIRST CGI is the most sensitive space-based optical instrument designed to date and aims to perform single photon imaging in the presence of radiation induced damage. This thesis follows a detailed investigation into the impact of radiation damage on the Coronagraph detectors, with a specific focus on how the properties of radiation induced trapping sites affect single-photon science.

The motivation for the WFIRST mission is presented within Chapter 2 in the context of modern exoplanet science. Discovery of an alien "pale blue dot" is seen by many to be the ultimate milestone of modern space science, and the WFIRST CGI represents a significant leap towards achieving that goal. At the heart of the CGI are detectors responsible for collecting the planetary signals, however, they introduce noise in the process. Appropriate detector selection was therefore a large focus of the mission design and resulted in a trade study that encompassed many competing state of the art technologies. EM-CCD detectors, in particular the CCD201-20, were predicted to provide the best planet yield for each of the coronagraph camera systems. The primary disadvantage of the EM-CCD was its low technological maturity, as it has yet to be flown on a large-scale space mission. Raising the maturity of the detector required in-depth studies on any risk the detector introduced when compared to the standard CCD counterpart, in particular the predicted performance prior-to and following a radiation dose consistent with the planned WFIRST mission. Understanding such risks requires a detailed understanding of the fundamentals of CCD and EM-CCD technology and how radiation damage can impact performance, discussed in Chapters 3, 4 and 5 respectively.

It is concluded that the primary source of damage is due to high energy protons that will give rise to displacement damage effects within the detectors for each camera system. The greatest problem for charge transfer based detectors such as the EM-CCD are radiation induced trapping sites that can capture and defer the planetary signal so that it is no longer detected. Understanding the true impact of radiation induced traps required a radiation damage study with measurements prior to and following irradiation with a proton fluence consistent with the WFIRST mission. The WFIRST irradiation campaigns are then discussed in Chapter 6, alongside the impact of cryogenic vs. room temperature irradiations and past investigations of a similar nature.

Chapters 8 and 9 describe the results of the irradiation campaigns, with discussion on how each of the different known defect species impacts Charge Transfer Inefficiency (CTI) measurements. Conclusions from these chapters include that the temperature at which the device is irradiated has a significant impact on the final predicted performance. With CTI identified as the greatest limitation to CGI science performance, attention then turns to amelioration strategies. The "trap

pumping" technique is introduced and development of the technique for the CCD201 is discussed in Chapter 10. The results of a trap pumping investigation into each of the four main defects thought to be responsible for CTI in a CCD are also presented, including trap densities prior to and following irradiation at room temperature. Chapter 11 discusses design modifications to the CCD201, aimed at improving both parallel and serial Charge Transfer Efficiency (CTE). Finally, a summary of key findings is given that spans the impact of irradiation temperature on EOL performance predictions, the future of defect identification using trap pumping and the benefit of customised EM-CCDs for single photon imaging for WFIRST and future space missions.

2 The Wide Field Infra-Red Survey Telescope (WFIRST)

The question of whether we are alone in the Universe had limited potential for science to answer until recent times. Many searches have been conducted for life in parts of own solar system (e.g. Klein, 1977), with additional searches proposed as future missions (Vago *et al.*, 2006), however, to date none have been successful in identifying living organisms even at the microbiological scale. Life outside the solar system will most likely be confirmed through direct observation of an extrasolar planet (hereafter, exoplanet) with properties analogous to that of our own (Spergel *et al.*, 2013). The eventual discovery of this alien "pale blue dot" is considered by many to be the greatest milestone of exoplanet science. The Wide Field Infra-Red Survey Telescope (WFIRST) represents a substantial advancement in the field of exoplanet detection and will be the first mission with the capability to directly image and characterise planets with properties similar to those within our solar system. This chapter introduces WFIRST in the context of modern exoplanet science. The leading techniques of exoplanet detection are discussed with their respective sensitivities to different regions of the exoplanet population. For the true detection of a planet that may sustain life, direct detection techniques offer a significant advantage. The CGI is introduced as an instrument specifically designed for direct exoplanet detection that requires an extremely sensitive detector to measure typical planet signals. The selection process that lead to the adoption of the EM-CCD is presented with respect to the projected exoplanet yield for 1 year of combined CGI observation time.

2.1 The demands of modern exoplanet science

Since the first confirmed discovery of an exoplanet in 1992 (Peale, 1993), the state of the art has advanced considerably and multiple techniques are now available to astronomers to detect and characterise planets depending upon the target's mass and distance from the parent star.

Transit photometry is responsible for the majority of exoplanet detections to date (Rauscher, 2015). The technique is based upon the principle that if a planet crosses in front of its parent star then the observed visual brightness of the star will fall by an amount that is proportional to the square of the planet's radius, shown by Figure 2.1.

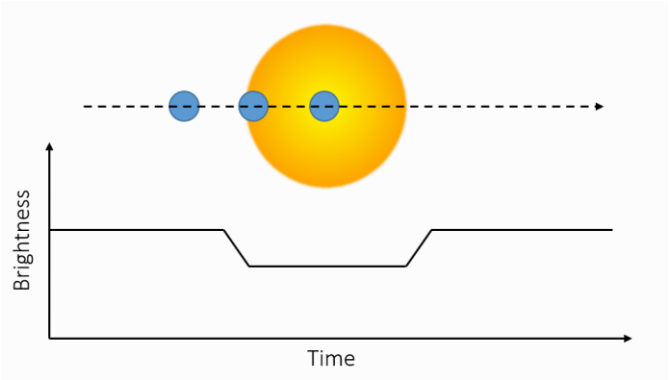

Figure 2.1: *Principle of Transit Photometry Technique. As the planet passes in front of the star, the apparent brightness decreases and manifests as a dip in the light curve. The fractional change in apparent brightness depends upon the ratio of the planet and host star's radii.*

Transit photometry was used by the largest exoplanet mission to date, Kepler, as well as ground based missions such as SuperWASP (Koch *et al.*, 2010, Pollacco *et al.*, 2006). While the method is useful to identify a large number of exoplanet candidates relatively quickly, it has disadvantages. The transits are only observable when the orbit of the planet is perfectly aligned with the viewpoint of the observatory. The probability of alignment is greatest for planets with small orbits and decreases with increasing orbital radius. The method is also sensitive to eclipsing binary star systems as well as planets, and so follow up observations are required to discount the presence of a binary star system. The measured dip in the intensity of the star is dependent on the planetary radius and orbital period, favouring larger planets that orbit the parent star quickly. NASA's Kepler mission has produced the largest number of confirmed exoplanet detections to date, however, the majority of these exoplanets are believed to be "hot", meaning they are likely too close to the parent star to harbour water. The loss of sensitivity with increasing orbital radius also means that, to date, few exoplanets have been discovered with properties analogous to the gas giants in our solar system. Due to this inherent bias in the detection technique, the current census of planets has been difficult to explain with standard theories of planet formation as the majority of confirmed planets have properties very different to those within our solar system. To remedy this, a complete survey of planets that includes the colder planets towards the outer edges of a solar system is required. (Spergel *et al.*, 2013).

To detect these colder planets, other detection techniques such as gravitational microlensing are more favourable. Microlensing surveys stare at dense stellar fields and detect the gravitational lensing of individual background stars when a foreground star passes directly across the line of sight. Figure 2.2 illustrates the detection principle; as the parent star passes in front of the source star, its gravitational field acts as a lens giving a factor of intensity magnification detectable from our solar system. If the parent star has a planet(s) orbiting around it, the gravitational field of the

planet gives rise to a detectable perturbation in the lens effect. The probability of the correct alignment for this observation is small, and so a very large number of background stars must be continually monitored to successfully implement this method.

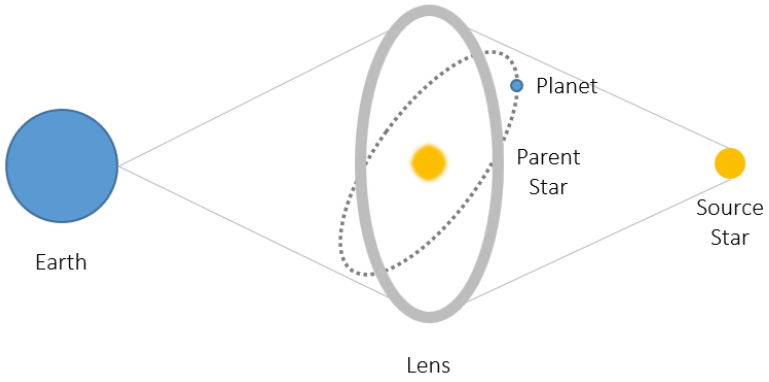

Figure 2.2: *Principle of the Gravitational Microlensing Technique. As the parent star passes in front of the source star, its gravitational field acts as a lens giving a factor of intensity magnification detectable from our solar system. If the parent star has a planet(s) orbiting around it, the gravitational field of the planet gives rise to a detectable perturbation in the lens effect. The probability of the correct alignment for this observation is small, and so a very large number of background stars must be continually monitored.*

Interstellar dust can be an issue when observing in the optical, however, in the infrared the dust is largely transparent. A large-scale microlensing survey performed in the infra-red therefore has the potential to complete the census of exoplanets begun by Kepler, extending the catalogue of known planets at and beyond a star's habitable zone and providing a more complete account of how the properties of planets are distributed.

The combination of transit photometry and gravitational microlensing can therefore complete the catalogue of exoplanets, however, the information they provide is often limited to properties such as mass, orbital radius and density. Transient spectroscopy can be used to detect compounds within the atmosphere of the planet but the technique is limited to the transit time and made difficult through the relatively small fraction of light that passes through the planet's atmosphere. Direct imaging is seen as a more powerful method to directly probe the atmosphere of the planet and confirm compounds consistent with a biological fingerprint. Direct detection is complicated by the requirement of a high-contrast optical system that allows the planet-star system to be resolved; the light from the star must be supressed as much as possible while maintaining the ability to image the small fraction of light reflected by the planet. The planets of highest interest are within the habitable zone and so quite close to the parent star. This translates into a small working angle for the detector system, making it particularly sensitive to opto-thermal

instability of the observatory (jitter). A coronagraph is an optical system suited to such an environment and has the potential to enable direct exoplanet detection and characterisation.

The original coronagraph, designed by Bernard Lyot in 1939, is shown by Figure 2.3. Modern coronagraphs use a more complicated optical beam train to improve performance however the underlying principles remain consistent. The first objective lens receives light from the telescope and forms an image of the solar disk and corona. The occulting disk blocks the majority of the light from the star, however, a small fraction diffracts past the disk and is focused by the field lens onto the Lyot stop, away from the focal plane. Light from the corona is able pass the occulting disk and is focused by the field lens and second objective lens into the focal plane, providing an image similar to that shown by Figure 2.4.

While coronagraphs are well suited to image exoplanets, significant technological development will be required to meet the contrast and working angle requirements to image planets similar to those within our own solar system. For comparison, the original coronagraph used to image the corona of the Sun required a contrast[1] of approximately 10^{-6} over a Field of View (FOV) of approximately 1900". A stellar coronagraph suitable for exoplanet imaging could be expected to image a star over a FOV of order 10^{-4} " and require a working contrast of 10^{-10}. Meeting such requirements with modern technology remains extremely challenging but will be absolutely necessary to directly image Earth-analogue planets.

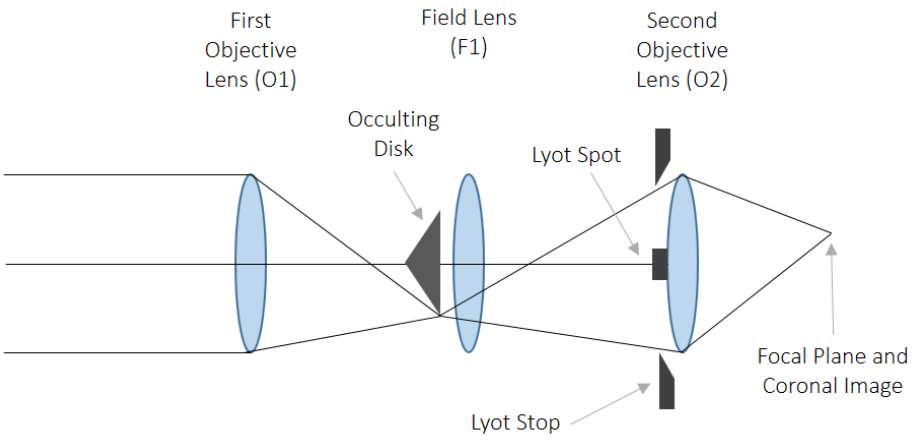

Figure 2.3: *The original Lyot coronagraph design used to image the corona of the Sun.*

[1] For a coronagraph, the contrast is defined as the ratio between the peak brightness of the central star and the mean brightness of the field of background stellar speckles averaged over a specified area in the coronagraph FOV.

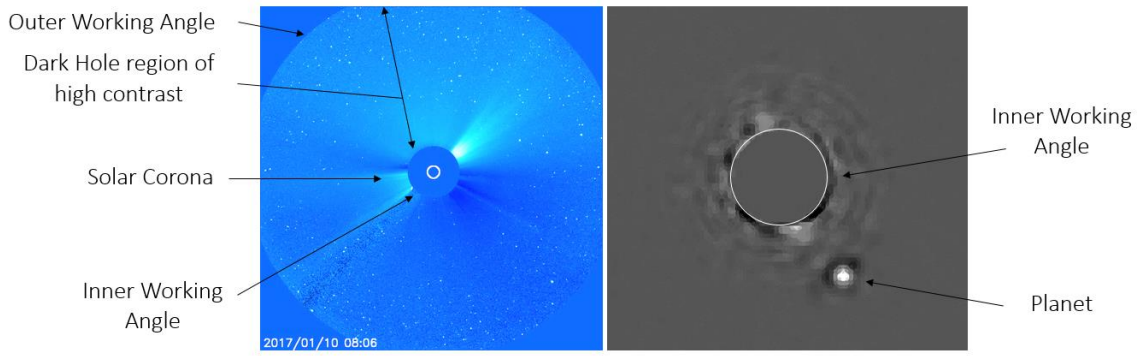

Figure 2.4: *Left: Example image obtained from the Large Angle and Spectrometric COronagraph (LASCO), an instrument onboard the Solar and Heliospheric Observatory (SOHO). Light within the inner working angle is supressed allowing fainter objects between the inner and outer working angle to be resolved. The FOV for this image is of order 500'' and the contrast is of order 10^{-6} (Brueckner et al., 1995). Right: Ground based coronagraph image from the Gemini Planet Imager showing planet Pictoris b* (*Macintosh et al., 2014*). *The image is of a similar format to what the WFIRST CGI shall produce.*

2.2 WFIRST

Modern exoplanet science has highlighted two key requirements for future observatories to advance the state of the art:

1. A large-scale microlensing survey in the infrared is required to augment to the population of planets discovered by Kepler and provide a more complete census of the planetary population.
2. The development of direct imaging techniques that will be able to image and characterise exoplanets with properties similar to those within our own solar system.

WFIRST (Figure 2.5) plans to address each of these requirements. The observatory is due to launch in 2026 and has a nominal 6-year mission duration. The telescope has a 2.4 m (Hubble class) primary mirror that feeds two on-board instruments, the Wide Field Imager (WFI) for microlensing surveys and the Coronagraph Instrument (CGI) for the direct imaging of exoplanets and debris disks. The WFI is the instrument that will perform the large-scale surveys of exoplanets in the infrared using the gravitational microlensing technique. The optical design of the telescope coupled with the focal plane array provides a 0.28 square degree FOV at 0.11 arc second pixel scale; equating to HST quality imaging over a FOV that is over ×200 larger than HST's Wide Field Camera 3. The focal plane consists of a 6 × 3 array of HgCdTe sensors that each have 4k × 4k pixels, totalling over 300 megapixels in total (Pasquale *et al.*, 2014). The WFI will be capable of

detecting planets beyond the snowline[2] up to 100 AU and, combined with Kepler, will provide a catalogue of planets that encompasses all planet types that are currently theorised (Figure 2.6).

The CGI shall be the first of its kind and significantly advance direct imaging capabilities. It is the result of at least 10 years of research and development at JPL, with each aspect of the design tailored to meet the demands of the low-light, high contrast imaging required for direct exoplanet science (Noecker *et al.*, 2016).

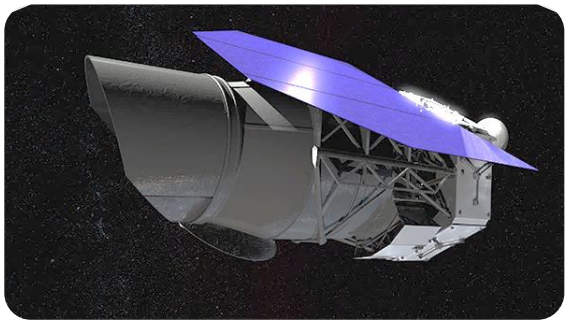

Figure 2.5: *WFIRST mission concept.*

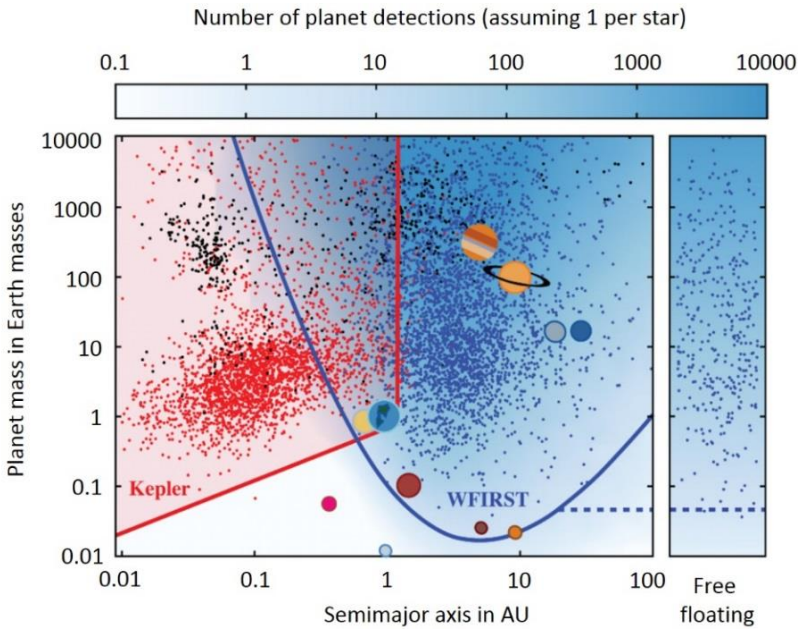

Figure 2.6: *Exoplanet population diagram adapted from Spergel et al. (2015). While Kepler is able to detect larger planets with small orbit radii through transit photometry, WFIRST is able to detect planets beyond the snowline through gravitational microlensing. The combination of both measurements provided a detection range that spans all of the planets within our own solar system, each of which are super-imposed onto the diagram.*

[2] In general, the snowline is the particular distance from a star where it is cold enough for volatile compounds such as water or methane to condense into ice. In this context, the reference is to the snowline of water.

2.3 The WFIRST Coronagraph Instrument (CGI)

The WFIRST Coronagraph Instrument (CGI) will, for the first time, be able to detect and characterise planets analogous to those within our own solar system. A total of three camera systems are on-board, the imager and Integral Field Spectrometer (IFS) are for planet imaging and characterisation, while the Low-Order Wave Front Sensor (LOWFS) is used for wave-front correction.

Blocking the parent star with a simple field stop such as in the classic Lyot coronagraph results in a diffraction pattern that can still be orders of magnitude brighter than any planet signal. This diffraction pattern must therefore be supressed, and many competing strategies exist that promote either working angle or total contrast. Planets and debris disks differ greatly in size, shape and brightness and so one single optical configuration would not return the best science from the mission. Instead, the CGI can operate in two separate modes; a Hybrid Lyot Coronagraph (HLC) for exoplanet photometry and a Shaped Pupil Coronagraph (SPC) for exoplanet spectroscopy and debris disk characterisation.

Both the HLC and SPC use the same core beam train with a different pupil mask that is switched using a rotary mechanism. There are several inclusions designed to reduce interference due to jitter, supress residual starlight speckle and hence maintain contrast stability over long integration times (10^2-10^3 seconds). Light from the telescope focal plane is first projected onto a fast steering mirror that corrects line of sight jitter. The starlight suppression optics then remove the light due to the parent star and any diffracted light that would otherwise obscure light reflected by the target planet. A pair of deformable mirrors act to remove speckles due to optical imperfections within the proceeding components of the beam train. The signal is fed-back into a low order wave front sensor which in connected via a feedback loop to the fast steering and dynamic mirrors such that the correction for optical misalignment is continuously adjusted as necessary. An overview of the instrument is shown by Figure 2.7, where it is shown that each of the focal plane arrays share the majority of the core optics but the use of the CGI as either a SPC or HLC is controllable.

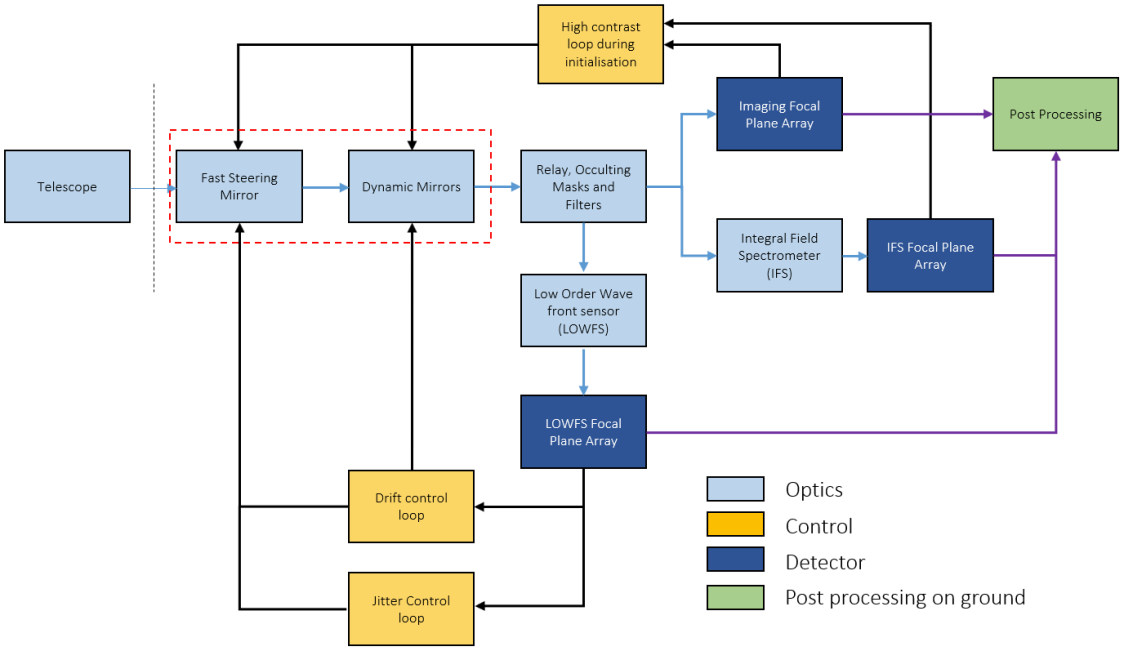

Figure 2.7: *Block diagram of optical beamtrain with key components identified.*

2.3.1 The Shaped Pupil Coronagraph (SPC)

The SPC uses binary pupil masks with tailored openings that control the pattern of diffracted light, distributing it outside of the desired dark hole region. Diffraction is strongly suppressed in some regions of the plane at the expense of much brighter diffraction patterns in other sacrificial regions that are blocked by an additional mask. The result is a "bow-tie" shaped image of high contrast, shown by Figure 2.8, which is projected into the lenslet array and spectrally dispersed before projection onto the detector. For imaging with the SPC, an alternate mask and field stop are selected that gives rise to a more conventional projection of a dark hole between an inner and outer working angle over 360°. Each of the masks, field stops and example projected images for the SPC are shown in Figure 2.8 and are taken from Noecker *et al.* (2016).

These two masks were selected based on the respective advantages for imaging and spectroscopy. The imaging mask creates a dark field with large outer working angle but increased inner working angle (Krist *et al.*, 2016, Noecker *et al.*, 2016). Both shaped pupil masks are tolerant to low-order wave front errors since any pointing error gives rise to an offset to the diffraction pattern as opposed to reducing the contrast within the dark hole. The shaped pupils are also achromatic and therefore highly suitable for spectroscopy as they can be used over a large bandpass.

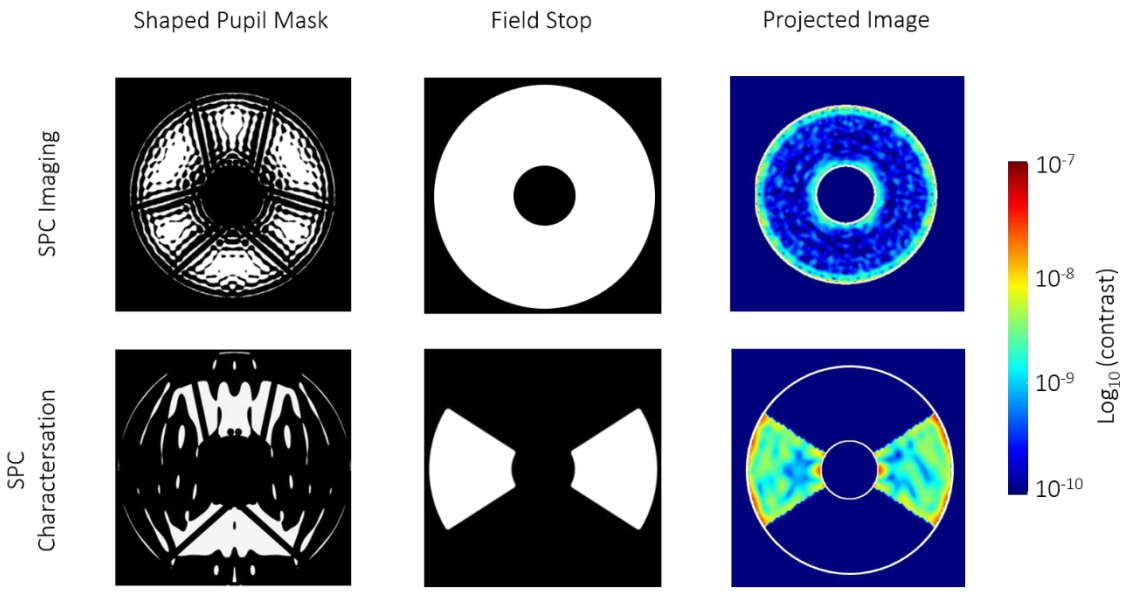

***Figure 2.8**: Shaped Pupil Coronagraph imaging and characterisation masks, field stops and projected images. The projected images are simulations taken from Krist, Nemati, & Mennesson, 2016. The designs may undergo further revisions before launch. The projected image consists of a dark hole of high contrast bound between the inner and outer working angles (white circles). For the SPC imaging mask, this is a 360° region, while for the characterisation mask a "bowtie" region is produced. Planet/disk imaging and characterisation will be conducted in these regions and will appear similar to that shown by Figure 2.4.*

2.3.2 The Hybrid Lyot Coronagraph (HLC)

The HLC is a modification of the classic Lyot coronagraph, which begins starlight suppression with a mask that has an occulting spot at the image of the star. The spot is apodised (tapered) in order to limit the degree of diffracted starlight that is projected to the next stage of the system. The remaining diffracted starlight is then suppressed by an additional matching Lyot mask at the next stage of the system. The key components are shown in Figure 2.9. The HLC is more sensitive to jitter but can achieve the higher contrast at certain working angles required for the imaging of planets. Unlike the SPC, the HLC is severely impacted by any obscuration in the telescope. The existing WFIRST telescope has six support struts and a central obscuration due to the positioning of the secondary mirror, shown by Figure 2.10. The telescope was donated to NASA by the National Reconnaissance Office (NRO) and modifications to the design were minimised in order to control cost. The support struts will likely retain their position for the final mission configuration. The struts introduce diffraction effects are compensated for through use of deformable mirrors that alter the wavefront as needed.

In summary, each operating mode provides a specific benefit for the different observational requirements of photometry and spectroscopy; the SPC is less sensitive to the effects of jitter

which would otherwise affect spectroscopic observations whereas the HLC can achieve a higher contrast for planet imaging within a given working angle. The ability to operate in either mode allows the system to take full advantage of other aspects of the telescope while reducing the dominant aspect of optical noise that affects each measurement. A more detailed account of each of the CGI operating modes and some of the finer details on the optical design and predicted performance can be found in Krist, Nemati, & Mennesson, 2016.

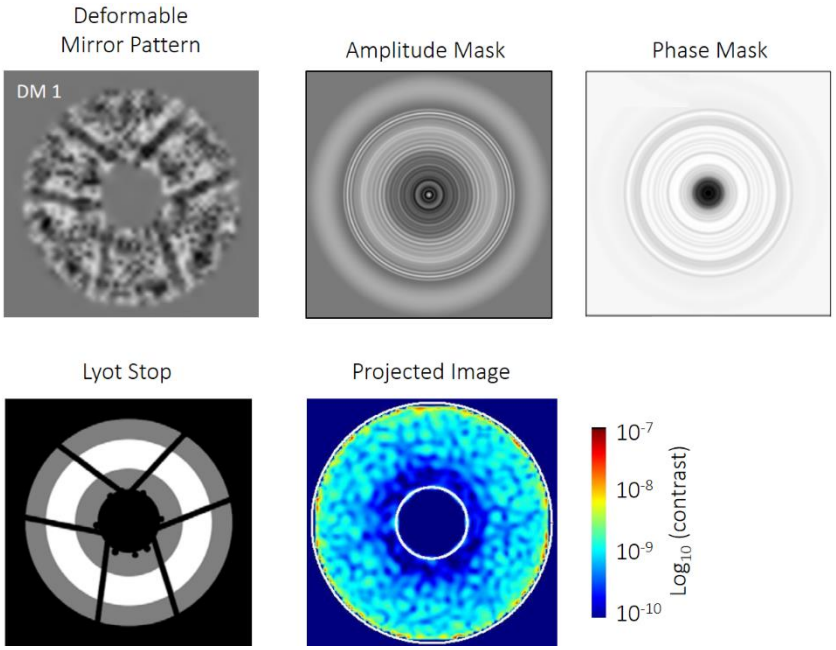

Figure 2.9: *HLC deformable mirror patterns, amplitude and phase masks, Lyot stop and an example projected image (assuming no jitter). The images are taken from Krist, Nemati, & Mennesson, 2016. The designs may undergo further revisions before launch. The deformable mirror pattern is one of two variants and is customised to account for the presence of the support struts shown in Figure 2.10. The amplitude mask is tapered to reduce diffraction. The Lyot stop pattern is shown in grey alongside the telescope support struts. The planet search is conducted in the dark hole bound by the inner and outer working angles (Figure 2.4).*

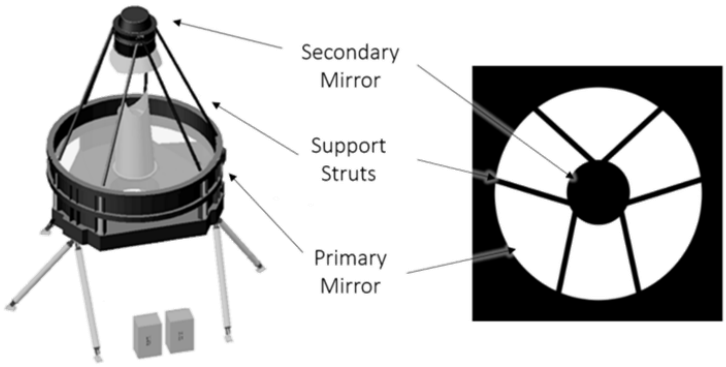

Figure 2.10: *Positioning of the support struts on WFIRST and the resulting wavefront* (Krist *et al.*, 2016).

2.3.3 The CGI camera systems

Following the masks and filters, the signal is fed into the focal plane of either the imager or IFS. Only one instrument can be used at any given time. For the imager, the projected image will consist of a dark hole of high contrast (as shown in Figure 2.9 and Figure 2.8) where the search for the planet will be conducted. The planet images will consist of a PSF that is spread within the dark hole depending upon the operating mode of the CGI.

For the IFS, a lenslet array spatially samples the dark hole with approximately 3×3 lenslets per PSF core. The PSFs are then fed to a two-element prism that spectrally disperses the signals along a single axis which is projected onto the image sensor, shown in Figure 2.11. The raw images from both the imager and IFS will have their contrast further improved through post-processing algorithms once the data has been received by the ground station. This post-processing will include data from a calibration star from which the residual speckle field is measured and then subtracted from that measured from the target star, thus increasing the total contrast. This post processing will be most useful for the identification of smaller planets that are closer to the parent star, where starlight speckle is expected to be equal in magnitude to the planetary signal.

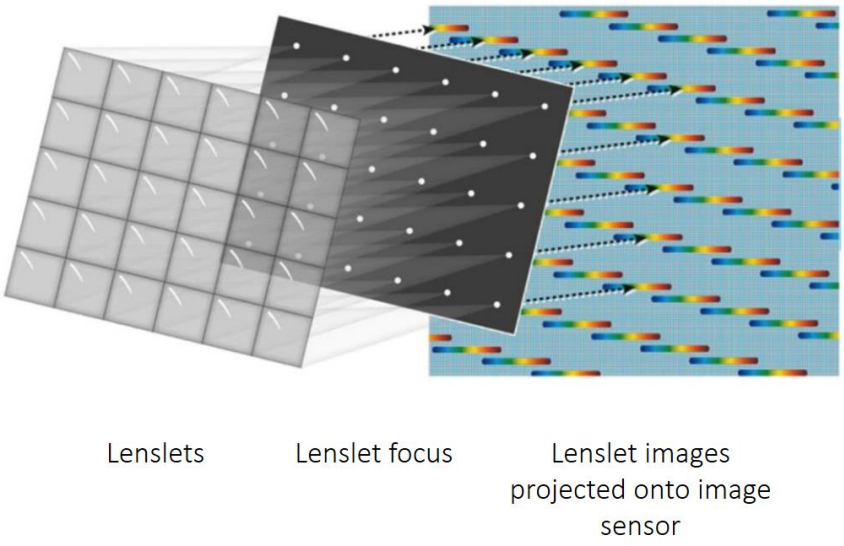

Figure 2.11: *Lenslet array used for the IFS whereby a pinhole mask is clocked with respect to the rows of the image sensor in order to optimise the separation between neighbouring spectra on the detector thereby reducing spectral crosstalk (Harding et al., 2016).*

2.4 Detector selection

For both the imager and IFS, the processed image will be projected onto a detector that will digitise the result for post-processing. The lower limit of optical throughput for the coronagraph optics is estimated at 40%, meaning the majority of the already scarce signal photons are lost in the process of starlight suppression (Krist *et al.*, 2016). The detector represents an additional

mechanism for signal loss since it will have a total non-perfect Quantum Efficiency (QE) for a given wavelength that further reduces the fraction of detectable photons. The coronagraph operating bands lie between 500 and 1000 nm (i.e. between the visible and near infra-red (NIR)) for which silicon solid state detectors exhibit high QE and are easily integrated into electronic subsystems. To evaluate the most suitable detector choice for the mission, a trade study was performed by Harding *et al.* (2015) in which candidate silicon-based detectors were ranked based on compliance with performance requirements for the instrument, flight heritage, the desired format and predicted scientific yield from a coronagraph model.

The candidate sensors fell into into 4 categories; scientific CCDs, scientific Complementary Metal Oxide Semiconductor (sCMOS) sensors, hybrid silicon CMOS arrays and Electron Multiplying CCDs (EM-CCDs). Scientific CCDs offered the highest Technological Readiness Level (TRL) since they have been successfully incorporated into a number of large scale space missions such as HST, Kepler and Gaia. CCD QE can be tailored according to the required wavebands through application of specialised anti-reflection coatings. For operation in the NIR, deep depletion technology exists whereby the charge collection depth of the device is extended to correspond with the increased absorption length of longer wavelength photons. Backside Illuminated (BI) devices exhibit near perfect QE in the visible and are technologically mature, commercially available and exist in the desired format. The limitations of CCDs include higher than desired read noise (minimum of ≈ 2 e^- RMS) which can also only be achieved in slow scan operation (up to around 200 kHz) and susceptibility to radiation damage that can degrade the detector throughout the mission lifetime.

Scientific CMOS sensors have advanced considerably throughout the past decade to the point where some sensors are able to offer sub-electron read out noise suitable for low light imaging (Chen *et al.*, 2012). CMOS detectors comprise two-dimensional arrays with a photodiode and readout circuitry in each pixel. The design of the CMOS image sensor allows column parallel readout, increasing the frame rate and mitigating potential noise sources that CCDs suffer from due to the charge transfer process. The limitation at the time of the trade study was the lack of a variant that offered high QE in all of the CGI passbands as well as providing low read noise compared to the CCD counterpart. The technology is also less mature than the CCD equivalent, with the Fairchild CIS2051 (sCMOS detector used in the study) attaining an estimated TRL of 4 as of 2016 (Harding *et al.*, 2016, Heim *et al.*, 2009), compared to some CCDs which had a TRL of 9 at the time of the study.

The hybrid silicon CMOS array selected for study was the HyVisi™ H4RG-10 for the Joint Milli-Arcsecond Pathfinder Survey (JMAPS) program. The HyVisi™ hybrid detectors consist of an interconnecting photodiode array to a CMOS readout circuit. The sensors therefore benefit from the high QE of silicon photodiodes and the low noise of the CMOS readout. The devices also have

the ability to read non-destructively, permitting removal of cosmic rays. The key disadvantage was the higher read noise (≈5 e^-) which made them unsuitable for the low flux conditions of the CGI (Simms *et al.*, 2007).

Electron Multiplying CCDs (EM-CCDs) are a variant of traditional CCD technology whereby an in-built charge multiplication mechanism amplifies signal prior to readout (Jerram *et al.*, 2001). Conjunction of the multiplication mechanism and the standard output amplifier of a CCD results in a factor reduction in the read noise equal to the applied multiplication gain. The read noise floor of standard CCD technology (minimum of ≈2 e^- RMS) is therefore eliminated, along with a relaxed constraint on pixel rate. EM-CCDs can be operated in either standard analogue mode (AN) or photon counting mode (PC), whereby the output of the multiplication register is set to a binary value and can provide an additional performance benefit. The majority of the design of the EM-CCD is identical to that of a scientific CCD and so benefits from decades of research, development and space flight heritage. Despite being considered for space-based instruments in the past (Smith *et al.*, 2006), at the time of writing they have not been used within a space environment and so have a lower TRL than standard CCDs. The promise of sub-electron read noise, high QE and low dark current made them very attractive to the CGI application.

From each of these categories, a total of 7 detector models were included within the trade study. Three scientific CCDs were included that were either baselined or used in large scale space missions. Two EM-CCD variants were studied, including a standard and deep depletion variant with enhanced QE in the NIR CGI band. For each detector, appropriate performance characteristics were fed into a JPL coronagraph performance model that evaluated the observing time required to reach a S/N ratio of 5 (deemed adequate for planet detection) for the CGI imaging and spectroscopy passbands. A detailed discussion of the results can be found within Harding *et al.*, (2016), however, the key findings are summarised within Table 2.1 and Figure 2.12, that shows the projected exoplanet yield for each technology. It was discovered that the EM-CCD offered the best performance in each of the CGI imaging bands compared to competing technologies. The standard variant offered greater performance than the deep-depletion EM-CCD for the simulated conditions since the reduced QE in the NIR bands was offset by the increased dark current exhibited by the deep-depletion variant. The standard scientific CCD technology was able to compete with both the sCMOS and HyVisi™ detectors across all passbands, while maintaining the advantage of higher TRL. The EM-CCD had a lower TRL yet retained the option of operating as a standard CCD with the multiplication register disabled. The technology therefore provided a situation whereby a significant performance benefit was attainable while retaining the mitigation strategy of operating as a standard CCD if necessary. As

a result of the study, the EM-CCD, in particular the commercial off the shelf (COTS) CCD201-20, was baselined as the detector for both the imaging and spectrograph camera systems.

Table 2.1: *Baselined performance requirements for candidate sensors for the WFIRST CGI alongside detector candidate values, taken from Harding et al. (2016).*

Parameter	sCMOS	Euclid CCD	HST CCD	Gaia CCD	JMAPS HiViSi™	EMCCD Std AN	EMCCD DD AN
ENF	1	1	1	1	1	1.41	1.41
CIC (e^-/pix/fr)	0	3×10^{-3}	3×10^{-3}	3×10^{-3}	0	3×10^{-3}	3×10^{-3}
I_{dk} (e^-/pix/sec)	7×10^{-3} (233 K)	5.5×10^{-4} (153 K)	5.5×10^{-3} (190 K)	1×10^{-3} (158 K)	1×10^{-3} (170 K)	3×10^{-5} (165 K)	5×10^{-4} (165 K)
RN (e^-)	1.5	3.6	3.1	4.6	5	0.2	0.2
QE (550 nm)	55	83	63	90	84	92	92
QE (660 nm)	52	83	65	89	89	90	90
QE (890 nm)	12	40	25	24	85	27	53

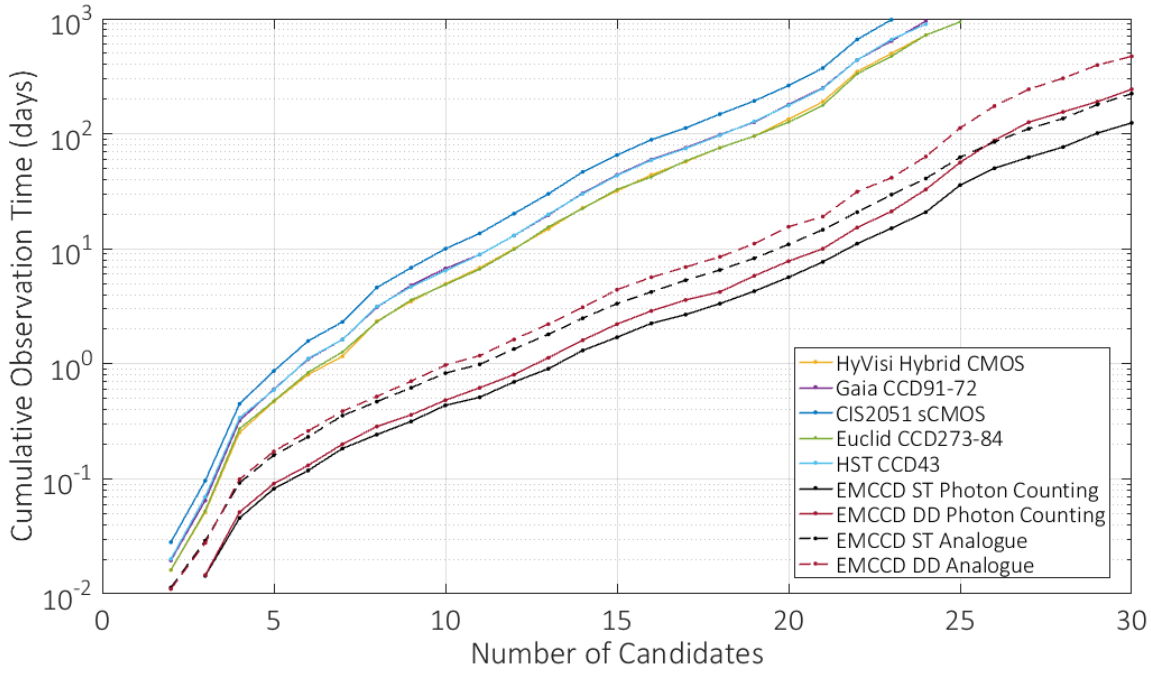

Figure 2.12: *Analytical prediction of observation time required to reach S/N = 5 versus the number of planets for each of the detector candidates. Adapted from Harding et al. (2016). This analysis applied to the CGI imager operating in HLC configuration at 550 nm using the HLC design as of January 2014.*

2.5 Chapter summary: EM-CCDs for exoplanet science

Exoplanet science within the coming decades is founded on two key requirements; the extension of the known catalogue of planets compiled by Kepler to incorporate colder planets with longer orbital periods, and the development of direct detection technology to aid the eventual confirmation of an alien "pale blue dot" with properties consistent with the Earth. The NASA WFIRST mission stands as a direct answer to each of these requirements, with the WFI and CGI separately satisfying each requirement yet remaining complementary in nature. As a technology demonstration, the CGI is an impressive display of optical engineering and will be the most sensitive optical instrument ever built at the time of launch. The EM-CCD has been selected as the detector for the instrument due to its sub-electron noise capabilities corresponding to a higher number of planet detections within the nominal mission duration. The one disadvantage of the EM-CCD was the low TRL, estimated as level 6 at the start of the study. TRL 6 describes technology that has been developed but not yet fully demonstrated and integrated into a subsystem representative of the coronagraph application. Improving the TRL of the detector prior to launch was deemed necessary to ensure that the CCD201-20 could perform in line with the expectations of the coronagraph throughout the mission lifetime. As is often the case, performance translates into the balance between signal and noise for the detector system. Performance at Beginning of Life (BOL) is dominated by intrinsic device noise sources that can be optimised through alteration of the operating conditions of the detector. Throughout the mission, however, radiation damage will degrade the device performance characteristics. The optimum operating conditions at the start of the mission may therefore not offer the best science performance throughout the entire mission lifetime. It is also possible that at some point in the mission, the detector may cease to adequately function due to the effects of radiation damage, thus severely impacting the science yield of the instrument. The act of improving the TRL of the detector therefore required knowledge of the best operating parameters of the device both at the BOL and EOL, which in turn required a detailed understanding of how CCD based technologies operate and can be optimised for this specific application. Discussion now turns to the underlying operating principles of the CCD with a focus on the specific case of WFIRST.

3 The CCD

The CCD201-20 EM-CCD that has been baselined for use on both the imaging and spectrograph camera systems of WFIRST is a variant of standard CCD technology that has been flown on a number of large scale space missions and has rich technological heritage. The longevity of CCD technology as a detector for infra-red through to X-ray applications is predominantly founded in the excellent properties of silicon as a detector material which can exhibit near perfect detection efficiency. This Chapter presents an overview of CCD technology, operating principles and a discussion of the dominant noise sources in the context of the WFIRST CGI.

3.1 Overview

The Charge Coupled Device (CCD) is a semiconductor-based image sensor capable of resolving the spatial distribution of incident radiation over a wide range of energies. The basic device structure is shown in Figure 3.1 and consists of an image area, readout register and output amplifier that perform the respective roles of signal storage, transfer and voltage conversion. The EM-CCD baselined for the coronagraph follows the same overall architecture, with an additional register for electron multiplication, discussed in the following chapter. The image area is photo-sensitive and is subdivided into an array of elements known as pixels. Each pixel behaves as a Metal Oxide Semiconductor (MOS) capacitor, and typically consists of 3-4 electrodes layered upon an insulator and silicon substrate. During image capture, optical light incident upon the photosensitive image area generates charge carriers through the photoelectric effect. If a bias is applied to one or more of the pixel electrodes the carriers will accumulate within the resultant potential well. Once image capture is complete, the charge can be transferred across the array through application of timed voltage pulses to each of the phases within a pixel in a process known as clocking. Charge is transferred in this way from the image area to the readout register, which functions similarly. The register terminates with output electronics that convert the analogue signal into a voltage for processing and reconstruction of the image. The fundamental operation of the CCD can therefore be split into four physical processes; charge generation, charge storage, charge transfer and digitisation, now discussed in more detail.

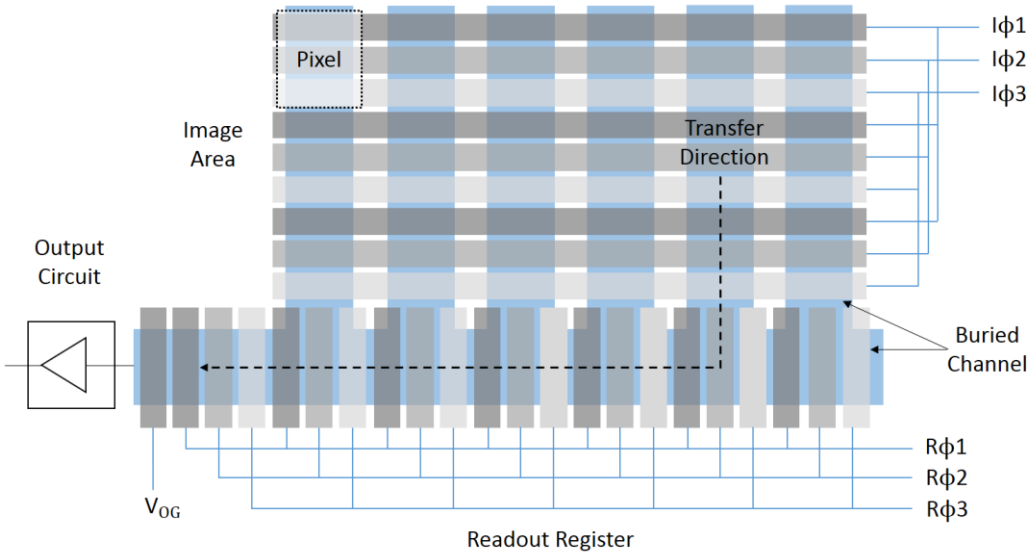

Figure 3.1: *Basic CCD structure showing the image area, readout register and output circuit. Throughout frame integration, a phase within each of the pixels is biased high that allows any photo-generated signal to collect beneath it. The charge is then transferred to the output through the sequential clocking of charge between pixels in the image area followed by the readout register. The analogue signal in electrons is converted into a voltage and digitised.*

3.2 Charge generation

The photo-sensitive nature of the CCD is owed to the crystal structure of the semiconductor substrate, which for optical and X-ray applications is predominantly silicon. A pure silicon crystal exhibits a "diamond" crystal structure, shown in Figure 3.2, whereby the 4 electrons in the outermost orbitals of the atom form covalent bonds with each of the nearest neighbours.

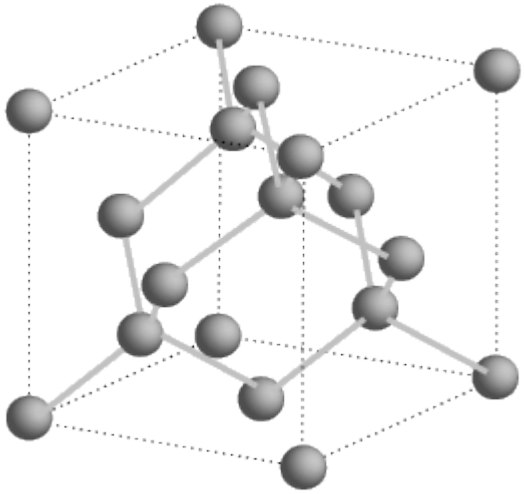

Figure 3.2: *The "diamond structure" of silicon, responsible for its properties as a semiconductor* (Kittel & Holcomb, 1967).

The fermionic nature of the electron prohibits the occupation of a single energy state by more than one particle and so the repeating crystal structure gives rise to a quasi-continuous "band" of allowed energies. Electrons localised to a single parent atom lie within the valence band and de-localised electrons are confined to the conduction band. The valence and conduction bands do not overlap at any point within momentum space, classifying silicon as a semiconductor material. The minimum energy difference between each band is termed the "band-gap" and is approximately 1.12 eV at 298 K (Sze & Ng, 2006). Silicon is an indirect semiconductor in the sense that the valence band maximum and conduction band minimum do not align within momentum space, as can be seen in Figure 3.3.

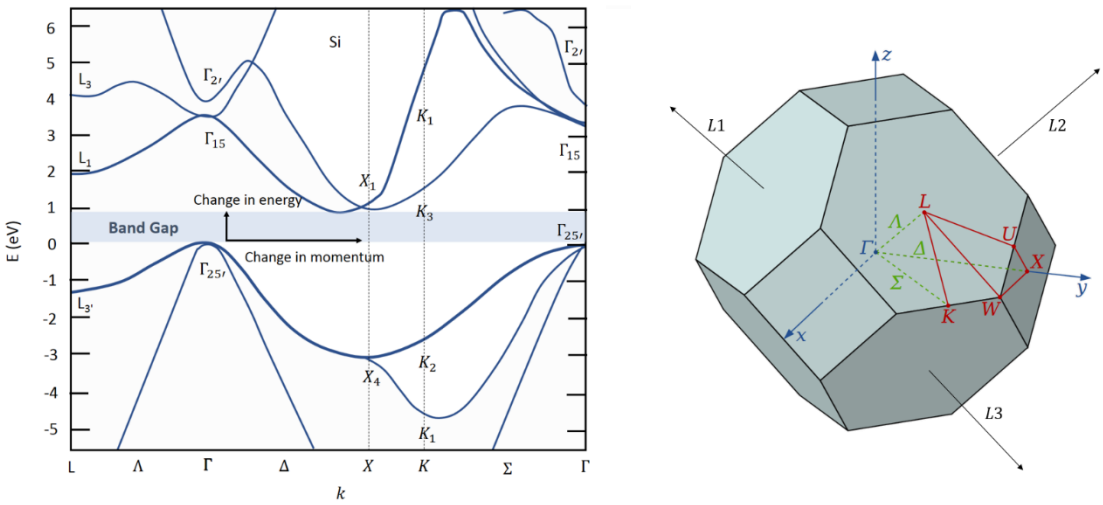

Figure 3.3: *Left*: *Band structure of silicon illustrated using an energy-momentum ("E-k") diagram adapted from Kittel & Holcomb, 1967. Right: First Brillouin zone of an FCC lattice (silicon) with symmetry labels relevant to the E-k diagram. A Brillouin zone can be loosely defined as a unit cell of the reciprocal lattice. It is constructed as a set of planes closer to the origin (Γ) than any other reciprocal lattice point. The x-axis, k, is the wavenumber, linearly related to the momentum of the carrier. The blue shaded region indicates the band-gap and corresponds to the difference in energy between the conduction and valence band minima. Points of symmetry and high interested are summarised in Table 3.1. The lines within the E-k diagram correspond to available quantum mechanical states for electrons in the material in different directions of the wavenumber (k) relative to the lattice. For a transition between the two bands, a change in momentum is required as well as energy, designating silicon as an "indirect" semiconductor.*

Table 3.1*: Description of symbols used in Figure 3.3*

Symbol	Description
Γ	Center of the Brillouin Zone
K	Middle of an edge joining two hexagonal faces
L	Center of a hexagonal face
U	Middle of an edge joining a hexagonal and a square face
W	Corner Point
X	Center of a square face
Δ	Directed from Γ to *X*
Λ	Directed from Γ to *L*
Σ	Directed from Γ to *K*

An electron can only make a transition from the valence to conduction band though absorption of both sufficient energy and momentum from other particles. The change in energy can be provided through absorption of a photon within a specific wavelength range, the photoelectric effect, or through Coulombic scattering of another particle such as a high-energy electron or proton.

The change in momentum is typically provided by the lattice vibrations, quantised as phonons, with a density that increases as a function of temperature. At typical CCD operating temperatures (150 to 300 K) the phonons follow Maxwell-Boltzmann statistics and have a distribution of energies and momenta that can also be supplied to the electron during scattering. The energy supplied through a phonon scattering event can compensate for energy supplied by a photon with an energy $E < E_g$ (band gap energy), for example NIR wavelengths. This dependence on phonon energy also means that the detection efficiency of longer (IR) wavelengths decreases with temperature, since less phonons with appropriate energy are available to partake in the necessary scattering.

For photons with an energy $E > E_g$, the remaining energy E_g-E_λ is translated into the Kinetic Energy (K.E.) of the mobile electron that is then typically lost to the lattice through acoustic phonon scattering. If the photon energy is high enough (> 3.1 eV) the remaining K.E. can generate additional carrier pairs through impact ionisation (Sze & Ng, 2006). High energy photons (e.g. X-rays) can generate “clouds” of charge within a device in this manner. The number of electrons collected can then be used to infer the energy of the X-ray. As the photon energy continues to rise, the likelihood of interaction through the photo-electric effect continues to decrease. Above 50 keV, the cross section due to Compton scattering begins to dominate and this becomes the primary interaction mechanism with the lattice, shown in Figure 3.4. The properties of the silicon

lattice therefore facilitate interaction of photons with wavelengths of approximately 1 µm and shorter until the attenuation length greatly exceeds the dimension of the crystal. In practise, this range is constrained further by the capability of the device to collect and store the charge generated at a given wavelength. The capability of silicon as a detector material is therefore primarily bound by the constraints on device dimensions necessary for a CCD to successfully collect, store and transfer charge.

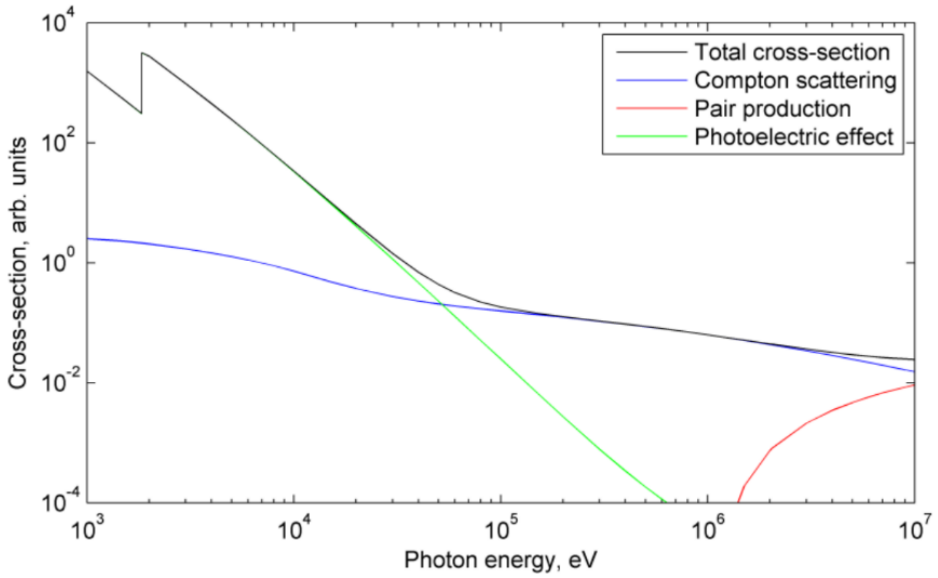

Figure 3.4: *Cross section of interaction with the silicon lattice as a function of incident photon energy (raw data obtained from NIST).*

3.3 Charge collection

For a photon to be detected the generated electron(s) must be collected within a CCD pixel. The basic pixel structure of the CCD is modelled on the MOS capacitor, which consists of an electrode layered upon an insulator and silicon substrate. The substrate is uniformly doped with boron and has an additional phosphorus N-implant to a depth of approximately 1.5 µm below the semiconductor-insulator interface. In the presence of the silicon lattice boron acts as a charge acceptor, with 3 electrons in the valence band, whereas phosphorus acts as a charge donor with 5 electrons in the valence band. At typical CCD operating temperatures (> 150 K) the thermal energy of the lattice is sufficient to ionise these impurities, creating a population of free electrons on the donor side of the junction which migrate to the acceptor side. The result is a region of fixed space charge, termed the depletion region, with an intrinsic electric field directed across the junction. The field can be enhanced further by biasing the polysilicon gate above the junction. A positive bias applied to the N side of the junction (termed reverse biasing) extends the width of the depletion region by attracting electrons from donor atoms to the gate and forcing holes into the P region of the junction, leaving a large region of fixed space charge, termed the depletion

region, that gives rise to a potential well structure. This is the state of operation for a biased pixel gate in a CCD, shown in Figure 3.5.

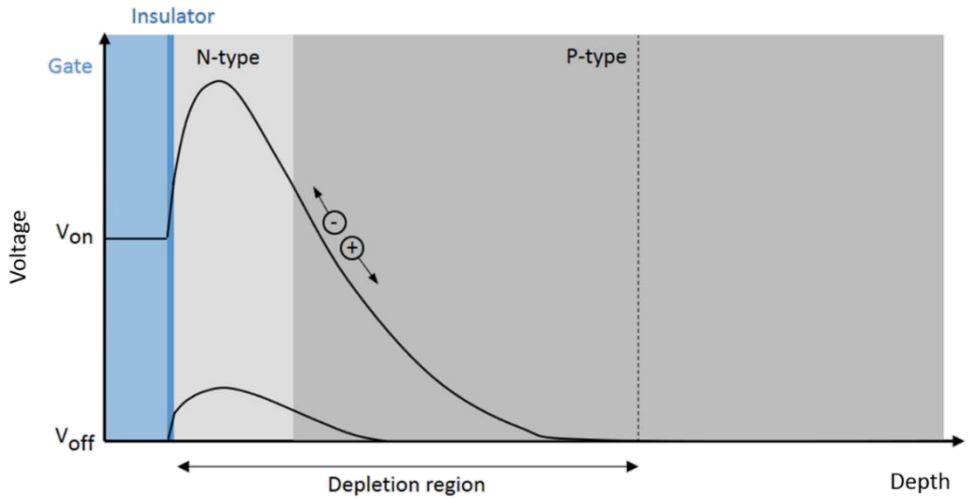

Figure 3.5: *Structure and potential profile of a buried channel CCD (side view). The depletion region is defined as the depth at which the potential due to the P-N junction reaches the substrate potential.*

The potential profile within the depletion region has a maximum that peaks below the semi-conductor interface (approximately 0.3 - 1.0 µm depending upon the device structure) that corresponds to the charge storage location for photo-generated electrons. The semiconductor-insulator interface has a high density of charge trapping sites (> 10^{10} cm^{-2} eV^{-1}) that degrades performance if charge comes into contact with this region. Storage of charge below the maximum allows the signal to avoid these sites, which greatly improves charge transfer performance.

Beyond the potential maximum, an electric field extends into the device that will act to promote the movement of charge towards the charge storage location. The distance between the interface and the point this electric field becomes equal to the substrate potential is termed the depletion depth. Charge generated within this region will be efficiently collected by pixels of the device, whereas charge that interacts beyond this depth must diffuse towards the depletion region to be collected. There is a fixed period of time that charge is able to diffuse into the region of the electric field before it recombines with a hole in the valence band and is lost as signal. This time is termed the recombination time, and is of order of a few milliseconds for typical CCD operating conditions (Sze & Ng, 2006). This time, coupled with the thermal velocity of the electron, gives rise to a diffusion length of approximately 5 µm which may be lateral as well as vertical with respect to the pixel layout.

Ideally, signal should be photo-generated within the depletion region so that it is efficiently collected within the pixel. The variable attenuation length across the optical photon wavelength

range places limits on the QE for standard device designs. The generation of electrons due to the absorption of incident light of a given wavelength follows the Beer-Lambert Law:

$$I(z) = I_0 e^{-\alpha(\lambda)z} \qquad \text{Equation 3.1}$$

where I is the remaining photon intensity at depth z, I_0 is the original intensity and α is the absorption coefficient of the material at a given wavelength, λ. The absorption length for silicon as a function of wavelength is shown by Figure 3.6, with typical device dimensions labelled.

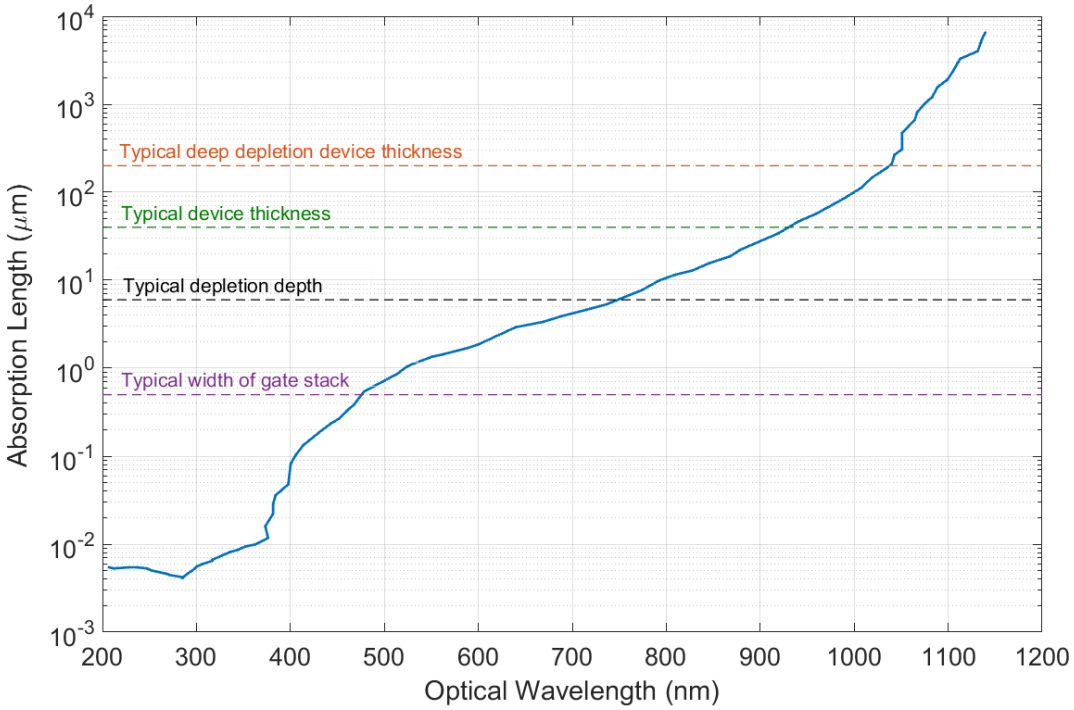

Figure 3.6: *Attenuation length as a function of wavelength with typical device dimensions labelled.*

Photons with wavelength below 500 μm have an absorption length comparable with the total width of the gate stack on the front side of the CCD (≈ 0.5 μm). QE within this wavelength range for Front Illuminated (FI) devices is therefore low since photons interact within the polysilicon gates and gate dielectric before reaching the silicon substrate. The opposite is true for infra-red wavelengths since the absorption length is greater than the width of the depletion region (≈5 μm), and often longer than the standard depth of the device (≈20 μm). The QE of intermediate wavelengths is also limited by reflection and transmission losses within the gate stack, such that it peaks at approximately 50 % with appropriate Anti-Reflection (AR) coatings suited for optical photons. Figure 3.7 shows the QE for a CCD 97 EM-CCD. The peak QE is approximately 50% and corresponds with an attenuation length comparable to the depletion depth.

Back-Illuminated (BI) devices and deep depletion devices were designed to improve QE for certain wavelength ranges. BI devices are those which have had the substrate layer removed to allow direct illumination of the epitaxial layer from the rear of the device such that the incident light

can interact directly with the substrate. The removal of the substrate layer and thinning of the device gives rise to a large number of charge trapping sites at the back-surface. Electrons generated near the back-surface may therefore be lost prior to collection, limiting the improvement in QE at short wavelengths. These back-surface traps are typically mitigated through a low-energy boron implant at the back surface, which provides a built-in voltage step that promotes the movement of charge towards the depletion region. The thinned silicon has high reflectivity, and so AR coatings are applied depending upon the desired wavelength response. BI devices with appropriate AR coatings have peak QE that exceeds 90%; and are typically used to improve response in the UV, visible and soft X-ray wavebands. Figure 3.7 shows the QE for the e2v back-illuminated CCD201 that peaks at approximately 90% for the selected AR coating and shows measurable photo-response over the 350-1000 nm wavelength range.

Deep depletion devices were fabricated to improve response and spatial resolution in the NIR waveband. The absorption length exceeds the depletion depth of standard devices once the wavelength surpasses 750 nm. Light may interact in the field free region, but then must diffuse towards the depletion region to be collected. It should be remembered that charge can diffuse laterally as well as vertically, and any lateral diffusion can act to degrade the spatial resolution of the detector if the charge is collected in a pixel adjacent to the generation location. To improve response in this wavelength regime, devices are made thicker and with a lower resistivity substrate that allows the depletion region to extend deeper into the device, often to the back surface. The limit on the background doping concentration is of order 10^{13} cm^{-3} (boron), which corresponds to a resistivity of order 2000 Ωcm and a maximum depletion depth for standard operating voltages of around 70 µm. The depletion region is extended further through application of a large negative bias to the substrate (of order -70 V). Additional modifications must be included in the output circuitry of these devices to prevent breakdown (Jorden, Pool, & Tulloch, 2002).

Backside biasing allows the depletion region to extend to the back surface of the device up to a thickness of 100-200 µm. The CCD261 is an example of a deep-depletion device manufactured by e2v Technologies, Figure 3.7 shows the QE response of this device in comparison to the aforementioned CCD97 and CCD201 devices that are much thinner (≈ 20 µm substrate). There is measurable photo-response up to wavelengths of approximately 1050 µm - close to the theoretical limit of silicon as a detector material.

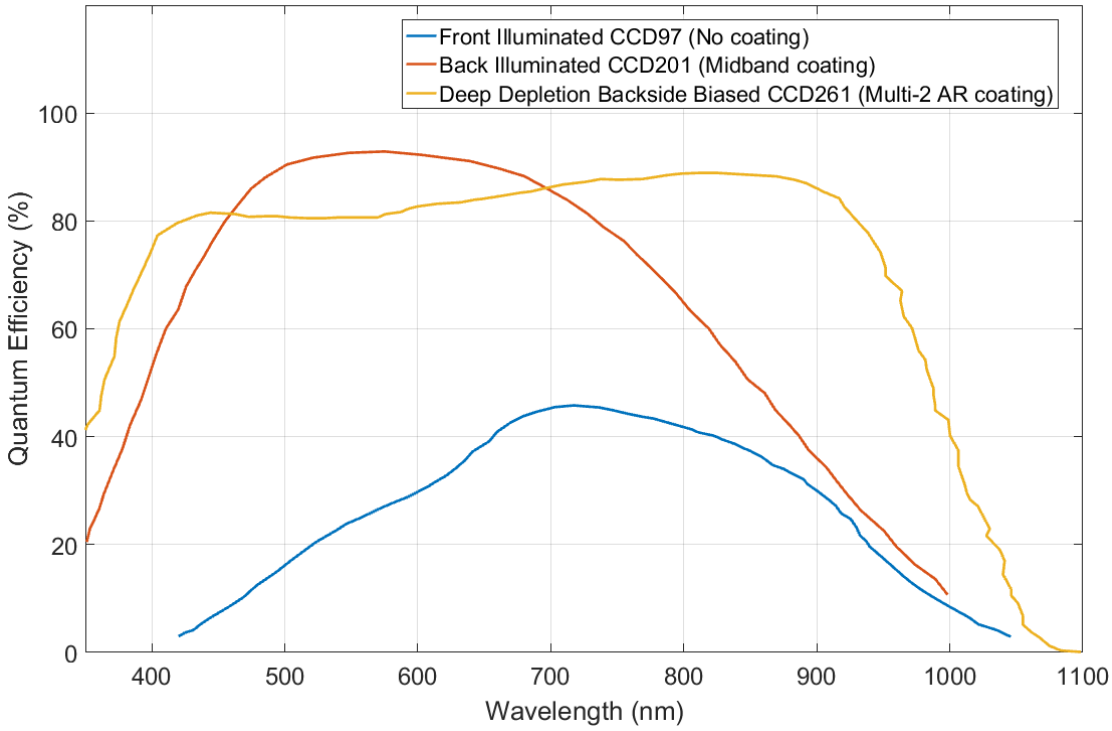

Figure 3.7: *QE as a function of wavelength for a standard FI device vs. BI and backside biased deep depletion variants. The BI device exhibits higher QE across the UV and visible since the silicon is illuminated directly. The increased device thickness and depletion depth for the CCD261 increases QE significantly in the NIR waveband. Data was obtained from device datasheets (e2v Technologies, 2015).*

3.4 Charge storage

Following generation and collection, charge is stored within the potential well generated by the buried channel structure and geometry of the pixel. For convenience, CCD dimensions are labelled X, Y, Z where X denotes the direction parallel to charge transfer, Y is directed into the device and Z is in the direction perpendicular to transfer.

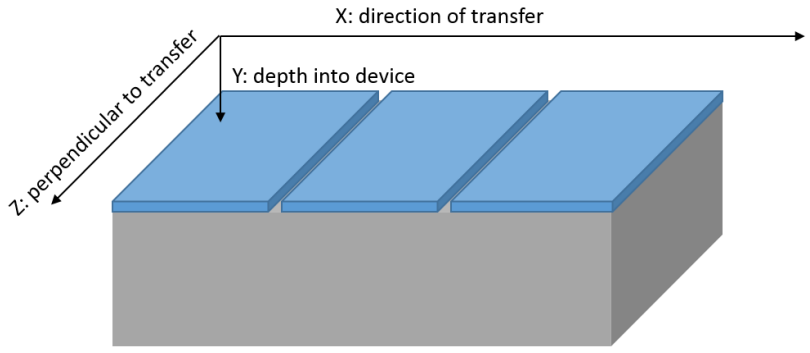

Figure 3.8: *Labelling of dimensions with respect to device structure and charge transfer.*

The “packet” in which the charge is stored is bound by a potential well structure that takes a different shape in each dimension and in turn limits the volume within which the majority of the charge is stored. The limit on the charge storage volume is due to a balance between the thermal energy of the electron and the potential barrier provided by the pixel. Under thermal equilibrium, the average thermal energy of a conduction band electron is given by:

$$K.E. = \frac{3}{2} k_B T \qquad \text{Equation 3.2}$$

which equates to an average energy of approximately 0.04 eV at 298 K. The individual energies follow a distribution that can be modelled by Maxwell-Boltzmann statistics for small charge packets (<1000 e^-) and typical CCD operating temperatures (> 150 K). The constant random thermal motion means the electron is best represented as a diffuse region of charge density as opposed to being confined at a single point. The charge density is confined by the potential well and distribution of energies for the charge packet, with a limit of 5σ from the mean energy distribution containing > 99% of the charge packet. The volume of the charge packet can therefore be estimated to reasonable accuracy by imposing this limit and equating it to the distance over which the corresponding change in voltage occurs in each dimension (Holland, 1993):

$$V = \frac{4}{3} \pi s_x s_y s_z \qquad \text{Equation 3.3}$$

where $s_{x,y,z}$ is the distance over which the corresponding change in voltage equals the mean thermal energy + 5σ in each dimension. This assumption is only valid for situations where the peak charge density is not comparable to the dopant density within the buried channel, which typically corresponds to signal levels of less than 1000 e^- but can vary according to the device.

For direction of transfer (*X*), the field structure is bounded primarily by the bias structure of the gate. Charge may be stored under many bias configurations (including no gate bias at all) so long as there exists a potential barrier to prevent charge flowing across the pixel boundary. In the absence of additional doping and for symmetric gate bias conditions, it follows that the charge storage location is at the centre of the gate in this dimension.

For the direction into the device (*Y*), the potential peak typically lies approximately 0.5-0.8 µm from the semiconductor-insulator interface with a location that varies according to the doping structure, gate bias with respect to substrate and amount of signal contained within the well. For an empty well under normal bias conditions (10 - 12 V), the voltage step between the interface and maximum is at least a few volts. This barrier is orders of magnitude above the thermal energy of the electron and so prevents charge interacting with surface trapping sites.

For the *Z* direction, the field is bounded by the channel stops; regions of silicon that are not implanted with the buried channel dopant in order define the edge of the pixel. In the absence of additional doping and for symmetric bias conditions, it follows that the charge storage location is at the centre of the gate in this dimension (e.g. Figure 3.9, Figure 3.10).

As the signal size within the potential well is increased, the positively charged doping atoms begin to become compensated. The result is that the effective doping concentration is reduced by a level comparable to the signal being stored. This becomes important for signal levels above approximately 1000 e^-, as the peak charge storage density reaches $\approx 10^{16}$ $e^- cm^{-3}$ (i.e. equivalent to the background doping concentration). The maximum charge storage capacity is termed the Full-Well Capacity (FWC), with a theoretical limit equal to the total number of doping atoms between the channel maximum and semiconductor-insulator interface. In practise, charge begins to bloom into adjacent pixels or encounter surface trapping sites before this condition is reached. The FWC is therefore specified when either of these conditions are met since charge transfer performance begins to measurably degrade in this regime (Janesick, 2001).

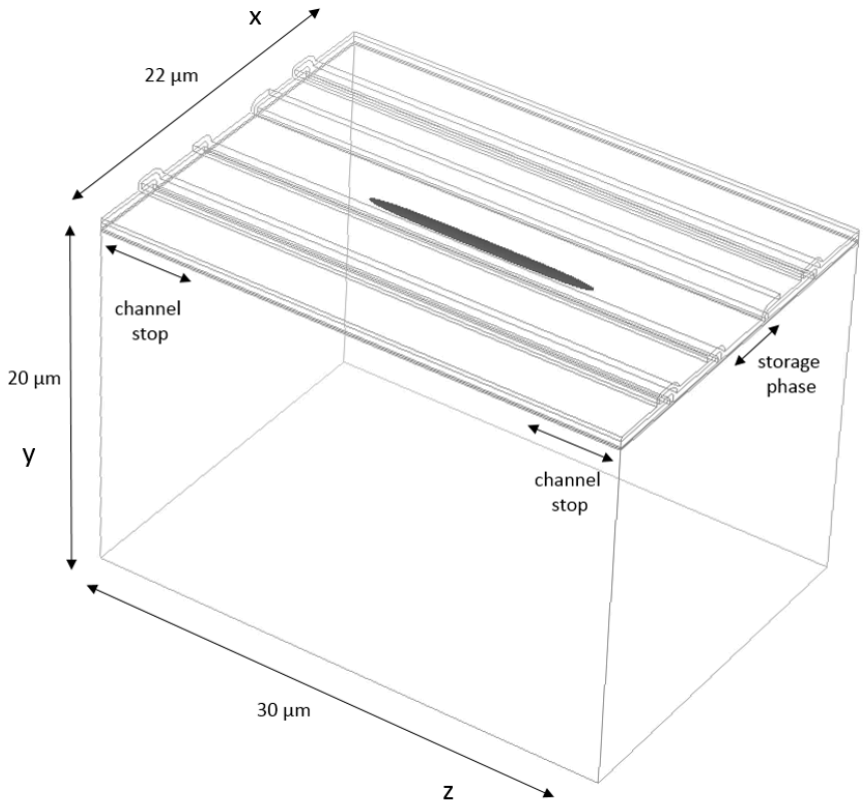

Figure 3.9: *Example pixel structure simulation (performed by author) with a collecting phase biased to 12 V containing approximately 1 e^- of signal charge. The iso-surface shows the boundary at which the electron concentration is above 10^{10} $e^- cm^{-3}$. For reference, the background doping concentration is 10^{16} cm^{-3}. It can be seen that the charge spreads laterally (Z) the most, since this is the dimension with the smallest electric field towards the centre of the pixel.*

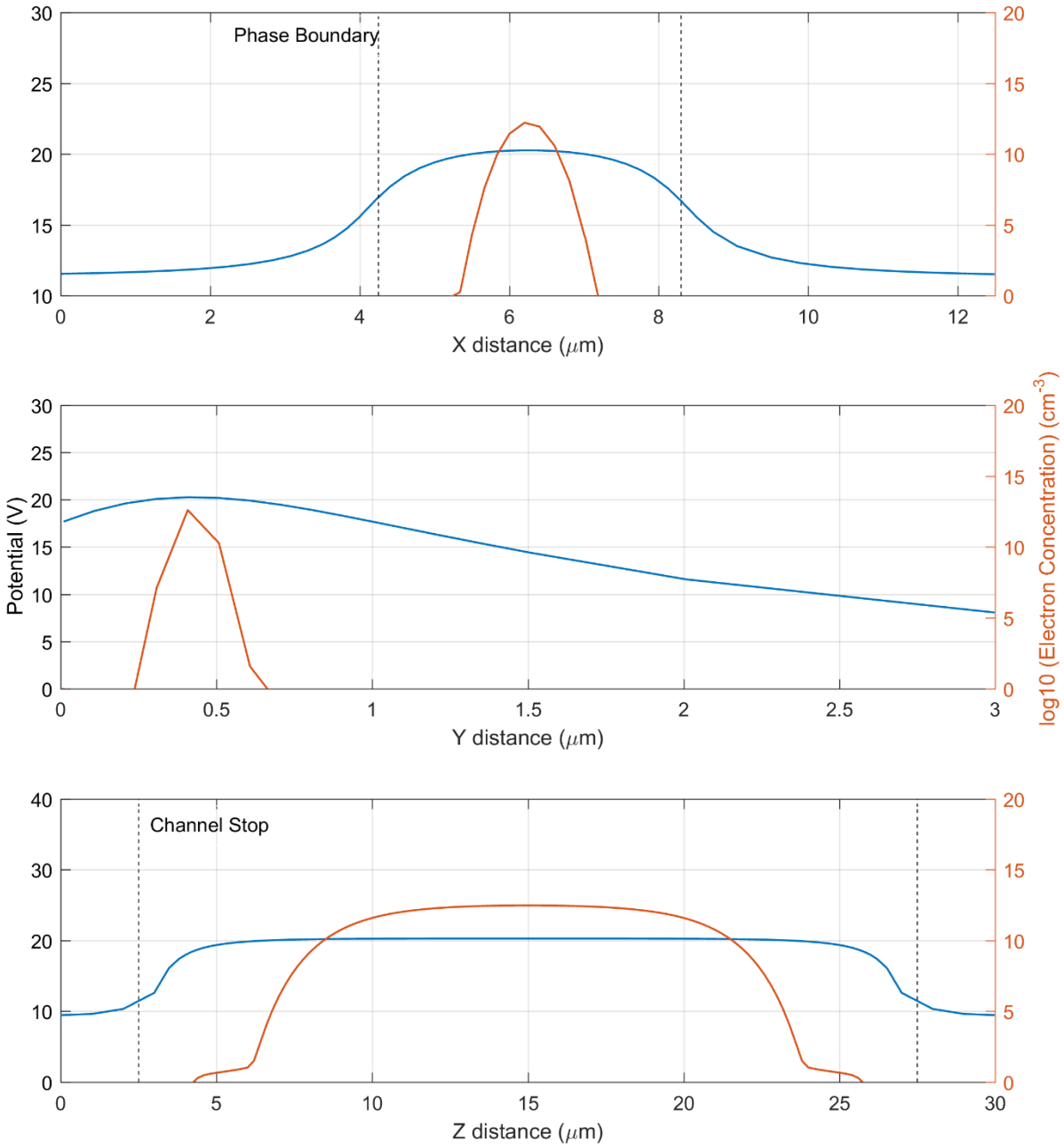

Figure 3.10: *3D TCAD simulation (performed by author) of how the potential and electron concentration vary beneath the collection phase for a signal size of approximately 1 e^-. It can be seen that the charge spreads laterally the most, since this is the dimension with the smallest electric field towards the centre of the pixel.*

3.5 Charge transfer

Following generation and storage, the charge must be transferred pixel by pixel to the output node. The transfer process is typically performed at least a thousand times in both parallel and serial directions and equates to a distance of a few centimetres for a standard device. Efficient charge transfer is crucial to overall device performance and is quantified through the measure of Charge Transfer Efficiency (CTE), defined as the fraction of charge successfully transferred from one pixel to the next. For computational purposes, CTE is often specified in terms of Charge Transfer Inefficiency (CTI); defined as the fraction of charge left behind in a single pixel transfer. Modern scientific CCDs are capable of CTI of order 10^{-6} when appropriately optimised (Jorden *et al.*, 2002).

The process of charge transfer within a CCD can be split into three stages, illustrated by Figure 3.11:

1. Charge is confined to a potential well beneath the starting phase. The surrounding phases are biased in such a way that a potential barrier exists between one pixel and the next so that charge remains confined to the pixel at all times.
2. The neighbouring phase is biased high, typically to the same level as the starting phase. For a period of time, both phases remain high and the charge moves to be situated at the potential maximum due to the combination of each phase.
3. The starting phase is powered off, and charge moves to the neighbouring phase. The process is then repeated until the charge crosses the pixel boundary.

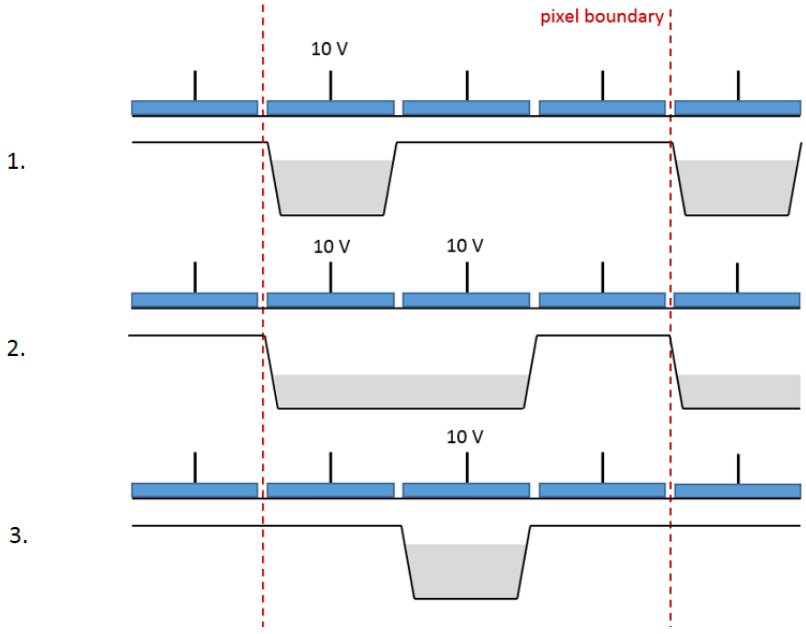

Figure 3.11: *The clocking process for a standard CCD image pixel. Through the systematic application of timed voltage pulses signal is transported from one pixel to the next.*

Two core physical mechanisms are responsible for the motion of charge between phases in a CCD; carrier drift and carrier diffusion. Either mechanism may dominate depending upon signal size and the stage of the transfer process. Understanding the relative importance of each mechanism is crucial for CTE optimisation under variable signal and speed regimes.

3.5.1 Carrier drift

In the absence of an electric field the kinetic energy of free electrons is due to the thermal energy supplied by the lattice:

$$\frac{1}{2}m_n v_{th}^2 = \frac{3}{2}k_B T \qquad \text{Equation 3.4}$$

Where m_n is the effective electron mass and v_{th} is the average thermal velocity of the electron (approximately 10^7 cms^{-1} at 300 K (Sze & Ng, 2006)). Motion due to the thermal energy of the charge is hereafter termed *thermal drift*. The motion is random in each dimension and can be visualised as a successive series of collisions with lattice/impurity atoms. The average distance between collisions is termed the mean free path, and the average time between collisions is termed the mean free time (τ_c) with values of 10^{-5} cm and 10^{-12} s respectively at 300 K (Sze & Ng, 2006). Although the thermal drift may not always be the dominant transport mechanism, it always forms a component of the particle velocity that remains random (shown in Figure 3.12).

In the presence of an electric field, the carriers are accelerated in the time between collisions and an additional velocity component is superimposed onto the thermal motion of the electrons, termed the drift velocity. The carriers now exhibit a net displacement over time. Motion due to this mechanism is hereafter termed *field induced drift*.

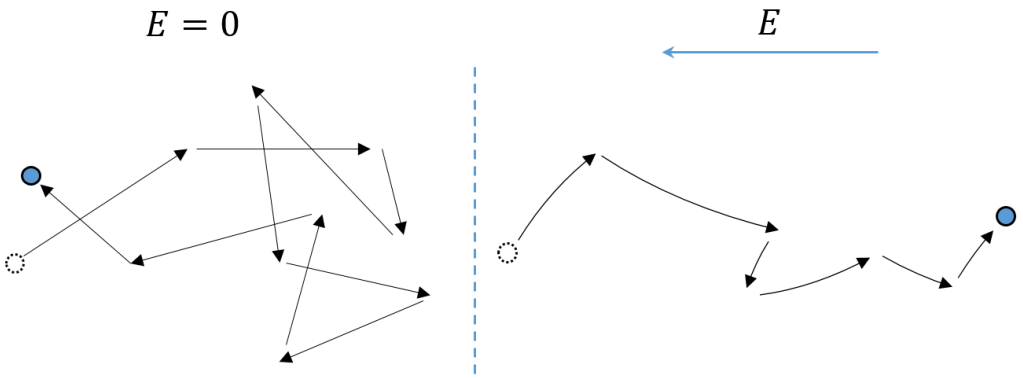

Figure 3.12: *Carrier motion in the absence and presence of an electric field.*

For small electric fields (less than 10^5 Vm^{-1}) the energy gained from the field during successive lattice collisions is efficiently lost to the lattice through phonon scattering (Sze & Ng, 2006). In this regime, the momentum gained due to the electric field can be equated to the momentum gained by the carrier within the same time interval, giving an expression for the drift velocity:

$$-qE\tau_c = m_n v_n \qquad \text{Equation 3.5}$$

$$v_n = -\left(\frac{q\tau_c}{m_n}\right)E \qquad \text{Equation 3.6}$$

In the low field regime, the drift velocity is proportional to the applied electric field. The bracketed terms are commonly grouped into one single constant of proportionality and referred to as the mobility of the charge carrier:

$$v_n = -\mu_{SI}E \qquad \text{Equation 3.7}$$

The mobility is directly proportional to the mean free time, τ_c , which for typical operating conditions is dominated by lattice and impurity scattering. Lattice scattering refers to the successive collisions between carriers and lattice during motion. As the temperature of the lattice increases, lattice scattering continues to limit mobility. Impurity scattering refers to the impact of atoms that are not part of the repeating crystal structure of the lattice, such as dopants and contaminants introduced during processing. If the impurities are ionised, such as dopants within the depletion region of the CCD, they exert a Coulomb force on the charge carrier during transport. Impurity scattering decreases as a function of temperature since carriers have a higher average K.E. and so experience the Coulomb force for shorter times. Mobility due to impurity scattering also decreases as the concentration of impurities within the crystal increases.

For the case of charge transport in CCDs, the mobility of signal will therefore vary according to the operating temperature and impurity concentration. The dominant impurity is the dopant introduced to form the buried channel structure, commonly phosphorus with a concentration of $\approx 10^{16}$ cm^{-3}. The change in mobility due to each of these variables is typically modelled empirically. One example is the analytical model based upon the work of Caughey and Thomas, summarised in Equation 3.8 with empirically derived parameters shown in Table 3.2 (Caughey & Thomas, 1967). Figure 3.13 shows the modelled mobility as a function of temperature, for the parameters supplied in Table 3.2. It can be seen that the mobility peaks at approximately 170 K below which impurity scattering begins to dominate due to the decreasing average K.E. of the signal carriers. This model shall now be used to illustrate how CTI can very across different signal level regimes owing to the competing mechanisms for charge transport.

$$\mu_{SI} = \frac{\eta \left(\frac{T_L}{300}\right)^{\beta}}{1 + \left(\frac{T_L}{300}\right)^{\gamma} \left(\frac{N}{N_{CRIT}}\right)^{\delta}}$$ Equation 3.8

Table 3.2: Summary of symbols, meanings and values for the Caughey and Thomas empirical mobility model (Caughey & Thomas, 1967).

Symbol	Meaning and Unit	Value from model for Silicon
η	Fitted parameter $cm^2V^{-1}s^{-1}$	1429.23
β	Fitted parameter (no unit)	-2.3
T_L	Lattice Temperature (K)	User defined, between 150-300
γ	Fitted parameter (no unit)	-3.8
N	Impurity (Dopant) Concentration (cm^{-3})	User defined, typically around 10^{16}
N_{CRIT}	Critical Impurity Concentration (cm^{-3})	1.072×10^{17}
δ	Fitted parameter (no unit)	0.73

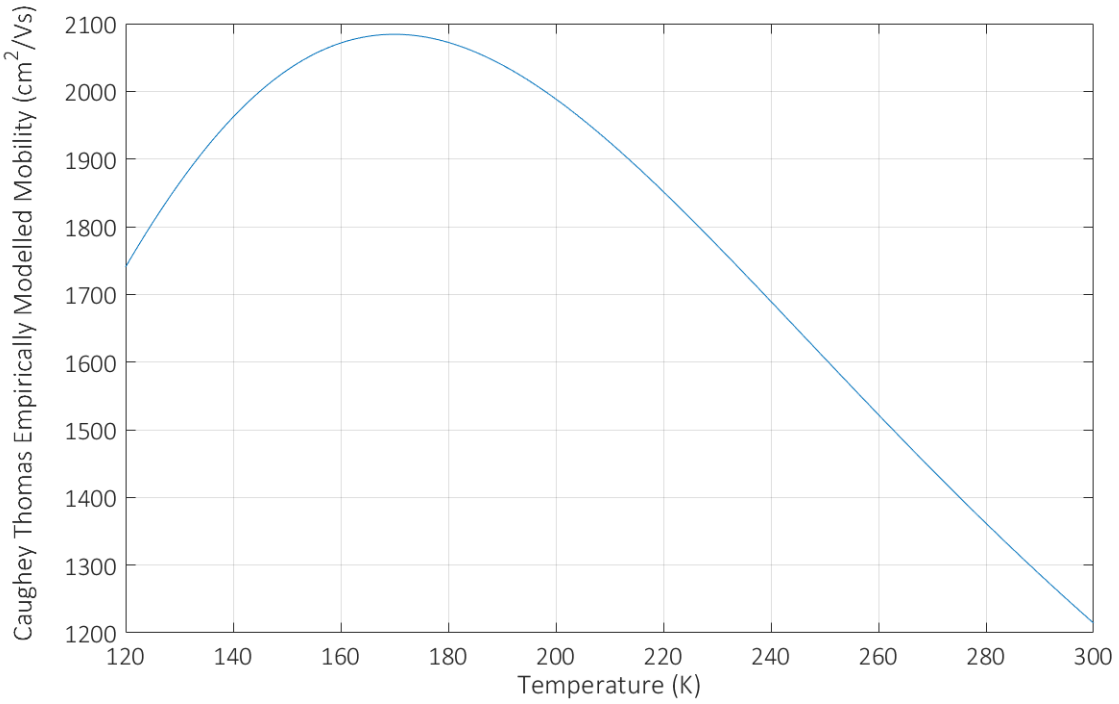

Figure 3.13: *Empirically modelled electron mobility in N-type silicon from the Caughey-Thomas low-field model, calculated using the parameters listed in Table 3.2.*

For the practical application of the CCD, both thermal and field induced drift contribute to the charge transfer process within certain regimes. Field induced drift contributes to the motion of charge when the electric field in the presence of the packet is non-negligible. This is typically the case for small charge packets that are not close to the pixel FWC. For transfer between phases one can approximate the CTI due to field induced drift using the approach detailed by (Janesick, 2001) where it is shown that the fractional charge remaining after transfer time t due to fringing field drift is:

$$CTI_{FF} = e^{-\frac{t}{\tau_{FF}}} \qquad \text{Equation 3.9}$$

where τ_{FF} is the fringing field time constant given by:

$$\tau_{FF} = \frac{L}{2\mu_{SI}E_{MIN}} \qquad \text{Equation 3.10}$$

and E_{MIN} is the minimum electric field strength (V/cm) under a gate of length L. E_{MIN} can either be returned through appropriate TCAD simulation of a pixel or be approximated as:

$$E_{MIN} = \frac{2.09\Delta V_G \varepsilon_{SI}}{L^2 C_{EFF}} \qquad \text{Equation 3.11}$$

where ΔV_G is the potential difference between gates, ε_{SI} is the permittivity of silicon and C_{EFF} is the effective storage capacitance between the gate and charge packet (F/cm^2):

$$C_{EFF}^{-1} = \frac{d_{OX}}{\varepsilon_{OX}} + \frac{d_{NI}}{\varepsilon_{NI}} + \frac{1}{\varepsilon_{SI}}(t_d - x_n) \qquad \text{Equation 3.12}$$

where:

- d_{OX} is the thickness of the silicon dioxide oxide (cm), typically 85 nm for standard e2v devices
- d_{NI} is the thickness of the nitride (cm) typically 85 nm for standard e2v devices
- t_d is the channel depth (cm), typically 1.5 µm for e2v devices
- x_n is the location of the potential maximum within the channel, typically 0.5-0.8 µm for e2v devices
- ε_{OX} is the permittivity of silicon dioxide and ε_{SI} is the permittivity of silicon nitride

Substitution of appropriate values into Equation 3.9 provides a first order estimate of the time required to successfully transfer charge from one phase to the next, illustrated in Figure 3.14 for a variety of commonly used voltage values. For CTI of order 10^{-6}, an approximate 0.5 ns wait period is required for a standard 3 phase register pixel, corresponding to a maximum theoretical pixel rate of 2000 MHz. To conclude, in the presence of fringing fields, transfer of small signals through field induced drift therefore proceeds incredibly quickly and provides no practical constraint on pixel rate within a CCD.

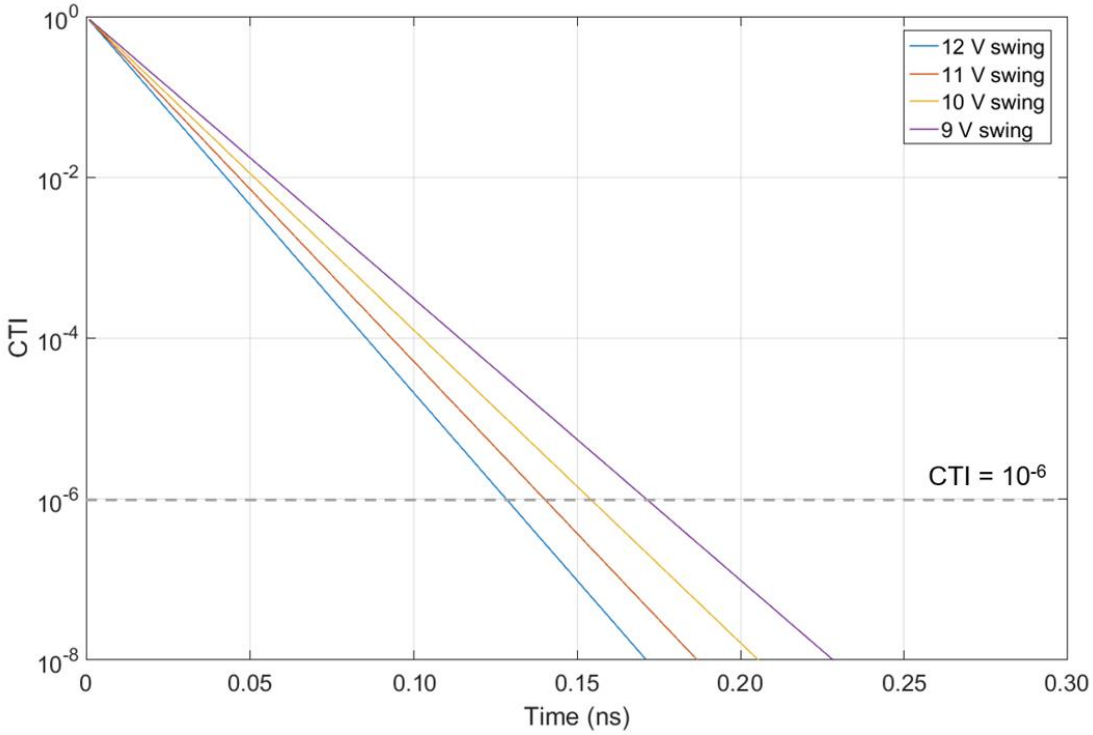

Figure 3.14: *The effect of clock swing on CTI for the field-induced drift transport mechanism using Equation 3.9 and Equation 3.10. Device dimensions chosen were representative of standard e2v devices, T=165 K and the mobility was calculated using the Caughey Thomas empirical model. The time taken to achieve a given value of CTI from one phase to the next is shown for various clock amplitudes and hence field strengths within the pixel (approximated using Equation 3.11). The clock swing has only a small impact for the time taken to achieve adequate CTI (≈10^{-6}). Note that the total time must be multiplied by the number of phases (usually 3 or 4) and this diagram is only indicative for the case where field induced drift dominates charge transport, such is the case for small (<1000 e^-) signal levels.*

Thermal drift is responsible for charge transfer when field induced drift is not present. This is typically the case for charge packets that are approaching the FWC of the pixel towards the end of the transfer process. Derived by Janesick (2001), the fractional charge that remains under a phase after a transfer time t is:

$$CTI_D = e^{-\frac{t}{\tau_{th}}} \qquad \text{Equation 3.13}$$

where τ_{th} is the time constant for thermal drift, defined as:

$$\tau_{th} = \frac{L^2}{2.5D_n} \qquad \text{Equation 3.14}$$

where L is the gate length (cm) and D_n is the diffusion coefficient. The remaining symbols take their previously defined meanings:

$$D_n = \frac{k_B T}{q} \mu_{SI} \qquad \text{Equation 3.15}$$

Thermal drift places constraints on pixel rate for the transfer of signals close to the FWC of the device. An estimated wait time of approximately 0.5 µs is required across a 3 phase 13 µm pixel (Figure 3.15); orders of magnitude longer than transfer due to field-induced drift. CTE can be improved in such situations by either increasing the gate voltage (and hence the magnitude of the fringing field) or decreasing the pixel rate. CTI due to thermal drift is predominantly an issue with the transfer of large signals in the serial register but is often mitigated by appropriate design choices whereby the register has double the allowable charge handling capacity compared to the image section.

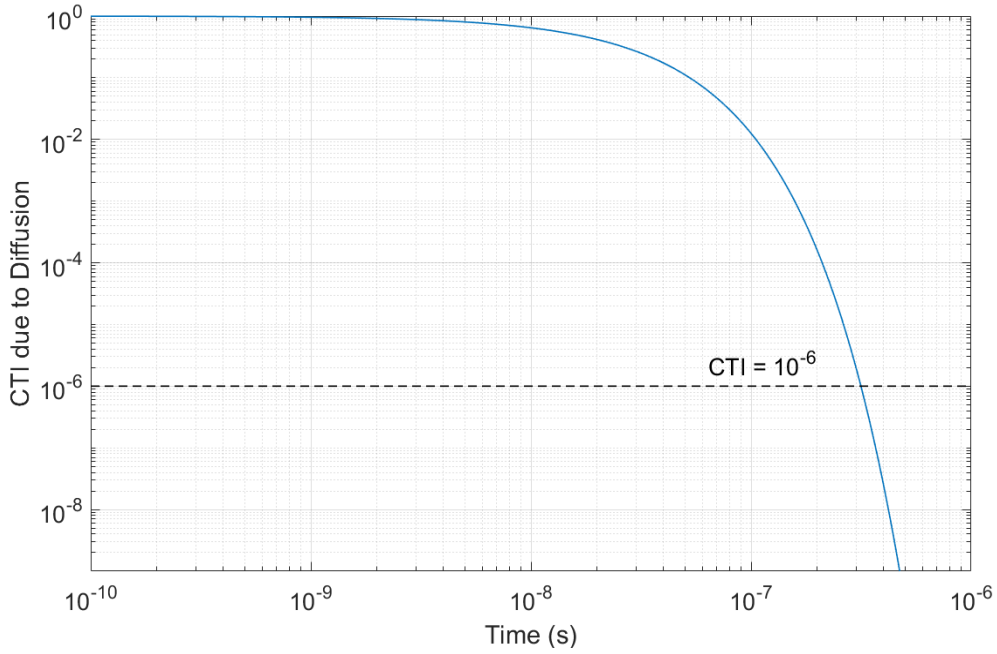

Figure 3.15: *Estimated CTI due to thermal drift for various "wait times". The CTI was calculated at 165 K using the mobility model of Caughey-Thomas and assuming a pixel width of 13 µm.*

3.5.2 Carrier diffusion

Charge stored within the potential well of a pixel experiences random thermal motion due to scattering events with the lattice yet remains confined to the presence of the electric field. During the transition from overlapping clocks to an isolated clock, the random thermal motion allows the packet to diffuse from the region of high to low concentration. Charge motion due to diffusion (often termed "self-induced drift") typically dominates at the start of the charge transfer process

for large signal packets where the fringing fields are negligible. The fractional charge remaining after time t due to diffusion is given by:

$$CTI_{SID} = \left(1 + \frac{t}{\tau_{SID}}\right)^{-1} \qquad \text{Equation 3.16}$$

where τ_{SID} is the time constant for diffusion:

$$\tau_{SID} = \frac{2L^2 C_{EFF}}{\pi \mu_{SI} q Q} \qquad \text{Equation 3.17}$$

here, Q is the number of electrons per unit area (e^-/cm^2) for the charge packet at the start of the transfer process, q is the charge of an electron and C_{EFF} is calculated using Equation 3.12. Self-Induced drift proceeds quickly at first (a few nanoseconds to transfer ≈99% of the charge, as shown by Figure 3.16) and then takes progressively longer to transfer the remaining fraction of the charge. It is in essence a self-limiting transfer mechanism. In practise, charge transfer due to diffusion proceeds quickly at the start of the transfer of large signals and after approximately τ_{SID}, field induced drift dominates.

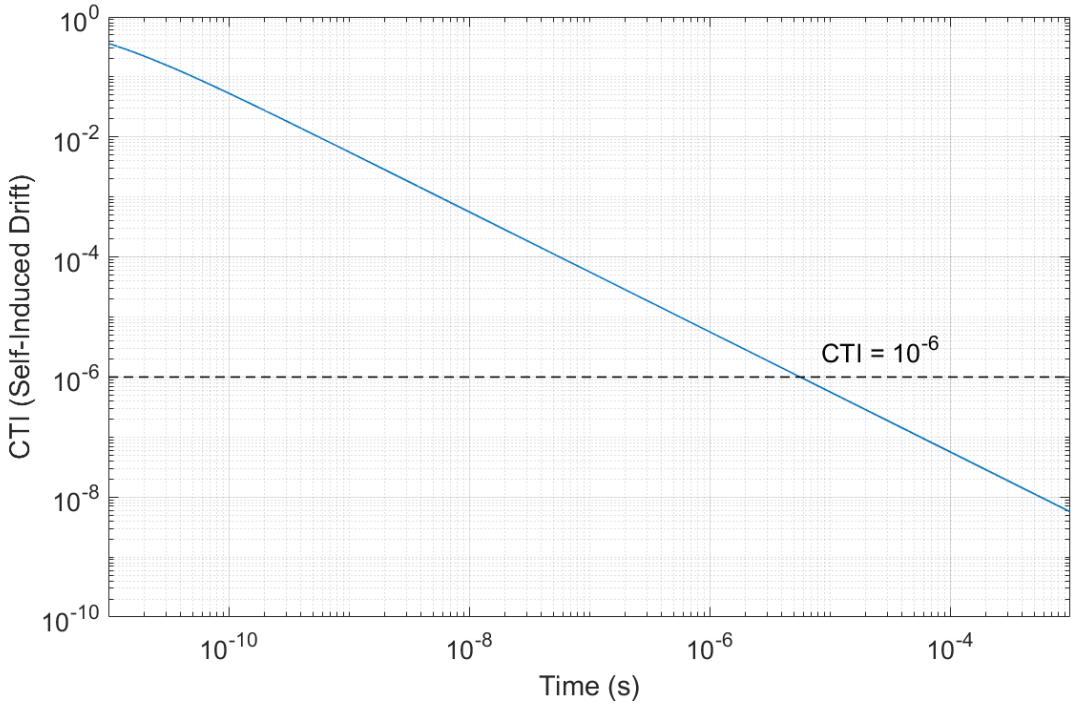

Figure 3.16: *Estimated CTI due to self-induced drift, calculated at 165 K using mobility taken from the Caughey-Thomas model. The number of electrons per unit area corresponded to approximately 8000 $e^-\mu m^{-2}$. From Equation 3.17 it can be seen that self-induced drift proceeds slower as the signal size gets smaller (owing to a lower concentration gradient across the transfer path).*

3.5.3 High field transport

The drift velocity of a charge carrier is proportional to the applied electric field as long as the energy gained between successive thermal collisions is small i.e. the drift velocity is small compared to the thermal velocity of the electrons ($\approx 10^7$ cms^{-1} for silicon). However, as the field strength continues to increase, the drift velocity will eventually become comparable to the thermal velocity, in this regime more complex physical processes begin to dominate the motion of charge within semiconductors (Fröhlich, 1947).

During successive thermal collisions, the carrier must lose energy to the lattice. The energy is lost through successive scattering events with phonons; quasi particles that represent single quanta of lattice vibrational energy. For the silicon crystal lattice, phonons can be divided into two categories:

1. Acoustic phonons represent coherent movements of atoms either in the longitudinal or transverse direction.
2. Optical phonons present out-of-phase movements of the atoms in the lattice either in the longitudinal or transverse direction.

Excitation of the silicon lattice through acoustic phonon generation requires less energy than that for optical excitation and so in the low field regime, energy is lost primarily through scattering with acoustic phonons. As the drift velocity becomes comparable with the thermal velocity of the electron, the carriers gain more energy between successive collisions than they lose to the lattice and so emission of optical phonons dominates. The "hot" carriers are no longer in thermal equilibrium with the lattice, and the velocity distribution begins to deviate from Maxwell-Boltzmann behaviour as their effective temperature has become higher than that of the lattice. Increasing the field strength further still means that carriers have enough energy to break bonds of the silicon lattice, creating an electron-hole pair, a process referred to as impact ionisation. At increasing field strengths, energy loss through optical phonon emission and impact ionisation events becomes more efficient such that the electron velocity no longer increases as a function of field strength. This point is known as the saturation drift velocity, for silicon devices it is of the order 10^7 cms^{-1} (Sze & Ng, 2006). Figure 3.17 shows the drift velocity as a function of the electric field for high purity silicon such as that used in CCDs. Note that the typical fringing field strength in a CCD is sufficient to accelerate electrons to the saturation velocity.

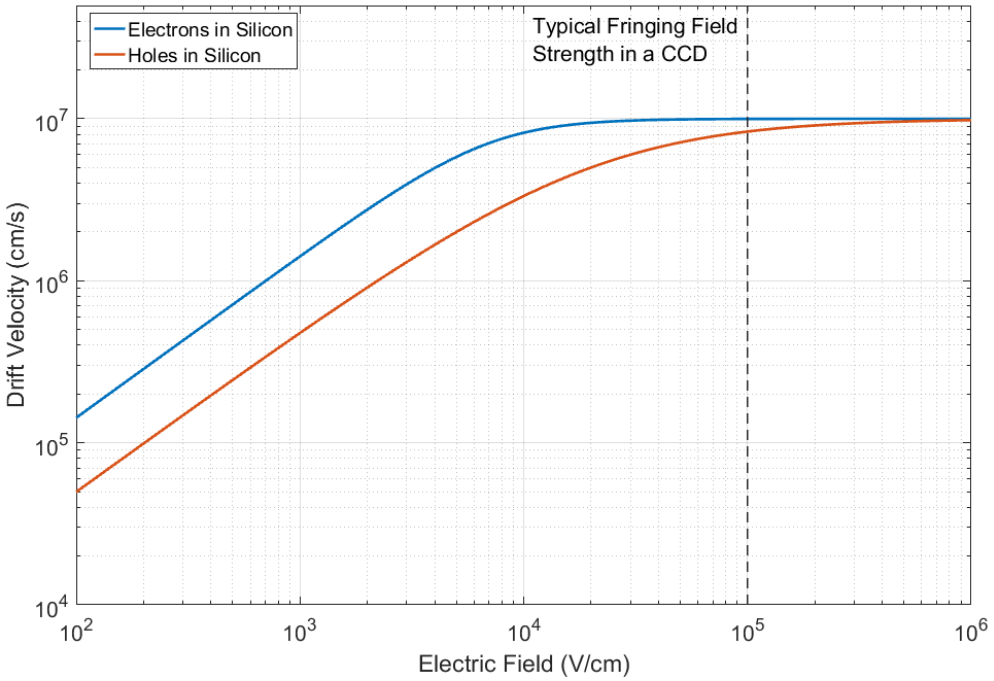

Figure 3.17: *Drift velocity versus electric field in silicon, taken from (Sze & Ng, 2006). Note that the typical fringing field strength in a CCD is sufficient to accelerate electrons to the saturation velocity, about 10^7 cms^{-1} in silicon.*

3.6 The CCD output circuit

The terminus for the transferred charge is the output circuit, which has the role of converting the analogue signal in electrons into a voltage for signal processing. The voltage conversion must introduce as little noise to the signal as possible in order to fully take advantage of the near perfect QE and CTE possible with a CCD. Successive iterations of output circuitry have managed to produce noise levels as low as 2 e^- RMS at slow-scan pixel rates (Jerram *et al.*, 2001).

The output circuit is located at the end of the serial register. Charge is transferred to Rϕ3 in the final register pixel, and as the Rϕ3 clock falls low, charge is transferred from the final pixel, beneath the output gate and onto the output node (Figure 3.18). The output gate is typically held at a fixed bias level (V_{OG}) in the order of 3-5 V and acts to shield the output node from the effects of clock feedthrough from the final register pixel. The output node is a highly N doped region with a capacitance C_N, connected to both an amplifier and reset MOSFET. Charge transferred onto the sense node results in a voltage applied to the amplifier MOSFET:

$$V = \frac{qN_e}{C_N} \qquad \text{Equation 3.18}$$

where q is the charge of an electron, N_e is the number of electrons transferred onto the output node and C_N is the capacitance of the output node. The voltage applied to the amplifier MOSFET

gate controls the current flow from source to drain, which results in an approximately linear potential drop across the external load attached to the output source, V_{OS}. Once V_{OS} has been measured, the charge in the output node can be reset to V_{RD} through application of the reset pulse ϕR.

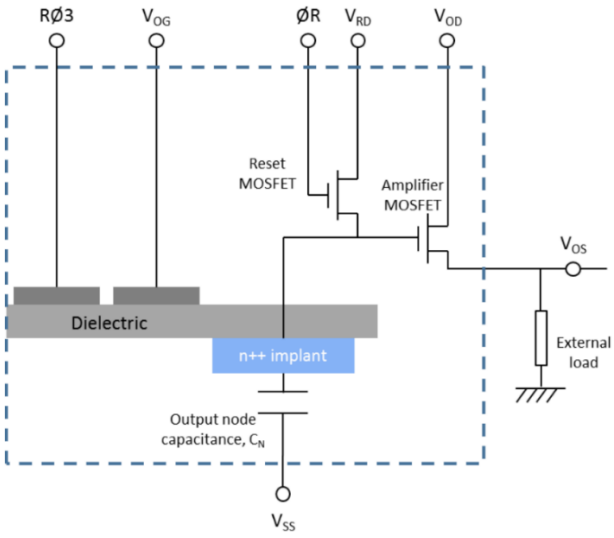

Figure 3.18: *Schematic of a single state output circuit.*

The performance of the output circuit is commonly quoted in terms of its responsivity, defined as the change in output source potential (V_{OS}) per electron added to the output node. Typical values are of order 5-10 μVe^{-1}. Higher responsivity is desirable for smaller signal levels, since a large voltage swing is less susceptible to feedthrough and amplifier noise. An increase in responsivity is given by a decrease in the capacitance of the sense node (Equation 3.18), typically achieved by reducing the feature size. Decreasing the capacitance of the node, however, reduces the maximum charge storage capacity and hence the dynamic range of the detector. The response time of the amplifier MOSFET is also lengthened, meaning slower readout rates are required for the best noise performance. The solution to maintaining a high responsivity and dynamic range without a reduction in readout rate is the multi-stage output circuit (Figure 3.19).

The 2nd stage MOSFET amplifier is physically larger than that of the 1st stage, giving it a reduced impedance and hence quicker response time. It acts to further amplify the output from the first stage, which remains identical in design to that shown by Figure 3.18. A floating capacitor is present between the first and second stages that has a larger capacitance than the output node. It does not need to be reset as often as the output node (reducing feedthrough) and so ϕC is commonly tied to a parallel transfer clock such that it is reset once per line readout to the level of V_{RD}. The scientific two-stage output circuit is standard on most modern-day CCDs, and the output amplifier responsivity is tailored to balance dynamic range and noise performance.

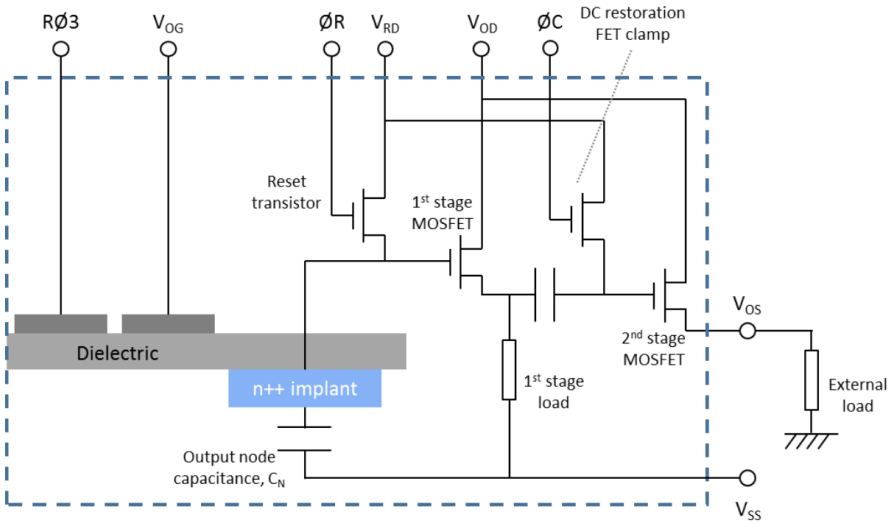

Figure 3.19: *Schematic of the standard scientific two-stage output circuit.*

3.7 Noise sources for CCDs

The possibility of near 100% QE and CTI of order 10^{-6} position the CCD as an almost perfect detector across a wide range of wavelengths. However, there are additional noise sources that must be considered and mitigated in order to achieve the best possible detector performance.

3.7.1 Shot noise

The detection of photo-generated electrons is a random process with the number of photon generated carriers as the random variable. The standard deviation of this random variable is termed the shot noise and is a property of the photon source as opposed to the detector. The noise follows Poisson statistics such that the probability of observing a signal level of k for a mean signal level of λ is given by:

$$P(k) = \frac{\lambda^k e^{-\lambda}}{k!} \qquad \text{Equation 3.19}$$

Where $k!$ is the factorial of k, defined as the product of an integer and all the integers below it. The variance of the distribution is equal to the mean, such that shot noise follows $\sqrt{\lambda}$. Photons with sufficient energy to generate multiple electron-hole pairs exhibit sub-Poisson noise performance due to a correlation between the primary carrier energy and the ionisation threshold of the detector. The reduction is termed the *Fano* factor (Fano, 1947) and is described as a ratio between the observed variance (σ^2) and mean (μ) of a random process, which for a standard Poisson process would result in a value of unity (Equation 3.20). F has a theoretical value of 0.115 in Silicon (Alig, Bloom, & Struck, 1980).

$$F = \frac{\sigma^2}{\mu} \qquad \text{Equation 3.20}$$

3.7.2 Dark current

Electrons can undergo promotion into the conduction band through thermal generation as well as through photo-absorption. Signal generated in this way is termed thermal dark current and consists of two components; surface dark signal generated at the silicon-silicon dioxide interface and bulk dark signal generated within the silicon substrate.

The silicon-silicon dioxide interface contains a large number of trapping sites due to the atomic mismatch of silicon and its oxide giving rise to “dangling bonds” which have energy levels within the silicon bandgap. The distribution of energy levels is broad, with a mean energy that is approximately mid-band (≈0.5 eV) that allows efficient thermal promotion from the valence band into the conduction band. The density of traps in an untreated interface is of order 10^{12} $cm^{-2}eV^{-1}$ and many hold a fixed positive charge. Such a large density is problematic not only in terms of excessive dark signal but the resultant flat-band shift that is the result of positive sheet charge at the interface. For the majority of MOS technologies, including CCDs, the interface state density is removed by performing a high temperature anneal in the presence of hydrogen. Traps at the interface react with the molecular hydrogen to form Si-H bonds that are stable and electrically inactive under normal operating conditions. This treatment results in an interface trap density of order 10^{10} $cm^{-2}eV^{-1}$, significantly reducing the contribution of surface dark signal and any flat-band voltage associated with any remaining fixed oxide charges.

Even following passivation, the surface component of dark signal is dominant and is typically two orders greater than the bulk component at 298 K (Figure 3.21). The surface component of dark signal can be reduced through Inverted Mode Operation (IMO). To operate in IMO, the substrate voltage is raised to a point greater than the potential at the interface when the pixel clocks are at the low level. At this point, holes migrate from the channel stop regions to the interface and saturate the trapping sites, thus inhibiting electron emission and so effectively eliminating the surface component of dark signal (Figure 3.20).

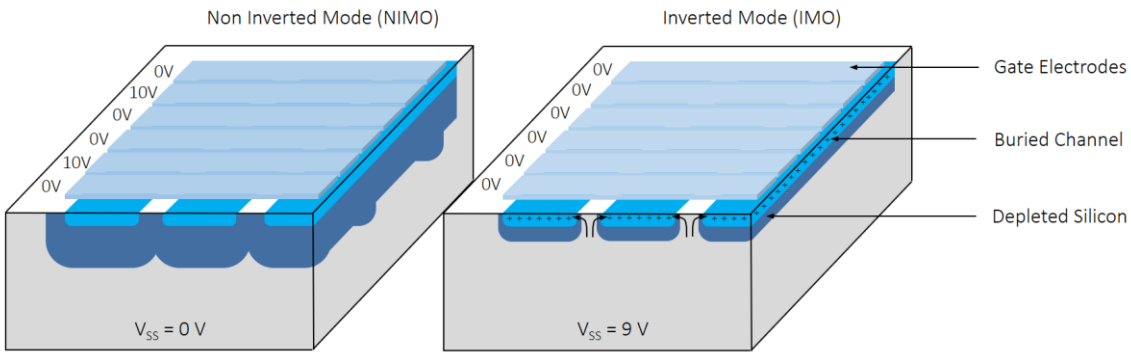

Figure 3.20: *Pixel schematic highlighting the differences between NIMO and IMO operation. IMO has the advantage of lower dark signal; however, they also increase the electrode capacitance (limiting clock speed), lower the depletion depth and cause an increase in Clock Induced Charge (CIC).*

During readout, phases must sequentially be switched to the non-inverted state in order to receive charge from an adjacent phase/pixel. The layer of holes at the interface is conductive, and so the field applied by the gate has no effect on the channel while in the inverted state. To move the phase out of inversion, the sum of the clock high level and NIMO interface voltage must exceed the substrate voltage. Typically, it is advised to raise the high level at least 0.5 V above this level, since the holes have low mobility and the phase takes time to move to the NIMO state. This time commonly exceeds the time taken for charge to move from one phase to the next, and so becomes an important consideration for high speed applications. The time can be reduced by increasing the clock amplitude further, thus subjecting the holes to a higher electric field, however, this is accompanied by a corresponding noise penalty in the form of spurious or Clock Induced Charge (CIC), discussed shortly.

The bulk component is also due to the presence of defects that are approximately mid-band and so allow the thermal promotion of carriers into the conduction band. The as-made silicon lattice is of a very high quality, however, and so contains a relatively small concentration of defects that contribute. A typical pixel with dimensions 13 µm x 13 µm x 20 µm, for example, could contain of order 10^6 interface traps compared to approximately 100 bulk traps. Despite this, the bulk component at room temperature can equate to dark signal levels of order 300 $e^{-}pix^{-1}s^{-1}$, adding considerable noise to an image and prohibiting long integration times (e2v technologies, 2015).

The bulk dark signal is the combination of both depletion and diffusion components. At temperatures below ≈240 K, the depletion current dominates and above 300 K the diffusion component forms the dominant contribution (e2v technologies, 2015). The bulk dark signal component is mitigated by cooling the detector, with an approximate 10 K decrease corresponding to a factor ≈2 reduction in the bulk dark signal (Figure 3.21).

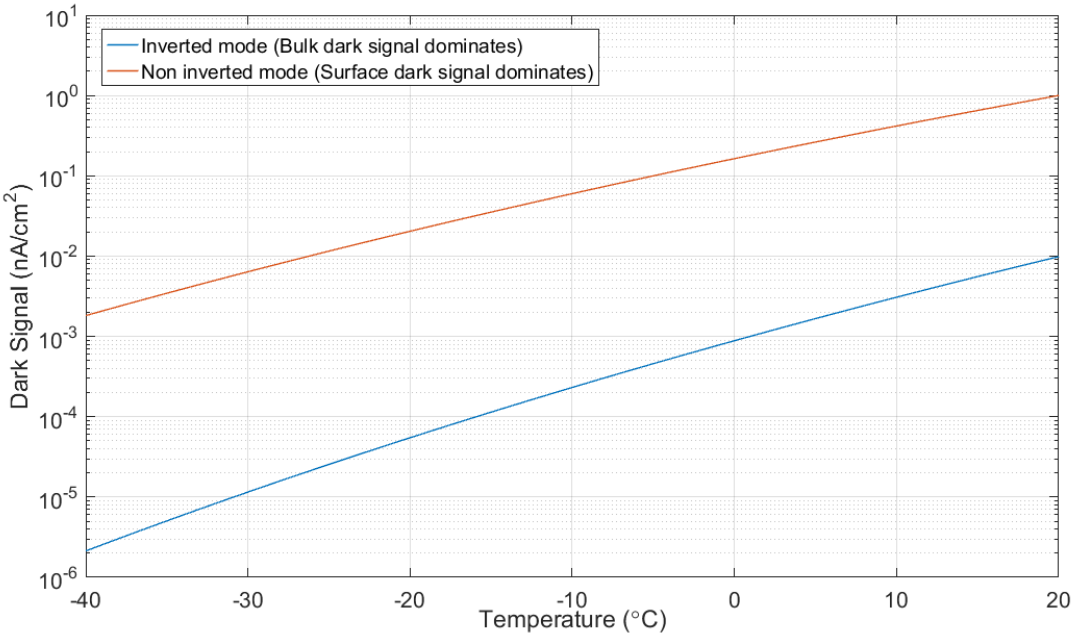

Figure 3.21: *Plot of empirically modelled surface and bulk contributions to total dark signal (e2v technologies, 2015).*

3.7.3 Clock Induced Charge (CIC)

The process of clocking signal towards the output can generate additional charge that is indistinguishable from signal electrons, termed Clock Induced Charge (CIC).

CIC is thought to be generated by minority carriers (holes for N channel devices) experiencing high electric fields as a phase is biased high. The high electric fields accelerate the carriers to energies sufficient for the generation of additional carrier pairs though impact ionisation. The electron is then collected and detected as signal, as shown in Figure 3.22.

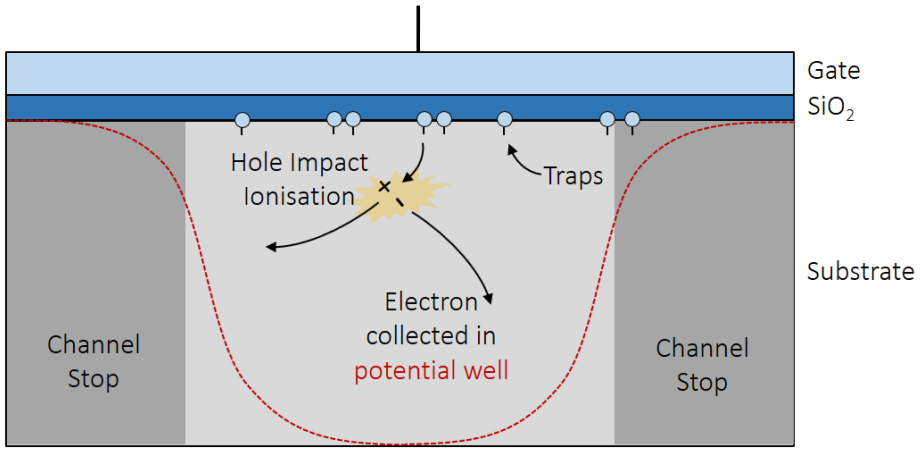

Figure 3.22: *CIC generation within a CCD pixel.*

CIC has been found to be exponentially dependant on the clock high-level amplitude with respect to substrate voltage (e2v technologies, 2015). The probability of impact ionisation is exponentially dependant on the applied electric field, which increases with clock amplitude. CIC can therefore be mitigated by limiting the high level to a point that the pixel is reliably driven out of inversion with sufficient time remaining for charge transfer to take place.

The longer a phase is held in the high state, the longer the possibility that a trap will accept an electron (and hence, donate a hole) that can generate CIC. Faster clocking speeds therefore mitigate CIC by limiting the time available for hole emission.

A dependence on clocking waveform shape has also been observed that can be explained through a similar principle. Sinusoid waveforms minimise the time that the holes are subjected to a high electric field when compared to a square waveform of the same operating frequency and result in lower CIC (Daigle *et al.*, 2008). The shaped waveform must still allow adequate time for the phase to be fully driven out of inversion and for charge transfer to take place for there to be no CTE penalty.

Little to no temperature dependence of CIC has been observed thus far over a 250 to 298 K measurement range (e2v technologies, 2015). A weak dependence of carrier mobility with temperature would explain the limited temperature dependence of CIC within the quoted measurement range. Evidence for similar behaviour at lower temperatures is presented in subsequent chapters.

Substantially higher CIC is measured when operating in IMO since the population of holes at the interface is orders of magnitude greater than for the NIMO case. Since IMO results in substantially lower dark signal, a trade-off is made dependant on operating temperature and integration time whereby either IMO or NIMO operation may be desirable to give the best possible noise performance.

Based upon these observed dependencies, CIC is mitigated by lowering the clock amplitude to a suitable level while maintaining CTE, operating at fast pixel rates and with optimised waveforms and through NIMO operation.

3.7.4 Read noise

With appropriate mitigation of dark current and CIC, the dominant noise source for a standard CCD is the noise added by the output circuit and associated signal processing chain. There are two main sources of noise introduced within the readout circuit, reset noise and transistor noise. Reset noise is introduced when the sense node is reset to the V_{RD} level by ϕR, whereas the transistor noise is due to fluctuations in the current that flows across the MOSFETs. Both reset

and transistor noise are due to the same phenomenon, termed Johnson noise, which describes the noise in the conductance of a component due to the random thermal motion of electrons within the channel. For the case of a resistor with resistance R, the RMS voltage V_N across the resistor is given by:

$$V_N = \sqrt{4k_B T R \Delta f} \qquad \text{Equation 3.21}$$

where T is the temperature and Δf is the frequency bandwidth. Both the fluctuating reset level and variable current across the MOSFETs can be interpreted as a varying level of charge in the node, thus adding noise to the system. This noise is significantly reduced though a technique known as Correlated Double Sampling (CDS). In CDS, the potential on the output node is measured after each reset prior to and following the transfer of charge onto the output node. The difference between each sampled level allows the subtraction of the true reset level, thus reducing the noise. The effect of MOSFET noise can be mitigated by sampling the output source voltage multiple times or by sampling once over a long-time period (of order μs). As the sampling period increases the noise is reduced, however each pixel consumes a larger processing time. Readout noise therefore increases as a function of pixel rate, with values of a few electrons possible at slow scan rates (20-200 kHz) rising to tens of electrons in the MHz regime (Figure 3.23).

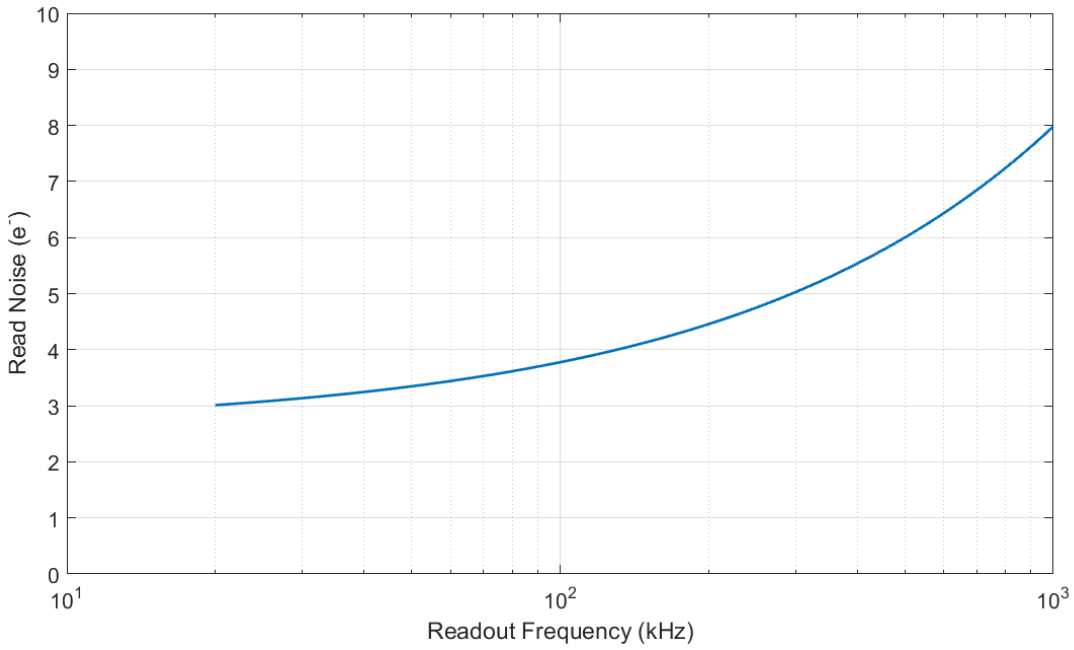

Figure 3.23: Relationship between frequency and read noise for the case of the e2v CCD 42-40 (e2v technologies, 2016).

3.8 CCD design variations

Modifications to the standard CCD design are available that further improve performance for certain applications. The frame-transfer device is one such example that is now widely available and commonly used for scientific applications. While the device is being read out, the image area remains photo-sensitive and will accumulate charge from a light source during the frame-read time. Depending upon the device size and readout speed, the read time may be significant and signal collected will create a noticeable “blur” or “smear” on the image. One solution is a mechanical shutter that is activated as readout begins, however, the mechanism required typically limits the shutter speed to the order of a few milliseconds. Another solution is to add an optically shielded section of the device, termed the frame store region, which can store the charge accumulated during integration without additional light being added during readout. The optical shield is typically added during processing by depositing a thin layer of aluminium. It is typically identical to the image area in terms of pixel dimensions and structure although the clocks must have separate connections to the image section to allow for frame transfer operation.

The slow scan rates required for low read noise coupled with large device dimensions give rise to a frame read time of order seconds. While frame-transfer operation can mitigate the effect of image smear, this time taken to read out limits the maximum frame rate. To increase the frame rate, some devices contain multiple outputs with a split register design at each end of the device. The disadvantage of such a design is that each output amplifier has slightly different properties (e.g. responsivity) and so requires separate pre-characterisation.

Modifications to the pixel design have also been developed with the aim of providing either added flexibility or simplicity for device clocking. The standard, most basic pixel design consists of three equal sized phases stacked on the gate dielectric. For a standard buried channel doping distribution, three phases are the minimum number for a CCD pixel such that a potential barrier can always be present to prevent charge blooming. Some pixels have a four-phase architecture with phases of asymmetric size that enable advanced clocking schemes that promote charge transfer efficiency and reduce CIC (Murray *et al.*, 2013).

As well as containing four phases, pixels may contain additional implants that reduce the number of clocking cycles required to move charge from one pixel to the next. The 2-phase architecture shown in Figure 3.24 is one such example and consists of a 4-phase electrode device with additional barrier implants beneath two of the phases that deform the electronic potential in such a way that the backflow of charge is prevented under standard clocking.

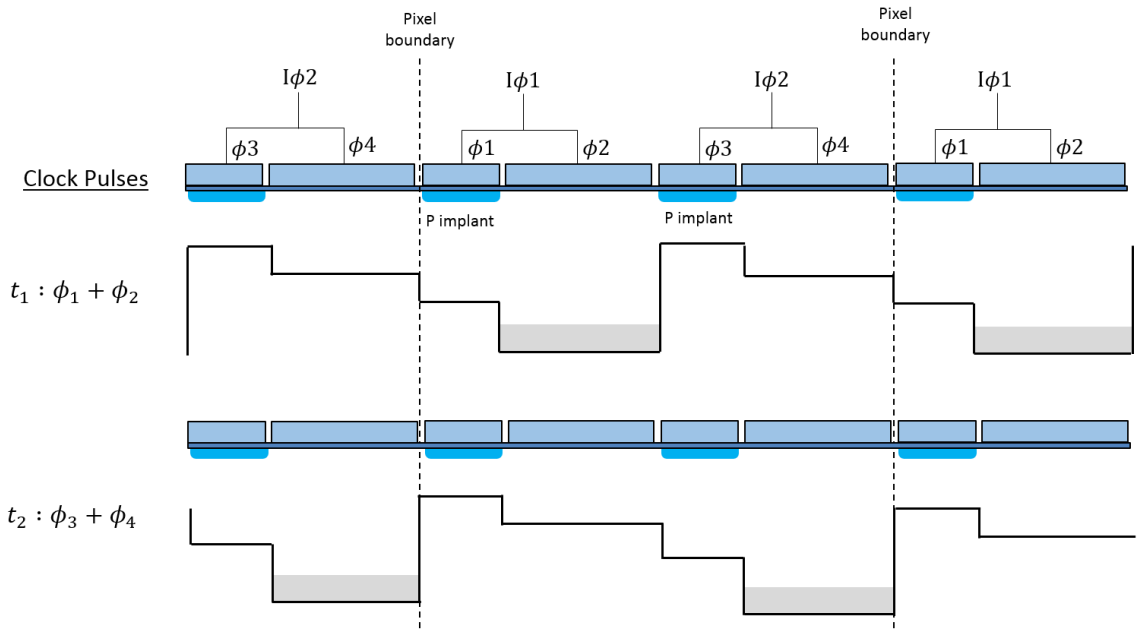

Figure 3.24: *Example of 2-phase pixel architecture where additional implants beneath the phases (in this case $\phi 1$ and $\phi 3$) deform the electric potential to prevent the backward flow of charge. Note how the phases are paired to form $I\phi 1$ and $I\phi 2$ and so only 2 clocks are necessary to move charge between pixels.*

3.9 Summary of CCD technology in relation to the CGI

Within this chapter the fundamental physical principles behind charge generation, storage and readout have been described that form the basis of more detailed analysis through subsequent chapters. The CCD has been presented as a near perfect detector for operation at optical wavelengths with near perfect QE and as-made CTI values of order 10^{-6}.

Appropriate mitigation of CIC and dark signal leaves read noise as the dominant noise component. However, even at low pixel rates the read noise is too high to permit the single photon detection that the WFIRST CGI will require. Imaging of single photon sources requires image intensification prior to the introduction of readout noise. The EM-CCD is one such solution, and benefits from the performance advantages detailed in this chapter with additional consideration required for operating with electron multiplication gain as will now be discussed.

4 The EM-CCD

Within the previous chapter it was highlighted how the minimum achievable read noise of a CCD is of order 2-3 e^- and can only be achieved using slow-scan pixel rates. The detection of single photons within a single image for the case of the WFIRST CGI therefore requires intensification either prior to or following charge generation. The EM-CCD is one such solution to this problem and makes use of an internal multiplication gain mechanism to raise the signal level above the noise introduced by the output circuit. An image area, store section and readout register are all included that follow standard CCD design and the same operating principles as detailed in the previous chapter. The main modification is the inclusion of the multiplication register; an array of elements that allow signal carriers to experience a region of high electric field that accelerates them to energies sufficient for the generation of additional carrier pairs through impact ionisation. Although a minor addition, the multiplication register fundamentally changes how EM-CCDs should be operated and optimised. Noise sources that are typically of little concern to standard CCDs now dominate performance due to the increased sensitivity that the EM-CCD can provide. The high electric fields within the EM-CCD give rise to a suite of physical phenomena unobservable in standard CCDs. Device ageing, register glow and surface trapping (all soon discussed) can limit the performance of the device if not properly optimised. For this thesis, the principle concern is noise mitigation in order to maximise the CGI planet yield from the CCD201-20 EM-CCD and so that is the topic that will now be addressed. The structure of the EM-CCD is described with a specific focus on the CCD201-20, although the majority of the discussion applies to any EM-CCD manufactured by e2v technologies. The statistics of electron multiplication gain (hereafter EM gain, for brevity) are introduced and discussed with respect to the principle operating modes of the EM-CCD for the CGI. The newfound relevance of dark signal and CIC is discussed with a focus on noise optimisation that exhibits complicated dependence on both the frame time and operating temperature of the device.

4.1 Structure of the CCD201-20 EM-CCD

The structure of the CCD201-20 is almost identical to that of the standard CCD albeit for the inclusion of the multiplication register (Figure 4.1) which is appended to the standard serial register and connected to its own output. A standard CCD output is also present on the device and operation through either node is possible through appropriate reversal of register clocking. The standard output has responsivity typical of a scientific CCD at around 5 $\mu V/e^-$, since the signal sizes are limited by the image area full well capacity (around 10^5 e). The EM output, termed “Large Signal” output on device datasheets (e2v Technologies, 2015), has lower responsivity at around

1.4 µV/e^- that allows sensing of larger signals and operation at higher pixel rates (10 MHz and above).

Additional register elements are present between the standard and multiplication registers that act as a buffer. The standard register undergoes a full 180° turn prior to the EM elements in order to reduce the die space required for a single device. The standard and EM register pixels have different widths and so there is a transition region between the two pixel types whereby the channel width is increased to avoid creation of potential pockets that would otherwise inhibit charge transfer performance. “Run-off” elements are also present following the EM register that follow the standard register pixel design so as to avoid any possible clock feed-through from the HV supply onto the output node. The register within the CCD201-20 is therefore fairly complex and consists of multiple pixel types tailored to electron multiplication and the transfer of large signal packets.

The image area of the CCD201-20 has a frame-transfer architecture with separate store and image sections. Both have a four-phase electrode pixel architecture with separate connections, giving a total of 8 parallel clock lines. The phases are of asymmetric width and the smaller phases have a barrier implant that facilitates 2-phase operation (Figure 3.24, Figure 4.1). The ability to clock as a two-phase device often means that adjacent phases are paired together to simplify electronics. Backward clocking of the image and store sections is possible by alternating how the phases are paired. An additional implant is also present for IMO operation that eliminates the surface component of dark signal.

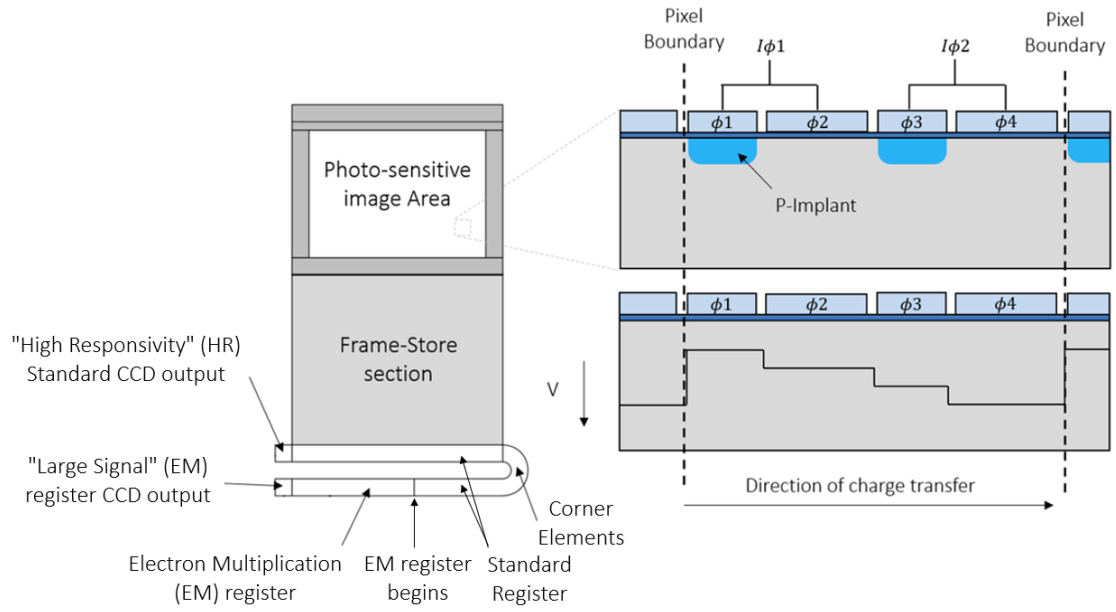

Figure 4.1: *Schematic of the CCD201-20, showing image area, frame store and standard/EM register placement. The image pixel schematic is shown perpendicular to the direction of transfer for clarity.*

4.2 The Electron Multiplication (EM) register

The EM register is the unique feature of the EM-CCD and consists of an array of pixels designed to allow carriers to experience electric fields sufficient for impact ionisation. For e2v devices, multiplication elements consist of a 4-gate structure where two of the electrodes are customised to generate the high-field region (Jerram *et al.*, 2001). The ϕDC gate is typically biased at a constant, fixed voltage (3-5 V) and acts as a barrier to prevent the motion of charge while the high field is being established. The Rϕ2HV gate has a timed, high-voltage pulse applied (in the region of 20-45 V) that gives rise to a peak electric field of order 10^7 Vm^{-1} between itself and the barrier phase. The remaining two gates, Rϕ1 and Rϕ3, operate at standard device potentials (10-12 V) and transfer charge from one element to the next once multiplication is complete. Application of a clocking scheme similar to that described by Figure 4.1 allows charge to be transferred into an element, experience multiplication and then be transferred to the next element where the process repeats.

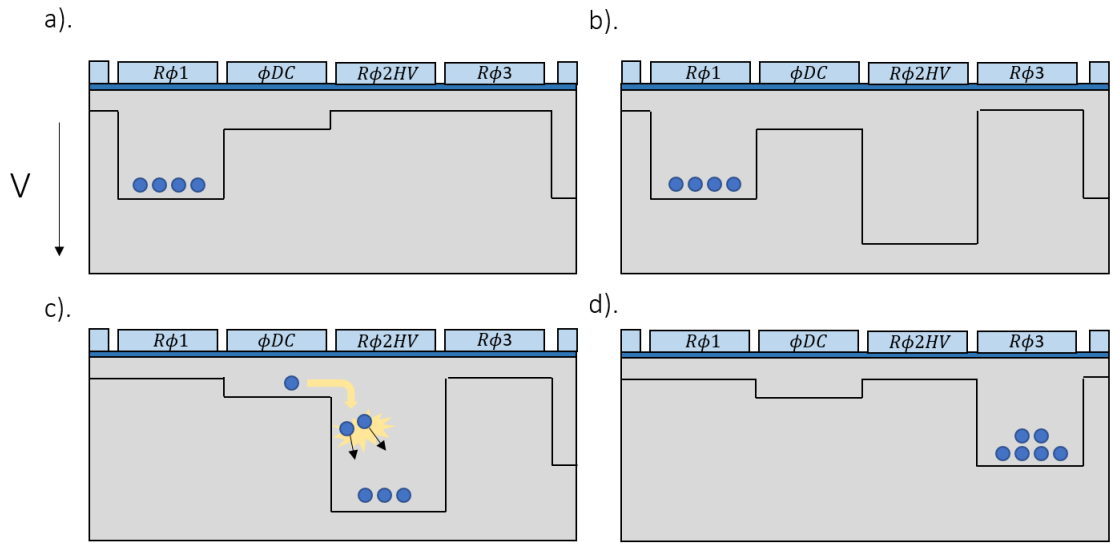

Figure 4.2: *Standard EM clocking sequence. a) Charge is transferred in from the previous element. b) the ϕDC gate acts a barrier to prevent the motion of charge while the high field is established. c) Rϕ1 is lowered, the electrons experience the high electric field between ϕDC and Rϕ2HV and undergo impact ionisation. d) Charge is transferred to the following element and the process repeats.*

TCAD simulation of the charge transfer process, described in detail by Bush *et al.* (2014), provides a more in-depth view of the multiplication process. The simulations showed that as the Rϕ1 clock is lowered, the signal packet moves beneath the ϕDC phase and is accelerated towards the interface region before settling beneath the Rϕ2HV phase. Figure 4.3 shows a "snapshot" of electron concentration during the simulation of a signal level of 300 e^- with clocks operating at 11 MHz and Rϕ2HV biased to 40 V. Figure 4.4 shows that the majority of the multiplication takes place between ϕDC and Rϕ2HV, where the electric field is sufficent for the physics of high field transport to apply (Section 3.5.3). The primary impact ionisation mechanism extends close to the interface of the device, indicating carriers within this region still have high energy ($\geq$ 3.6 eV) and can interact with either interface states or the gate dielectric, discussed later. A second region of impact ionisation is also seen directly beneath the ϕDC phase and aligned with the oxide boundary. The region of primary impact ionisation is a source of holes as well as electrons and the holes experience a field similar in magnitude yet opposite in direction. The ϕDC phase is the region of least positive potential in the vicinity, and so the holes are accelerated towards the interface beneath ϕDC and form a second region of impact ionisation. The threshold energy for impact ionisation due to holes is higher than that of electrons (5.0 eV compared to 3.6 eV (Sze & Ng, 2006)), meaning this is another region where carriers can interact with the gate stack. The secondary physical phenomena associated with the high energy carriers are remarked upon in more detail later within this chapter.

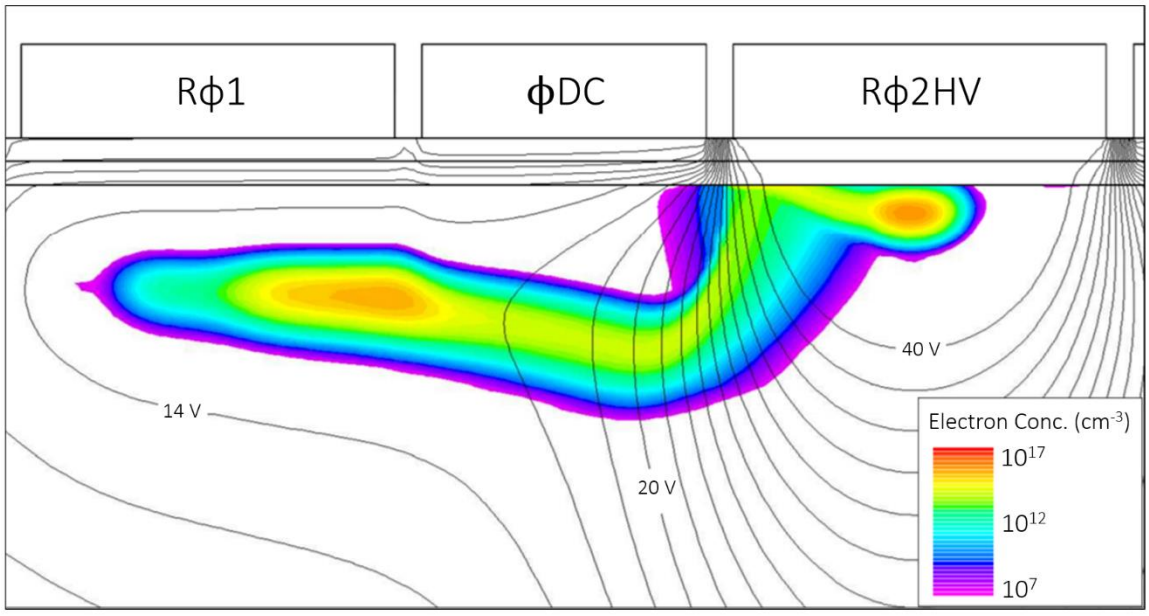

Figure 4.3: *Electron concentration at a point during transfer with Rϕ2HV = 40 V, adapted from Bush et al. (2014). Potential contour lines are illustrated at 2 V/contour.*

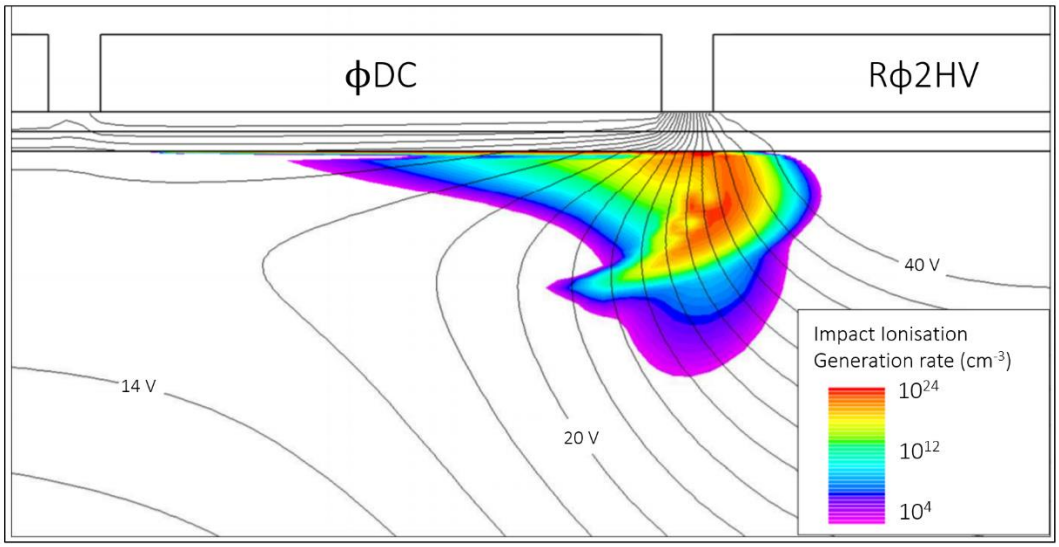

Figure 4.4: *Regions of impact ionisation at the same point during transfer as Figure 4.5, adapted from Bush et al. (2014). Two regions of impact ionisation are present, one between ϕDC and Rϕ2HV, and another thin region directly beneath the ϕDC phase.*

The multiplication gain is a strong function of the applied electric field since this increases the proportion of carriers with energy sufficient for impact ionisation to take place. The dependence is approximately exponential and well-illustrated by Figure 4.6 and e2v datasheets (e2v Technologies, 2015).

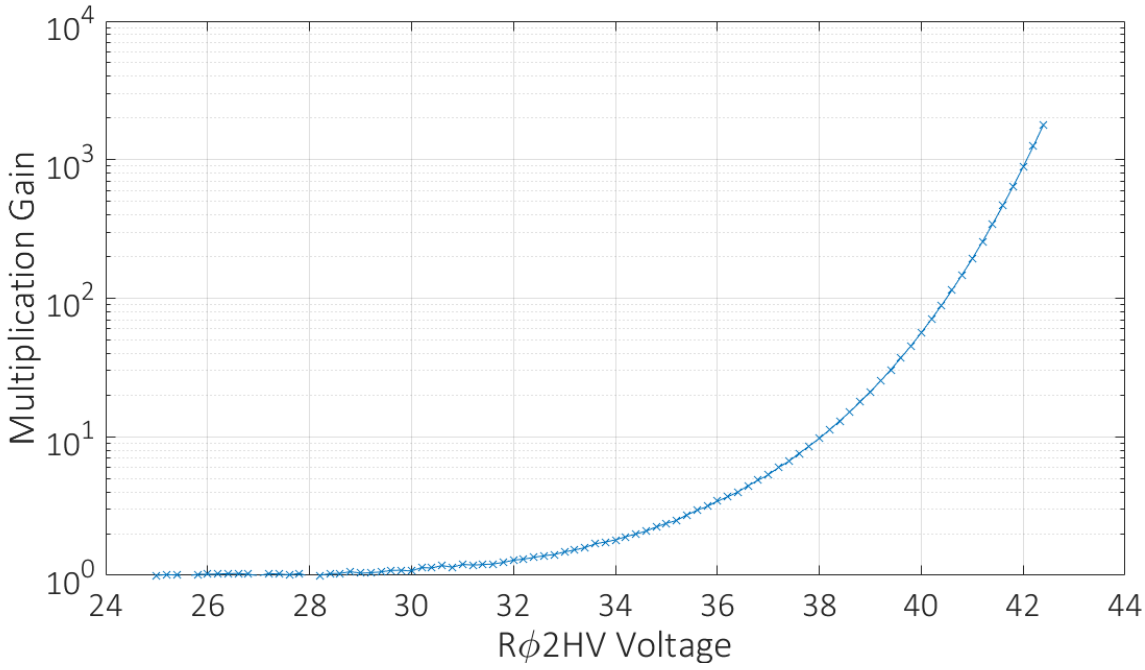

Figure 4.6: *Multiplication gain with a CCD201 EM-CCD measured as a function of Rϕ2HV voltage (measurement made by author).*

The operating temperature of the device also influences the gain since a decrease in temperature corresponds to an increase in carrier mobility (as described in Section 3.5). The dependence is weaker than that of electric field. As an indicative figure a decrease in operating temperature of 100 K allows the Rϕ2HV voltage to be dropped by 5 V while maintaining equivalent multiplication gain (e2v Technologies, 2015).

Even for high operating voltages and cryogenic temperatures, the multiplication achieved per element is rarely greater than 1%. A large number of elements (typically around 500) are within a complete register and this facilitates multiplication gains in the region of ×100-1000 depending upon the applied Rϕ2HV voltage.

The average multiplication gain of the device, G, is parameterised by the number of gain elements in the register, N, and the probability, p, of generating an additional carrier pair within each element:

$$G = (1 + p)^N \qquad \text{Equation 4.1}$$

In practise, however, the gain per multiplication element is not constant and varies according to variations in pixel geometry, usage history and the signal size being transferred.

4.3 Noise sources for EM-CCDs

The use of multiplication gain means previously small signals are amplified by a large factor such that the impact of noise from the output amplifier is dramatically reduced. Additional noise sources become the focus of device optimisation and place limits on the regime where EM-CCD technology can provide a noise benefit.

4.3.1 Effective read noise

With the inclusion of multiplication gain it becomes convenient to redefine read noise such that it is quoted with respect to the input signal at the start of the register. The readout circuit is now said to have an *effective* read noise, equal to the standard readout noise divided by the mean multiplication gain, G (Equation 4.2):

$$RN_{eff}(e^-) = \frac{RN\ (e^-)}{G} \qquad \text{Equation 4.2}$$

In practise, the noise introduced by the output always remains constant, but the impact on signal degradation has been reduced. The typical readout noise introduced by the output amplifier is of the order 2-3 e^- for slow scan operation (50-200 kHz) rising to a few tens of e^- for MHz pixel rates (Jerram *et al.* 2001). The use of modest multiplication gain can therefore reduce the read noise to sub-electron levels, rendering amplifier noise negligible and relaxing the constraint of pixel rate. Modern readout electronics are capable of producing noise levels of order 50 e^- RMS at pixel

rates of 11 MHz, for example, at which point a modest multiplication gain of 50 or above will bring the camera into the sub-electron read noise regime and permit the detection of single photons (Harding *et al.*, 2016).

4.3.2 The Excess Noise Factor (ENF)

The quoted multiplication gain is typically an average value for a device under a specific set of operating conditions. In practise, the multiplication process is stochastic since it depends upon the carrier energy distribution and probabilistic scattering mechanisms with the lattice. For an input integer signal level, *n*, there is therefore a probability distribution of the output, x, once it has been transferred through the EM register and experienced multiplication. This distribution was derived by Basden *et al.* (2003) as:

$$p(x) = \frac{x^{n-1} exp\left(\frac{-x}{G}\right)}{G^n (n-1)!} \qquad \text{Equation 4.3}$$

Where G retains its meaning as the mean multiplication gain. In practise, the input signal cannot be treated as integer but instead is a Poisson distribution with a mean light level (Section 3.7.1) In Basden *et al.* (2003), the Poisson probability distribution is used in place of the input signal in Equation 4.3 to give:

$$p(x,\mu) = \sum_{n=1}^{\infty} \frac{e^{-\mu-\frac{x}{G}} \mu^n \left(\frac{x}{G}\right)^{n-1}}{G(n-1)!\, n!} \qquad \text{Equation 4.4}$$

Where $p(x,\mu)$ is the probability that the EM-CCD output will be x for a mean signal level of μ (e^-). This stochastic nature of the multiplication process adds noise to the output. This can be seen in Figure 4.7 where Equation 4.4 has been applied to various signal levels. The output distributions have considerable overlap that corresponds to the uncertainty in the determination of the input signal level for a given mean gain G. This additional noise requires formalism and is best described as a factor increase over the Poisson noise, termed the Excess Noise Factor (ENF), and was shown by Robbins *et al.* (2003) to tend to $\sqrt{2}$ for a large number of elements at high multiplication gain. For high energy photons, the sub-Poisson variance in the input signal corresponds to a reduction in the ENF, described in detail in Tutt *et al.* (2012), but has no further relevance here.

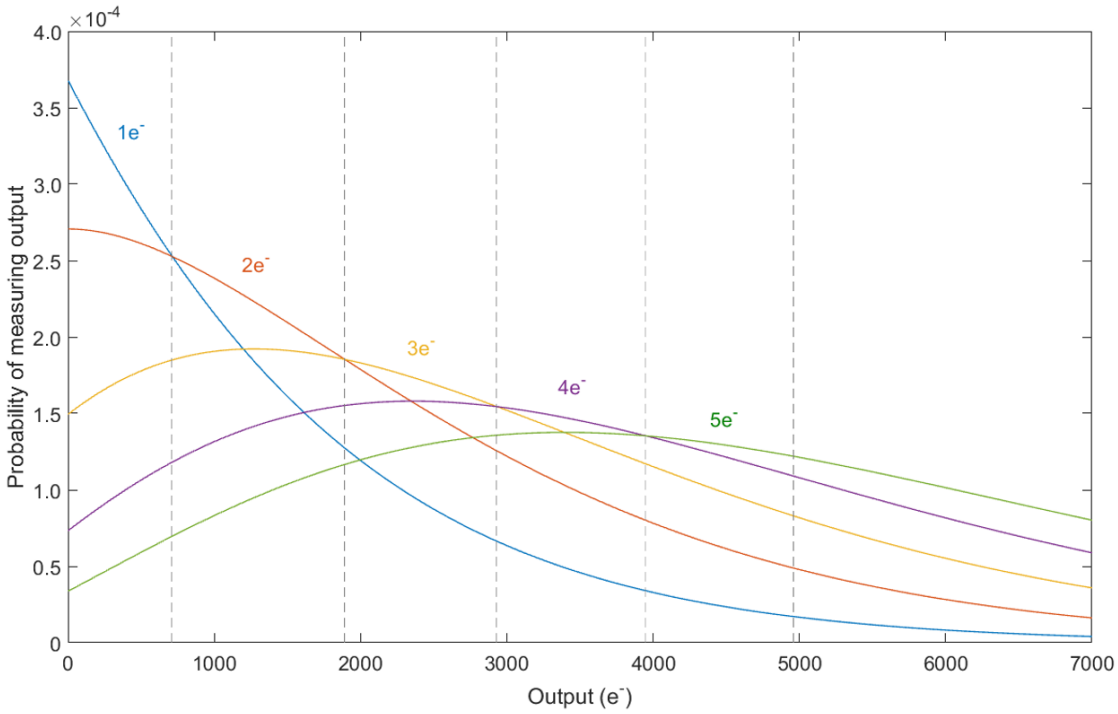

Figure 4.7: *Output probability distribution with input Poisson distribution of signal levels ranging from 1-5 e⁻ with a mean multiplication gain of ×1000. Note that there is significant overlap between different inputs, giving rise to the additional noise of estimating the input from the output. For large signal levels, the output distribution tends to a Gaussian and the overlap widths tend to a constant value resulting in an ENF of* $\sqrt{2}$.

The ENF acts to place limits upon situations where EM-CCD technology will provide a noise benefit to the system. For any given image, the total image area noise will be multiplied by a factor equal to the applied multiplication gain and then increased further by the ENF. Consequently, use of EM gain in a situation where the signal level is large compared to the noise introduced by the output amplifier may result in a *decrease* in total noise performance when compared to standard CCD technology. The regime where EM-CCD technology provides a benefit therefore requires attention and is derived through consideration of the total noise of the system with and without multiplication gain, σ_{tot}.

For a standard CCD, the total noise of the detector can be expressed as:

$$\sigma_{tot,CCD}^2 = A^2(\sigma_{signal}^2 + \sigma_{dark}^2 + \sigma_{readout}^2) \qquad \text{Equation 4.5}$$

Where $\sigma_{readout}$ is the readout noise, *A* is the video chain gain, σ_{signal} is the noise on the optically generated signal and σ_{dark} is the noise on the dark signal. For the EM-CCD, any signal passed though the EM register is multiplied and subject to the ENF, including the shot noise on the optical and dark generated signal. For a mean gain, G , and a noise factor denoted F the noise of the EM-CCD is therefore:

$$\sigma_{tot,EMCCD}^2 = A^2G^2F^2\left(\sigma_{signal}^2 + \sigma_{dark}^2\right) + A^2\sigma_{readout}^2 \qquad \text{Equation 4.6}$$

The ratio of Equation 4.5 and Equation 4.6 therefore highlights the regime where use of an EM-CCD will provide a noise benefit (Figure 4.8). The key determinant is the ratio of readout noise to the mean signal flux where if the signal flux is low compared to the read noise the EM-CCD improves performance. As the flux approaches and exceeds the read noise, use of a standard CCD becomes preferable. Both the read noise and the flux per frame are dependant on pixel rate and so demands on the frame rate also have an impact on the most suitable detector. For the CGI, or indeed any photon counting application, the EM-CCD will almost always be more suitable since the read noise always dominates the expected signal level by a large factor, regardless of pixel rate.

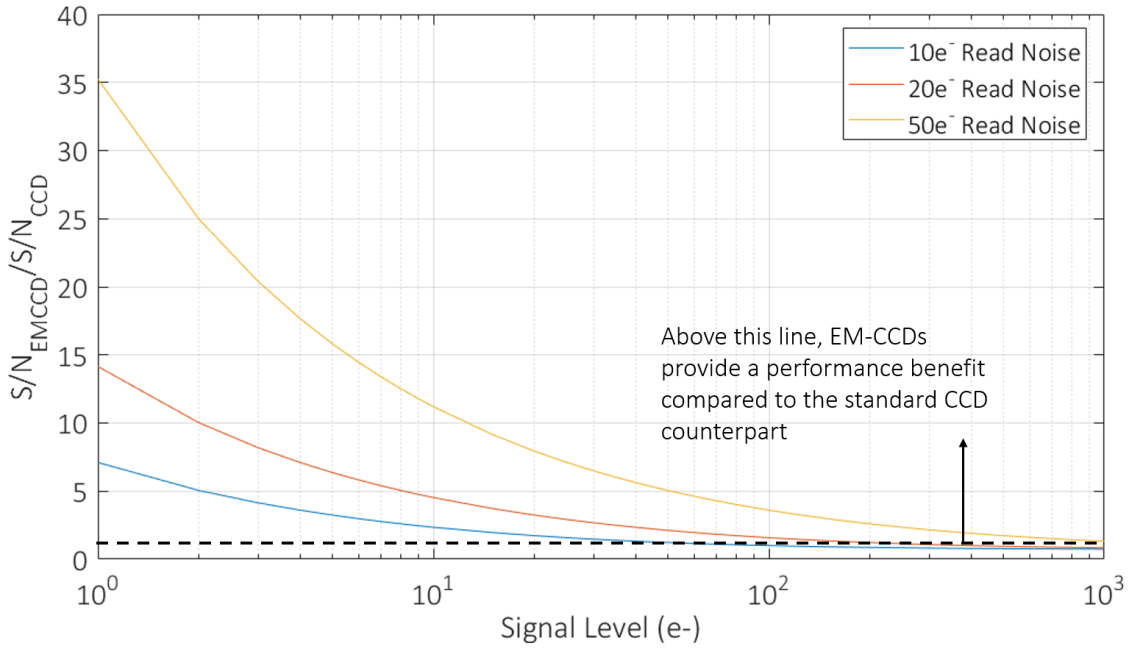

Figure 4.8: *Comparison of SN ratio for the CCD and EM-CCD. For this example, dark signal was assumed to be negligible and the video chain gain was assumed to be identical for each case. The Poisson noise was assumed to be the root of the signal size and the ENF was assumed to be* $\sqrt{2}$ *for all signal levels. The EMCCD can provide a substantial benefit to total noise performance for the case where the signal level is comparable to the read noise.*

4.3.3 Photon counting mode

The ENF arises from the degeneracy of the output signal from the EM register that could be from multiple photon inputs. If the probability of obtaining more than one photon is significantly reduced, i.e. by operating in extremely low flux, then this degeneracy is removed. In this regime, only the output distribution from the single photon is required and a fixed threshold can be introduced whereby any event that exceeds it is considered a single photon event, rendering the

ENF irrelevant. Operation with the single threshold applied is termed *photon counting mode* since in this regime the device is capable of counting individual photon hits.

Maximum noise performance is obtained by placing the threshold as close to unity signal as possible. In practise, this is limited by other competing noise sources; dark current and CIC give rise to "false positives" in the sense they are counted as photon hits but have not been photo-generated like the true signal. The choice of threshold is therefore typically a balance between rejecting as many false positives as possible while retaining the ability to detect optically generated electrons. The process is not completely noiseless, as the fact the output probability distribution peaks at unity signal means that some photon hits will always be lost no matter the choice of threshold. The noise is best quantified through the Detection Quantum Efficiency (DQE), defined as the ratio of detected photons divided by input photons. Operation with high multiplication gain pushes a larger fraction of the output distribution above the chosen threshold, shown by Figure 4.9, and so multiplication gains in excess of ×1000 are typically required to achieve adequate DQE in photon counting mode using an EM-CCD.

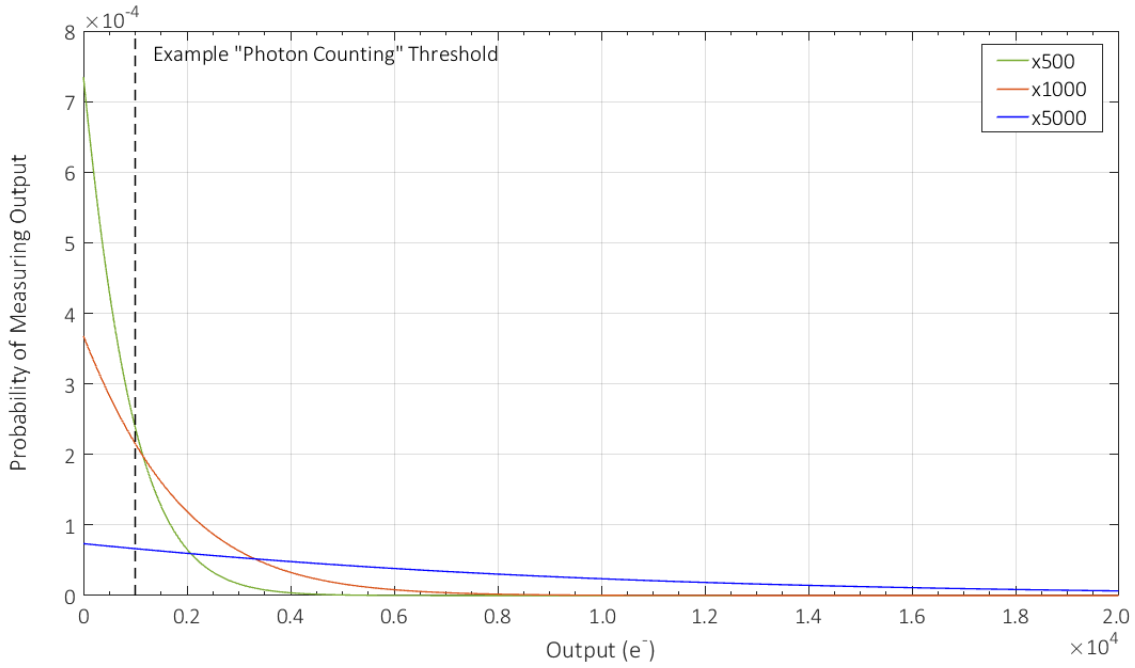

Figure 4.9: *Output probability distribution (using Equation 4.4) for a single photon with 3 different multiplication gain settings. As the gain increases, the integrated fraction of the output distribution above the threshold increases, translating to a higher DQE. For the examples shown (threshold of 500 e^-), the DQE is 19% for a gain of 500, 46% for a gain of 1000 and 60% for a gain of 5000.*

4.4 Dark current and CIC

For standard CCD technology, dark current and CIC are no longer significant once they have been reduced to a level comparable with the read noise. The sub-electron noise possible with an EM-CCD, however, means that each of these noise sources remains significant and must therefore be mitigated where possible. Dark signal is significantly reduced though operating in inversion and cooling the detector, whereas CIC is significantly reduced by operating in NIMO. There is therefore a trade-off between operating in IMO or NIMO for an EM-CCD system in accordance with the dominant noise source for a given combination of integration time, clocking scheme and operating temperature.

The total noise contribution from both CIC and dark current can be expressed as:

$$D(T) = S_D(T) \cdot t + mC(T, f) \qquad \text{Equation 4.7}$$

Where:

- $S_D(T)$ is the dark signal contribution at a temperature, T
- t is the total integration time (s)
- m is the number of parallel transfers
- $C(T, f)$ is the CIC component at temperature T, operating at frequency f.

The condition for which IMO and NIMO give the same noise performance for a given integration time, *t*, is given by:

$$S_I(T)t_0 + mC_I(T) = S_N(T)t_0 + mC_N(T) \qquad \text{Equation 4.8}$$

Where the subscripts, I, N denote noise performance for IMO and NIMO respectively. Solving for t_0 gives:

$$t_0 = \frac{mC_I(T, f) - mC_N(T, f)}{S_N(T) - S_I(T)} \qquad \text{Equation 4.9}$$

If the integration time exceeds t_0 then inverted mode operation is desirable as dark signal becomes the dominant noise component. If the integration time is lower than t_0 then operation in NIMO is desirable to mitigate the increased CIC.

4.4.1 EM-CCD noise sources for the CGI

Signal flux for the CGI is estimated to vary between 10^{-2} and 10^{-4} e^-/pix/s depending upon the planet target (Krist *et al.*, 2016) and so the instrument is in the regime where photon counting mode can still apply even with long frame integration times. Operation in analogue mode still offers a noise improvement over standard CCD technology (refer back to Figure 4.8) but translates into a longer observation time for a given planet due to the inclusion of the ENF. Photon counting mode is therefore the baselined operating mode for the CGI and predicted to provide the best noise performance (Harding *et al.*, 2016). An adapted version of Figure 2.12 is shown by Figure 4.10, this time showing only the EM-CCD vs a comparable CCD to illustrate the point further.

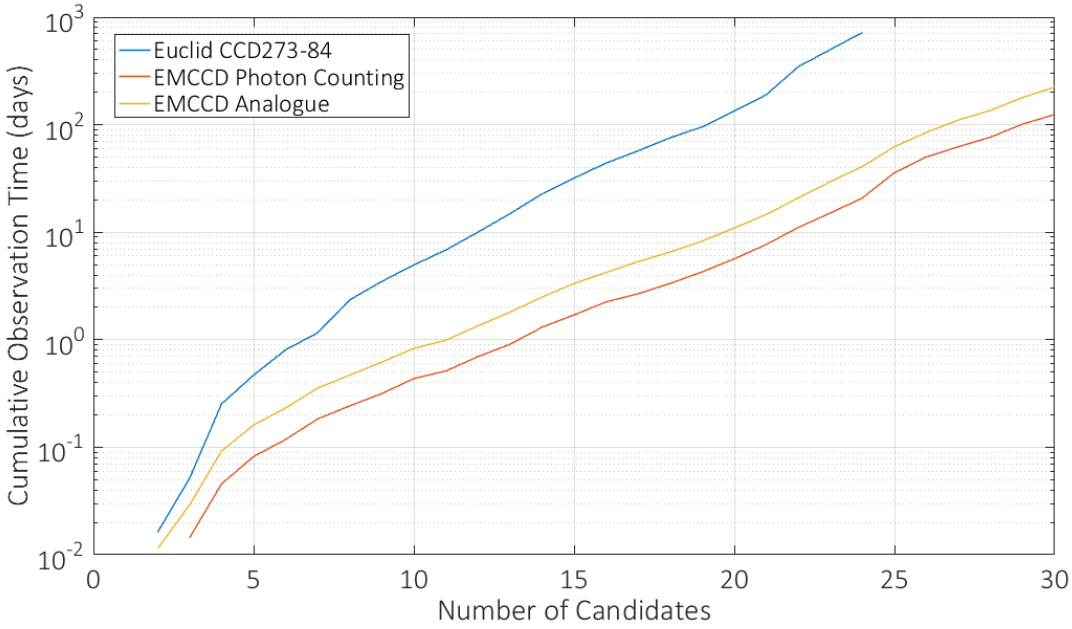

Figure 4.10: *Analytical prediction of observation time required to reach S/N = 5 versus the number of planets for each of the detector candidates. Adapted from Figure 2.12. The improvement in performance using an EM-CCD in either analogue or photon counting mode is clear in the context of the discussion in this chapter.*

Operation in photon counting mode means both CIC and dark current must be minimised. The CGI requires long integration times to accumulate enough signal within a single image. For example, the estimated total observation time for a typical planet target is of order 22000 s (Krist *et al.*, 2016), however, this will be split into multiple frames to limit the impact of cosmic rays on the available detection area. For typical values of dark signal and CIC, IMO is predicted to be the preferred operating mode for single-frame integration times of approximately 25 s or greater (Figure 4.11). The baselined single-frame integration time is of order 100 s and so IMO is the planned operating mode. Radiation damage can impact both dark current and CIC, and so the

preferred operating mode may change throughout the mission lifetime. CTI due to radiation induced traps can also be mitigated through changes to the operating temperature, pixel rate and integration time so in practise there may also be a trade-off between optimum CTE and the preferred operating mode, not accounted for in this model.

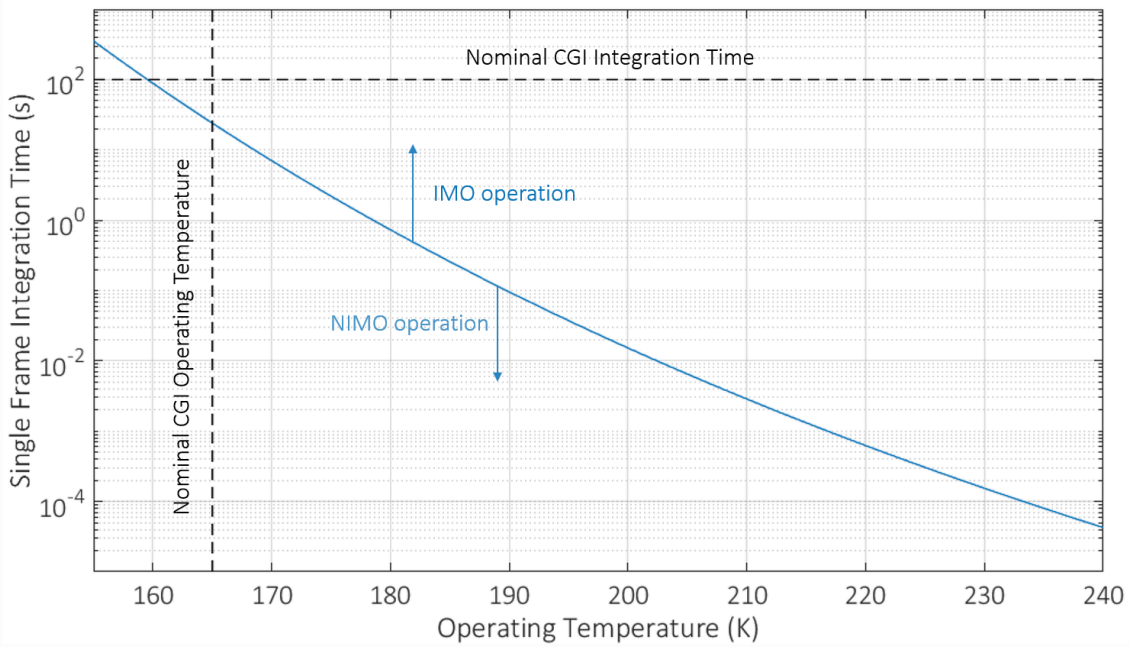

Figure 4.11: *Plot of Equation 4.9 for typical values of dark current and CIC that were taken from Harding et al. (2016), e2v Technologies, (2015) and from measurements made by the author.*

4.5 Additional performance considerations

The high electric fields within the EM register give rise to a suite of physical phenomena associated with high energy carriers that can degrade performance if not appropriately mitigated. The effects can be broadly categorised as carrier injection, carrier trapping and light emission and manifest as surface CTI effects, register "glow" and device ageing respectively. Although the exact impact of each phenomena differs, they share the common mitigation strategy of operating with the minimum required multiplication gain, and hence electric field, to achieve the desired read noise. Since high electric fields are essential for the multiplication gain process, complete elimination of these effects is not possible and so discussion turns to the underlying principles of each phenomena, how they can impact an image and a discussion on the potential impact for the CGI.

4.5.1 Surface CTI of the EM register

The buried channel CCD is reliant upon a potential barrier between the semiconductor interface and charge storage location that inhibits interaction with interface traps. Under normal operation, the charge storage location is typically ≈0.5 µm from the interface, with a potential barrier of a few volts for gate voltages comparable to or below the channel parameter of the device (Janesick, 2001). This barrier is significantly greater than the mean thermal energy of the charge packet ($\frac{3}{2}k_BT \approx$ 0.04 eV at 298 K) and so it is clear that interaction with the surface is prohibited for typical operating conditions. Two factors can increase the likelihood of interaction with the surface:

1. Operation with a gate voltage that is significantly in excess of the channel parameter.
2. Storage of a signal size comparable to the full well capacity of the device.

Each condition means more depletion is due to the gate as opposed to the channel, causing the location of the potential maxima to move towards the interface. For the EM-CCD, both factors are equally relevant. Gate voltages in the range of 30-45 V shift the location of the potential maximum to within 0.1 µm of the interface and so the minimum required thermal energy for interaction with surface state traps is significantly lower. It should be stressed that for small signal levels, the barrier is still sufficient to prevent interaction with the surface. Capture of a single electron signal level when operating at high gate voltages (40-45 V), for example, is predicted to be extremely unlikely. The concern is instead for larger signals that easily exceed the effective FWC at some point within the multiplication chain. These signals can fill a large population of surface state traps that then release charge into subsequent pixels. This charge can also be multiplied, raising it above the noise and resulting in “smearing” within images across the horizontal transfer direction (Figure 4.12). The charge tails that follow these large signal events can mask a photon-detection event and so impose a penalty on the total usable image area. For space-based applications such as the CGI, the cosmic ray flux places a limit on the integration time of a single frame in order to preserve as much usable-image area as possible for photon detection. The impact of cosmic ray smearing is therefore a key concern and the length of the tails must be minimised in order to preserve as much of the image area as possible.

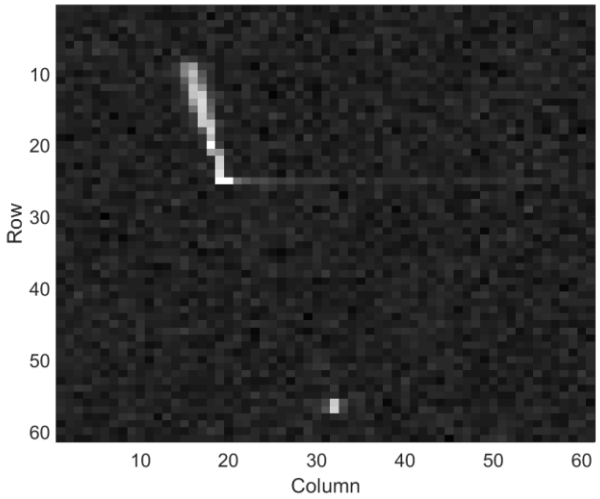

Figure 4.12: *Example of "smearing" due to an energetic cosmic ray depositing signal within the image area which was then multiplied when transferred through the EM register. Multiple columns are affected following the initial event.*

Multiple authors have noted "tails" of charge consistent with that shown in Figure 4.12 and have ascribed the phenomena as "blooming" due to the multiplied charge exceeding the FWC of the EM register (Daigle *et al.*, 2009). In some sense this explanation is correct, however, there is a distinction to be made between the standard, expected FWC of the device and the "effective" FWC when operating with EM-gain. The stated FWC of the EM register of standard e2v EM-CCDs is of order 400,000-700,000 e^- (e2v Technologies, 2015) and when this signal level is exceeded, charge does indeed preferentially bloom against the direction of transfer due to the fixed bias of the ϕDC gate, as described in Tutt *et al.* (2014) and Daigle *et al.* (2009). In this regime, the majority of the excess charge spills into the neighbouring pixel, however, some charge is also captured by surface states and emitted in a tail that follows the primary interaction. Interaction with the surface states can in fact occur at signal levels much lower than the stated FWC of the device (≈100,000 e^-, depending on operating conditions) and in this regime no blooming occurs, nevertheless, a tail of charge can follow the primary interaction and still significantly impact performance. Modelling and measurements for the surface trapping phenomena are discussed further in later chapters that illustrate this point in greater detail.

4.5.2 EM-CCD ageing

The multiplication gain of e2v EM-CCDs has been observed to decrease as a function of use - a phenomenon referred to in the literature as "device ageing" (Evagora *et al.*, 2012, Smith *et al.*, 2006). The Rϕ2HV clock must be continually increased as the device is used in order to maintain constant multiplication gain and it is therefore useful to describe an equivalent voltage shift required to maintain a constant multiplication gain as a function of either time or signal level (e2v technologies, 2006):

$$V = A(1 - e^{-\frac{t}{\tau}}) \qquad \text{Equation 4.10}$$

Where A is a scaling constant, τ is a time constant and t is either time or the amount of signal passed through the register. Ageing has been described as having both short and long-term components, to the extent that one single time constant cannot accurately describe the entire ageing history of the device. e2v typically perform a "burn-in" whereby the component due to short term ageing is removed prior to delivery to a customer. Following the burn-in, only the long-term component remains which is reported to have an equivalent time constant of the order 8000 hours. The device can continually be used until the voltage shift required to maintain sufficient gain causes CTE to significantly degrade, reported to occur at a ΔV shift of between 4 to 5 V (e2v technologies, 2006).

Small variations in the geometry of each device give rise to a unique field distribution with the EM register which in turn affects the rate of ageing. The dependencies on signal level, multiplication gain and Rϕ2HV bias also mean that many permutations for the rate of device ageing exist that have not been fully characterised. Consequently, ageing cannot necessarily be predicted for a given device and set of operating conditions but must be continually characterised in order to determine the adjustment to Rϕ2HV required for constant multiplication gain.

The nature of the degradation implies ageing is due to charge carriers becoming trapped within the gate-stack of the device. Carrier trapping can act to decrease the effective electric field within the substrate and hence the effective multiplication gain (Figure 4.13).

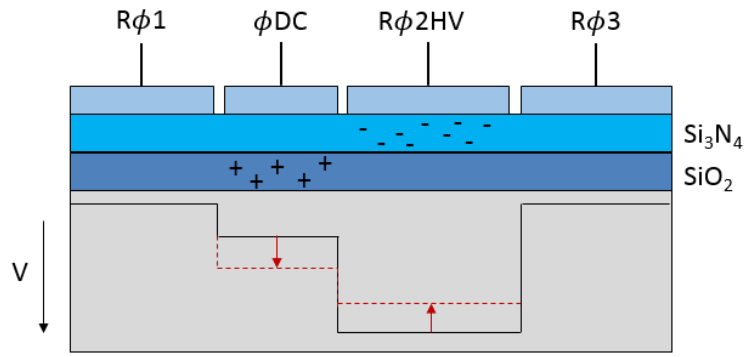

Figure 4.13: *Device ageing is thought to be due to charge carriers becoming trapped within the gate dielectric layers in the device. Holes trapped beneath the ϕDC gate, electrons trapped beneath the Rϕ2HV or a combination of the two could act to decrease the potential difference experienced by signal during transfer and cause a decrease in multiplication gain for a constant Rϕ2HV voltage.*

The standard dielectric stack for e2v EM-CCD devices consists of a layer of silicon dioxide and a layer of silicon nitride of equal thickness of approximately 85 nm, which can act as receptors for trapped charge. Ageing can be caused by either a fixed positive charge building beneath the ϕDC gate or a fixed negative charge between the Rϕ2HV gate. It is unlikely that permanent negative charge build-up will occur in silicon dioxide since electrons are relatively mobile within the oxide layer. Holes, however, are relatively immobile and so build-up within the SiO_2 layer is a plausible explanation and one that is supported by past studies (Evagora, *et al.* 2012). De-passivation of the interface is known to occur in the presence of both hot carriers and ionising damage. The bonds formed during the passivation process are Si-H which for silicon has a de-passivation energy of order 2.9 eV. Since this energy is lower than the ionisation energy for electrons (3.65 eV) it is plausible that de-passivation can occur during operation with EM-gain. It should be noted that this de-passivation will be accompanied with a corresponding increase in dark current beneath ϕDC, since the density of mid-band traps that contribute to the surface component of dark signal will increase significantly. For charge storage in the nitride layer, hole trapping requires a greater energy and so electron trapping would be the favoured mechanism yet both are technically possible.

While ageing technically limits the lifetime of the device it is significantly exacerbated through the use of the device with both high signal levels and a high multiplication gain (e2v technologies, 2006). For the WFIRST CGI the signal flux is so low that ageing represents a small concern with respect to the net performance of the instrument.

4.5.3 EM register "glow"

The electric fields required for EM gain accelerate the carriers to high energies such that they gain energy at a rate greater than can be lost through phonon scattering and so are no longer in thermal equilibrium with the lattice. Carriers that meet this condition are described as "hot carriers" and have an energy distribution best described by Maxwell-Boltzmann statistics with a high-energy tail. Hot carriers are known to induce photoemission within semiconductor devices, with studies on N-MOSFETs highlighting that the photoemission region coincides with the region carriers experience the highest lateral electric fields (Hublitz & Lyon, 1992).

The electric fields within an EMCCD operating with multiplication gain are thought to be sufficient to induce photoemission through the same process. This light can then either be collected within the same register pixel or travel to other regions of the device where it generates signal and contributes to the total noise. Light emission from the EM register is commonly termed "glow" since its appearance is similar to the glow seen due to the output amplifiers. The mechanism for light generation is disputed but thought to be due to one or more of the following three mechanisms:

- Bremsstrahlung radiation due to hot carriers scattering off ionised dopant atoms. The acceleration associated with the scattering event causes the carrier to emit radiation. Any radiation with an energy comparable to the silicon bandgap can photo generate electrons which are then collected as signal (Matsuda *et al.*, 1999).
- Recombination of hot electrons with holes. When the electron recombines with a hole a photon is emitted with energy equal to the difference between the two carrier energy levels. Visible light corresponds to photon energies in the range 1.8-3.1 eV - lower than the threshold energy for impact ionisation (Matsuda *et al.*, 1999). It is therefore plausible that carriers with sufficient energy can generate light which is then collected within the device.
- Radiative transitions between the conduction bands in silicon. Some studies have shown intensity peaks in the photo-emission spectra that are consistent with the separation of conduction band energy levels in silicon (Hublitz & Lyon, 1992). The difference in energy corresponds to approximately 1.8 eV, corresponding to a wavelength of approximately 700 nm which could be collected within the CCD.

Regardless of the dominant physical mechanism, glow from the EM register appears unavoidable since the energies required for impact ionisation will also induce light emission. During operation, the glow will manifest as spuriously generated electrons in the image area that are indistinguishable from CIC. Running the EM register for an extended period of time while

integrating in the image area shows the glow profile more clearly Figure 4.14 and it is interesting to note that it does not appear to peak at the end of the EM register as one may expect.

The reason for this is thought to be due to a combination of the placement of the EM register with respect to the image area, and the signal distribution throughout the register due to the multiplication gain mechanisms. The signal within each element of the EM register rises according to Equation 4.1, with the largest signal towards the end of the register. If the emitted glow is proportional to the magnitude of the signal experiencing impact ionisation, then this explains the rise in glow as a function of column position seen in Figure 4.14. In addition, if each of the EM register elements are treated as isotropic emitters of radiation, then less light is collected towards the edge of the image area when compared to the centre. This would explain the drop-in signal seen towards the end of the register near to the output. The explanation is speculative, and additional investigations into the nature of the glow are recommended.

For the CGI, the glow will increase the total dark signal within the image area and hence affect the maximum possible DQE in photon counting mode yet the impact is not thought to be significant when compared to CIC and bulk dark current.

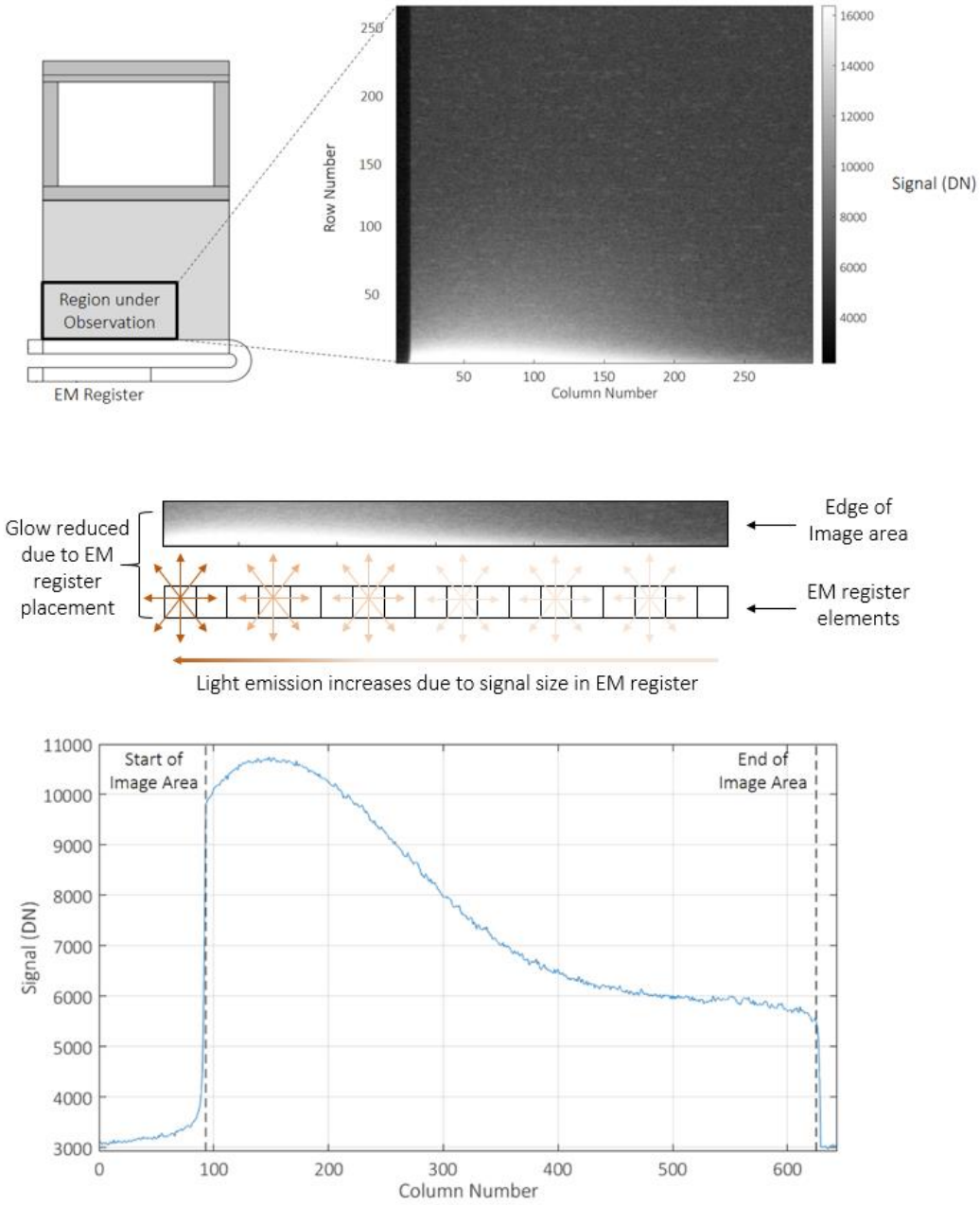

Figure 4.14: *Top: Image of EM register glow measured in a CCD97 generated by running the EM register with Rϕ2HV at 44.0 V (corresponding to a multiplication gain of approximately 2000) for approximately 10 seconds while integrating signal in the frame store region (measured by author). The glow corresponds with the location of the EM register, but it is interesting to note that the maximum glow does not occur towards the end of the register as one may expect. The middle panel provides a possible explanation; the placement of the EM register with respect to the image area means that some of the glow towards the end of the register can escape out of the device and not be collected as signal. The bottom panel shows the glow as a function of column number, where the profile is more visible.*

4.6 Summary: BOL performance considerations for EM-CCDs

While the EM-CCD and CCD are very similar, the addition of the multiplication register fundamentally changes how the device should be optimised and introduces additional performance considerations that are not normally of concern for standard CCDs. The choice to use a CCD or EM-CCD for a given application has been shown to be founded in the ratio between the expected signal flux and detector read noise, with the EM-CCD the clear choice for photon counting applications such as the CGI. Both thermal dark current and CIC contribute to the remaining total noise and the choice to operate in either IMO or NIMO is dependent upon a balance between the total dark current accumulated within frame integration and the total CIC accumulated in readout.

Operation with multiplication gain gives rise to additional performance considerations that include surface CTI within the EM register, carrier injection into the gate di-electric and light-emission from the EM register. Each of these issues are mitigated through operation with the minimum required gain to achieve the desired read noise level.

For the WFIRST CGI, operation in photon counting mode and IMO is predicted to provide optimum noise performance for the nominal operating conditions of 100 s frame integration at 165 K. This was, however, a calculation based upon BOL performance measurements. Throughout the nominal 6-year mission, the detector will be subjected to both ionising and non-ionising damage that can act to increase the net dark current and degrade CTI. Appropriate optimisation in the presence of radiation damage requires detailed knowledge of the expected trends and effects of radiation on EM-CCD technology; the subject of next chapter.

5 Radiation damage effects on CCD-based technologies

CCD technology has been successfully implemented onto many large-scale missions where the impact of radiation damage has been a concern. Radiation damage on CCD technology is a subject that has therefore received substantial attention in the literature. In particular, the reader is directed towards the works of Kinchin & Pease (1955) and Srour *et al.* (2003) for an overview of displacement damage effects within silicon devices. For the specific case of damage to CCDs, the reader is directed to the works of Hopkinson *et al.* (1996) and Janesick *et al.* (1989) where the link between damage processes and device performance is better established.

The process of radiation damage in CCD technology is underpinned by the simple fact that exposure to energetic particles creates silicon lattice defects within the device that degrade performance. In almost all cases, the degradation in performance can be linked to the presence of "traps"; defects within the periodic lattice structure or gate dielectric that enhance charge capture, emission and recombination processes. The variety and complexity of how defects behave in silicon (and indeed the gate dielectric) is another vast research discipline with a substantial amount of information in the literature. The types of trap and their relative abundance within a given device are dependent on many factors, including the quality and type of the starting silicon and subsequent manufacturing processes. Exposure to radiation increases the total population of defects within the device and the final distribution is known to be dependent on the temperature at which the irradiation was performed, the degree of background illumination present and even the type of particle responsible for the damage. To complicate the matter further, the final performance of the device depends also upon the interaction of these trapping sites with the illumination field, clocking conditions and temperature at which the device is operated. The best prediction of performance is therefore derived from customised investigations where the illumination pattern and test conditions are as representative of the in-flight case as practically possible. Knowledge of the landscape of silicon defects then allows performance to be optimised further to limit the impact of radiation induced damage.

This chapter provides an overview of the near-Earth space environment, where the orbit of a mission determines the primary mechanisms for damage in a device. The orbit choice for WFIRST is then discussed and the expected particles fluences are modelled. Discussion then moves to an overview of the radiation damage processes in silicon. For WFIRST, displacement damage effects and the formation of trapping sites in the buried channel are the primary concern due to the low signal levels under observation. The current literature information on defect species within CCD technology is reviewed alongside the motivation for a radiation damage study specific to the CGI.

5.1 The near-Earth space environment

The near-Earth radiation environment dictates the nature and magnitude of the damage that an instrument will experience and is modulated by the interaction of the Sun with the Earth's magnetic field. It consists of three main components; solar particle flux, trapped radiation within the Earth's magnetosphere, and galactic cosmic rays.

The solar particle flux encompasses any particle emission from the sun and includes the solar wind, coronal mass ejections and solar flares. The solar wind is a stream of charged particles released from the upper atmosphere of the Sun. It consists of mostly electrons, protons and alpha particles with energies up to approximately 10 keV. Solar flares are the result of a burst of energy being released from the coronal magnetic field. The majority of the particle emission is comprised of electrons and typically lasts a few hours. Coronal Mass Ejections (CMEs) are a large eruption of plasma that gives rise to a shock wave that accelerates particles outward into the solar system. CMEs typically have a larger impact on the near-Earth environment than solar flares as the total amount of ejected material can be quite large (between 10^{15} and 10^{17} grams typically). The increased fluences that accompany these solar events can mean they form the dominant component of radiation damage for instruments with high altitude orbits. Even for instruments in other orbits, a solar flare or CME can result in a drastic increase in the accumulated dose over short timescales.

The Earth is shielded from the Sun's radiation by the Earth's magnetic field and the interaction of the two gives rise to the magnetosphere. Approximately 99% of the particles directed towards the Earth are deflected, however, a small percentage become trapped, giving rise to the Van Allen radiation belts, illustrated by Figure 5.1. The inner belt is comprised mainly of trapped protons at an altitude between 300 km and 25,000 km. The outer belt extends between an altitude of 25,000 km to 50,000 km and consists mainly of electrons. The magnetic and rotational poles of the Earth are not aligned, and so the magnetic field is centred off axis with respect to the rotation of the Earth. The result is that the inner belt subtends to a low altitude around the South Atlantic, giving rise to the South Atlantic Anomaly (SAA). Low altitude orbits therefore experience an increased proton flux as they traverse this region. For Low Earth Orbits (LEO), damage from the SAA can be the dominant component of radiation damage throughout the mission.

Galactic cosmic rays are high-energy charged particles that originate outside of the solar system but are generally accepted to originate from within our galaxy. They primarily consist of high energy protons and alpha particles with smaller components of heavier nuclei up through Uranium (Z = 92). The relative abundance typically falls as a function of atomic number, becoming effectively flat after iron (Z = 26). The energy per nucleon follows a spectrum that typically peaks

at approximately 1 GeV. Events with energy greater than 10^5 MeV/nucleon quickly become increasingly rare but have been occasionally measured. The energy spectra for galactic cosmic rays is summarised by Figure 5.2, as modelled by (Tylka *et al.*, 1997).

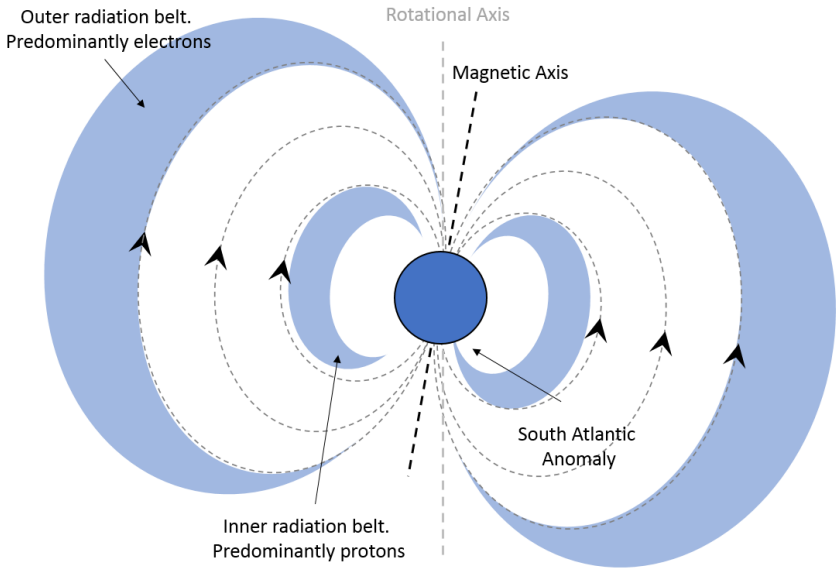

Figure 5.1: *The positioning of the Earth's magnetic field with respect to the axis of rotation gives rise to the South Atlantic Anomaly (SAA).*

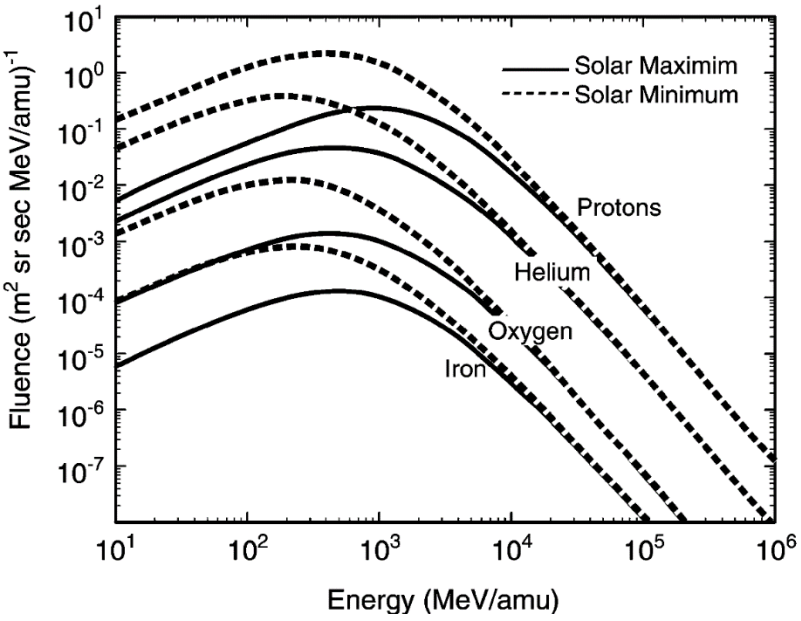

Figure 5.2: *Galactic Cosmic Ray energy spectra for protons, helium, oxygen and iron during solar maximum and solar minimum conditions, modelled by* (Tylka *et al.*, 1997).

Solar activity follows an approximate 11-year cycle whereby activity is seen to oscillate between a minimum and a maximum. Within an 11-year cycle, there are typically 7 years associated with solar maximum where activity rises and peaks and 4 years of solar minimum. Transition through

the cycle is continuous though the magnitude of activity from one cycle to the next can vary significantly and is not easily predicted. A commonly accepted measure of solar activity is the number of sunspots, areas of reduced surface temperature that appear darker than the surroundings, with a higher number of sunspots correlated with an increase in solar output activity. Sunspot numbers have been monitored continuously since the early 1700s and illustration of the number vs time shows the clear repeating pattern of activity with variable peak and trough magnitudes (Figure 5.3).

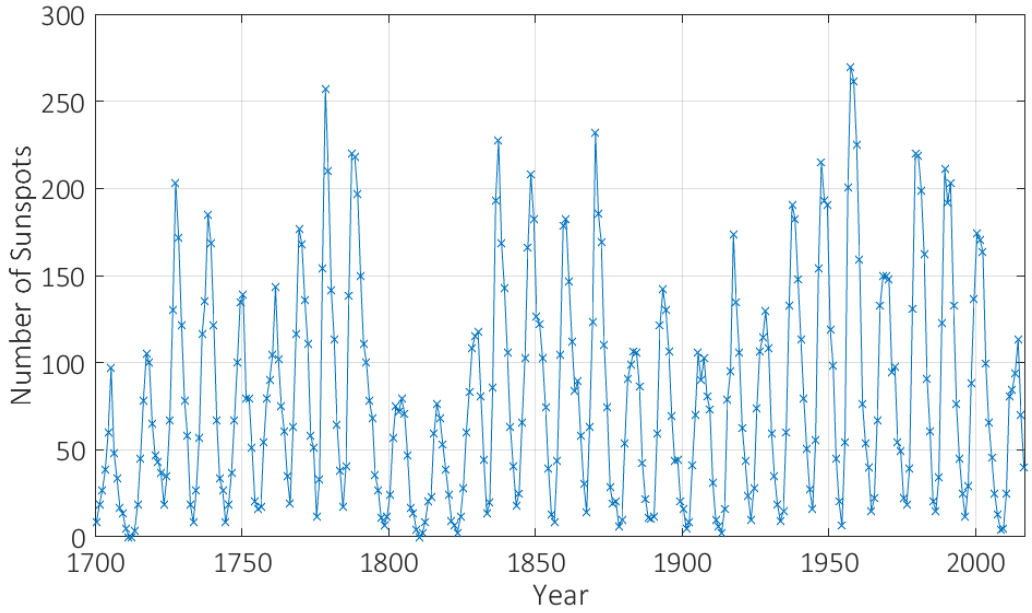

Figure 5.3: *Plot of number of recorded sunspots per year from 1700 to present day. The solar maximum typically coincides with the peak number of sunspots within an approximate 11-year period. Data source: WDC-SILSO, Royal Observatory of Belgium, Brussels.*

The solar cycle modulates the frequency of solar particle events, trapped particle fluxes within the radiation belts and galactic cosmic ray flux. Large solar particle events such as CMEs and solar flares are known to occur with greater frequency during the declining phase of the solar maximum. Detected galactic cosmic ray fluxes tend to be higher during solar minimum (due to less influence from the solar wind) yet peak at a slightly lower energy (Figure 5.2). Within the radiation belts, trapped electron fluxes typically tend to be higher during the declining phase. Trapped proton fluxes within the inner radiation belts reach their maximum during solar minimum. The launch date of a mission with respect to the current state of the solar cycle can therefore have a measurable impact on the total radiation dose the instruments will receive. Predictions of total fluences typically rely on a “worst case scenario” assuming the conditions of maximum particle flux within the radiation belt and the maximum flux of cosmic rays. Risk is mitigated further by incorporating safety factors of between 2 and 4 to account for the possibility

of abnormally high dose due to CMEs or a particularly active environment within the mission duration.

5.2 Orbit selection for WFIRST

The radiation environment of the CGI is highly dependent on the orbit type of the observatory since this will determine the degree of exposure to both trapped and non-trapped radiation sources (Table 5.1). At the time of writing, two orbital configurations are under consideration for WFIRST; an inclined geosynchronous orbit (GEO) and a halo orbit around the 2nd Lagrangian point of the Sun-Earth system (L2).

A geosynchronous orbit is one whereby the orbital period is equal to the period of rotation of the gravitational host. The altitude is fixed at approximately 36,000 km for orbit around the Earth and so geosynchronous orbits are within the outer Van Allen radiation belt. The baselined geosynchronous orbit for WFIRST is a 28.5° circular inclined geosynchronous orbit with an initial right ascension of the ascending node (RAAN) of 228°. These parameters were chosen based upon the baselined launch location and the visibility of the galactic bulge for microlensing observations of the WFI (Spergel *et al.*, 2013). The principle argument for the GEO configuration is the higher data downlink rate. At GEO more detailed information could be downloaded from the WFI that will aid the dark energy observer program and allow other ground-based observatories to perform follow-up observations quickly.

The L2 orbit is positioned approximately 1.5 million km from the Earth and at a position where the observatory maintains a relatively fixed position with respect to the Sun and the Earth. The L2 point is one of 5 solutions where this condition is met with L2 being most convenient for observatories that wish to be shielded from the sun as much as possible. The dominant source of radiation at L2 is from the solar wind and galactic cosmic rays, providing a lower total dose than at GEO, however the larger separation places limits on telemetry and data would likely have to be compressed and stored on-board prior to scheduled downlinks that would occur multiple times each day. Operation at L2 would provide fewer observing constraints for both the WFI and CGI. The microlensing fields would be available throughout the year at L2, whereas at GEO they would be limited to two 72-day seasons centred in March and September. For the baselined coronagraph operating in GEO, 66.5% of the sky would suffer an Earth viewing cut-out that would last up to 5 hours. The observatory would have to perform complex operations to avoid and then re-centre on a given science target to account for this cut-out. At L2 this would not be necessary (Spergel *et al.*, 2013). Table 5.1 summarises a few typical orbit configurations with the dominant sources of radiation exposure, while Figure 5.4 shows the differences in the geostationary and L2 orbit configurations.

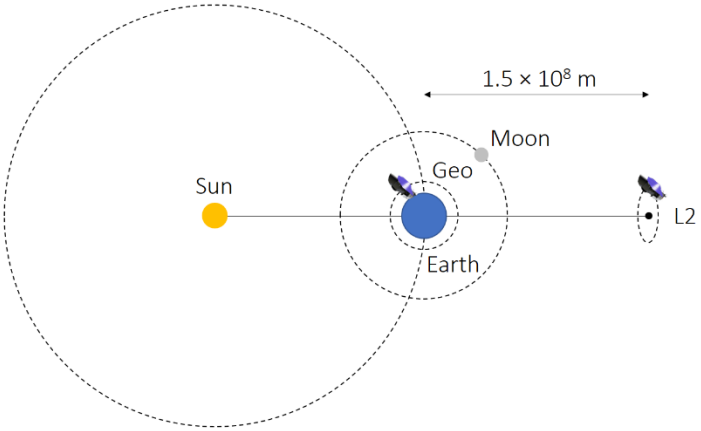

Figure 5.4: *Schematic of L2 and geo orbits (not to scale). The geostationary orbit is positioned on the outer edge of the outer Van Allen belt. At L2, the dominant particle flux is due to solar protons.*

Table 5.1: *Typical orbits with description and the dominant sources of radiation.*

Orbit Type	Description	Main Source of radiation	Other source(s) of radiation
Low Earth Orbit (LEO)	Altitude below 2000 km	Trapped	-
Geocentric/Geosynchronous Earth Orbit (GEO)	Altitude 35,790 km	Non-Trapped	Trapped due to outer belt.
L2	Transfer orbit to L2 at an altitude of 1.5 million km	Non-Trapped	Trapped during transfer

5.3 WFIRST radiation environment

Operation at GEO is considered to be a harsher radiation environment due to energetic electrons in the outer Van Allen belt. At this altitude, there is also a component of solar protons though this is reduced compared to L2 due to shielding from the Earth's magnetic field. At L2, the dominant radiation component is solar protons.

The CGI will be shielded to protect the CCDs against the effects of radiation damage with the exact dependent upon what the devices can tolerate with respect to the total fluence (both ionising and non-ionising components). In each case, the instrument will be subjected to particles that span a wide range of energies. Quantification of the total damage experienced is therefore simplified by normalising the fluence to a specific energy.

The 10 MeV equivalent fluence is the industry standard for protons, as this energy is achievable by most proton accelerator facilities and so allows ground testing consistent with the expected

mission fluence. The use of the Non Ionising Energy Loss (NIEL) function in silicon is described in detail by Srour *et al.* (2003) and is approximated using the following equations:

$$\text{10 MeV NIEL Function} = \frac{8}{E_p^{0.9}} \qquad \text{Equation 5.1}$$

where E_P is less than 13.5 MeV.

$$\text{10 MeV NIEL Function} = \frac{1.6}{E_p^{0.28}} \qquad \text{Equation 5.2}$$

where E_P is greater than 13.5 MeV.

Different functions are available for other particle types (Dryer *et al.*, 2016). From this point onwards, proton fluences are normalised to the 10 MeV equivalent using the above equations.

To assess the impact of each type of orbit, a total of 6 shielding configurations were considered in a study by Harding *et al.* (2016) that consisted of variable thickness of either aluminium or tantalum. The cumulative displacement damage dose (10 MeV equivalent) was simulated using NOVICE[3], a commercially available software package that calculates and models radiation transport methods and effects. The simulations incorporated a 3D CAD model of the CGI with the prospective shielding thicknesses including a safety factor of ×2. With the minimum shielding configuration (10 mm of aluminium) the 10 MeV equivalent proton fluence following a 6-year mission was estimated to be approximately 7×10^9 p/cm^2. This is in line with estimates provided for similar missions such as Euclid, which will have a 6-year mission and has an estimated EOL proton fluence of approximately 5.8×10^9 p/cm^2 (Laureijs *et al.*, 2010). The total ionising dose was seen to be a maximum of a few krad and is reportedly significantly reduced through the inclusion of a 1 mm glass window affixed to the outer CCD package (Harding *et al.*, 2016). A summary of the 10 MeV proton fluences and ionising doses expected for each shielding configuration is provided within Table 5.2.

In addition to the investigation performed by Harding *et al.*, the radiation environment in GEO and at L2 for a nominal 6-year mission was simulated by the author using the ESA Space Environment, Effects and Education System (SPENVIS) using the baselined conditions for WFIRST GEO and L2 orbital configurations. The simulations assumed a "worst case scenario" whereby the conditions for maximum trapped particle flux and cosmic ray flux were assumed. Despite this, the

[3] http://empc.com/novice-software/

solar particle fluence was found to be near identical for each case whereas at GEO the trapped component dominates for energies less than a few MeV, as shown in Figure 5.5.

Table 5.2: *Summary of the 10 MeV proton fluences and ionising doses expected for various shielding configurations. Doses and fluences are estimates based on the results of Harding et al. (2016).*

Shielding Material	Thickness (mm)	10 MeV equivalent. Total Fluence proton cm^{-2} (6-year mission)	Total Ionizing Dose with 1 mm window (rad, Si)
Aluminium	10	$\approx 7\times10^{9}$	≈2600
	15	$\approx 5\times10^{9}$	≈1900
	20	$\approx 4\times10^{9}$	≈1600
Tantalum	3	$\approx 6\times10^{9}$	≈2300
	5	$\approx 4\times10^{9}$	≈1600
	10	$\approx 2\times10^{9}$	≈750

The impact of different shielding thicknesses was simulated with the caveats that only aluminium was available as the shielding material and the geometry of the shielding was assumed to be spherical. Nonetheless, similar results were obtained to those presented within Harding *et al.* with estimated fluences ranging between 2.0-7.5×10^9 p/cm^2 depending upon the shielding thickness (shown by Figure 5.6 and Figure 5.7). For either orbit, the damage was found to be dominated by solar proton events. Even at the minimum shielding thickness, the flux due to trapped protons and electrons was reduced to a negligible level compared to that of the solar proton fluence (shown by Figure 5.8).

Estimates of the Total Ionising Dose (TID) are shown by Figure 5.9 and were also similar to those within Harding *et al.* whereby at the minimum thickness of Al shielding the TID was estimated at a few krad. These simulations do not include the presence of the 1 mm glass window which perhaps explains the slightly higher estimate for an equivalent shielding thickness.

The conclusion from this simulation work and the work of Harding *et al.* (2016) is that, even at the highest levels of shielding, the instrument will be subjected to a significant proton fluence by the end of the mission lifetime. The effects of proton damage on the EM-CCD must therefore be understood in detail to ascertain the impact on science performance.

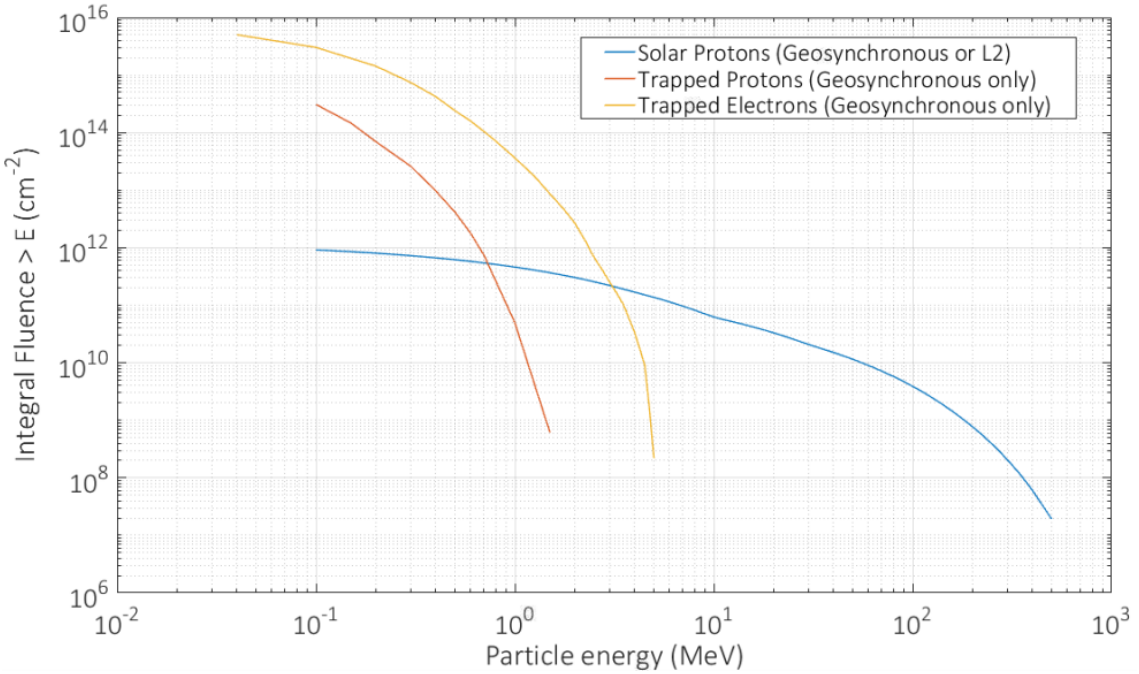

Figure 5.5: *Simulated unshielded integral fluence for WFIRST assuming 6-years at L2 and at GEO. The trapped electron and proton components were simulated using the National Space Science Data Center (NSSDC) AE-8 and AP-8 models, assuming maximum fluence for each case within a given solar cycle. The solar proton fluence was simulated using the JPL solar particle model with 95% confidence interval. The integral fluence for GEO and L2 was found to be near identical for the assumptions of this simulation.*

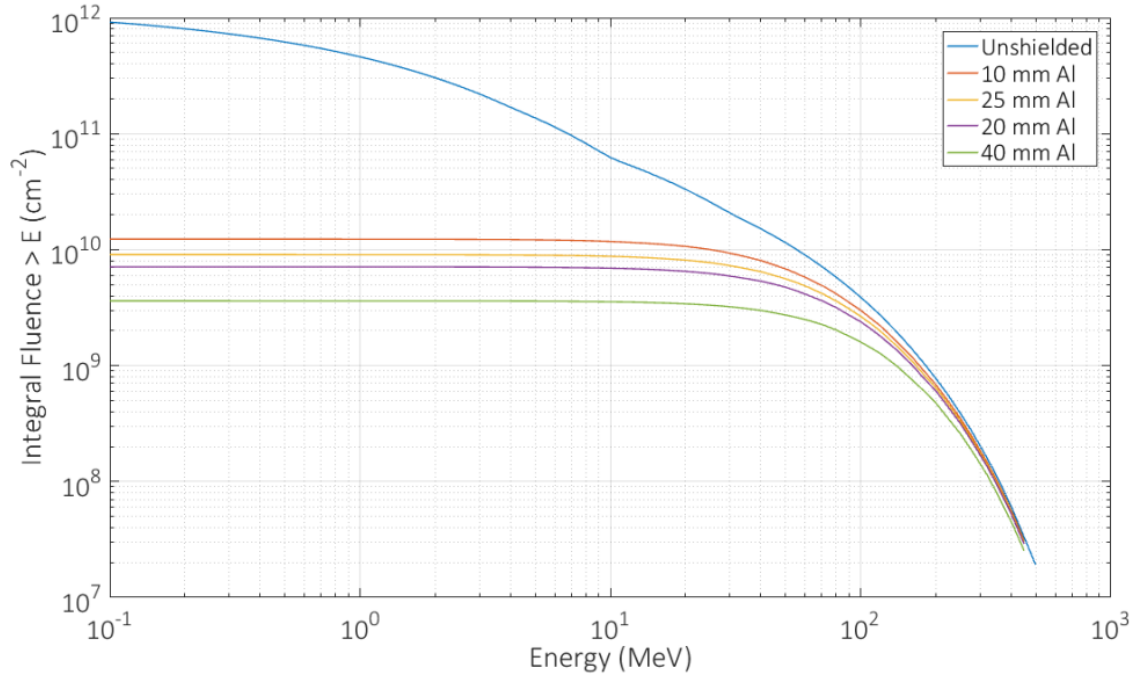

Figure 5.6: *Integral proton fluence due to solar protons for 4 aluminium shielding thicknesses. Proton energies of order 10 MeV are well shielded by even small thicknesses of Al. At energies approaching 10^2 MeV and beyond the protons cannot be practically shielded against.*

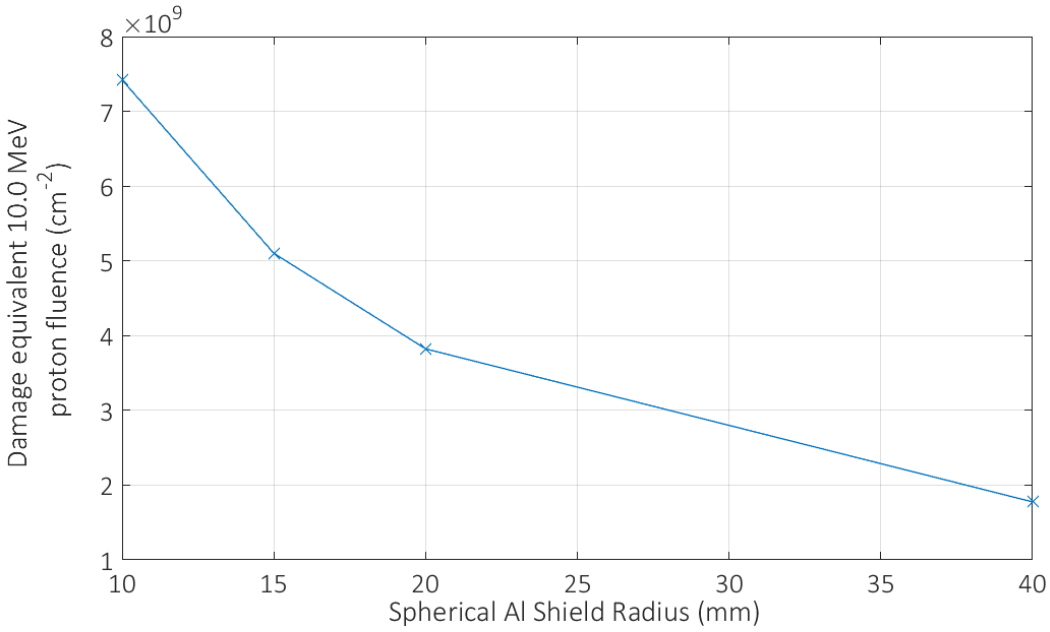

Figure 5.7: *10 MeV equivalent fluence estimated for WFIRST at L2 using the SPENVIS tool for various shielding thicknesses. The damage is dominated by high energy solar protons.*

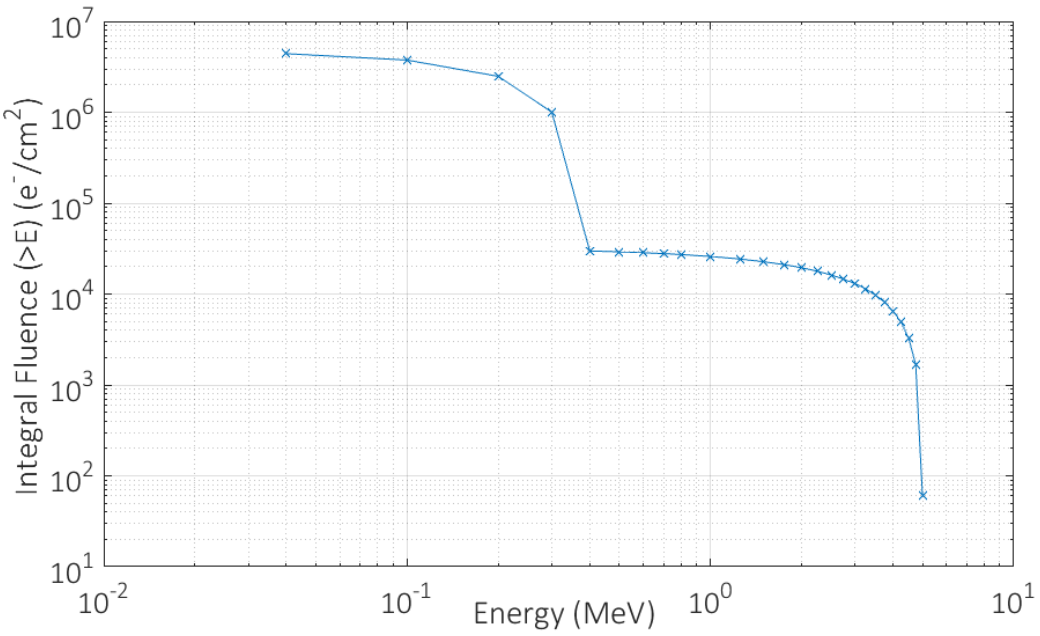

Figure 5.8: *Integral electron fluence in GEO for a spherical 10 mm Aluminium shield. For the entire 6-year mission, the integral fluence at low energy is reduced to the order of 10^6 e^-/cm^2 - 4 orders of magnitude less than the proton fluence (Figure 5.6).*

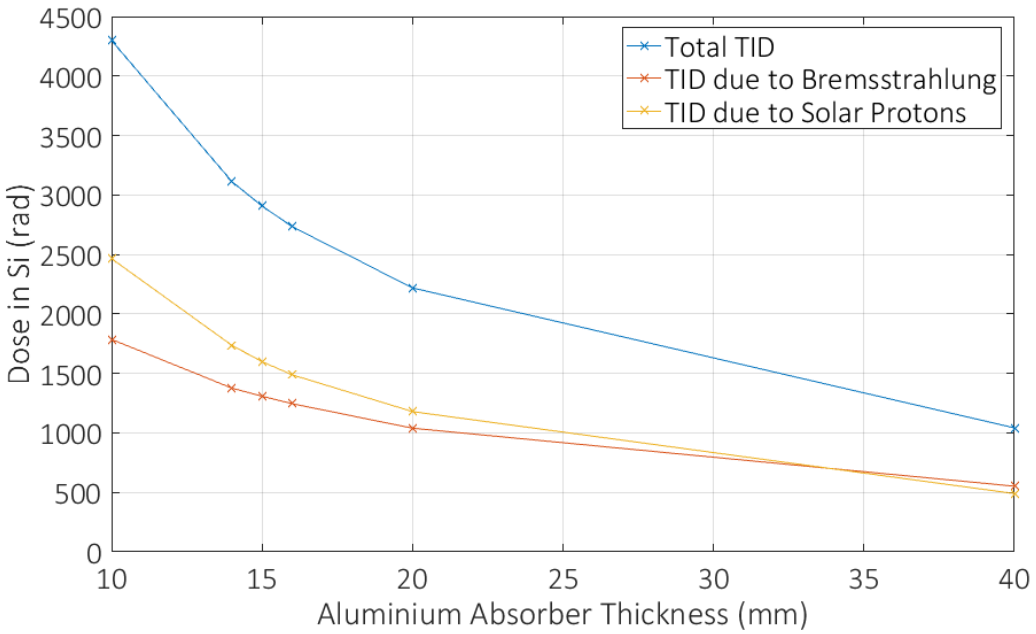

Figure 5.9: *Total ionising dose estimated for WFIRST at L2 for various shielding thicknesses. Components due to solar protons and bremsstrahlung (ionising radiation created through the deceleration of charge particles within shielding) are comparable. The maximum TID is estimated at at approximately 4 krad and assumes no modifications to the CCD package.*

5.4 Proton damage effects in CCDs

As an energetic proton traverses through the CCD it will lose energy through the generation of electron-hole pairs and the displacement of atoms from their lattice position, termed ionising and non-ionising energy loss (NIEL) respectively. The vast majority of the energy loss goes into ionisation and the creation of electron-hole pairs and a small fraction displaces atoms from lattice sites giving rise to a vacancy-interstitial pair (Frenkel pair), illustrated by Figure 5.10. Each energy loss mechanism has a different impact on the performance of the device.

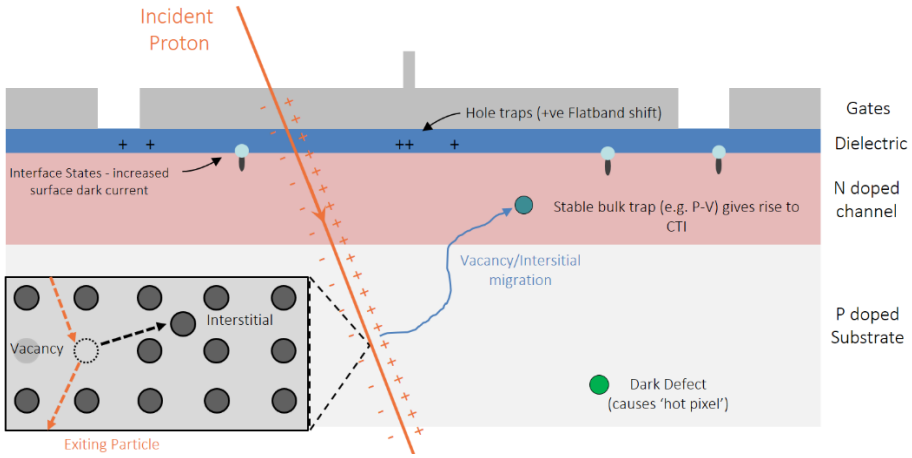

Figure 5.10: *Diagram summarising both ionising and non-ionising damage effects for CCD image sensors (adapted from Srour et al., 2003).*

5.5 Ionising effects

As an energetic proton travels through the device it loses the majority of its energy (≥ 99%) through coulombic interactions with the lattice, generating electron-hole pairs along its trajectory through ionising damage. During operation, a proton event (included under the collective term 'cosmic ray') may therefore manifest as temporary signal since any charge generated in the bulk may diffuse into the potential wells of one or more pixels. The effects due to ionising damage within the bulk silicon are mostly transient and do not cause permanent damage. A high number of proton events within a given frame, however, can be problematic in the sense that they can obscure the true signal under observation. Cosmic rays can therefore place a limit on the total permissible single frame integration time. An additional complication is present for EM devices whereby if a cosmic ray deposits a large amount of signal within one or more pixels it will be multiplied within the EM register and can bloom across the row (Section 4.5.1). A discussion concerning one of the possible physical mechanisms behind this effect can be found in Bush *et al.* (2012), and a study concerning ground-based measurements of cosmic ray fluence for the CCD201-20 can be found in Harding *et al.* (2016).

While the effects within the bulk are transient, ionising damage within the gate dielectric can give rise to permanent degradation. Charge generated within the insulator layers can be less mobile than within the bulk, with holes being much less mobile in the oxide layer than electrons (Hopkinson *et al.*, 1996). The electron may therefore migrate away from the generation site within the oxide before it is able to recombine, leaving behind a net positive charge. The accumulation of this charge over time gives rise to a flat-band voltage shift which can affect CIC and CTE. Traps are also generated at the silicon-silicon dioxide interface that can increase the component of surface dark signal (Hopkinson *et al.*, 1996). The degree of ionising damage has also been shown to be dependent on whether the detector is biased during the time that it is irradiated. During operation, the gates are periodically biased which gives rise to an electric field within the dielectric layers, shown in Figure 5.11. A carrier pair generated by an incident particle in the presence of this field therefore experiences forces in opposing directions, reducing the possibility for recombination (Hopkinson *et al.*, 1996). The best estimate of performance degradation due to ionising damage is therefore obtained by irradiating the detector biased if this represents the in-flight case.

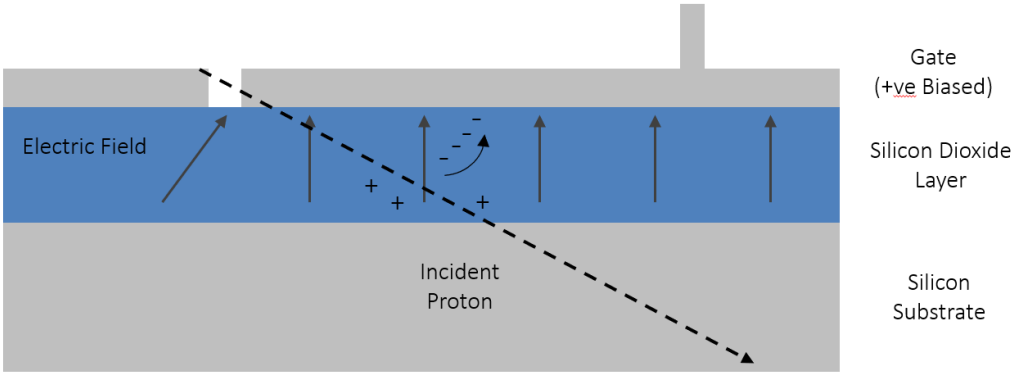

Figure 5.11: *Ionising damage within the gate dielectric in the presence of an electric field due to a gate bias. Electrons are more mobile than holes within the oxide layer, and so move freely up towards the gate. Holes, however, are less mobile and form stable trapping sites within the oxide layer and at the semiconductor-insulator interface.*

5.6 Non-ionising effects

Although the fraction of energy deposited through NIEL is small compared to the ionising component, it commonly constitutes the majority of the measurable damage for a CCD in a radiation environment. Protons traversing through the material undergo predominantly Columbic interactions with lattice sites, displacing atoms from their equilibrium position to create Frenkel pairs.

Formation of a Frenkel pair requires a minimum energy to be imparted, termed the displacement energy, which for silicon is approximately 20 eV. Any additional energy above the threshold energy is imported as the K.E. of the interstitial, now termed the primary knock-on atom (PKA). If the PKA has sufficient energy, additional Frenkel pairs can be created each with another PKA. The resting location of the interstitial corresponds with the point at which it has lost the majority of its K.E. Most of the interactions are Coulombic in nature and so impart enough energy for one to a few displacements. The resultant interstitial will usually only be a few interatomic distances away from its corresponding vacancy. For sufficiently high energy protons (> 100 MeV), “hard sphere” collisions with the nucleus can result in a PKA with energy 3-15 times the displacement energy that gives rise to defect clusters (Kinchin & Pease, 1955). Such clusters are still limited to approximately the energy of the PKA divided by the displacement energy and so rarely extend beyond a few nm in size. Figure 5.12 shows the possible damage mechanisms due to the energy of the PKA as a function of the incident proton energy.

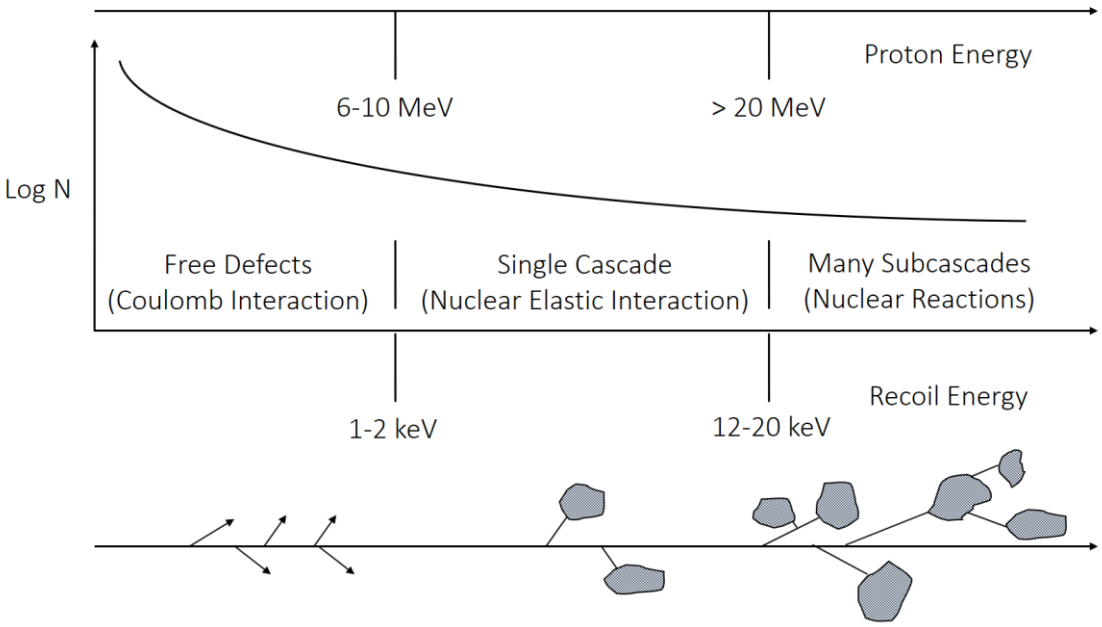

Figure 5.12: *Diagram adapted from Srour et al. (2003) that relates the initial defect configuration to the PKA energy for silicon.*

Following their initial formation, the vast majority (> 90%) of Frenkel pairs recombine and the fraction that do not dissociate and migrate through the lattice until meeting with another impurity or defect to form a stable trapping site (Srour *et al.*, 2003).

These defects can have energy levels within the bandgap and so give rise to an increase in bulk dark current, including the formation of hot pixels and Random Telegraph Signal (RTS) pixels. Hot pixels are defined by an excessive dark current generation rate compared to other CCD pixels, while an RTS pixel is characterised by a temporally fluctuating dark current generation rate. Defects within the bandgap can also act to trap and defer signal charge to subsequent pixels. It is often the case that these trapping sites become the limiting performance factor of modern CCD based instruments operated in a space environment.

5.7 Charge trapping sites relevant to CCD technology

For the WFIRST CGI, the low expected signal levels mean the effect of bulk trapping sites must be understood to high precision since the loss of a single electron to a trapping site may represent the loss of the entire signal packet. The properties of charge trapping sites vary according to their composition. Different impurities and lattice complexes give rise to different energy levels with respect to the conduction band which is linked to variable times for both capture and emission. For CCDs, at least 5 different defect species have been identified that can contribute to CTI and are summarised within Table 5.3. These were predominantly measured using a technique known as Deep Level Transient Spectroscopy (DLTS). The technique investigates defects present within

the depletion region of a device, commonly a p-n junction, through application of a sudden voltage pulse. The pulse allows carriers from the silicon bulk to populate traps within the depletion region and charge defects to their non-equilibrium charge state. Following the pulse, the defects emit trapped carriers which, over time, causes a change in the capacitance of the depletion region. Measuring the change in capacitance over time, at different temperatures, allows determination of trap properties including energy level and cross section. Widespread adoption of the technique has meant that many results for "common" silicon defects are published, but the spread in published values is often high (Table 5.3).

Table 5.3: *Summary of literature values of known silicon defects in N-Channel CCDs, taken from Hall et al. (2014) and Pichler (2004) Note that the emission cross sections are not well constrained and quoted values can vary by at least an order of magnitude.*

Trap species	Energy level below the conduction band (eV)	Emission cross section (cm^2)
Si-E	0.43-0.47	5×10^{-15}
VV^-	0.39-0.42	2×10^{-15}
Unknown	0.30-0.34	5×10^{-16}
VV^{--}	0.21-0.23	5×10^{-16}
Si-A	0.16-0.18	1×10^{-14}

The Si-E centre is formed from a phosphorus vacancy pair and so is also referred to as the PV centre. It has literature values for the energy ranging from $E = E_C$ - 0.43-0.47 eV (Pichler, 2004). Its presence has been noted in many past investigations of CCD performance following irradiation (Holland, 1993 and Hardy *et al.* 1998). Phosphorus is commonly said to be responsible for the defects noted around this energy level as the defect is not found to be present in P-Channel devices where boron is the buried channel dopant. In addition, annealing studies have found a defect with energy level consistent with the Si-E centre to disappear following extended annealing in the range 353-373 K, consistent with the annealing temperature of the phosphorus vacancy complex (Moll, 1999).

The silicon divacancy (VV) is one of the best studied defects within Silicon and is formed of two silicon vacancies that have combined to form a single complex. The defect has two charge states relevant to N-Channel devices (namely, VV^- and VV^{--}) since their energy lies between the silicon mid-band level and conduction band edge (Table 5.3).

The Si-A centre is formed from an oxygen atom occupying an off-centre position in a vacancy between two silicon atoms (Pichler, 2004). The background oxygen concentration in silicon used to fabricate e2v devices is high at $\approx 10^{17}$-10^{18} cm^{-3}, compared to $\approx 10^{16}$ cm^{-3} for the dopant concentration. As a result, the Si-A centre is often assumed to be the most abundant silicon defect that can potentially impact CTI prior to and following irradiation. Its shallow energy level, however, typically means that it predominantly affects serial CTI when operating at fast scan rates since the emission time constant is typically sub-microsecond at scientific CCD operating temperatures (< 200 K).

The "Unknown" trap species originates from a paper first published by Holland (1993). The trap was seen to measurably increase in density following irradiation and significantly contribute to CTI measurements performed with X-rays. The energy was estimated to be approximately E_C-E = 0.30 eV. The origin of the trap was not known at the time and it has since been referred to as the "Unknown" or "Holland trap". Subsequent investigations of CTI in various e2v devices have implied its presence while others have suggested it is not present at all. For this reason, it is thought to possibly be linked to an impurity such as carbon which may be present in some device batches but not others. Candidate defects in this energy range include the boron interstitial (B_i E = E_C-0.37 eV) and the C_iP_s complex in either the IIB or IA configurations (E = E_C - 0.32 eV and E = E_C - 0.38 eV respectively, (Pichler, 2004)). At present, the carbon complexes appear more likely since boron is present in all e2v devices whereas the concentration of carbon may vary. It should also be noted, however, that since the defect structure is unknown, the cross section has large error which may impact the "effective" energy level measured within devices. The nature of this defect therefore remains speculative. Figure 5.13

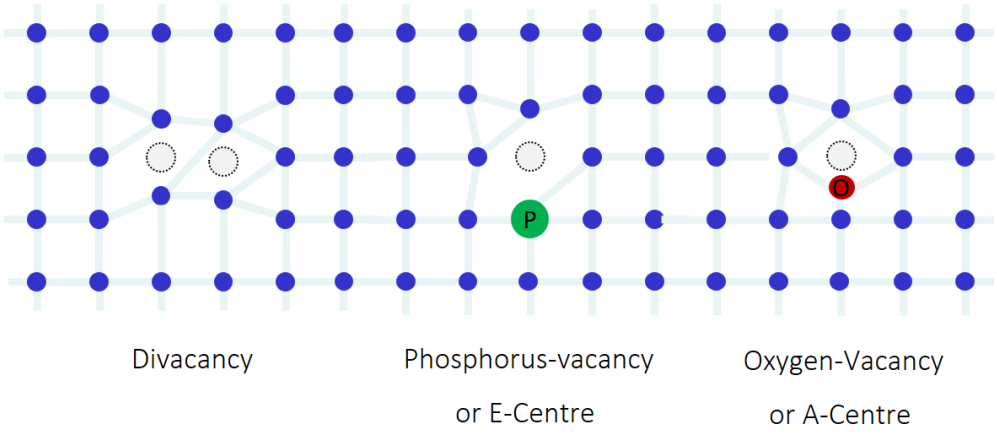

Figure 5.13: *Illustration of the Divacancy (VV), E-centre (Si-E or PV) and Si-A centre (Si-A). The blue dots represent silicon atoms.*

The impact of each of these defects on CGI CCD performance is rooted in the capture and emission time constants of the defects, described by Shockey Read Hall (SRH) theory (Shockley & Read, 1952 and Hall, 1952) and modelled through the use of two exponential time constants, the capture time constant τ_c and the emission time constant τ_e:

$$\tau_C = \frac{1}{\sigma n v_{th}} \qquad \text{Equation 5.3}$$

$$\tau_e = \frac{1}{X\chi\sigma N_c v_{th}} \cdot e^{\left(\frac{E}{k_B T}\right)} \qquad \text{Equation 5.4}$$

Where v_{th} is the thermal velocity, σ is the capture cross section, n is the electron concentration, X is the entropy factor that is associated with the entropy change for electron emission from the trap and χ is a factor included to allow for any field enhanced emission which can affect the trap emission time. N_c is the electron density of states and given by:

$$N_C = 2\left(\frac{2\pi m_{dos} k_B T}{h^2}\right)^{\frac{3}{2}} \qquad \text{Equation 5.5}$$

Where m_{dos} is the effective mass for the electron density of states and h is Planck's constant. The remaining symbols take their usual meaning. For the case of CCD optimisation, it is convenient for the entropy change due to electron emission and the effects of field enhanced emission to be contained within the value for the time constant. Equation 5.4 is therefore commonly stated as:

$$\tau_e = \frac{1}{\sigma N_c v_{th}} \cdot e^{\left(\frac{E}{k_B T}\right)} \qquad \text{Equation 5.6}$$

To explain the impact on charge transfer performance further, we consider the case of a charge packet transferred underneath a phase with a trapping site present. While in the presence of this trap, there is a probability that some charge will be captured. When the signal packet is transferred onwards, there is a probability within a given time t_1 that the trap will emit the charge. To minimise CTI and the impact of radiation damage, either capture should be minimised and/or charge should be emitted at a point where it can re-join the original signal packet.

The corresponding probabilities for capture and emission within a given time t_1 are given by integrating the probability density function within the time interval that the charge cloud is in the presence or absence of the defect, respectively.

$$P_C = \int_0^{t_1} e^{-\frac{t}{\tau_x}}\, dt \qquad \text{Equation 5.7}$$

where here, τ_x can be substituted with the relevant function for capture or emission, respectively. The timescales for capture are primarily dependant on the local charge storage density. For the limit of a large signal packet, it was discussed earlier (Section 3.4) that the charge storage density is approximately equal to the dopant concentration (≈10^{16} cm^{-3}) near the centre of the packet. In this regime, the capture probability approaches 1 for dwell times of order 100 ns. Hence, charge capture is difficult to prevent at clocking at speeds slower than a few MHz and for large signal packets. At high speed and with smaller signal packets, charge capture can be mitigated in the serial direction, discussed in later chapters. For the parallel direction, transfer rates are limited to below 1 MHz where optimisation is focused on allowing as much time as possible for the captured charge to re-emit into the signal packet. The emission time constant is therefore often the most important parameter for a defect. Optimisation is made difficult, however, by the fact that the CCD operates over a large time domain. Taking the example of the CGI, integration times are expected to be of the order 10^2 s, and parallel transfers typically operate in the µs to ms regime and serial transfers can operate in the ns to µs regime. Different traps therefore impact performance in different ways, depending upon their emission time constant at a given temperature, *T*, and so it is convenient to plot Equation 5.6 as a function of temperature for each of the defects shown within Table 5.3 to highlight how each defect can impact performance. This "trap diagram" forms the basis of performance discussion in future chapters though it should be remembered at this point of the study there were large uncertainties associated with the values presented in Table 5.3.

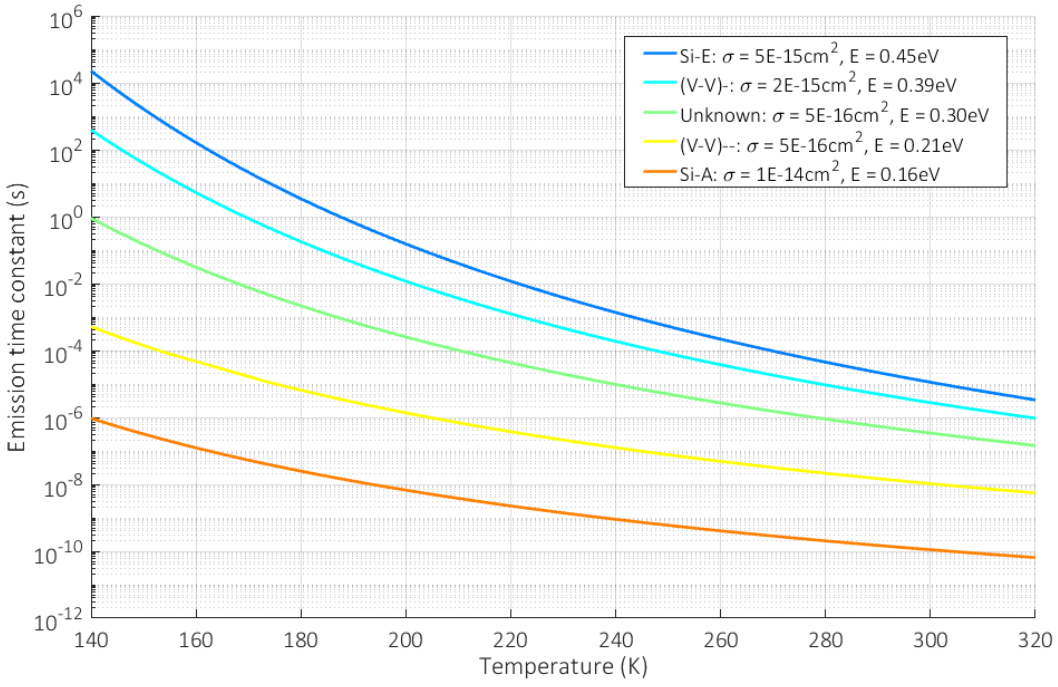

Figure 5.14: *"Trap diagram" adapted from Hall et al. (2014) showing the emission time constant of defects as a function of temperature.*

5.8 Past studies of radiation damage on EM-CCDs

The potential of EM-CCD technology for use within a space environment lead to a variety of studies aimed at testing the susceptibility of devices to radiation damage and comparing it to standard CCD technology. These studies were useful to gain an impression of the possible impact of radiation damage on the CGI detectors.

The largest studies to date were performed alongside CCD development for the Gaia Radial Velocity Spectrometer (RVS) instrument. Investigations were performed whereby EM-CCDs were irradiated with proton levels up to 10^{10} (10 MeV equivalent) the estimated Gaia EOL proton fluence (Smith *et al.*, 2006). Devices under test included the CCD65, CCD97 and customised deep depletion variants of the CCD97 designed for enhanced QE in the RVS operating bands. Most of the testing in the first phase of the study was performed on the CCD65 of which 22 were irradiated to 2×10^{10} protons/cm^{-2}. All devices remained functional following the study and exhibited degradation in line with that expected from the standard CCD counterpart.

A follow-up study was also performed by Smith *et al.*, whereby a total of 94 CCD97 devices were irradiated to a 10 MeV equivalent proton fluence of 2×10^{10} protons/cm^{2}, the equivalent of ≈ 50 RVS focal planes. The devices were irradiated unbiased at room temperature using 9.65 MeV protons normalised to a 10 MeV equivalent fluence. All devices remained operational following the proton irradiation, and exhibited the expected increase in dark current and bright pixel population compared to standard CCDs. The multiplication gain of devices for a given effective Rϕ2HV was unchanged following irradiation for each device. It was noted that some devices exhibited poor serial CTE, presumably due to the multiplication register, and that this appeared unchanged following irradiation (Smith *et al.*, 2006).

An investigation into the effects of ionising damage was performed by Hadwen *et al.* (2004), whereby three CCD87s were irradiated biased to levels of 2, 5 and 10 krad (Si). The devices were then tested and an additional 10 krad (Si) fluence was administered after 3 weeks to bring the total fluence levels up to 12, 15 and 20 krad (Si). Following each irradiation three measurement techniques were used to measure the voltage shifts in the different structures of the device. The change in pinning voltage was used to give a measure of the voltage shift in the image/store sections of the device. The change in reset drain bias to attract charge onto the output node was measured to give the flat-band voltage shift in the output circuitry. Finally, the change in the Rϕ2HV voltage required to maintain multiplication gain equivalent to pre-irradiation levels was measured to determine any voltage shift in the multiplication register. The first two methods produced relatively consistent results and an estimated “global” voltage shift of 0.14 V/krad (Si)

for each of the devices. The third method showed a negligible shift, meaning no adjustment was required to maintain constant multiplication gain following the irradiation.

An additional concern for the high field EM register was the susceptibility to Single Event Gate Rupture (SEGR), a phenomenon whereby a heavy ion passing through a high field region may create a temporary conductive path of ions. A large current then flows, heating and melting the gate stack thus leaving a permanent gate short and complete device failure (Figure 5.15). For EM-CCDs, the large electric field between the Rϕ2HV electrode and the ϕDC gate can approach the critical field when a plasma channel is created due to an incident heavy ion.

Susceptibility of EM-CCD technology to SEGR was tested by Evagora *et al.* (2012), whereby 14 CCD97s were irradiated with heavy ions with equivalent mass stopping power extending up to 135 MeV cm^2/mg (Evagora *et al.*, 2012). Stopping power is defined as the retarding force acting on charged particles due to interaction with matter, this value is then divided by the density of the material (in this case Si) to obtain the mass stopping power in units of MeV cm^2/mg. No gate rupture events or device failures were observed in the investigation. The fluxes used were consistent with a mission that would spend between 5-10 years at L2, indicating that the risk of complete device failure during a mission was too small to be measured.

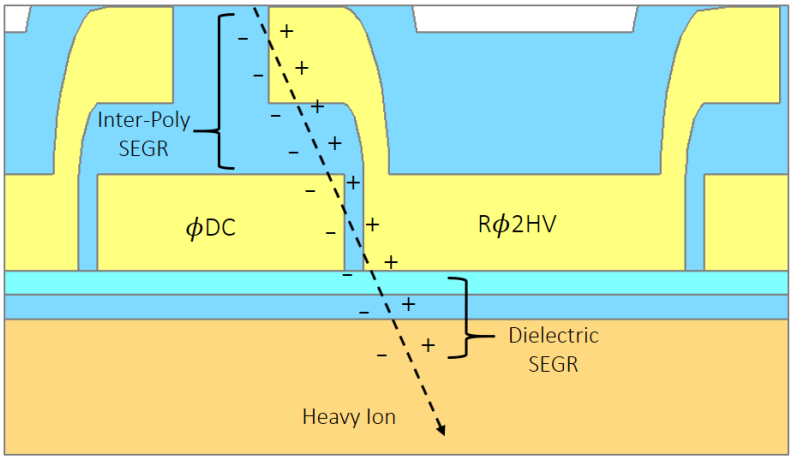

Figure 5.15: *EM-CCD electrode structure, showing SEGR vulnerability.*

5.9 Cryogenic irradiations

It has long been understood that the temperature at which silicon is irradiated has an impact on the final distribution of stable defects within the lattice (Kinchin & Pease, 1955, Pichler, 2004). This is illustrated well by Figure 5.16 that shows the annealing temperatures of a selection of defects. The most accurate EOL performance estimate for a CCD based instrument operating within a radiation environment will therefore be provided through irradiation at the nominal operating temperature, since this re-produces the same relative proportion of defects that would be expected in-flight. The WFIRST CGI is in a unique position whereby it has been allocated 1 year

of observations throughout the 6-year total mission duration. At times where the instrument is idle, the detector can either be stored at room temperature or cooled to the nominal operating temperature (165 K). The results from the room temperature irradiation campaign represent a performance estimate for the former case, however, a cryogenic irradiation was required to estimate performance for the latter. It is worth noting that even if the detector is stored at room temperature, it shall spend a significant proportion of time cooled and operational, during which it will experience displacement damage effects and the results from a cryogenic irradiation will be applicable.

The concept of irradiating at the nominal operating temperature to estimate EOL performance is relatively recent compared to the timescales that CCD based instruments have been active in space. A brief overview of past investigations is provided here to justify the requirement for a cryogenic investigation.

The first recorded cryogenic irradiation of a CCD was performed in 2003 with the aim of investigating the introduction rate of hot pixels and their annealing characteristics following irradiation at 190 K (Polidan, 2004). A key conclusion of the study was that there was a population of hot pixels that annealed following a warmup from 190 K to 303 K, as well as a decrease in the net bulk dark current. A further study based upon in-flight data of the same detector highlighted that a significant proportion of these bright defects annealed within an estimated temperature range of 268-273 K, whereas another proportion was not seen to anneal at any temperature below 293 K (Kimble, 2000). Each of these studies, and others (Marshall, 2005) were based upon e2v CCD43 sensors for the Hubble Space Telescope Imaging Spectrograph (STIS). The results for dark current and hot pixel behaviour alone demonstrate the measurable differences in the defect landscape between the room temperature and cryogenic case.

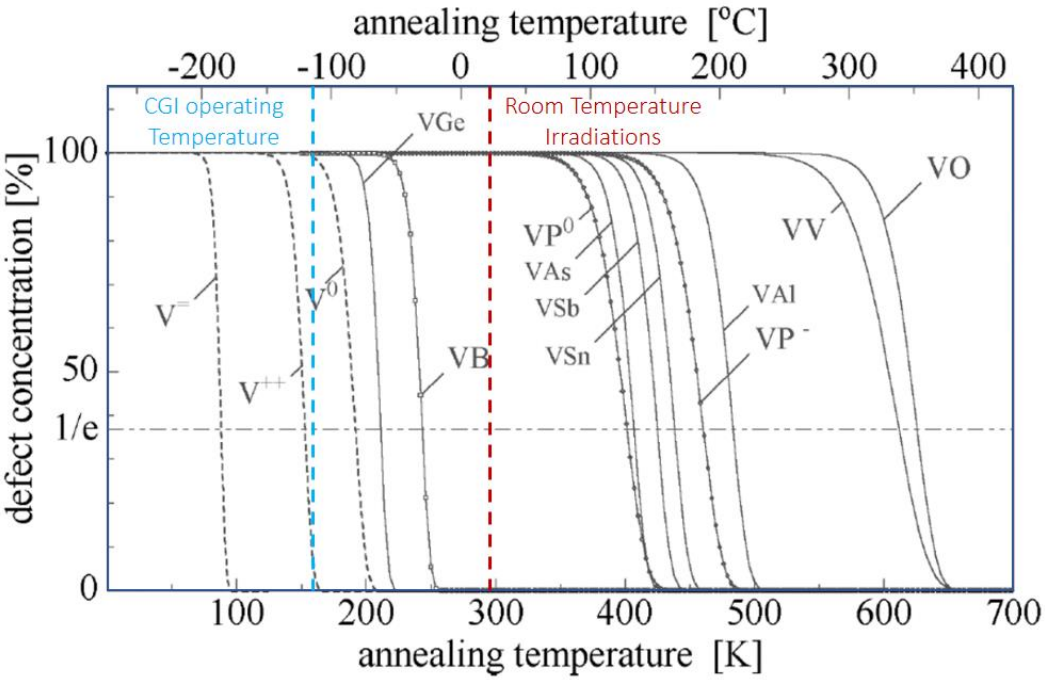

Figure 5.16: *Schematic representation of vacancy and vacancy-defect pair annealing in silicon (Moll, 1999), based on literary values circa 1970-1980. It should be noted that information on the annealing temperature of defects is dependent on many parameters and so this plot cannot be directly applied to a standard CCD without more detailed consideration. Despite this, it can be seen that a number of defects that are mobile at room temperature (≈300 K) are not mobile at the nominal operating temperature of the CGI (165 K). The population of trapping species and hence the EOL performance is likely best estimated by irradiation at cryogenic temperatures as opposed to the room temperature equivalent.*

Significant attention has been paid to the effects of room temperature annealing for the case of the Chandra X-ray observatory. Shortly after launch, the Advanced CCD Imaging Spectrometer (ACIS) experienced higher than expected degradation as soft protons (≈10^2 keV) were focused by the telescope mirror onto the front illuminated CCDs. To reduce the damage, the detectors were warmed from 173 K to 303 K for approximately 8 hours before than being cooled back down to 173 K. The expectation was that the devices would exhibit improved performance as some of the defects responsible for CTI were thermally annealed, however, in practise the CTI was measured to increase by 35% (Bautz *et al.*, 2005). Subsequent investigations (Marshall *et al.*, 2003) attributed this "reverse annealing" mechanism to the carbon interstitial (C_i) which is not mobile at the ACIS operating temperature and has too shallow an energy level to significantly contribute to CTI at ACIS clocking speeds. At room temperature, however, C_i is mobile and is free to form defects such as C_i-P_s with energy levels such that charge is emitted on the timescales of the ACIS clocking, causing an increase in the measured CTI.

Also of note are the investigations by Hopkinson which entail the low temperature (143 K) irradiation of the e2v CCD91-72 for the ESA Gaia satellite (Hopkinson, 2009). The CCD had separate sections irradiated at both room temperature and at 143 K and CTI was measured using both the EPER and FPR technique. For the operating conditions of this study, it was found that CTI due to a cryogenic irradiation was less than the room temperature equivalent (an approximate 20-30% difference in most cases). A room temperature anneal caused a measurable change in the defect landscape such that CTI improved following 1 day at room temperature, but then degraded following a further week annealing under the same conditions.

In summary, differences between room temperature and cryogenic irradiations have been clearly demonstrated in the literature for several high-profile space missions, including the HST, Chandra and Gaia. The choice to pursue a cryogenic irradiation investigation for the WFIRST CGI is therefore well founded since the demands for single photon imaging require the in-flight defect landscape to be replicated and understood as accurately as possible.

5.10 Summary of radiation damage considerations for the WFIRST CGI

Even with the highest levels of shielding, simulations presented in this chapter support results in the literature that the proton dose expected for each of the CGI detectors is non-negligible and so has the potential to alter the performance of the instrument considerably. From the basic theory outlined at the start of the chapter, the proton damage can be expected to increase the detector dark current and CTI through the creation of bulk trapping sites. Since the detectors will be operated biased, a small component of ionising damage may also be expected that should not be totally ignored. The degradation due to proton damage therefore needed to be quantified in terms of the impact on the performance metrics deemed most critical for the CGI such that the impact of increased CTI and dark current on planet detection efficiency could be better established. Discussion therefore turns to the WFIRST irradiation campaigns where the aim was to assess this degradation as accurately as possible through measurement of performance parameters deemed critical to the CGI both prior to and following exposure to proton fluences representative of EOL conditions, both at room temperature and the nominal operating temperature of the mission.

6 The WFIRST CGI radiation damage campaign

From the previous chapters, we have concluded that the EM-CCD represents the future of exoplanet science through implementation in the WFIRST CGI, however, radiation damage threatens to limit science performance of the mission if not properly mitigated. The aim of the WFIRST radiation campaigns was to assess the impact of radiation damage on the CCD201-20 and measure key performance values that would help de-risk the utilisation of EM-CCDs for the mission.

This chapter discusses the background of the radiation campaign and the differences between the room temperature investigation and the cryogenic equivalent. The differences in irradiation condition and pattern are also discussed with respect to how the results in the following Chapters should be interpreted.

6.1 Campaign overview

The WFIRST radiation campaign presented in this thesis is the most detailed investigation into the effects of radiation damage into EM-CCD technology to date. A total of 6 CCD201-20 devices were irradiated by the author over the course of approximately 3 years. The irradiation conditions varied for each device, including different proton fluences, energies, irradiation patterns and temperature of the device during irradiation, with details summarised in Table 6.1. The devices can be broadly separated into two categories; those that were irradiated unbiased at room temperature (298 K) and those which were irradiated biased at the nominal operating temperature of the mission (165 K). Historically, investigations of a similar nature base EOL performance predictions upon results from room temperature irradiations since they are comparatively simple and inexpensive to perform. Recent investigations have shown, however, that the best estimate of performance is provided through irradiation at the nominal operating temperature of the instrument, hereafter referred to as *cryogenic* irradiations (Gow *et al.*, 2016). The CGI is in a unique position whereby the results from each investigation could be directly applicable to the EOL case. Only one year of the nominal 6 year mission is scheduled for CGI observation time, between which the detectors may be held at room temperature alongside other components of the CGI optics. The instrument may also experience periods of controlled thermal annealing following extended periods at cryogenic temperatures, and so the impact of a room temperature anneal was also explored following the cryogenic irradiation.

The WFIRST radiation campaign initially started as a small investigation into the effects of displacement damage on EM-CCD technology. At the start of the study, the WFIRST mission was still in the formulation stage and the CGI was an optional addition that was subject to both cost

and the technology development process associated with the optical design and detector choice. While the EM-CCD was not the only risk factor associated with the inclusion of the CGI, it was considered a priority for TRL development since it had not yet been flown in space and the true impact of radiation damage was unknown. Although the previous chapter highlighted that displacement damage investigations had been performed on other EM-CCD detectors (primarily the CCD97 (Smith *et al.*, 2006)), published CTI measurements remained scarce, particularly in the low-flux regime that the CGI was expected to operate within. The aim of the initial irradiation campaign was therefore simple; assess the impact of radiation induced damage on the CCD201-20 EM-CCD on low signal CTI. Other metrics were measured prior to and following the irradiation, with the full suite of tests discussed later. Two engineering grade devices were selected for the original study, with properties summarised in Table 6.1, that were irradiated to a fluence of 2.5×10^{9} protons/cm^{-2}, deemed a realistic EOL proton fluence for the CGI following 6 years at L2.

The results from the original investigation highlighted that CTI was likely the limiting performance factor for the CGI since other noise sources could be appropriately mitigated. At such low signal levels, deviations in the population of silicon defects present in the device following irradiation had the potential to significantly alter the final predicted performance value. A separate investigation that was performed at the same time as the initial radiation damage study had highlighted how the final predicted performance of the CCD could vary significantly according to the temperature at which the device was irradiated (Murray *et al.*, 2014). Discussions with the CGI technology development team at JPL regarding the results of the initial investigation therefore lead to the proposal and adoption of a second investigation where a science grade CCD201 was irradiated biased at the nominal operating temperature of the mission (165 K). The irradiation was performed in stages, with multiple fluences delivered to the device that were representative of the different levels of shielding that could be implemented on the CGI. The results of the study supported the initial hypothesis that the temperature at which the irradiation is performed is critical to the prediction of EOL science performance. Following the irradiation of the science grade device, additional engineering grade devices were irradiated independently by the author to provide a more complete basis of comparison between the cryogenic and room temperature irradiation case. The result of the campaign is a set of CCD201s that have been irradiated at both room temperature and the nominal operating temperature of the mission to fluence levels that represent a variety of possible shielding configurations for the CGI. The experimental conditions for each type of irradiation are discussed separately, however, the results are discussed as a set.

6.2 Detectors for study and timeline for testing

A total of 6 CCD201-20 detectors were irradiated throughout the study, with properties summarised in Table 6.1. The devices were all back-illuminated, frame transfer variants with an aluminium store shield. The majority of the devices were classed "engineering grade", meaning they were fully operational but had not met the requirements to be classed as "science grade" devices. The single science grade device was irradiated under biased, cryogenic conditions. No differences in performance were noted between the engineering and science grade chips during pre-irradiation characterisation, with the exception of device 10091-16-09 that was known to exhibit high dark signal.

The irradiation and associated testing of devices took place over the course of approximately 3 years. Between testing, devices were stored under ambient conditions. Device 11153-13-14 was re-characterised towards the end of the campaign since it had spent the longest time at room temperature since the original irradiation. No change in bulk CTI was measured because of the prolonged room temperature anneal, however, other changes were measured as discussed in the following chapter. Figure 6.1 summarises the testing timeline for each of the devices.

Table 6.1: Summary of devices irradiated through the WFIRST irradiation campaign.

Serial number	Device grade and notes	Proton fluence (p/cm^2) (10 MeV equiv.)	Irradiation condition	Irradiation pattern
14222-11-2	Engineering grade trap at FWC	1.0×10^9	298 K unbiased 74 MeV protons	Serial and parallel regions, with parallel control region
10091-16-09	Engineering grade high dark signal	2.5×10^9	298 K unbiased 74 MeV protons	Parallel region irradiated. Parallel and serial control region.
11153-13-14	Engineering grade hot pixels	2.5×10^9	298 K unbiased 74 MeV protons	Serial and parallel regions, with parallel control region
14222-11-6	Engineering grade trap at FWC	5.0×10^9	298 K unbiased 74 MeV protons	Serial and parallel regions, with parallel control region
14222-14-2	Engineering grade dark columns	$<1.0\times10^9$	165 K and biased 5 MeV protons	Entire device
12231-13-14	Science grade	1.0×10^9	165 K and biased 5 MeV protons	Entire device
		2.5×10^9		
		5.0×10^9		
		5.25×10^9		

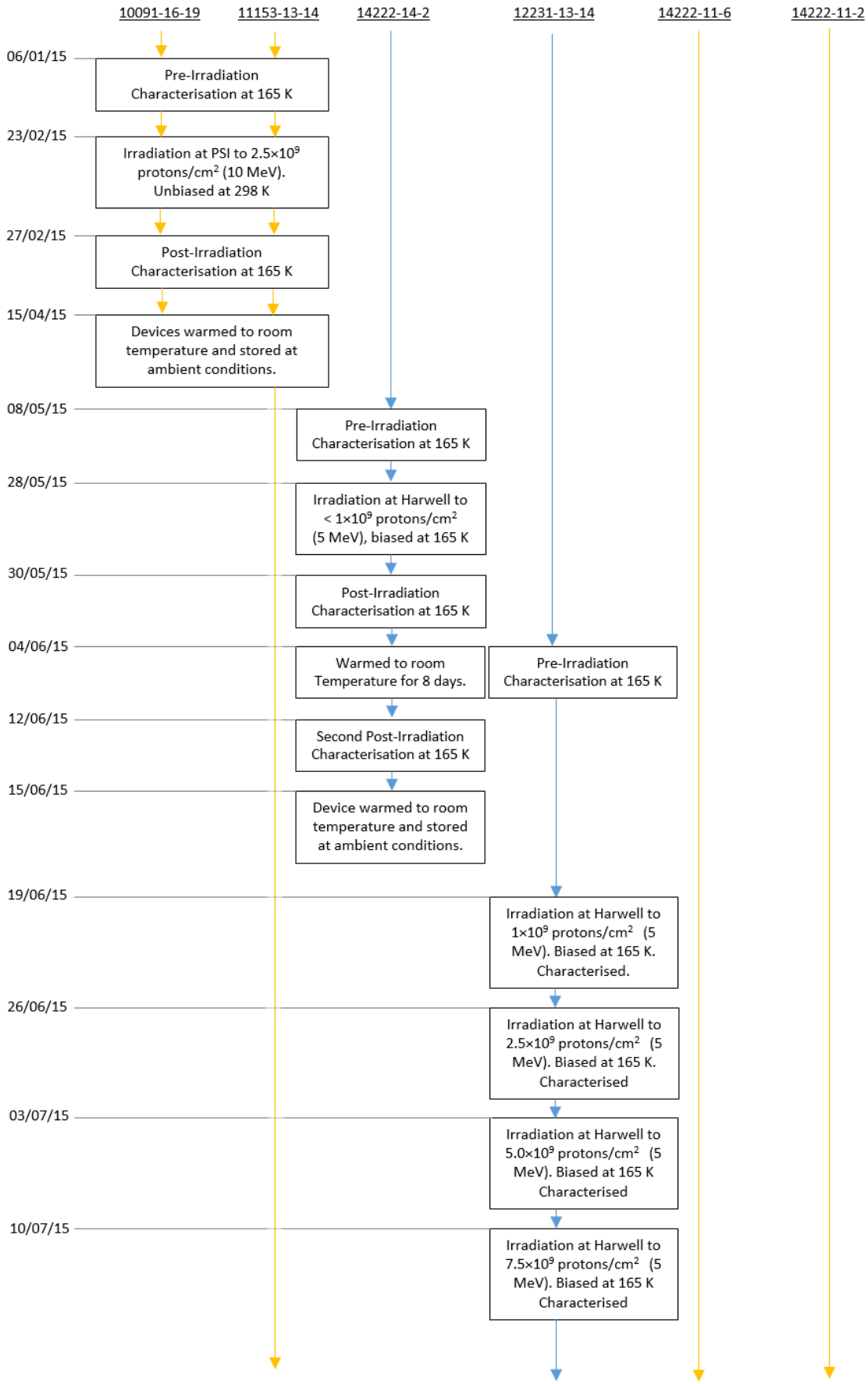
10091-16-19
11153-13-14
14222-14-2
12231-13-14
14222-11-6
14222-11-2
06/01/15
Pre-Irradiation Characterisation at 165 K
23/02/15
Irradiation at PSI to 2.5×10⁹ protons/cm² (10 MeV). Unbiased at 298 K
27/02/15
Post-Irradiation Characterisation at 165 K
15/04/15
Devices warmed to room temperature and stored at ambient conditions.
08/05/15
Pre-Irradiation Characterisation at 165 K
28/05/15
Irradiation at Harwell to < 1×10⁹ protons/cm² (5 MeV), biased at 165 K
30/05/15
Post-Irradiation Characterisation at 165 K
04/06/15
Warmed to room Temperature for 8 days.
Pre-Irradiation Characterisation at 165 K
12/06/15
Second Post-Irradiation Characterisation at 165 K
15/06/15
Device warmed to room temperature and stored at ambient conditions.
19/06/15
Irradiation at Harwell to 1×10⁹ protons/cm² (5 MeV). Biased at 165 K. Characterised.
26/06/15
Irradiation at Harwell to 2.5×10⁹ protons/cm² (5 MeV). Biased at 165 K. Characterised
03/07/15
Irradiation at Harwell to 5.0×10⁹ protons/cm² (5 MeV). Biased at 165 K Characterised
10/07/15
Irradiation at Harwell to 7.5×10⁹ protons/cm² (5 MeV). Biased at 165 K Characterised

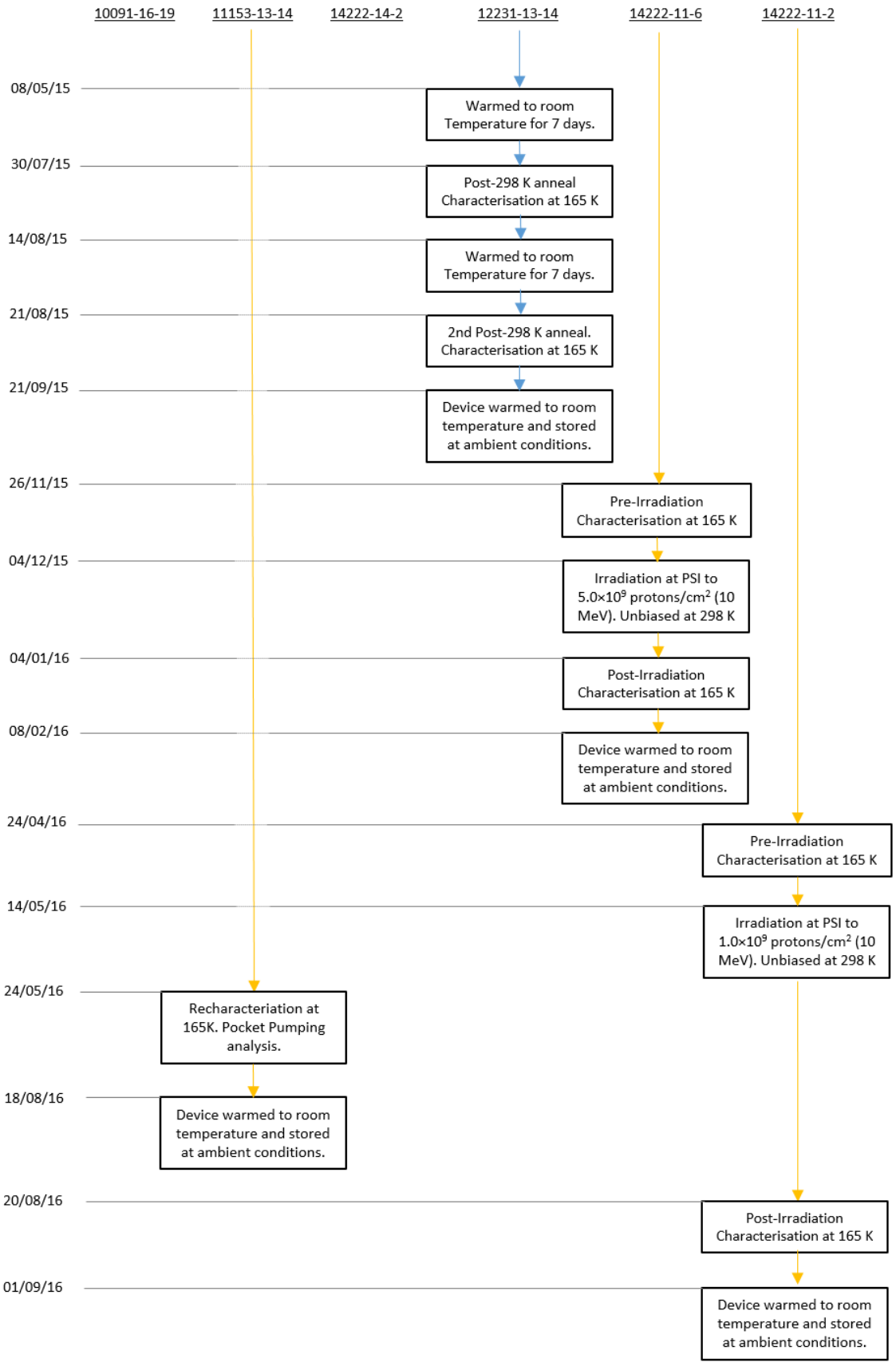

Figure 6.1: *Timeline of irradiation and testing for the CCD201-20s studied within the campaign. Blue arrows represent devices irradiated at 165 K while yellow arrows represent devices irradiated at 298 K.*

6.3 The WFIRST room temperature irradiations

Room temperature irradiations remain the most common method for estimating EOL performance due to radiation damage since irradiation under ambient conditions usually eliminates the requirement for additional vacuum and cooling equipment to be transported to the irradiation facility. For cases where on-chip shielding is required, this can be inspected and aligned by eye without the need for internal vacuum mechanisms. Finally, the lack of thermal cycling allows multiple devices to be irradiated quickly since devices can then be transported back to the facility at ambient temperature where post-irradiation characterisation can be performed.

6.3.1 Facility

Each of the room temperature irradiations described within this thesis were performed at the Proton Irradiation Facility (PIF), at the Paul Scherrer Institute (PSI), Switzerland. The PIF was constructed for the testing of spacecraft components under contract between ESA and PSI, and is capable of providing a range of proton energies consistent with spectra that would be expected within a space environment. The key properties are summarised within Table 6.2.

Table 6.2: *Key features of the PIF beamline.*

Parameter	Value
Lowest primary beam energy	74 MeV
Beam Profile	Gaussian with typical FWHM = 10 cm
Neutron Background	Less than 10^{-4} neutrons/proton/cm^2

The lowest primary beam energy available at PSI was 74 MeV, with lower beam energies possible though the use of moveable copper degraders. The use of degraders is typically undesirable since energy degradation leads to a broadening of the energy distribution of the beam and uncertainty in the delivered 10 MeV equivalent fluence. Figure 6.2 shows an example of this effect whereby a simulated proton beam of 74 MeV was passed through copper of various thicknesses and the resultant energy distribution measured. For the irradiations described in this study, the 74 MeV primary beam was requested and the fluence normalised to the 10 MeV equivalent using the NIEL function, detailed within the previous chapter and described in more detail by Burke *et al.* (1986), Van Lint *et al.* (1987) and Srour *et al.* (2003).

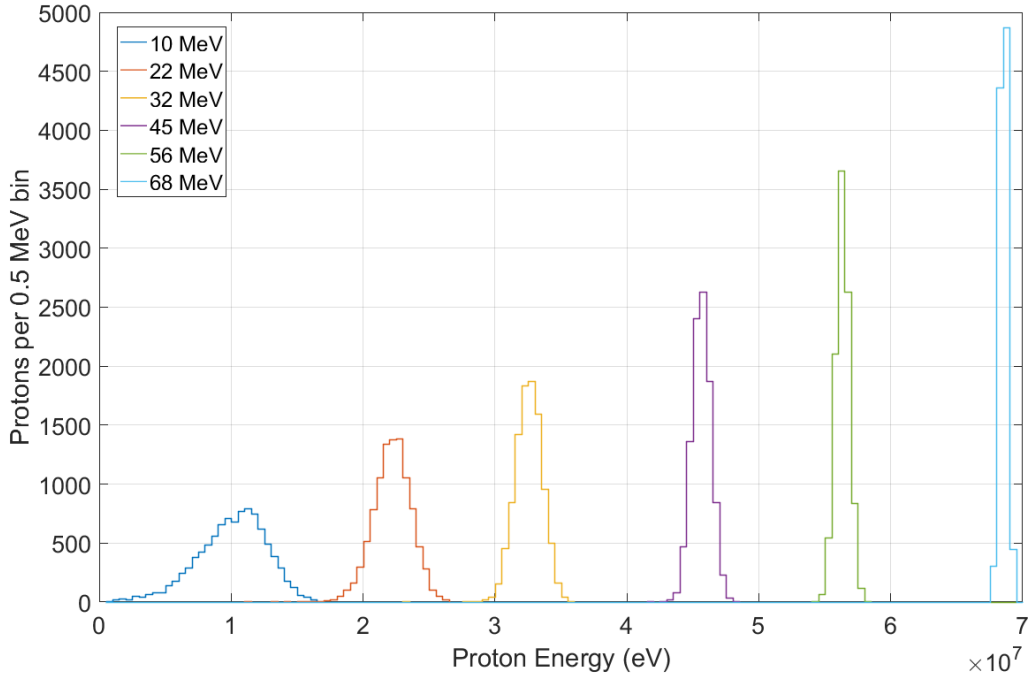

Figure 6.2: *Illustration of how the spread of the beam energy increases with increasing energy degradation, simulated using SRIM. The input was a 74 MeV delta function beam that was degraded by various thicknesses of copper (similar to the method used at PSI). The increased spread in beam energy makes use of the NIEL equivalent fluence unreliable.*

6.3.2 Shielding

Each of the devices irradiated at PSI had shielding in place in order to preserve an on-chip control region for post-irradiation analysis. Performance parameters within the on-chip control region (e.g. dark current) should remain consistent between the pre- and post-irradiation cases such that any potential drift due to the camera electronics or otherwise can be excluded during post-irradiation analysis. Shielding was designed that would allow irradiation of the selected regions of each device while protecting the on-chip control regions from the primary beam. Monte Carlo simulations were performed using the SRIM package that estimates the maximum penetration depth of the beam into stainless steel, the material chosen for the shielding. The maximum penetration depth was seen to be no more than 9 mm, shown in Figure 6.3. Based on these results, a thickness of 14 mm was chosen to allow for the Gaussian energy distribution of the beam at PSI and uncertainties in the SRIM package.

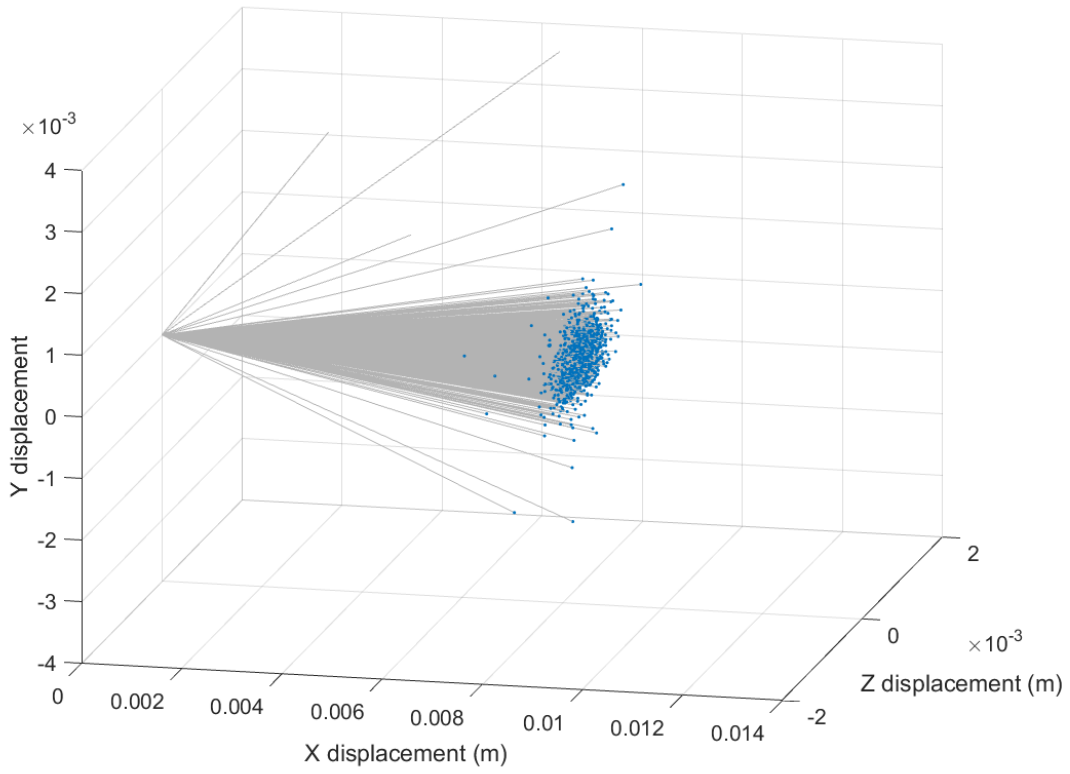

Figure 6.3: *3D simulation of 74 MeV proton paths in 14 mm of stainless steel. No protons are observed to pass the 10 mm mark. Scattering in other dimensions was limited to approximately ±2 mm which was used to estimate the widths of the transition region and the required distance of the shielding edge from the die within the target areas.*

While the shielding prevents primary protons from interacting with the silicon, these protons can generate secondary events that may then interact with the silicon and give rise to performance degradation. Simulation of primary beam interactions with the steel shielding showed that the estimated secondary neutron fluence within the control region was of order 10^6 n/cm^2. It has been reported that neutron damage gives rise to noticeable effects on CTE when fluences reach the order of 10^8-10^9 (Brau & Sinev, 2000). Damage due to neutrons from the beam is therefore expected to be near negligible within the control regions for the irradiation conditions used in this study. A background neutron fluence was also present within the primary beam however this is estimated to not have exceeded 10^6 n/cm^2 and is negligible when compared to the damage due to primary protons.

Two shielding patterns were used for the room temperature irradiations with the aim of separating the effects of parallel and serial CTI. Both the irradiation pattern and shielding design are shown in Figure 6.4. Small safety margins were added in the parallel section to ensure that the serial register was either irradiated or un-irradiated as required.

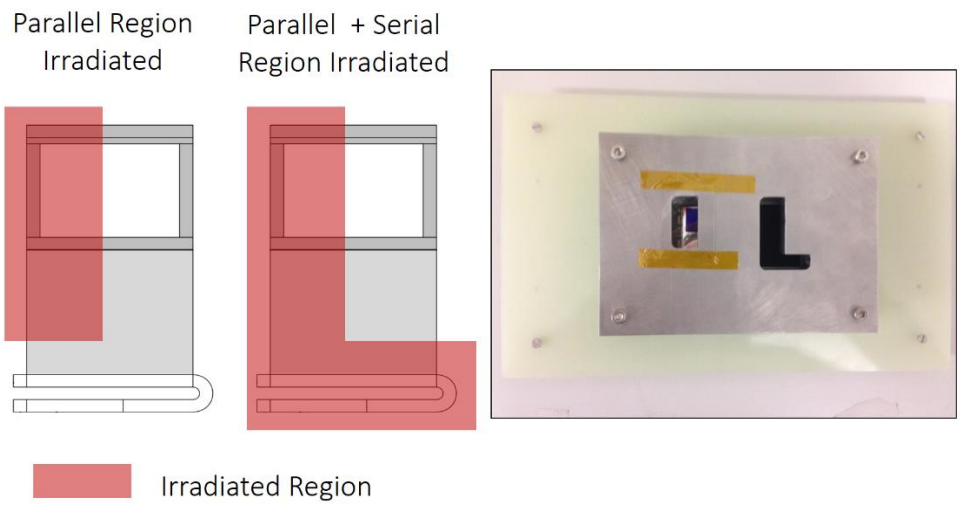

Figure 6.4: *Left: Irradiation pattern for each device. Note, the size of the serial and multiplication registers in this schematic are not to scale. Right: Steel shielding design with device positioned for parallel irradiation*.

Maintaining on-chip control regions produces an additional complication whereby protons incident upon the shielding edge can scatter and lose energy before interacting with the silicon. This produces a region surrounding the shielding edge where protons of undefined energy have caused an undefined amount of damage between the primary irradiated region and the control region. This area is commonly termed the "transition region" and should be excluded from post-irradiation analysis. The width of the transition region depends upon the shielding alignment, thickness and proton beam energy and was estimated to be approximately 2 mm for shielded devices in this study, based on SRIM calculations. Figure 6.5 shows a dark current profile from a CCD201 that was irradiated at PSI using the "L" shaped shielding configuration shown by Figure 6.4. The transition region can be seen clearly at the centre of the device. For this example, the width was found to be approximately 1.5 mm however beyond this width small changes in the dark current profile remain observable, albeit a small (< 5%) difference compared to the net increase within the target region.

The high-energy proton beam allowed irradiation without the need for vacuum (74 MeV protons have a projected range of ≈30 m in air) and so the irradiations at PSI were performed under ambient conditions. The devices were mounted to handling jigs compatible with the target area of the beamline and were mounted and positioned within the target area using a laser alignment system.

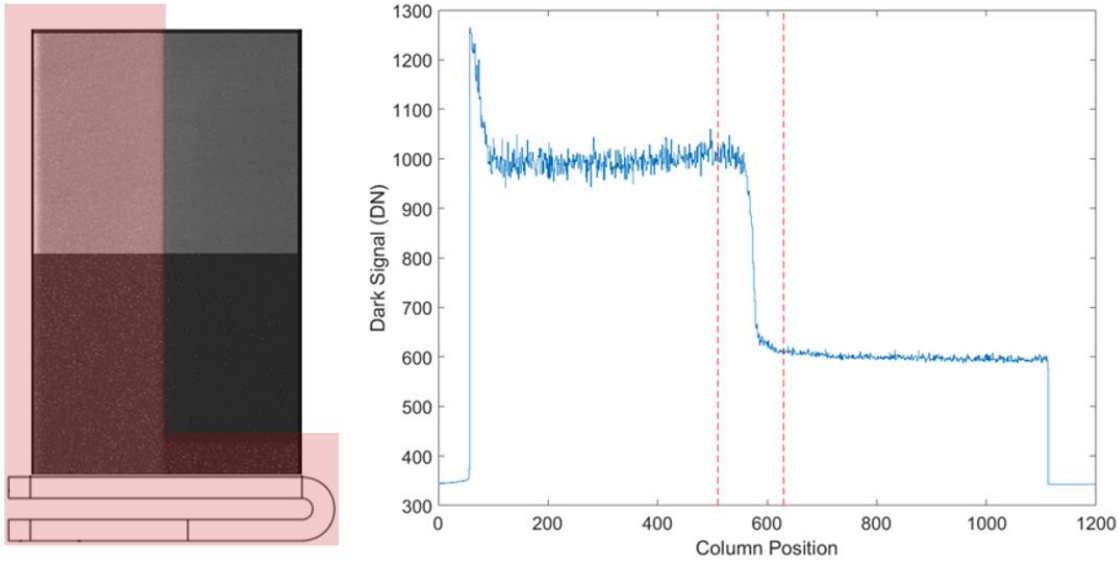

Figure 6.5: *Left: Dark current image from a CCD201-20 irradiated in both the serial and parallel regions using the "L" shaped shielding shown by Figure 6.4. Right: the dark current profile as a function of column position. Image obtained at 243 K. The transition region is approximately bounded by the red dashed lines. The spike in signal within the first few columns of the device is thought to be due to additional ionising damage because of the shielding position with respect to the device. It was not possible to measure the difference at colder temperature (165 K).*

6.3.3 Beam profile and dosimetry

The intensity of the PIF beamline was mapped around the target area by the PSI staff to ensure that the beam intensity across irradiated regions was uniform. The data are presented in Figure 6.6 alongside basic fitted curves to illustrate the trend. A 2D contour map was generated based on the assumption that a 2D profile could be treated as a function that is separable into 1D components. The contour map was then mapped onto the surface of each device to provide an estimate for the beam intensity gradient across the target regions, shown in Figure 6.7. Using this method, the maximum non-uniformity due to the proton beam was estimated to be approximately 6% for devices 10091-16-19 and 11153-13-14. For the other room temperature irradiated devices, the shielding was rotated in order to take advantage of the greater beam uniformity on the Y-axis which lead to a maximum non-uniformity of approximately 3% using the same method.

Dosimetry was performed on-site by PSI staff and is quoted to be accurate to within 10%. The proton flux was monitored in real time and was of order 2×10^7 protons/cm^2/s such that the irradiations were complete within a few minutes.

Following irradiation, devices were transported back to the Open University for post-characterisation, which took place within a few weeks of the initial irradiation, with the exception

of device 14222-11-2 where the post-irradiation characterisation took place approximately 3 months after the irradiation (Figure 6.1 shows the entire timeline). Following irradiation and characterisation, all devices were stored at ambient conditions.

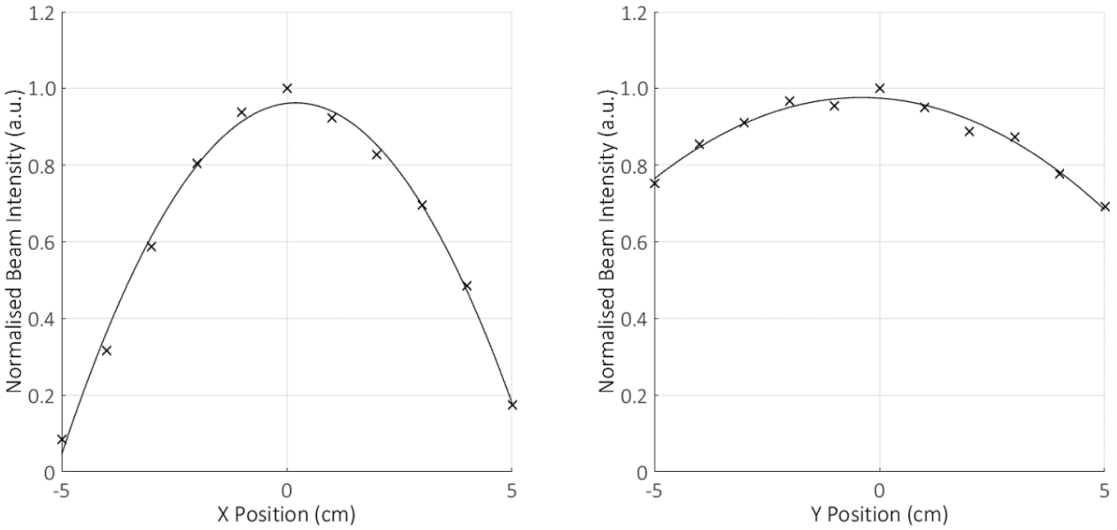

Figure 6.6: *Normalised beam intensity as a function of position from the target.*

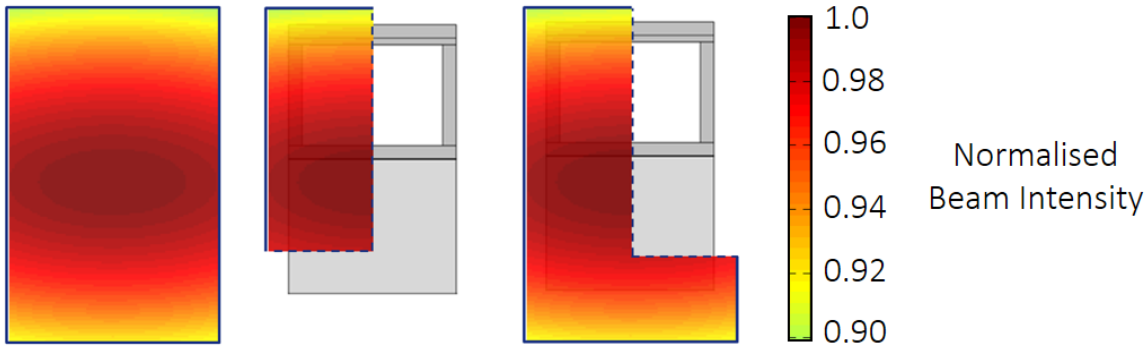

Figure 6.7: *Approximate 2D map of Beam Intensity over targeted device regions for devices 10091-16-19 and 11153-13-14 (2.5×10^9 10 MeV proton fluence).*

6.4 The WFIRST cryogenic irradiations

The cryogenic section of the campaign had a similar goal to the room temperature investigation; whereby the device was tested for performance metrics deemed critical to the CGI prior to and following irradiation to a nominal EOL proton fluence. The difference was that for this investigation, the detector was both cooled and biased during each irradiation.

6.4.1 Facility

The cryogenic irradiations were performed at the Synergy Health ion beam facility, located in Harwell, U.K. The site employs a 5 MV tandem accelerator that is suited to the delivery of light ions, such as protons, with an energy range of 0-10 MeV. Lower energy protons were desirable for this investigation in order to prevent activation of material surrounding the CCD which may then alter the effective proton fluence or provide unwanted background signal during post-irradiation analysis. The lower primary energy also demands that the beam is deliverable under vacuum which in turn aided compatibility with the test equipment which was also maintained under cryogenic, vacuum conditions.

6.4.2 Beam profile and dosimetry

Direct measurement of the beam profile was not possible using the same method highlighted at PSI, however, in this instance the diameter of the beam was much larger than the CCD active area and so non-uniformity across the target region was less of a concern. Dosimetry was quoted to be accurate to within 10%, and measured prior to and following the irradiation through use of a Faraday cup positioned at approximately the same location as the CCD during the irradiation. The Faraday cup measurement was not available during the irradiation and so real-time dosimetry was not available for these irradiations.

6.4.3 Consideration of the final fluence (cumulative 7.5×10^9 protons/cm^2)

In the cryogenic phase of this study the science grade device was irradiated with four fluence levels designed to give a total cumulative fluence of 7.5×10^9 protons/cm^2 (10 MeV equivalent). Performance degradation following the first three fluence levels provided results consistent with expectations; however, delivery of the final 2.5×10^9 protons/cm^2 fluence provided little to no further performance degradation. Both dark current results and X-ray CTI results were consistent with that measured for the previous cumulative fluence of 5.0×10^9 protons/cm^2.

The final fluence was therefore believed to be unsuccessful with the final cumulative fluence estimated at approximately 5.25×10^9 protons/cm^2 rather than the targeted 7.5×10^9 protons/cm^2. Additional evidence in support of this conclusion is presented in later chapters and the final fluence is therefore labelled as 5.25×10^9 protons/cm^2 within the results.

6.5 Differences between the cryogenic and room temperature irradiations

6.5.1 Impact of beam energy

The room temperature and cryogenic irradiations performed in this study were performed at different primary proton beam energies with 74 MeV for the room temperature irradiations and 5 MeV for the cryogenic irradiations. The comparison of results from each investigation is therefore somewhat clouded by the potential impact of primary proton beam energy on the total energy deposited into the silicon as well as the difference in how this damage manifests within the lattice.

It is common for beam energy to vary across different radiation damage investigations since typically the experiment is limited by the primary energy a given facility can practicably provide. Proton fluences are therefore scaled to a 10 MeV equivalent using the NIEL function, which for protons in silicon is relatively well understood (Srour *et al.*, 2003). For this study, the proton fluence was scaled using the NIEL function such that the total energy deposited into the lattice was consistent for each investigation. A good comparison of proton damage at different energies is provided by Hopkinson *et al.* (2003) who measured CTI in devices irradiated using 10 and 60 MeV protons. A factor difference of approximately 1.5 was measured in the damage, which agrees well with the difference in fluence required for the same damage as estimated by NIEL. In other words, if the fluences used within the investigation by Hopkinson *et al.* were normalised using the NIEL functions used in this study, one would expect the net damage to be consistent between the two cases.

It should be noted that the NIEL function is only valid when the energy deposited as a function of unit length within the device is linear across the device thickness. The devices used in this study were a maximum of 20 µm thick (likely closer to 16 µm), significantly lower than the predicted Bragg peak location of ≈250 µm for a 5 MeV proton. The NIEL relationship is therefore believed to be appropriate for the scaling of the proton fluence for this study.

The NIEL scaling only accounts for the total energy deposited into the lattice per proton, but does not account for how the damage due to the energy manifests within the silicon lattice. As the proton energy increases, the total amount of energy that can be transferred to the primary knock on atom also increases. The difference between a 5 MeV proton and 74 MeV proton is significant, with the a 5 MeV beam only capable of producing point defects (isolated Frenkel pairs) and the 74 MeV proton producing PKAs with sufficient energy for cluster damage (Kinchin & Pease, 1955). Nonetheless, even at high proton energies, the majority of the energy deposited is through Coulombic interactions and hence the formation of isolated Frenkel pairs even at high proton

energies. The conclusion based on the literature is that, although there are some differences in how the damage can manifest due to a difference in primary beam energy, the damage due to 5 MeV protons and 74 MeV protons should be consistent as long as the delivered fluence is scaled appropriately using the NIEL function.

6.5.2 Biased vs unbiased irradiations

As well as a difference in beam energy, there was a difference in how each device was operated during the irradiation at both room and cryogenic temperatures. The room temperature irradiation was performed with the device unbiased, whereas the cryogenic irradiation was performed with the detector biased and clocking. The difference due to unbiased vs biased irradiation is well documented with respect to the degree of ionising damage deposited within the device; biased irradiations are known to give rise to a greater flat-band voltage shift. The effect of a biased irradiation on the degree of non-ionising damage is not as well documented except for a study performed by Robbins *et al.* (2013) whereby devices were irradiated both biased and unbiased with a comparison of the post-irradiation annealing and final damage once the annealing had stabilised. The conclusion was that although there were differences in the anneal characteristics, the final performance measured by CTI was approximately equivalent. Since both the cryogenic and room temperature devices were left to anneal for multiple days following the irradiation, the difference in displacement damage due to the two cases is believed to be negligible.

6.6 Experimental setup

6.6.1 Characterisation at the Open University

All characterisation performed at the Open University and Harwell facility made use of the same experimental setup and utilised the same set of operating conditions. Devices were controlled by a fully customisable XCAM^{TM} CCD drive box modified to operate the CCD201-20. Signal conversion and noise suppression was controlled by a clamp and sample CDS card coupled to a 14-bit ADC. Bias and clock cards within the drive box controlled the device potentials and clocking. Datasheet operating voltages were used for image and register clocks and fixed bias lines (e2v Technologies, 2015). Exceptions were the output gate voltage and output drain voltage that were adjusted to the values within Table 6.3. V_{OG} was increased to mitigate the effect of “charge tails” (described in section 4.5.1) while the changes to V_{OD} reduced read noise slightly.

Table 6.3: *Differences between e2v datasheet biases and those used for testing.*

Connection	Description	e2v Nominal Value (V)	Value used during testing (V)
V_{OG}	Output Gate Voltage	3.0	5.0
V_{OD}	Output Drain Voltage	28.0	28.7

The ϕDC and Rϕ2HV voltages were optimised on an individual basis for optimum charge transfer efficiency within the multiplication register. The parallel clock timing was set to ≈6 µs for a pair of phases, such that the time taken to transfer from one pixel to the next was 12 µs plus the time taken to read out the serial register. The parallel clocks overlapped at least 50% clock amplitude. The serial clocking frequency was set to 700 kHz, with each serial clock overlapping at 100% amplitude for at least 30 ns.

Devices were cooled to the nominal operating temperature of 165 K through use of a CryoTiger™ cooling system that was coupled to the device through a copper cold finger (shown by Figure 6.8). The cryostat was held at a pressure of approximately 10^{-6} millibar through use of a Pfieffer™ roughing and turbo-pump system (on the left-hand side of Figure 6.9). Temperature control was handled by PT-1000 temperature sensors mounted to the device package and linked to a Lakeshore Model 325 temperature controller alongside a 25 W resistive heater. The sensor was connected in a configuration to minimise the offset due to additional series resistance and so temperature measurement accuracy is believed to be within 0.5 K for the entire study.

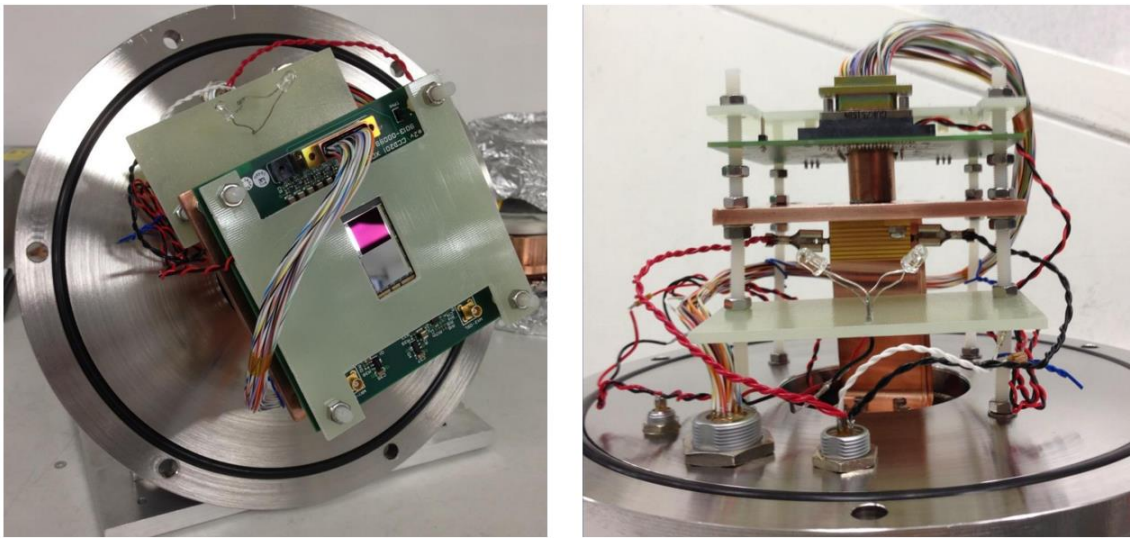

Figure 6.8: *CCD201 mounted to camera electronics and cold bench with top-down view.*

Figure 6.9: *Experimental setup used for device testing.*

6.6.2 Characterisation at the Harwell facility

The cryogenic irradiation within this investigation necessitated a customised experimental setup that was able to maintain a stable cryogenic temperature alongside the ability to attach and detach from the Harwell beamline for irradiation. The setup was as consistent as possible to that used during the room temperature irradiation characterisations, albeit with certain modifications that allowed the system to be moveable and operate without an external power source for a short amount of time.

A gate-valve and beamline adaptor flange was mounted to one side of the chamber to allow the system to mount to the proton beamline and expose the device to radiation (Figure 6.10). The mounting was aligned such that the centre of the gate-valve opening was also central with the position of the CCD201 to ensure the device was safely within the beam path. This equipment was designed as part of an ESA funded P-Channel CCD study and first commissioned in 2014 (Gow *et al.*, 2016).

The main system cryostat and CCD drive electronics were kept consistent with the room temperature irradiation investigations, with two exceptions:

1. The CCD201-20 headboard amplifier gain was increased from 1.5 to 3.0 (measured using 50 Ω termination). The purpose of this was to reduce read noise. The corresponding reduction in dynamic range was not deemed detrimental to this study.
2. The store clocks within the drive electronics were coupled such that a single clock controlled Sϕ1 + Sϕ2 and another controlled Sϕ3 + Sϕ4. This modification was to provide frame-transfer capability and hence the ability to measure FPR, discussed later.

No adverse effects of either modification were noted during pre-irradiation testing. All electronic components of the system were connected to an Uninterruptable Power Supply (UPS) so that the system could survive off external power for a short period of time (up to approximately 5 minutes). The entire setup was also securely mounted to a heavy duty, moveable trolley so that the equipment could be moved from the characterisation room into the beam-line room during operation. The experimental setup is shown within Figure 6.11 and Figure 6.12).

Two CCD201-20s were irradiated at the Harwell facility, each to a different final fluence level. The engineering grade CCD201-20 was irradiated to a single fluence level to observe annealing trends deemed important to the analysis of the science grade device, discussed shortly. The science grade device was subjected to four separate irradiations, with the post-irradiation performance measured between successive fluences (Table 6.1, Figure 6.1). Following the characterisation of the final fluence, the device was warmed to 298 K for a week and then characterised to assess the impact of a room temperature anneal. This was then repeated to determine whether the annealing at this temperature had completed or was still proceeding.

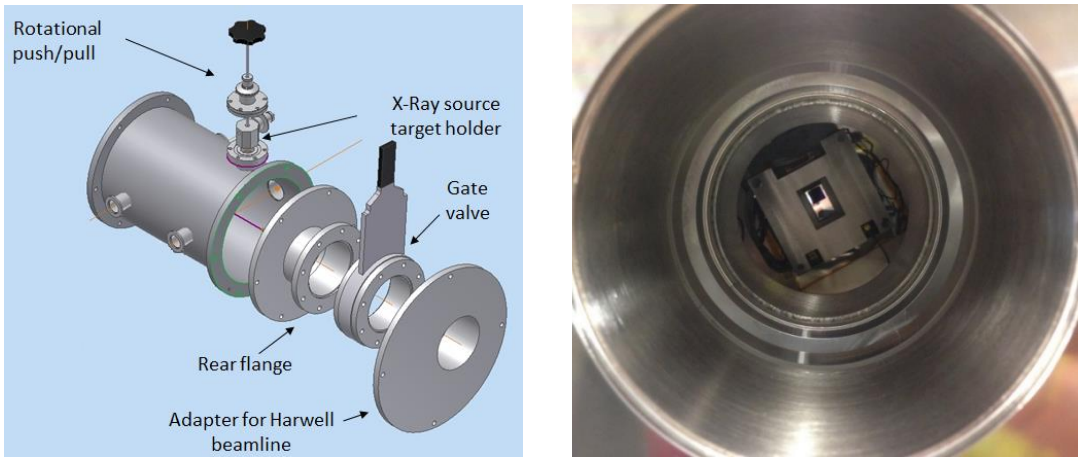

Figure 6.10 *left: 3D CAD of the main Cryostat with gate valve and beamline adaptor (adapted from Gow 2014). Right: View of CCD201 through beamline adaptor showing the central position of the CCD201-20.*

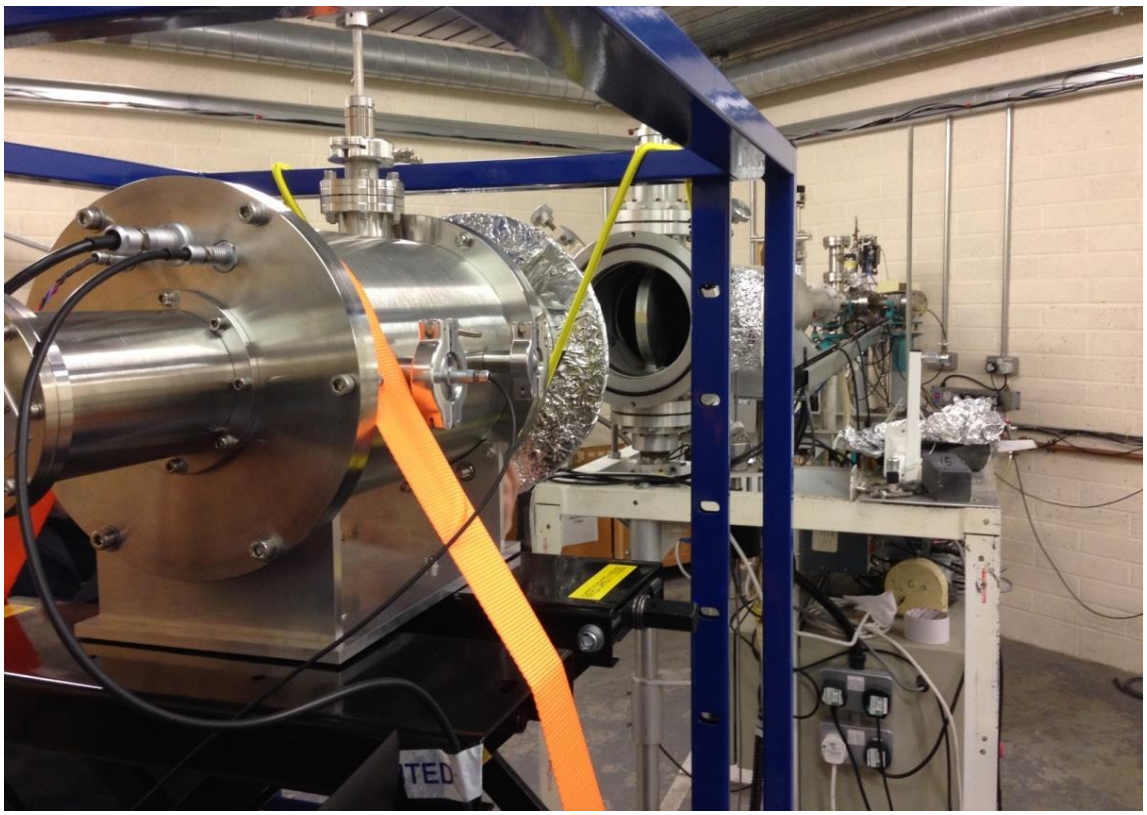

Figure 6.11: *Alignment of the system with the Harwell beamline prior to an irradiation.*

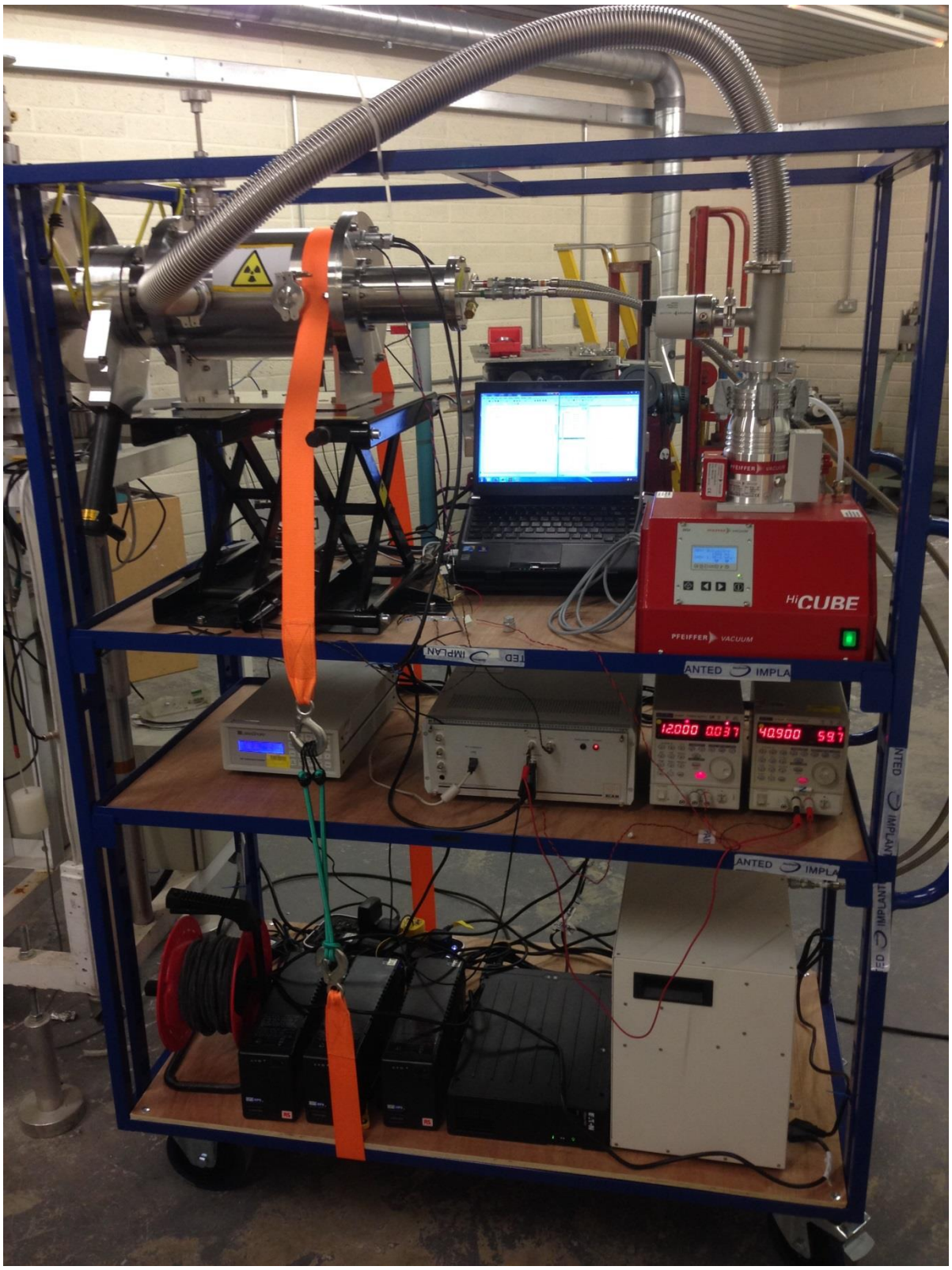

Figure 6.12*: Experimental setup mounted to the moveable trolley. Bottom shelf: UPS and CryoTiger™ cooling system. Middle shelf: Temperature controller, XCAM™ CCD drive electronics and power supplies. Top shelf: Cryostat, analysis PC and vacuum pump.*

6.7 Test procedures and operating conditions

Prior to and following each irradiation, the devices were tested for performance metrics deemed most critical to the CGI, including thermal dark signal, hot pixels, parallel CIC, Fe^{55} X-ray CTE and low signal CTE (10 e^- signal) using both the Extended Pixel Edge Response (EPER) and First Pixel Response (FPR) techniques. Where possible, measurements of silicon defects were made using the "trap pumping" technique, discussed in detail by Hall *et al.* (2014), but also discussed later in this section for context.

6.7.1 Methods for CTI measurement

The CTI of the CCD201-20 was measured using three methods; Extended Pixel Edge Response (EPER), First Pixel Response (FPR) and Fe^{55} X-rays. EPER and FPR measurements were typically performed at around 10 e^- signal size, whereas the Fe^{55} measurement provides a constant fixed signal of approximately 1603 e^- at the measurement temperature of 165 K. Each method provided a distinct insight into the effect of trapping sites on CTI for the operating temperatures of the study.

EPER consists of a flat field exposure which is then read out of the device along with a region of parallel and serial overscan. A fraction of the charge emitted from the flat field will be captured by traps and re-emitted when the original signal packet has been transferred onwards, giving rise to a "tail" of deferred charge in both parallel and serial directions. The amount of charge emitted within the tail is then summed and used to calculate the CTI (Equation 6.1):

$$CTI_{EPER} = \frac{S_D}{S\ N_P} \qquad \text{Equation 6.1}$$

where S_D is the total deferred charge measured in the extended pixel region (e^-), S is the signal level (e^-) and N_P is the number of pixel transfers in the horizontal direction for serial CTE, or number of pixels in the vertical direction for parallel CTE. EPER probes the trap emission process and only does so for trap species that have an emission time that is comparable to the row/column readout time for the operating conditions of the measurement.

First Pixel Response (FPR) follows a similar measurement technique to EPER whereby the device is exposed to a flat field, however in this case the amount of charge lost from the leading edge of the illumination (S_L) is used to calculate the CTI:

$$CTI_{FPR} = \frac{S_L}{S\ N_P} \qquad \text{Equation 6.2}$$

where FPR probes charge capture and so therefore encompasses CTI due to all the trapping sites relevant to CGI operation, regardless of the expected emission time.

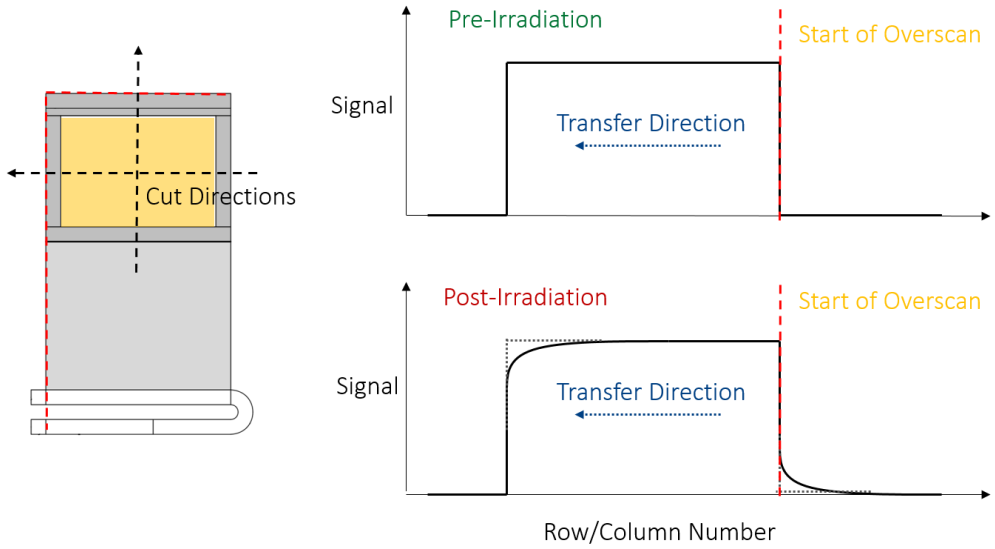

Figure 6.13: *Illustration of the EPER measurement process. The left panel shows a device with illumination incident upon the image area. The dotted arrows indicate the directions plotted by the signal/position graphs on the right and represent the transfer directions the signal experiences before reaching the output node. Reading out more rows/columns than present on the device results in parallel/serial overscan respectively – indicated by the red dotted boundaries. Any signal charge captured by traps can then be emitted in the overscan pixels. This charge is summed and divided by the illumination level to give a value for EPER CTI. For FPR, the charge lost from just the leading pixel is measured to give a CTI value.*

CTI measured using Fe^{55} X-rays is a widely-used method that provides an absolute measurement of the process of the charge loss as the signal is transferred through the device. The signal due to Fe^{55} X-rays is considerably larger than that the CGI will expect to observe, however the measurement remains relevant since the test utilises a signal distribution across the image area similar to that expected by the visible imager. X-ray CTI results also allowed performance comparison between other e2v CCDs and previous irradiation campaigns.

The X-ray source exhibits isotropic emission and so the distribution of X-rays across the device is uniform when a large enough sample is considered. Following frame integration, the image is read out and charge is transferred in both parallel and serial directions towards the output node. Since the X-ray events are distributed randomly, each of them experiences a different number of parallel and serial transfers before reaching the output. X-rays that are a greater distance from the output node on average lose more of their charge to trapping sites. Measurement of the remaining signal measured at the output as a function of both the row and column position of

the X-ray interaction gives an approximately linear line (shown in Figure 6.14) that can be used to calculate the average charge loss per pixel-to-pixel transfer for this signal level and thus a measure of CTI (Equation 6.3):

$$CTI\ (Fe^{55}) = \frac{S_P}{S} \qquad \text{Equation 6.3}$$

Here, S_P is the charge lost per pixel transfer. S still refers to signal size, which for Fe^{55} is fixed at 1616 e^-.

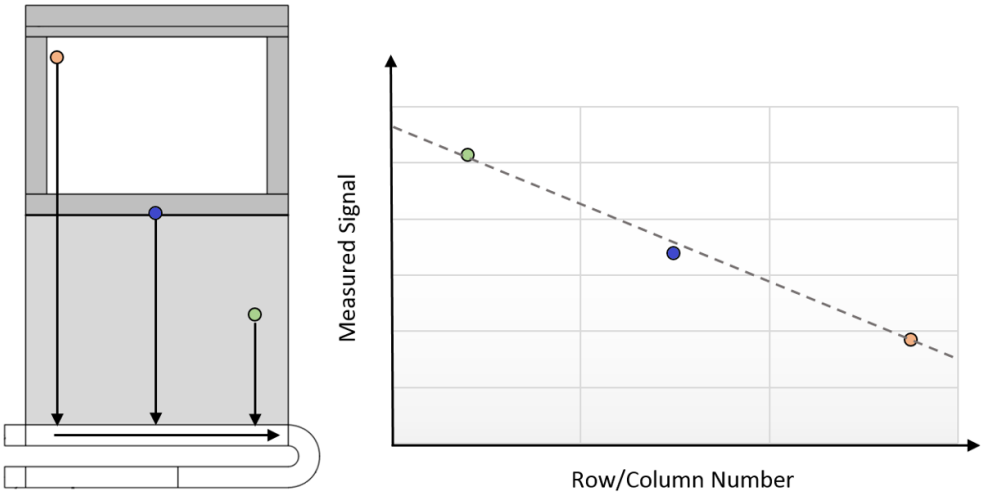

Figure 6.14: *Measurement of the remaining X-ray signal as a function of either row or column number gives an approximately linear relation that can be used to calculate the parallel or serial CTI. Note that the X-rays pass through the store shield as the attenuation length is far greater than the thickness of aluminium used to block the optical light.*

6.7.2 Methods for dark signal measurement

Parallel CIC was measured using a customised sequencer based on a method used by e2v. The technique consists of binning many image area rows (e.g. 10^5) into the serial register to create a single line of signal that is predominantly CIC generated due to image area clocking. This line is then read out of the device. The image area of the device is then held with a frame integration time equivalent to the time taken to bin and read out the chosen number of image area rows, during which time dark signal collects in the array. All of the rows of dark current are then binned into a single line of the register, which is then read out.

Implementation of this method gives an image that consists of alternate lines of parallel CIC + dark current and solely dark current. An example image is shown by Figure 6.15. The dark current can then be subtracted from the row containing both sources of signal so that only signal due to parallel CIC remains. Although a small amount of CIC is present within the row of dark current signal, this can easily be removed in post processing since the number of parallel transfers is

known (2069 for the CCD201-20). These rows of CIC with dark current subtracted were then averaged and divided by the number of parallel transfers binned into the register to provide a mean value for the parallel CIC in units of e^-/pix/frame.

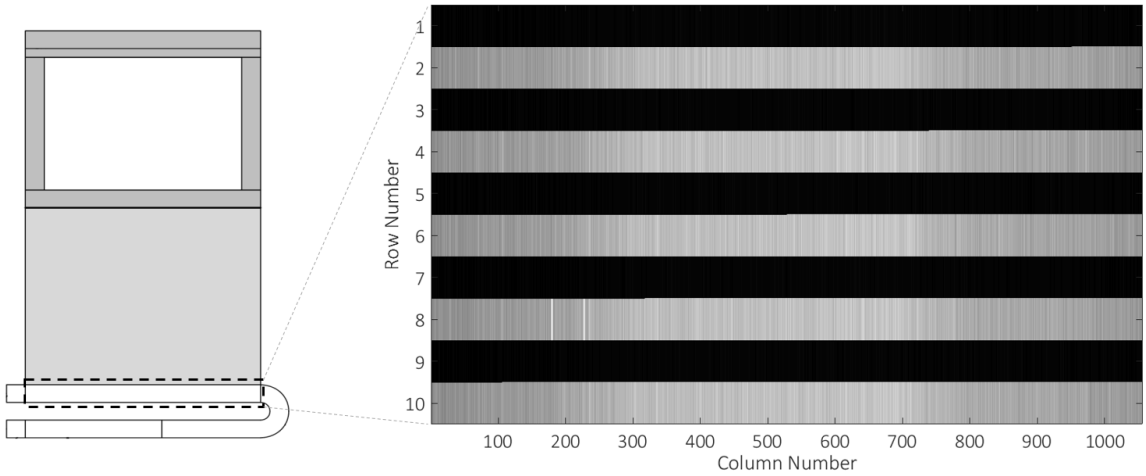

Figure 6.15: *Example image obtained using customised CIC sequencer showing alternate lines of signal due to CIC + dark current and dark current. Row by row subtraction gives a signal level that is due to CIC alone that can be used to calculate the parallel CIC generation rate in units of e^-/pix/frame.*

Dark signal was measured using a standard technique whereby multiple sets of images were obtained each using a different integration time. Bright pixels caused by incident charged particles were removed by comparing at least two images and taking the lowest pixel value. Hot pixels were not removed by this method, since they are present in all images at the same location. The mean signal level was then calculated in both the image and store sections for each integration time, giving a dark signal value in units of e^-/pixel. The signal levels were then plotted as a function of integration time and a straight line was fitted to the data that returned a dark current generation rate in units of e^-/pix/s. Hot pixels were identified by first confirming they were not signal due to a charged particle or RTS artefact, and then imposing thresholds to bin each of the defects according to a "generation rate in units of e^-/pix/s.

6.8 Defect identification through "trap pumping"

In the previous chapter, the importance of individual silicon defects to charge transfer performance was highlighted. "Trap pumping" is a technique that enables the identification of individual silicon defects, and so can provide additional information for CTI measurements and annealing effects to help explain any measured trends. The technique involves the clocking of signal charge back across phase boundaries in such a way that charge is captured by a trapping site and then preferentially emitted into a neighbouring pixel. The repetition of the process over

numerous cycles (typically > 10^3) results in a net transfer of charge that is seen within an image as a bright-dark pixel pattern, referred to as a "dipole". The dark pixel typically represents the physical location of the trap (at pixel level resolution) and the bright pixel is due to charge that has been captured by the trapping site and released into the neighbouring pixel many times, adding to the background signal level. An example "dipole" is shown by Figure 6.16.

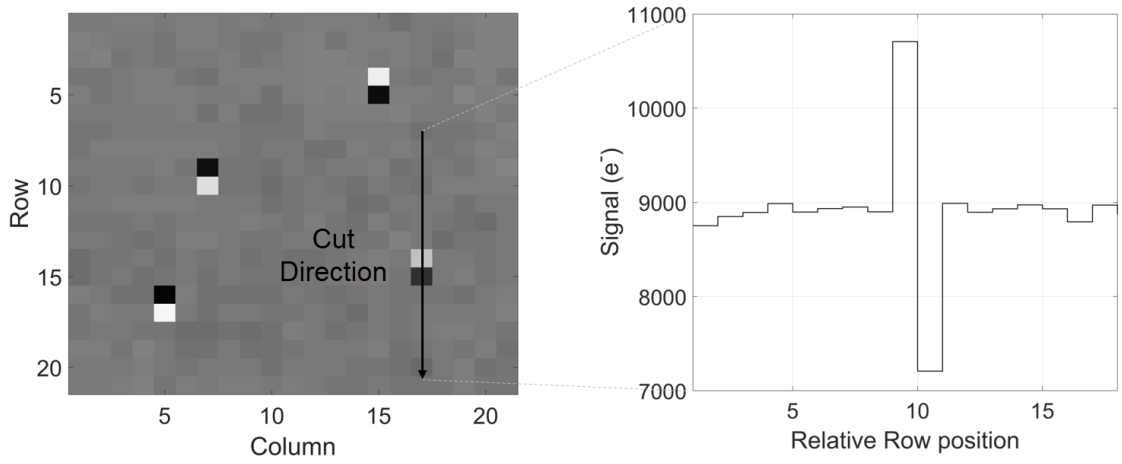

Figure 6.16 Left: *Image of dipoles following the trap pumping process. The dark pixels represent the pixel location of the trapping site. Right: Intensity profile of a dipole whereby the drop below mean intensity represents the location of the trapping site and the rise above mean intensity is due to the trapped and released signal charge over multiple cycles.*

For a given trap pumping routine, three conditions must be satisfied:

1. The pumping routine must allow a trapping site to capture signal charge.
2. The pumping scheme must promote the emission of the trapped signal charge into a neighbouring pixel.
3. The final location of a charge packet following a pumping cycle must be equal to the starting location. Otherwise, over multiple cycles the charge will be clocked through the device and no net effect of pumping will be observed.

Clocking a device using a pumping scheme that satisfies the above three conditions will typically produce images with features consistent with Figure 6.16, from which the location of a trapping site can be inferred. Determination of a trap location alone is typically not useful for modelling or optimisation purposes; the trap properties must also be calculated. Determination of the properties of trapping sites, including the emission time constant, requires the knowledge and application of Shockley Read Hall (SRH) theory to the data obtained from trap pumped images.

The trap pumping process capitalises on the capture and emission process of silicon defects to infer their properties. This capture and emission is best described by two exponential time

constants; the capture time constant τ_c and the emission time constant τ_e, discussed in the previous chapter but included again here for clarity.

$$\tau_C = \frac{1}{\sigma n v_{th}} \qquad \text{Equation 6.4}$$

$$\tau_e = \frac{1}{\sigma N_c v_{th}} \cdot e^{\left(\frac{E}{k_B T}\right)} \qquad \text{Equation 6.5}$$

The probability that an electron will either be captured or emitted at a given time *t* for a given trap species follows an exponential distribution with the time constants for capture and emission, respectively. The probability density functions for capture and emission are therefore:

$$PDF_{c(t)} = \tau_c e^{-\tau_c t} \qquad \text{Equation 6.6}$$

$$PDF_{e(t)} = \tau_e e^{-\tau_e t} \qquad \text{Equation 6.7}$$

Due to the nature of the pumping process, it is typically more useful to consider the cumulative distribution function for both emission and capture which gives the probability of capture of emission within a time period t_1 and t_2. The cumulative distribution function is given by the integral of the probability density function within the chosen time period:

$$P_c = \int_{t_1}^{t_2} \tau_c e^{-\tau_c t} = e^{-\tau_c t_1} - e^{-\tau_c t_2} \qquad \text{Equation 6.8}$$

$$P_e = \int_{t_1}^{t_2} \tau_e e^{-\tau_e t} = e^{-\tau_e t_1} - e^{-\tau_e t_2} \qquad \text{Equation 6.9}$$

The timescales for charge capture have a strong dependence on the local signal density (Equation 6.4). The upper limit of signal density within a CCD is given by density of donor atoms within the buried channel, which is typically of order 10^{16} cm^{-3} for buried channel CCDs. Typically, the maximum charge storage density approaches this value for signal packets of approximately 1000 e^- or more. Trap pumping is usually performed with signal levels of comparable or higher size such that the probability of capture for signal sizes commonly used for trap pumping is approximately 1 for the vast majority of the signal packet for all trap species, as shown by Figure 6.17.

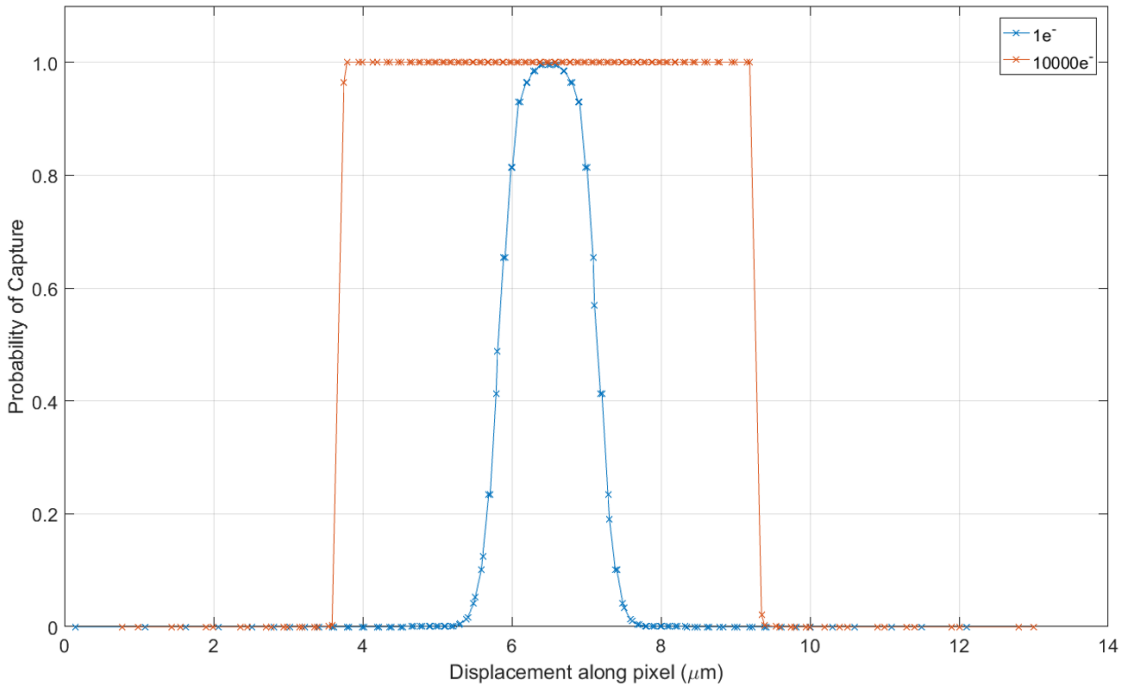

Figure 6.17: *A cut through both a 1 e^- and 10000 e^- charge packet (in direction parallel to transfer) showing the probability of capture assuming a cross section of 1×10^{-14} cm^2 (Si-A) and a dwell time of 1 µs. For the large signal the probability of capture is equal to 1 for the vast majority of the packet. The assumption of instantaneous capture is valid in this regime.*

Since the signals used for pumping are typically quite large it is appropriate to assume that a trap will instantaneously capture charge when in the presence of a charge packet. This is a simplifying assumption made when designing trap pumping routines and analysing results. It is thought to be valid throughout the pumping process so long as the change in volume of the charge packet between the start and end of pumping is not significant.

The assumption of P_C = 1 also implies that the start time for emission is set equal to 0 at the point charge has been transferred away from the trapping site. When applied to Equation 6.9, t_1 = 0 and the probability of emission within a time $t_2 = t$ is given by:

$$P_e = 1 - e^{-\tau_e t} \qquad \text{Equation 6.10}$$

With respect to clocking charge within a CCD pixel that is clocked with equal phase times between transfers, denoted t_{ph}, Equation 6.10 can be applied as follows:

1. A trapping site, denoted × is in the presence of a large signal charge packet (in orange) and captures charge. The charge packets within neighbouring pixels are shown in grey.

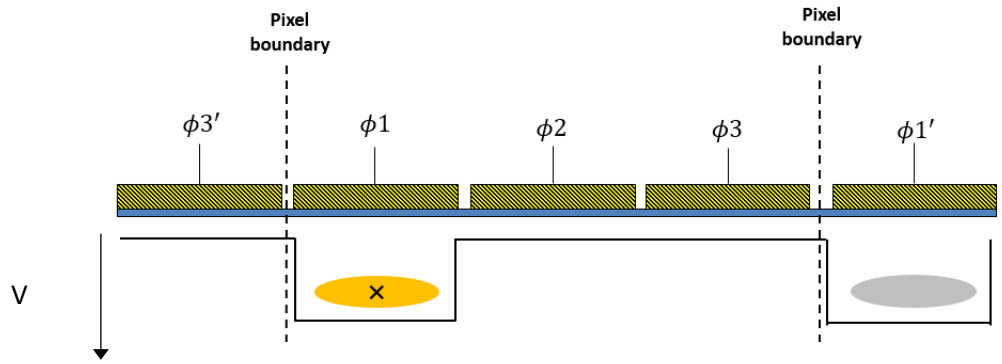

2. The charge packet is transferred to the neighbouring phase ($\phi 2$) and stored beneath it for a wait time equal to t_{ph}. The probability that the trap will emit charge within the time period 0 to t_{ph} is given by Equation 6.10. However, if the trap does emit in this time-frame then it will re-join the original signal packet. No net change in charge distribution will occur.

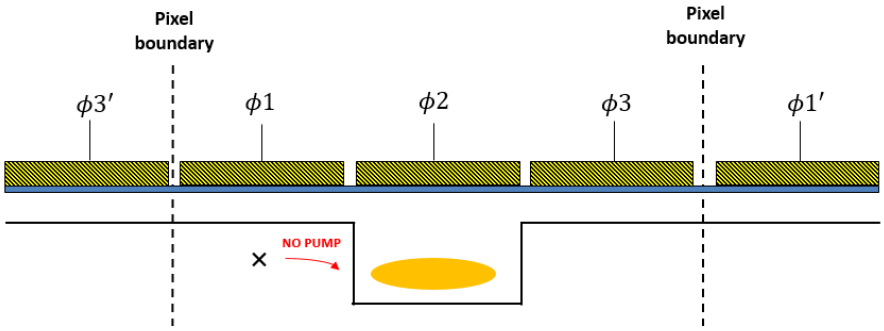

3. The charge packet is transferred to the neighbouring phase ($\phi 3$) and stored beneath it for a wait time equal to t_{ph}, such that the total time elapsed since the charge packet left the trap location is equal to $2t_{ph}$. If the charge packet emits within this time period, it will join a neighbouring signal packet. There has therefore been a net transfer of charge from the original signal packet to a neighbour. If the trap emits within this time period, then it is said to have "pumped".

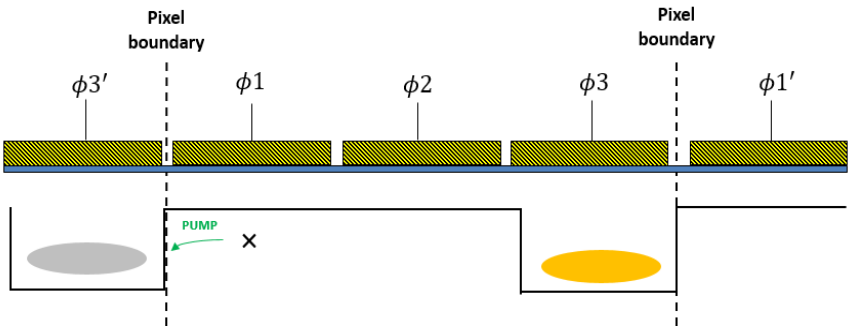

The probability of pumping, P_P, for this example is given by Equation 6.9 where in this instance $t_1 = t_{ph}$ and $t_2 = 2t_{ph}$:

$$P_p = e^{\frac{-t_{ph}}{\tau_e}} - e^{\frac{-2t_{ph}}{\tau_e}} \qquad \text{Equation 6.11}$$

Note that if the clocking scheme is different, t_1 and t_2 may also differ and so the equation that describes P_p may take a different form. Following a large number N of the clocking cycles shown above, the intensity of the dipole for a trap under $\phi 3$ due to the above process will be given by:

$$I = NP_P = NP_C\left(e^{\frac{-t_{ph}}{\tau_e}} - e^{\frac{-2t_{ph}}{\tau_e}}\right) \qquad \text{Equation 6.12}$$

Measurements of I for a range of t_{ph} give rise to an Intensity curve that takes the form of Equation 6.12 (Figure 6.18). The value for the emission time constant can then be calculated by locating the value of t_{ph} that equates to the maximum of the curve and substituting into a form of Equation 6.13 that is applicable to the pumping scheme:

$$\text{At peak intensity: } \frac{dI}{dt} = 0$$

$$\therefore \ \tau_e = \frac{t_{ph(max)}}{ln(2)} \qquad \text{Equation 6.13}$$

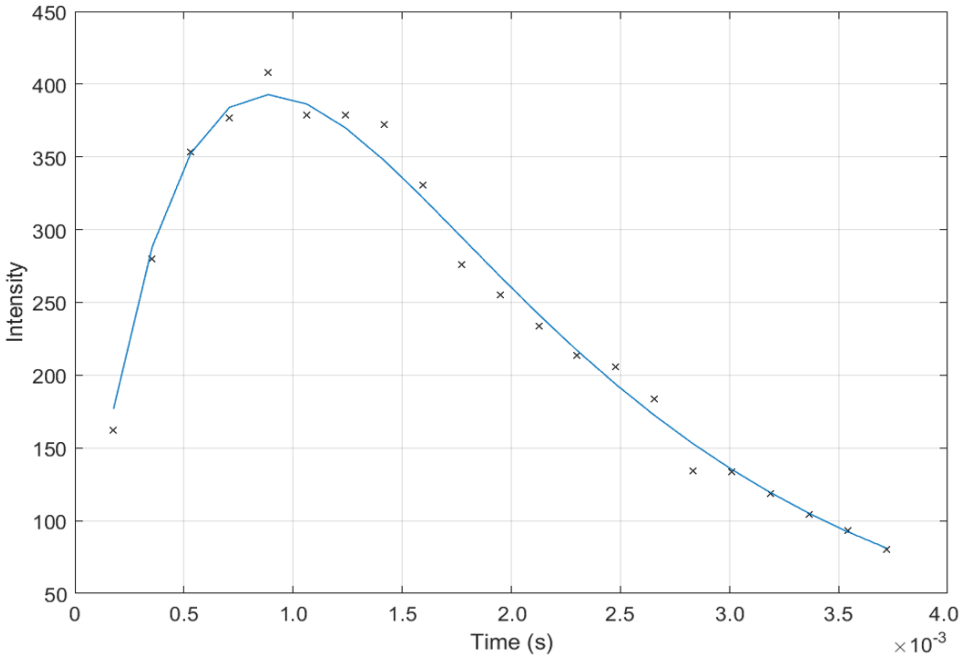

Figure 6.18: *Example intensity curve that has the form of Equation 6.12. Fitting Equation 6.12 to this curve allows the emission time constant at a given temperature to be extracted.*

As well as the emission time constant, the phase location of the trap can be inferred through knowledge of the direction that the released charge "pumps". In the previous example of trap pumping it can be seen that the charge will only pump into the pixel to the left. The standard direction of clocking is such that charge proceeds from $\phi 1$ to $\phi 2$ to $\phi 3$ and so forth. From this information, and the orientation of the dipole with respect to the direction of readout, it can be deduced that the trap is under $\phi 1$ (Figure 6.19).

Thus, this technique can allow the determination of both the defect location and emission time constant to high precision. The example shown here was for a simple 3-phase pixel. Development of the technique for the more complex pixel architecture of the CCD201-20 formed a significant portion of the work of this thesis and so is discussed in a later chapter. The technique was used in a more basic manner during the room temperature and cryogenic irradiations to assess the magnitude of the damage and measure annealing trends. For further discussion of the technique and its applications, the reader is referred to the works of Hall *et al.* (2014) and Wood *et al.* (2014).

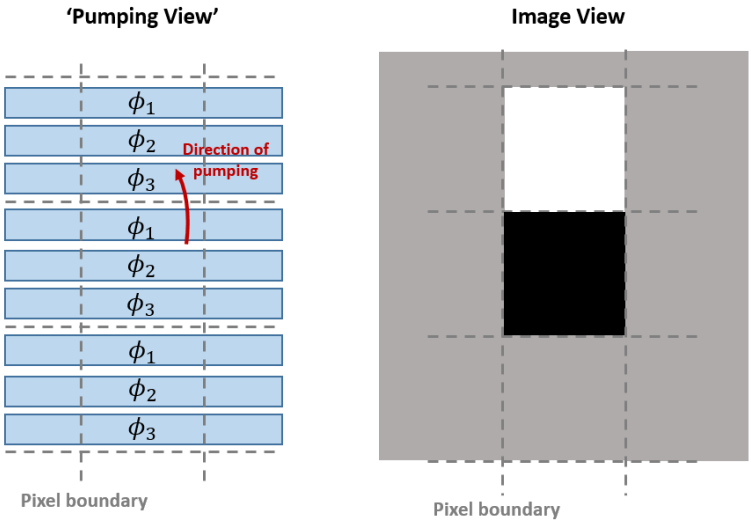

Figure 6.19: *Illustration of how the phase location of the trap under investigation can be inferred through knowledge of the pumping scheme and direction of readout.*

6.9 Summary

This chapter has described the background of the WFIRST irradiation campaign, including devices used for study, the timeline for testing and the methods used to characterise each of the devices. Discussion now turns to the results from post-irradiation characterisation of each device in the context of cryogenic vs room temperature irradiations and the impact on performance on the WFIRST CGI.

7 Activation and isothermal annealing

Following the delivery of a large dose of radiation to a sensor, some annealing takes place shortly after the irradiation (Kinchin & Pease, 1955). This is known to occur for room temperature irradiations and has also been observed when irradiating P-Channel devices under cryogenic conditions (Gow *et al.*, 2016). For the room temperature irradiations performed in this study, devices were re-characterised at least 4 days following the irradiation, by which point the vast majority of annealing would have completed. For the cryogenic phase of the study, the timescales for the isothermal annealing to complete were unknown since a sensor of this type has never been irradiated under these conditions. Post-irradiation characterisation needed to be performed when the vast majority of the annealing had taken place since this was the most representative of the in-flight case. To characterise the time required for the annealing to take place, dark current and the population of a specific defect species (thought to be the VV^{--} centre) were monitored during and following each cryogenic irradiation for a period of 48 hours. This chapter summarises the experimental measurements made immediately following each cryogenic irradiation to ensure that post-irradiation measurements were made when the device had reached a stable state.

7.1 Transient signals caused by charged particles

Signal deposited du to charged particles was also monitored following each irradiation to ensure that the background would not interfere with measurements through an artificial “fat zero”. Interaction events were identified using a simple thresholding algorithm that identified transients through comparison of a pair of subsequent frames. During irradiation, the device was saturated with signal due to the ionising energy loss of protons passing through the CCD. Following irradiation, the recorded number of signal events due to charged particles was seen to drop to the background level within approximately 10 minutes, shown by Figure 7.1. It can also be seen that the charged particle event background prior to irradiation was slightly higher than the background level following irradiation. This was attributed to the system being attached to the Harwell beamline prior to irradiation but disconnected approximately 10 minutes following irradiation. The activation of the system was reduced to a negligible level within approximately an hour following irradiation and therefore not expected to interfere with any measurements.

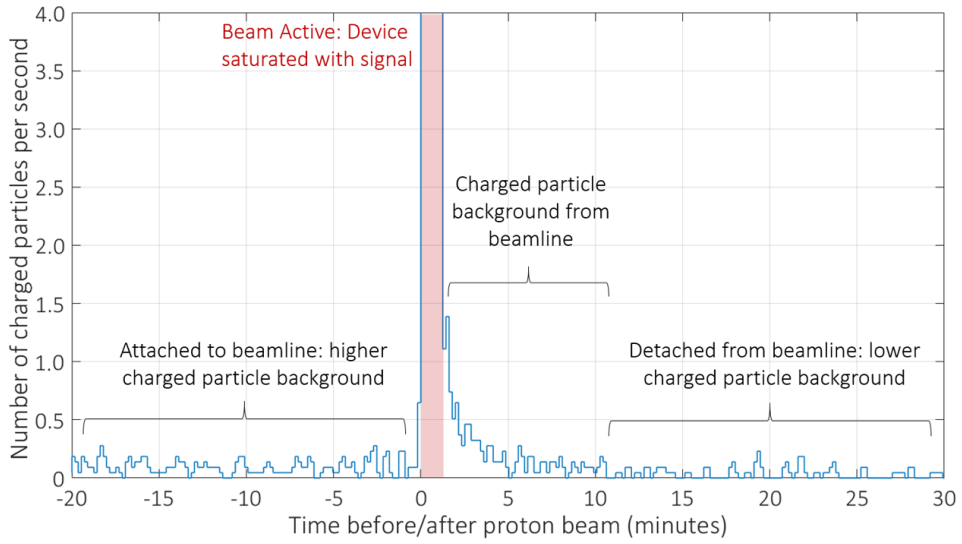

Figure 7.1: *Number of events due to signal deposited by charged particles recorded immediately prior to and following irradiation from the proton beam during an irradiation to 1.0×10^9 p/cm^2 (10 MeV equivalent).*

7.2 Thermal dark signal

Thermal dark signal was monitored for approximately 48 hours following each cryogenic irradiation using frames with a 30 second integrated time. The dark signal was too low to be resolved within a single frame and so successive frames were averaged that produced a "rolling" value. Figure 7.2 shows the result for each of the cryogenic irradiations. For the 1.0×10^9 irradiation, the dark current remained beneath the noise floor of the measurement for the entire measurement period. for the 2.5×10^9 and 5.0×10^9 protons/cm^2 cumulative fluence, significant annealing was observed as shown by Figure 7.2. The annealing appears exponential in nature but in practise was not adequately modelled by a single exponential term. Multiple exponential terms were required to provide a good fit to the data, indicating the possibility of multiple mid-band trap species contributing to the trend. With the addition of so many terms, extraction of defect properties became unreliable and so these results are not included. The time constant for the annealing of the measured signal was of the order of an hour, and within 24 hours it had settled to a value comparable to the noise floor for each irradiation.

It should be noted that for this measurement, "dark signal" encompasses any signal that was not optically generated, and so can also include any bulk persistence effects from the device being saturated with signal due to the irradiation. The decay may therefore not be due to annealing of a trap species but also exhibit a contribution due to deep-level trapping sites with long emission time constants at this temperature. Following the final irradiation (the failed 7.5×10^9 protons/cm^2 cumulative fluence described in section 6.4.3), no annealing trends were observed. Despite the less than desired fluence, the device was still fully saturated with signal during this irradiation and

so bulk persistence effects consistent with the previous irradiation would be expected if persistence formed a dominant component of the measurement. The trends observed here are therefore largely due to the annealing of mid-band defects that contribute to dark current as opposed to traps within the bulk emptying over long timescales.

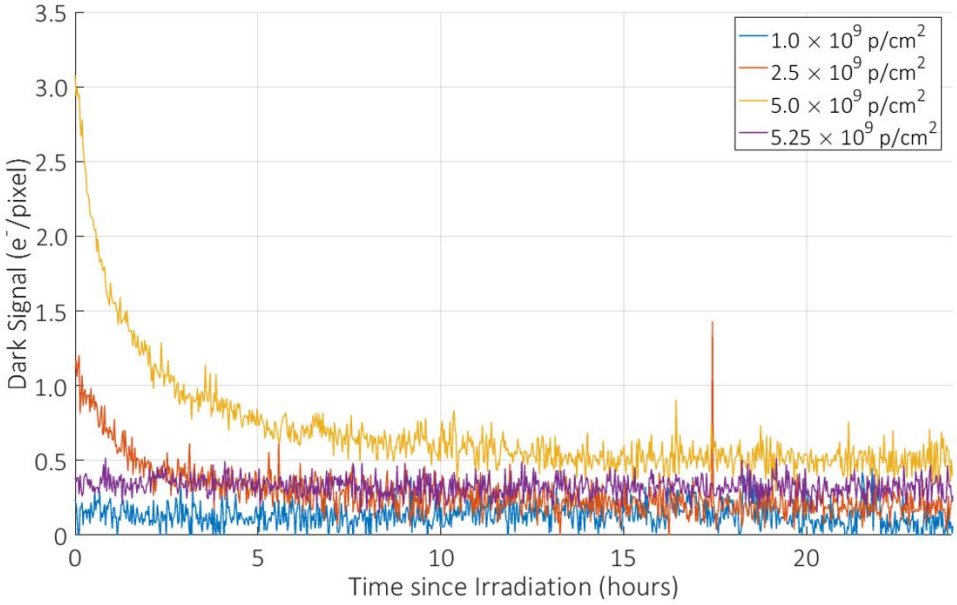

***Figure 7.2**: Dark current measured following each of the cryogenic irradiations. The annealing was not well modelled by a single exponential term, indicating there may be multiple defect species annealing within this time. The spike seen at approximately 17.5 hours following the 2.5×10^9 protons/cm^2 fluence was investigated and found to be due to charge deposited by a cosmic ray.*

7.2.1 Isothermal annealing of trapping sites

Annealing was also monitored using the trap pumping technique (Section 6.8) performed at a single-phase time (t_{ph} ≈ 10^{-4} s) that, at the operating temperature of this study (165 K), was thought to probe the VV$^-$ defect. Prior to the irradiation, the defect landscape was observed to be stable over long time frames. While this may seem obvious, some defects are known to exhibit meta-stability depending upon their charge state and so the confirmation of a stable landscape prior to the irradiation was required in order to isolate the effects of annealing (Bautz *et al.*, 2005). Following the irradiation, the defect landscape was observed to be dynamic with some defects immediately annealing and others appearing in places they had not previously been seen. Figure 7.3 shows "snapshots" of images at fixed time intervals following the irradiation alongside the changes in the landscape between each of the fixed time measurements. The decrease in defects as a function of time is an expected phenomenon, as some of the traps are expected to be unstable following their initial formation (Kinchin & Pease, 1955). The appearance of additional traps, however, was unexpected. The physical mechanism behind this observation remains

unclear as it could be that new defects are forming that can then be probed through the trap pumping technique, or it could be that the defect was already present, but not in the specific charge state being probed in this measurement. In this instance, it is believed that the double acceptor (VV^{--}) state of the divacancy is under observation. It is conceivable that the divacancy forms in a different charge state and takes time to accept carriers such that the energy level of the defect is within the parameter space that is probed here. Further work is required to investigate the physical mechanisms that underpin this measurement, however the observation is believed to be the first for an N-Channel CCD.

Figure 7.4 shows the total number of defects identified as a function of time for the first hour following the irradiation to 1.0×10^9 protons/cm^2. An exponential decrease in the visibility of defects was observed over time such that 30 minutes following the irradiation, there was an approximate factor ×3 drop in the measurable number of traps. The same exponential decrease as a function of time was observed for each of the irradiations as shown by Figure 7.5. The annealing for this defect was observed to proceed for at least a week, however the percentage change per hour in number of traps had dropped below 1% within the first 48 hours. Post-irradiation characterisation began following this time, as the changes in the landscape were believed to be too subtle to affect CTI measurements.

Table 7.1 shows that the time constant for the decay was similar for each measurement, indicating that the annealing trend was not a function of either the delivered or accumulated proton fluence. It is worth noting that this was the anneal characteristic for this species alone; the annealing curves associated with other species within CCDs are, at present, not known and could exhibit different time constants.

The total number of traps identified using the technique was used to provide a measure of dosimetry, since the density of defects should increase linearly as a function of proton fluence (Hopkinson *et al.* 1996). Table 7.2 and Figure 7.6 show the results. For the first three fluences, the increase is approximately linear as one may expect. For the final fluence, the increase in trap density was much less than anticipated.

The final two irradiations were performed with a 10 MeV equivalent fluence of 2.5×10^9 protons/cm^2, and so comparison of trap pumping of each irradiation provided further evidence that the final fluence was less than expected. Figure 7.7 shows an overlay of the number of identified traps for the final two irradiations. The factor increase in trapping sites following the final irradiation was approximately ×1.05 compared to the expected ×1.5 increase for a linear dependence. The peak trap density following the proton beam is also significantly less for the 7.5×10^9 fluence than for the 5.0×10^9 fluence, suggesting that the possibility of any non-linear

damage mechanisms is extremely unlikely. Based on the trap density information, the final cumulative fluence was estimated to be of the order 5.25×10^9 protons/cm^2, within error on the dosimetry for the 5.00×10^9 cumulative fluence.

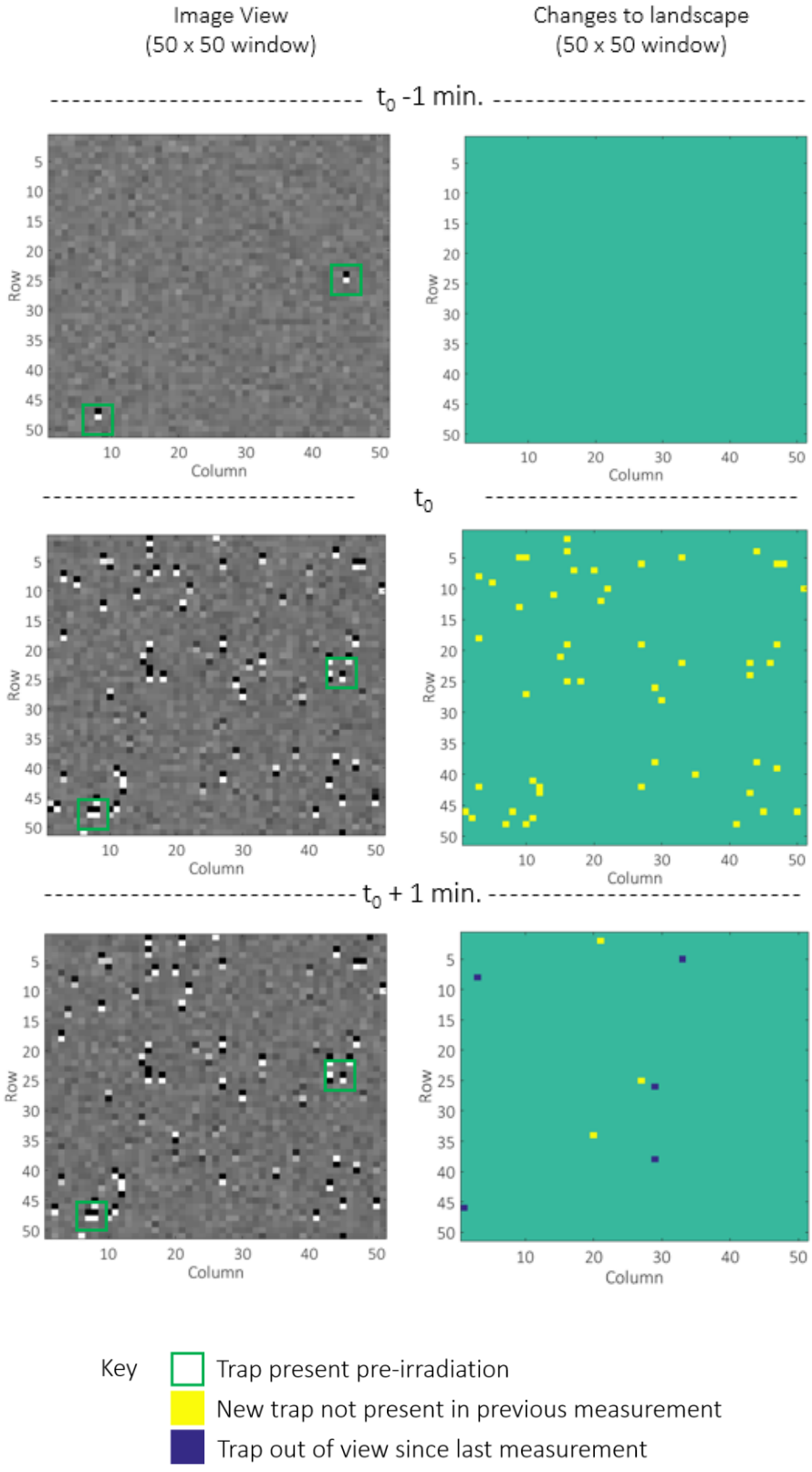

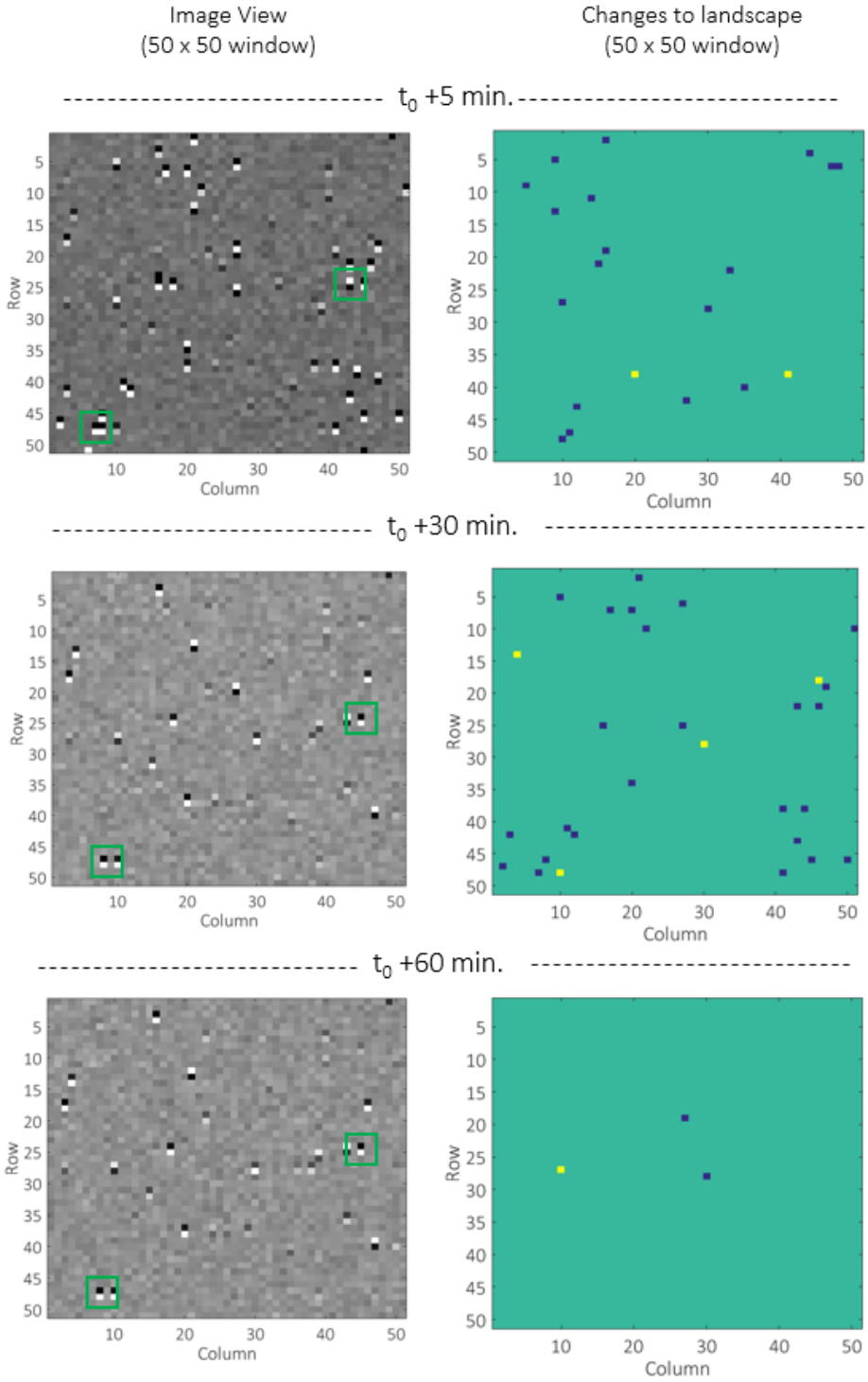
Image View
(50 x 50 window)
Changes to landscape
(50 x 50 window)
t0 +5 min.
t0 +30 min.
t0 +60 min.
Row
Column
Key
Trap present pre-irradiation
New trap not present in previous measurement
Trap out of view since last measurement

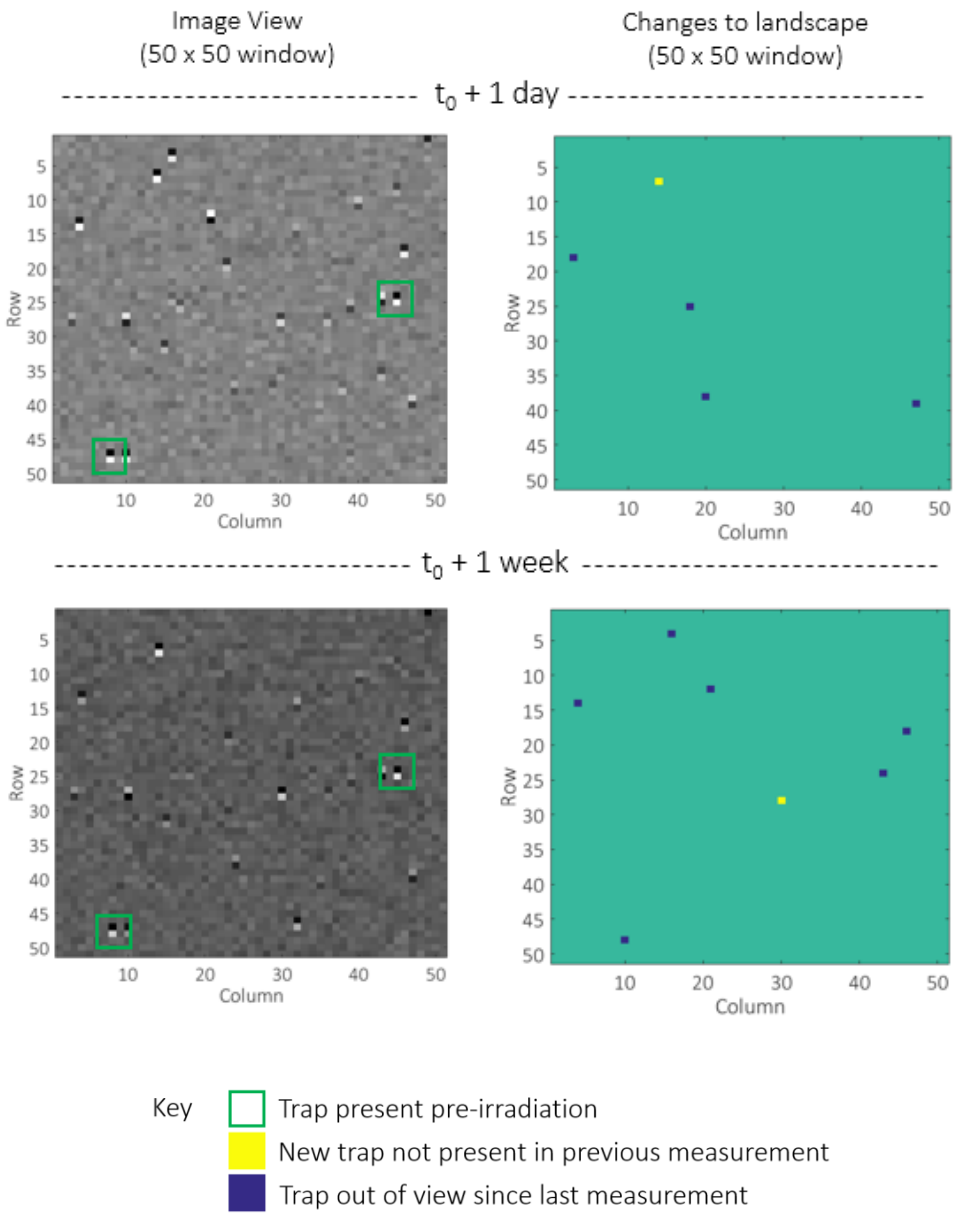

Figure 7.3: *50 x 50 pixel windows showing the defect landscape prior to and following the cryogenic irradiation performed at 165 K to a cumulative fluence of 1.0 × 10^9 protons/cm^2. A significant increase in defects is seen following the irradiation. The total number of visible defects then falls exponentially as a function of time. Some defects come into view that were not previously seen in other pixel locations, despite the fact that the beam was no longer active. This is the first experimental evidence to show how dynamic the defect landscape is following irradiation for an N-Channel CCD.*

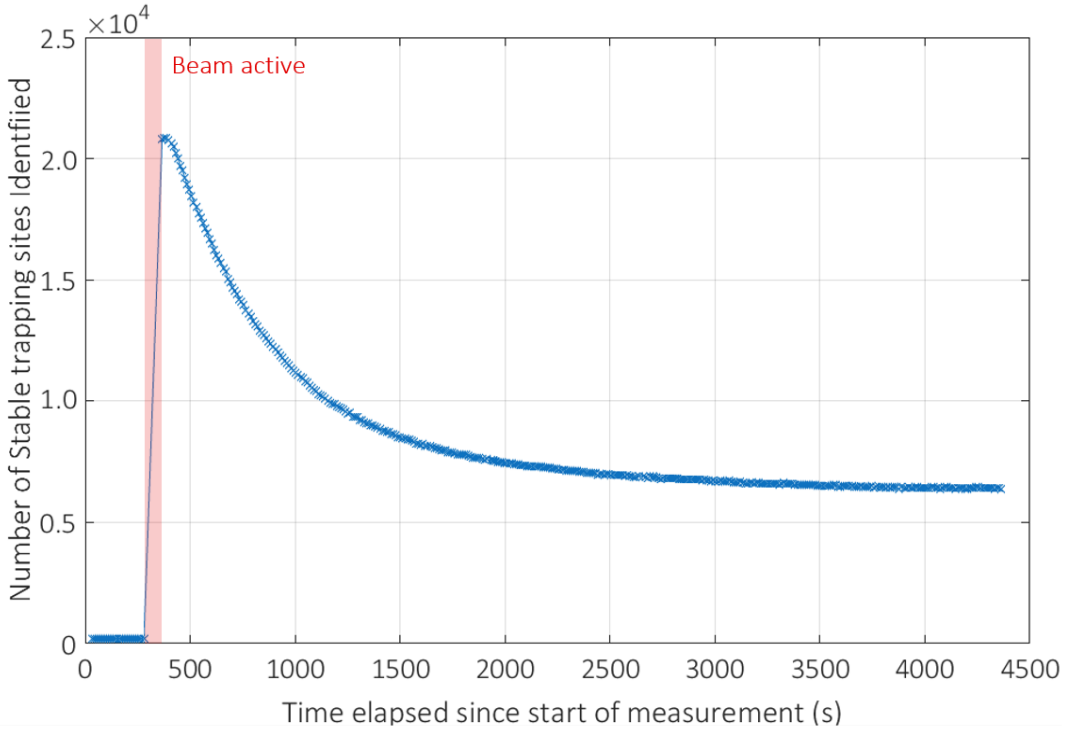

Figure 7.4: *Trapping sites identified immediately prior to and following irradiation during the irradiation to 1.0 × 10^9 protons/cm^2. The measurement started at t=0, and the irradiation began approximately t= 300 s and ended at approximately t = 400 s. During irradiation, the number of identified trapping sites appears to drop to zero since the device is saturated with signal. Immediately following the irradiation, a small increase in the number of trapping sites is observed. This is believed to be a secondary effect due to charged particles interacting with the CCD that increase the net noise within the image. Within a few minutes this effect becomes negligible and the number of trapping sites follows an exponential decay.*

Table 7.1: *Summary of time constants fitted to the VV$^-$ annealing following each irradiation. There is no discernible trend with proton fluence.*

Irradiation (Cumulative fluence p/cm^2)	Fitted time constant (τ_{anneal}) (s)
1.0×10^9	477
2.5×10^9	431
5.0×10^9	520
5.25×10^9 (Failed 7.5×10^9)	422

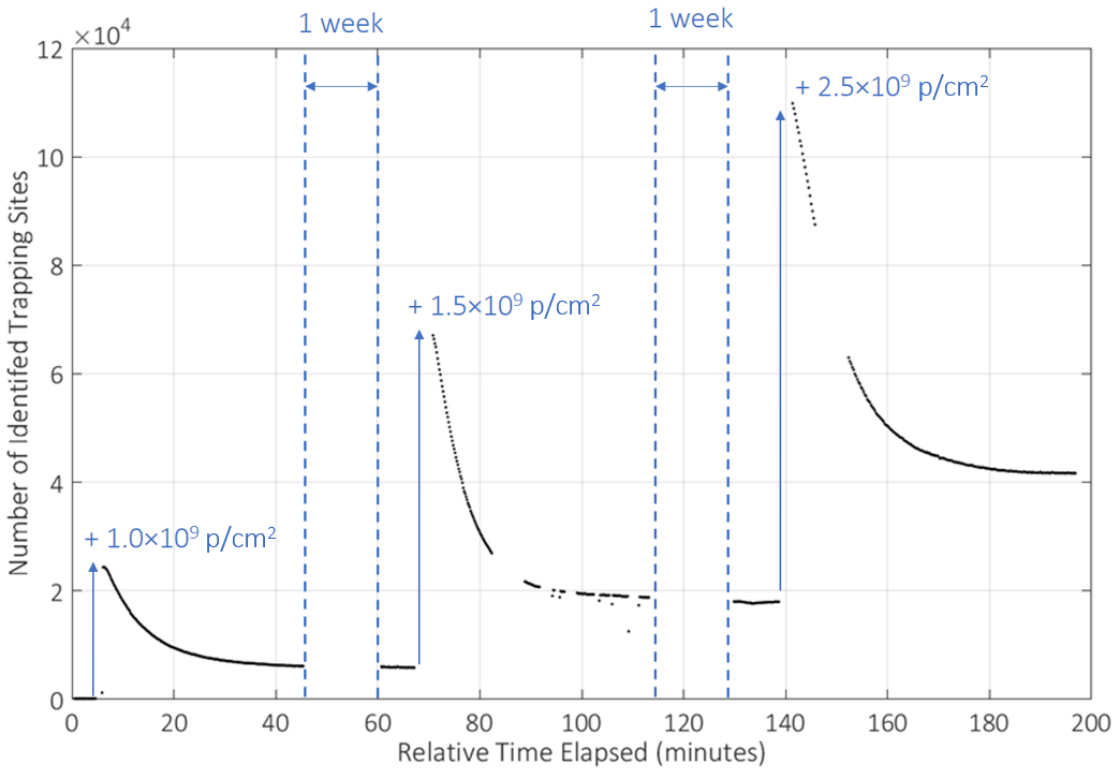

Figure 7.5: *Number of stable trapping sites identified after irradiation using a single-phase time of ≈1×10^{-4} s for the first 30 minutes following each irradiation. The vast majority of observable annealing had completed by this point however a small decrease in trap density can still be observed 1 week following each irradiation (bounded by the dashed lines).*

Table 7.2: *Summary of number of trapping sites identified using the trap pumping method 1 week following each irradiation. The factor change in defects following each proton fluence is consistent with the dosimetry estimated by Harwell, with the exception of the final fluence. The number of identifiable traps is dependent on the noise within the image. An effort was made to remove this dependency through appropriate thresholding. The error introduced by this effect is estimated to be no larger than 20%, measured by altering the threshold and recording how the number of identified traps varied.*

Irradiation (cumulative fluence p/cm^2)	Number of stable trapping sites identified	Factor change from previous measurement	Expected factor change
Pre-irradiation	167±34	N/A	N/A
1.0×10^9	6036±1207	36.13	N/A
2.5×10^9	17994±3598	2.98	2.5
5.0×10^9	40733±8146	2.26	2
5.25×10^9 (Failed 7.5×10^9)	42506±8501	1.05	1.45

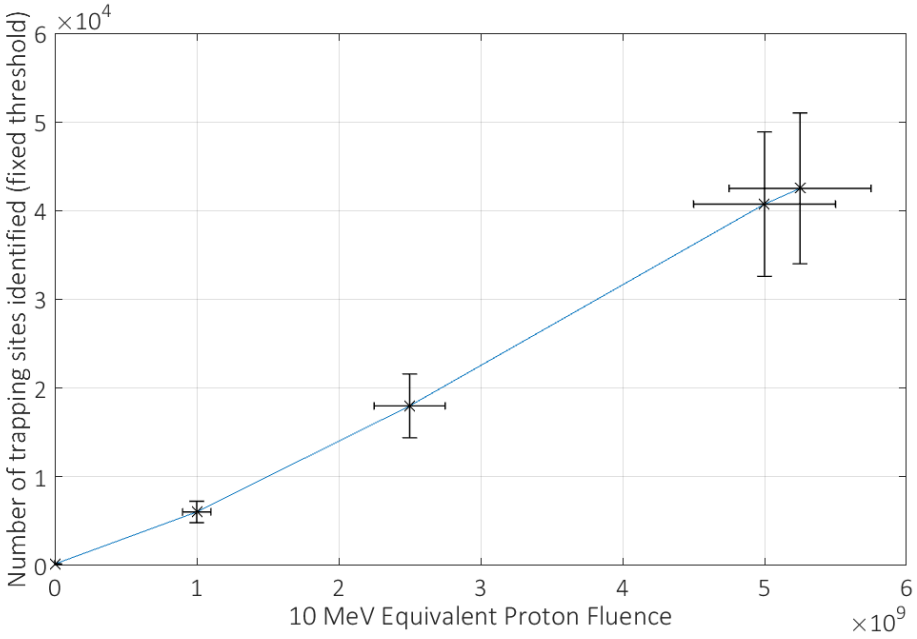

Figure 7.6: *Plot of number of trapping sites identified as a function of proton fluence. Note this is a single trap species and not representative of the entire defect landscape. The relationship was linear once the final fluence had been re-normalised to a representative value. The 1.0×10⁹ protons/cm² fluence was observed to be a little lower than expected.*

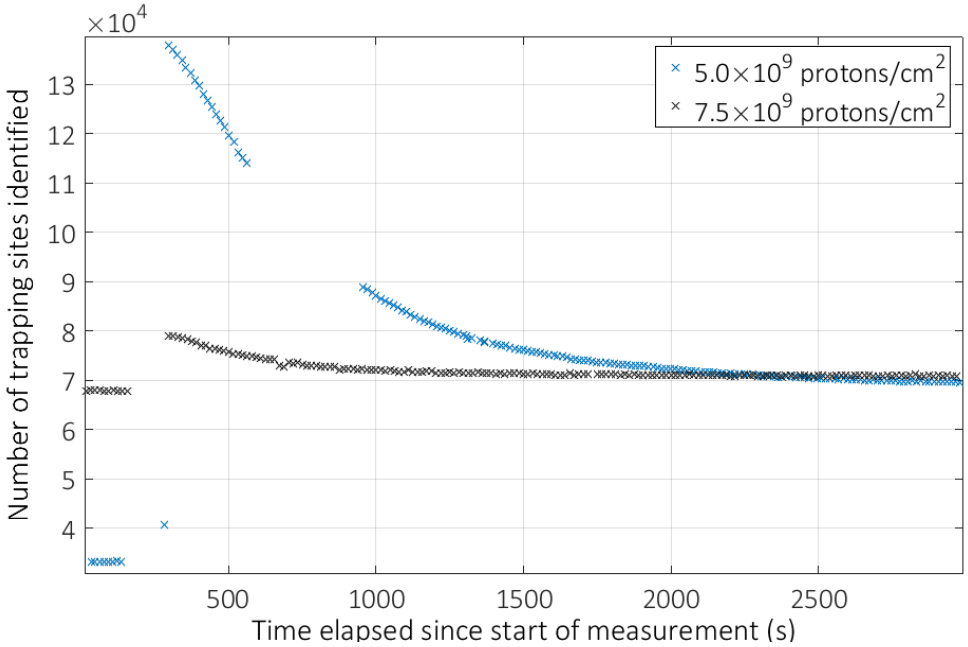

Figure 7.7: *Number of trapping sites identified during irradiation for the case where the target cumulative fluence was 5.0×10⁹ protons/cm² and 7.5×10⁹ protons/cm². The data have been set to the same start point but in reality, the irradiations were spaced a week apart. The 5.0×10⁹ cumulative fluence shows a significant factor increase in the number of trapping sites, whereas the 7.5×10⁹ cumulative fluence shows a negligible increase.*

7.3 Summary

The purpose of the measurements presented in this chapter was to verify that the device had settled to a stable state within 48 hours following irradiation so that post-irradiation measurements could begin. The number of observable trapping sites, dark signal and charged particle interactions within the device were all seen to experience the vast majority of decay within this time, and so this condition was satisfied.

Measurements of dark signal and trap density also allow additional conclusions to be drawn that were not originally a goal of this study. This chapter has shown that, the defect landscape takes a non-negligible time to settle to equilibrium following irradiation. For the specific case of the VV^-, the time constant for decay was measured to be approximately 450 s at 165 K. This decay was independent of the delivered fluence and accumulate damage, however, dependencies on signal level, proton flux and temperature remain unclear. In addition, it is unclear whether the time constant is the same for all defect species or differs according to the specific properties of the defect. Presumably, the latter is the more likely case since each lattice configuration has a different enthalpy of formation and hence energy requirement for dissociation (Pichler, 2004). Since dark current is primarily due to mid-band defects, the dark current annealing trends in this chapter provide some evidence that other defects take longer to reach an equilibrium state. Nonetheless, this is an indirect observation that may be clouded by another physical phenomenon not considered by the author.

While at first these results may not seem directly applicable to WFIRST, there are some interesting future avenues for research that may be beneficial to large scale space missions. In Section 5.3, it was discussed that at L2 the majority of radiation damage can be delivered in short bursts from solar flares. A large solar flare will likely replicate conditions similar to irradiation from a beamline and so the defect landscape will likely be dynamic for some time following this point. Annealing of dark current and trapping species will directly impact the performance of devices during this time, and so the phenomenon shown in this chapter should be investigated further to ascertain whether the annealing can be controlled in such a way as to limit the total damage and/or impact on performance.

Since it has now been shown that the cryogenic post-irradiation measurements were made with the device in a "stable" state, discussion now turns to the results from each of the irradiation campaigns and how they can impact CGI science performance.

8 The impact of CTI on CGI performance

The CTI measurements throughout the WFIRST testing campaigns were extensive and only a small subset of the results deemed most interesting for discussion is included in this thesis, summarised by Table 8.1. A key conclusion that should be stated immediately is that there is a clear difference between measurements of the device irradiated under cryogenic conditions and the devices irradiated at room temperature. The origin of this difference will be explored in more detail throughout this chapter, but it is enough for now to say that it is due to differences in the relative abundance of trapping sites that are responsible for CTI. This result has implications not only for the CGI, but any CCD-based mission where radiation induced CTI may limit science performance. The factor differences are large in many cases, with X-ray CTI exhibiting between ×3-×4 worse degradation per proton for the cryogenic case, EPER exhibiting a ×2-×3 difference and parallel FPR exhibiting an approximate ×2 difference. Following a room temperature anneal, the CTI did not return to levels expected by an equivalent room temperature irradiation in any case, although small changes were noted. A comprehensive explanation of this observation is not possible due to the overwhelming number of physical processes that may be possible for the final landscape of silicon defects. Nonetheless, an attempt is made to describe possibilities to aid future investigations that may explain the difference. Regardless of the explanation, it appears that irradiation at the nominal operating temperature provides the most realistic estimation of EOL science performance for any CCD-based mission, including the CGI.

The other key conclusion is that, at some point throughout the mission lifetime, CTI will become a limiting factor for science performance of the CGI. It should be clarified that this does not mean that the CGI will not achieve the science requirements, however it does mean that the instrument will primarily benefit from CTI mitigation techniques as opposed to dark signal/CIC reduction strategies. The exact mitigation strategies are dependent on the relative proportion of trapping sites within the device and so it is appropriate at this point to introduce Figure 8.1 that shows the fraction of filled trapping sites as a function of time, alongside each of the key transfer times used in this study. This diagram helps explain the majority of the trends observed in this chapter as each CTI measurement is shown to probe a different region of the defect landscape. The CTI results from each method are now discussed in turn with a focus on the dominant trap species responsible for each measurement and the possible reasons for differences between the room temperature and cryogenic irradiation equivalent.

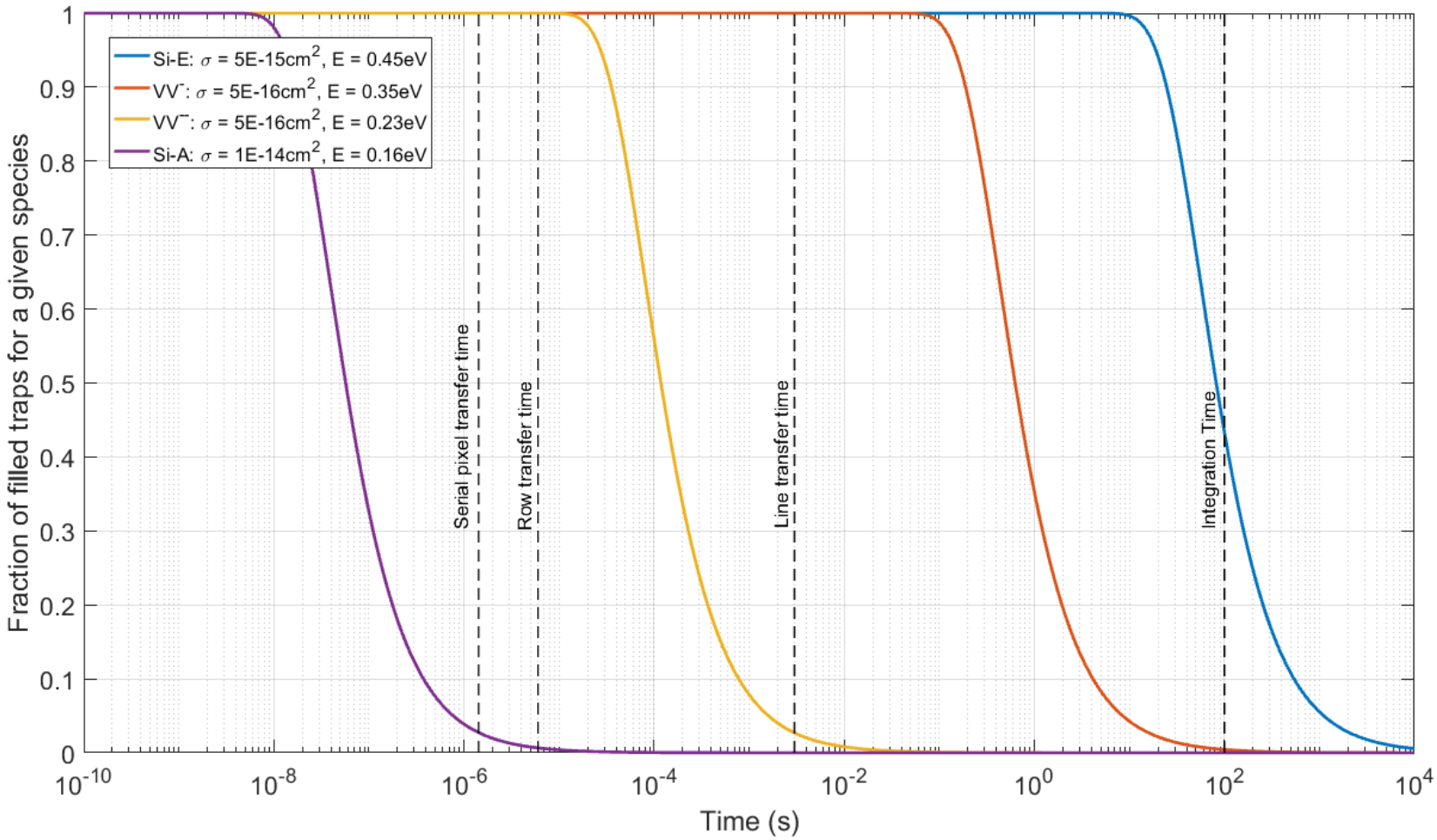

Figure 8.1: *Predicted fraction of filled traps as a function of time for the 4 major silicon defects thought to affect CTI in the CCD201-20. The properties of the defects were taken from results presented in chapter 10 that were not available at the time these values were measured but are introduced here since the results explain many of the observed trends in the CTI results. The fraction of filled traps was calculated using the theory presented in section 5.7.*

Table 8.1: CTI results from WFIRST irradiation campaigns using the FPR, EPER and X-ray CTI methods. Anomalous result in black and discussed in text.

	10 MeV equivalent cumulative Proton Fluence (protons/cm^2)							
	Pre-Irradiation		1.0×10^9		2.5×10^9		5.0×10^9	
Parameter	Irradiated at 165 K	Irradiated at 298 K	Irradiated at 165 K	Irradiated at 298 K	Irradiated at 165 K	Irradiated at 298 K	Irradiated at 165 K	Irradiated at 298 K
Parallel FPR CTI (≈10 e$^-$ signal)	(3.79±5.45) × 10^{-6}	(1.25±0.17) × 10^{-5}	(1.66±0.07) × 10^{-4}	(9.26±0.22) x 10^{-5}	(4.08±0.08) × 10^{-4}	Technique not implemented at this point (Section 6.6.2)	(7.06±0.29) × 10^{-4}	(2.97±0.04) × 10^{-4}
EPER Parallel CTI (summed charge in 600 trailing pixels at ≈ 10 e$^-$ signal)	(8.88±0.49) x 10^{-5}	(1.13±0.20) × 10^{-4}	(3.46±0.16) x 10^{-4}	(2.72±0.48) x 10^{-4}	(8.31±0.52) x 10^{-4}	(4.72±0.99) x 10^{-4}	(2.33±0.11) x 10^{-3}	(1.30±0.10) x 10^{-3}
EPER Serial CTI (summed charge in 600 trailing pixels at ≈ 10 e$^-$ signal)	(1.65±0.47) x 10^{-5}	(2.37±0.70) × 10^{-4}	(1.50±0.10) x 10^{-4}	(1.00±0.11) x 10^{-4}	(6.84±0.15) x 10^{-4}	(2.32±0.38) × 10^{-4}	(1.59±0.03) x 10^{-3}	(5.49±0.50) x 10^{-4}
EPER First Trailing Pixel Parallel CTI (≈10 e$^-$ signal)	(6.93±1.56) x 10^{-6}	(3.84±1.12) × 10^{-6}	(3.50±0.28) x 10^{-5}	(1.84±0.20) x 10^{-5}	(1.09±0.10) x 10^{-4}	(5.70±0.16) × 10^{-5}	(2.15±0.22) x 10^{-4}	(5.00±0.20) × 10^{-5}
EPER First Trailing Pixel Serial CTI (≈10 e$^-$ signal)	(7.89±1.09) x 10^{-6}	(1.53±0.13) × 10^{-5}	(1.32±0.11) x 10^{-5}	(1.14±0.10) x 10^{-5}	(3.36±0.29) x 10^{-5}	(1.72±0.19) × 10^{-5}	(7.73±0.79) x 10^{-5}	(2.50±0.40) × 10^{-5}
X-Ray Parallel CTI (X-ray density ≈ 1 event per 2700±100 pixels)	(0.569±1.0) × 10^{-6}	(5.14±3.90) × 10^{-6}	(2.76±0.13) × 10^{-5}	(2.02±0.01) × 10^{-5}	(1.31±0.05) × 10^{-4}	(4.07±0.08) × 10^{-5}	(3.18±0.18) × 10^{-4}	(9.95±0.04) × 10^{-5}
X-Ray Serial CTI (standard register, X-ray density ≈ 1 event per 2700±100 pixels)	(1.67±2.08) × 10^{-6}	(1.05±1.36) × 10^{-6}	(8.63±2.32) × 10^{-6}	(4.02±2.00) × 10^{-6}	(4.12±0.35) × 10^{-5}	(1.08±0.67) × 10^{-5}	(1.03±0.08) × 10^{-4}	(2.08±0.38) × 10^{-5}

8.1 Extended Pixel Edge Response (EPER)

8.1.1 Parallel EPER

The EPER technique probes traps with an emission time constant comparable to the row and column read times for parallel and serial CTI respectively. The parallel EPER CTI is the result of the parallel readout conditions of the device which for this study consisted of two stages; a 12 µs row transfer time whereby charge is transferred forwards one row, and an approximate 4.6 ms line transfer time corresponding to the readout of the serial register. The row transfer time is split into two equal clock cycles whereby the charge is transferred from one pair of phases to another such that the charge spends approximately 6 µs under $\phi 4$. The remaining 6 µs of the row transfer time is spent beneath $\phi 2$ of the following pixel where the charge remains for an additional 4.6 ms as a row is read through the serial register. Figure 8.2 summarises this clocking scheme. Any charge that is captured and not emitted back into the original signal packet contributes to the CTI measurement.

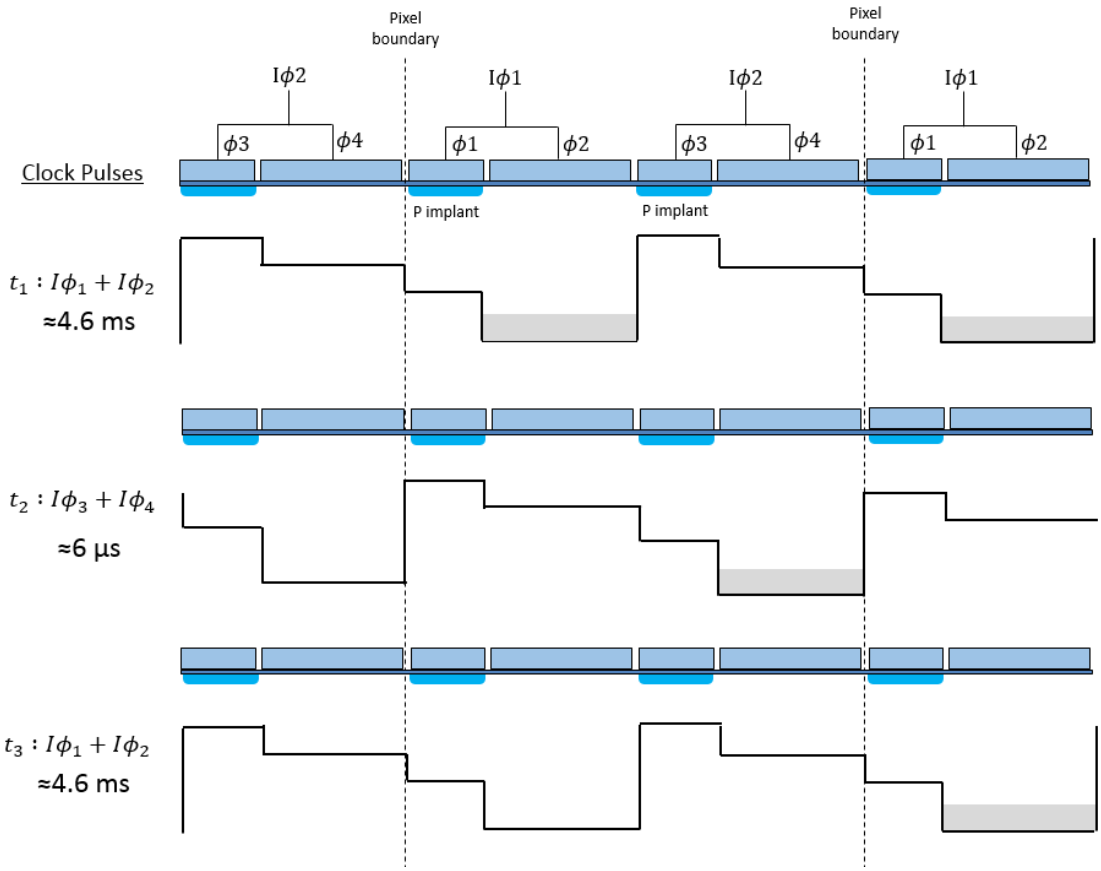

Figure 8.2: *Schematic of parallel charge transfer in the CCD201. Charge is moved from one pixel to the next through two clock cycles each lasting 6 µs. The charge waits beneath $\phi 2$ while the line is read out, which takes approximately 4.6 ms for the EPER measurements discussed in this study.*

For the first transfer step (t_1 to t_2), any charge captured beneath $\phi 2$ in the primary pixel has approximately 6 µs to emit and re-join the signal packet while it rests beneath $\phi 2$. The vast majority of charge captured by Si-A centres will be re-emitted to join the signal packet since at this temperature the emission time constant is much lower than the row transfer time. Figure 8.1 shows this to be true, and over 99% of this defect species is expected to have emitted following this wait period. Charge lost to other trapping sites, however, will likely not emit until the packet has been transferred onwards. Figure 8.1 shows this is the case for the VV^{--}, VV^{-} and the Si-E centre. Following transfer to the next pixel, any charge captured beneath $\phi 4$ has 4.6 ms to emit back into the original signal packet. Charge captured due to the Si-A centre and the VV^{--} is expected to re-join the original packet and hence not contribute to CTI. Within the same wait period, however, any charge captured due to the VV^{--} centre beneath $\phi 2$ will emit into the first trailing pixel behind the original charge packet. The remaining filled trapping sites are the VV^{-} and the Si-E centre. The Si-E centre has an estimated emission time constant of order 60 s for the operating conditions of this study (165 K). A fraction (estimated at approximately 45%) empty between successive frames with a 100 s cadence, however, the remainder are expected to remain filled. Practically no charge emission from the Si-E centre is expected within the measurement timescale and so it does not contribute to the parallel EPER tail. The VV^{-} has an emission time constant of approximately 0.4 s at 165 K. The entire parallel EPER overscan region contained approximately 900 rows, and so spanned a time domain of approximately 4 s. Approximately 90% of charge captured by the VV^{-} is expected to emit within this time and be spread over the parallel overscan region (shown by Figure 8.1). In summary:

- The Si-A centre is not expected to contribute to the parallel EPER CTI measurement.
- The VV^{--} is expected to contribute to the CTI measurement, with the vast majority of the captured charge emitted in the first trailing pixel. Only charge trapped beneath $\phi 2$ due to the VV^{--} will contribute to CTI.
- The VV^{-} is expected to contribute to the CTI measurement, with charge emitted over the entire overscan region. Charge captured beneath $\phi 2$ and $\phi 4$ contributes to the measurement.
- The Si-E centre does not contribute to the measurement, since the estimated emission time constant is significantly longer than the timescales of readout.

For both the room temperature and cryogenic case, parallel EPER CTI was observed to increase approximately linearly with proton fluence. The exception was an anomalous result for the parallel first trailing pixel CTI for the device irradiated at 298 K to 5.0×10^9 protons/cm^2 or 2.5×10^9 protons/cm^2 (Table 8.1)

(It is unclear which of the two is anomalous, since one may be considered high for the respective fluence while the other could be considered low). Figure 8.3 shows a comparison between each of the two measurements, where it is clear the cryogenic case was consistently worse than the room temperature irradiation case by a factor of approximately ×2. Figure 8.4 shows the first 50 rows following each cryogenic fluence, where the total charge within the tail increases as a function of proton fluence as expected.

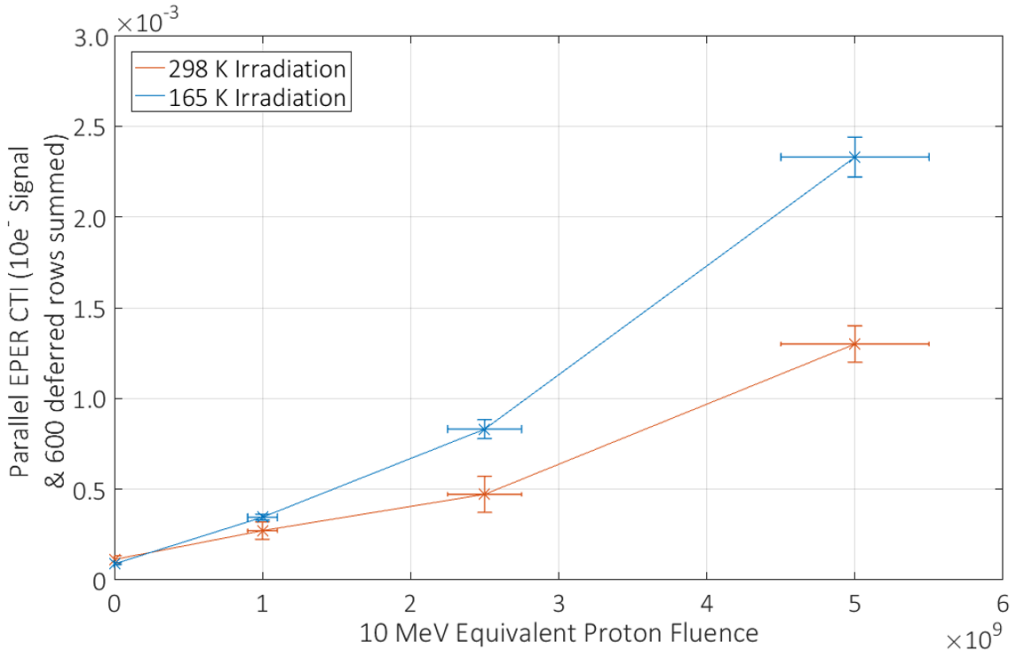

Figure 8.3: *Parallel EPER results from devices irradiated at room temperature and under cryogenic conditions.*

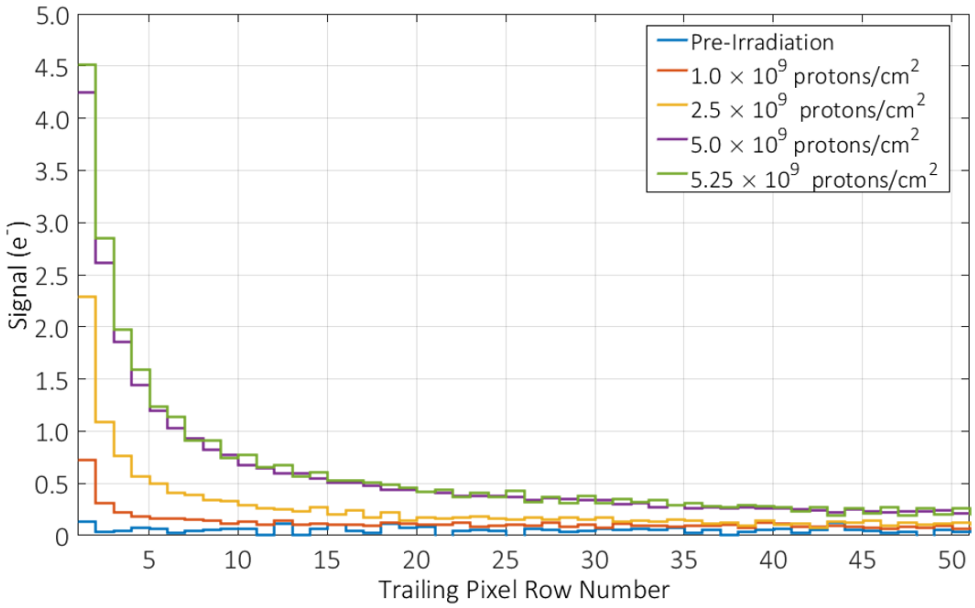

Figure 8.4: *The first 50 rows of the parallel EPER tail for each cryogenic fluence level. Pixel 1 is the first pixel after the flat field.*

The implication of this result is that at, cryogenic temperatures, there are more defects present that emit within the timescales of the parallel tail, thus corresponding to higher CTI when measured with this technique. This may correspond to either an increased density of the VV^- and/or VV^{--} or the presence of a new defect entirely. Speculation regarding additional defects that may have contributed to this measurement is complicated by the degeneracy of the cross section and energy level of defects that gives rise to the emission time constant, however for sensible cross sections (5.0×10^{-16} - 5×10^{-15} cm^{-2}) there are several candidate defects that may be responsible, summarised by Table 8.2. Carbon features heavily on the list and has different energy levels owing to metastable configurations of the defect that dominate depending upon temperature. Carbon can be present as an impurity within devices with a concentration of order 10^{15} cm^{-3} (i.e. comparable to the background boron concentration of the substrate) and so may form a non-negligible component of the defect landscape. Carbon complexes are known to have exhibited complex behaviour in cryogenically irradiated devices and given rise to changes in CTI following a room temperature anneal (Bautz *et al.*, 2005), proving that the temperature of the irradiation dramatically affect their impact on device performance.

In this study, the EPER measurement was repeated following both a one and two-week room temperature anneal of the cryogenically irradiated device. The results are summarised by Table 8.3 and the result from a room temperature irradiated device is also included for comparison. In this case, the total charge within the EPER tail (600 rows) is shown, where a higher amount of signal within the tail corresponds to poor CTE.

Table 8.2: *Potential defects that may be responsible for the increased CTI observed at cryogenic temperatures* (Pichler, 2004)*. This list is not comprehensive and is almost certainly missing other possibilities. It is also worth noting that an increase in the concentration of the known VV^{--} or VV^- defects would give rise to the same phenomena.*

Defect	Energy Level (E_C - E) (eV)	Emission time constant range at 165 K (assuming $5\times10^{-16} < \sigma < 5\times10^{-15}$ cm^2)	Section of measurement predominantly affected
V_2O	0.23	1×10^{-5} to 1×10^{-4}	First trailing pixel
C_iP_S (III)	0.23	1×10^{-5} to 1×10^{-4}	First trailing pixel
C_iP_s (IIA)	0.26	8.4×10^{-5} to 8.9×10^{-4}	First trailing pixel
B_iO_i	0.27	2.0×10^{-4} to 2.0×10^{-3}	First trailing pixel
C_iP_s (IIB)	0.32	6.0×10^{-3} to 6.0×10^{-2}	Tail of charge
C_iP_s (IA/ IB)	0.38	0.4 to 4	Tail of charge

Table 8.3*: Summary of charge within EPER tail for the cryogenically irradiated device both before and after a room temperature anneal. Results from a room temperature irradiated device are also included.*

	Total charge within Parallel EPER tail (e^-)
Sustained at 165 K (5.25×10^9 p/cm^2)	49.80± 2.2
1 week at 298 K (5.25×10^9 p/cm^2)	69.9 ± 12.2
2 weeks at 298 K (5.25×10^9 p/cm^2)	52.4 ± 11.8
Room Temperature Irradiated Device (5.25×10^9 p/cm^2)	26.8 ± 2.1

It can be seen that little/no change in parallel CTI was observed following a room temperature anneal for this technique, hence the difference in the defect landscape must correspond to either a defect that does not anneal at room temperature or one that anneals to a more stable configuration with similar emission time constant. The carbon interstitial is known to become mobile at room temperature and evidence has been presented that the defect landscape re-orients to produce more divacancies following a 298 K anneal (Gow *et al.*, 2016). Should the same phenomena occur within the devices of this study, one may expect only a small change in CTI since both defects are captured within the measurement time of the parallel EPER tail and so this postulation remains consistent with the observed effects of a 298 K anneal.

Other candidates that could explain the difference include the V_2O complex which has been observed in irradiated devices, however since its energy lies so close to the VV^{--} it has been hard to distinguish the two using in-situ techniques (Pichler, 2004) . It may be present in a higher concentration at cryogenic temperatures, however, the mechanisms behind this are unknown. The B_iO_i should in principle be present within devices, as the concentration of boron is $\approx 10^{15}$ cm^{-3} and the concentration of oxygen is $\approx 10^{18}$ cm^{-3}, once again the physical mechanisms behind the difference between a room temperature and cryogenic irradiation for this defect are unknown. Regardless of the defect responsible, the approximate factor 2 difference implies a density difference between room temperature and cryogenic that is comparable to if not slightly less than that of the VV^-/VV^{--}.

Some supporting evidence for this density difference was provided by trap pumping data of an engineering grade device irradiated under cryogenic conditions that has also experienced a 298 K anneal (this time for 8 days). Trap pumping measurements were taken prior to and following the room temperature anneal at 165 K with a small signal level. The conditions for the

measurement were consistent in each case. Unfortunately, the phase time was not varied during the measurement and so exact identification of the defects was not possible using this measurement alone. Nonetheless, at this phase time we may expect to probe defects in the energy level range of ≈0.23-0.26 eV. Between the two measurements, some defects remain fixed in location whereas others have disappeared following the room temperature anneal and others have formed in previously unoccupied pixels. Figure 8.5 shows a comparison between two frames obtained under the same conditions both prior to and following the room temperature anneal. Approximately 50% of the defects were observed to remain fixed at this temperature and phase time, the remainder annealing at some point during the 8-day 298 K period. Despite these changes, the number density across the array remained relatively constant (a 10% difference, within the scope for error on the measurement). In other words; some defects present at cryogenic temperature have annealed but lead to the formation of other defects with similar energy levels in different physical locations. The constant number density at this phase time is consistent with the minor change in CTI observed through the parallel EPER tail measurement following the room temperature anneal. A full suite of trap pumping measurements where defects are identified at cryogenic temperatures and then following the room temperature anneal will inform the situation further.

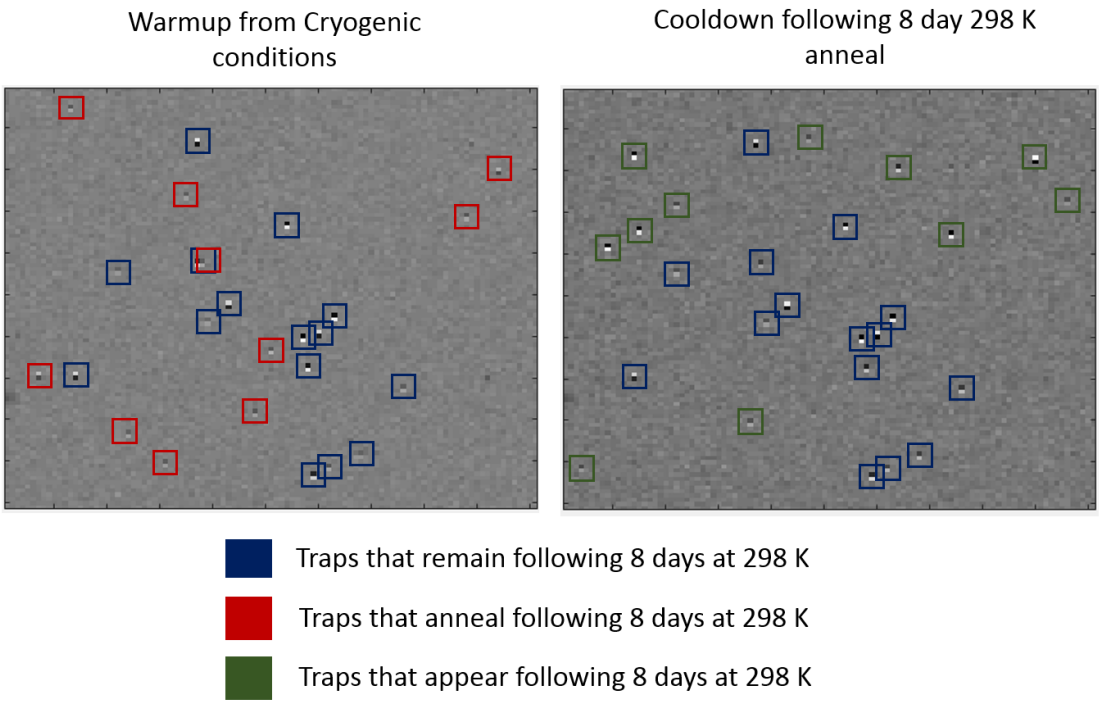

Figure 8.5: *Comparison of trapping sites measured using trap pumping at 165 K using a pumping phase time of order 10^{-4} s. At this regime, we expect to probe defects with an energy level around 0.23 eV below the conduction band. Approximately half of the defects were observed to anneal whereas the other half remained fixed in position.*

8.1.2 Serial EPER

The profile of the serial EPER tail is a consequence of the serial clock rate and total line readout time. The clock rate for this study was 700 kHz, corresponding to approximately 1.5 µs for pixel to pixel transfer, and approximately 0.5 µs for phase to phase transfer for standard 3-phase equal mode clocking. The line readout time was 4.6 ms, as 1040 overscan columns were added to the 2160 physical register pixels of the CCD201 so that the tail profile could be measured. For these operating conditions, the majority of Si-A centres are expected to emit charge that can re-join the original signal packet (Figure 8.1) with a small fraction (≈ 5%) emitting in the first trailing pixel of the EPER measurement. The remainder of the trapping sites remain filled during the successive pixel to pixel transfer time. Throughout the line readout, however, charge captured due to the VV^{--} is expected to emit. The VV^{--} will therefore contribute to charge measured within the tail that extends beyond the first trailing pixel. Charge captured by the VV^{-} and Si-E centre is not expected to contribute to the serial EPER tail since the emission time constants are much longer than the pixel transfer time (estimated at ≈4 s and ≈60 s respectively).

The well-established trend of increasing CTI with fluence was seen for each of the serial EPER measurements for both the room temperature and cryogenic temperature case (

Figure 8.6 and Figure 8.7). The trend was approximately linear, however the result for the 1.0 × 10^9 fluence appears slightly low. The cryogenic case was also seen to be worse than the room temperature case by a factor between ×2 and ×3, depending upon the exact measurement (see summary in Table 8.1 and

Figure 8.6). The serial first trailing pixel CTI was consistently skewed by additional CTI due to the EM register that was found to be present for all devices even prior to the irradiation. Changes to serial voltage or clock timings did not ameliorate this effect, and so it was believed to be related to the phenomenon described in section 4.5.1. The measurements did not follow a clear defined trend for the room temperature irradiation case since the factor change due to bulk damage remained small compared to the pre-irradiation CTI. For the cryogenic case, the increase in CTI was much larger and so the expected linear trend was observed.

Many of the trapping species responsible for the first pixel of deferred charge in the parallel direction are also responsible for the charge emitted in the serial EPER tail. Differences in the concentration of carbon related defects and other possibilities listed in Table 8.2 could also explain the factor difference between the room temperature and cryogenic case. CTI was not observed to change significantly following the room temperature anneal. Table 8.4 summarises the total charge measured in a tail of 600 columns for the cryogenically irradiated device both before and after the anneal. Following one week, an increase in charge within the tail is observed,

however, it falls to the pre-anneal level following another week at room temperature. This fluctuation is unusual, as no other CTI results exhibited this trend. The signal level calibration and device temperature throughout the measurement were checked and found to be consistent with the other measurements. Remembering that some of the defects giving rise to serial CTI also affect parallel CTI, this trend would have been visible in other measurements if it was indicative of defect annealing. The result is therefore believed to be anomalous.

Table 8.4: *Summary of charge within EPER tail for the cryogenically irradiated device both before and after room temperature anneal. Results from a room temperature irradiated device are also included.*

	Total charge within Serial EPER tail (e^-)
Sustained at 165 K (5.25×10^9 p/cm^2)	35.1 ± 0.86
1 week at 298 K (5.25×10^9 p/cm^2)	47.7 ± 1.4
2 weeks at 298 K (5.25×10^9 p/cm^2)	35.6 ± 0.86
Room Temperature Irradiated Device (5.00×10^9 p/cm^2)	11.9 ± 1.1

The serial CTI was seen to be consistently better than the parallel CTI for the operating conditions of this study for the case of both the room temperature and cryogenic irradiations (Table 8.1). This is consistent with the prediction that only the VV^{--} is the significant contributor to the serial EPER CTI, whereas for the parallel CTI both the VV^{-} and VV^{--} are expected to contribute. The faster serial transfer speed also corresponds to a reduced probability of capture for the serial EPER charge packet when compared to the parallel, that in turn may be expected to reduce the magnitude of the tail. This phenomenon is discussed further in Chapter 11.

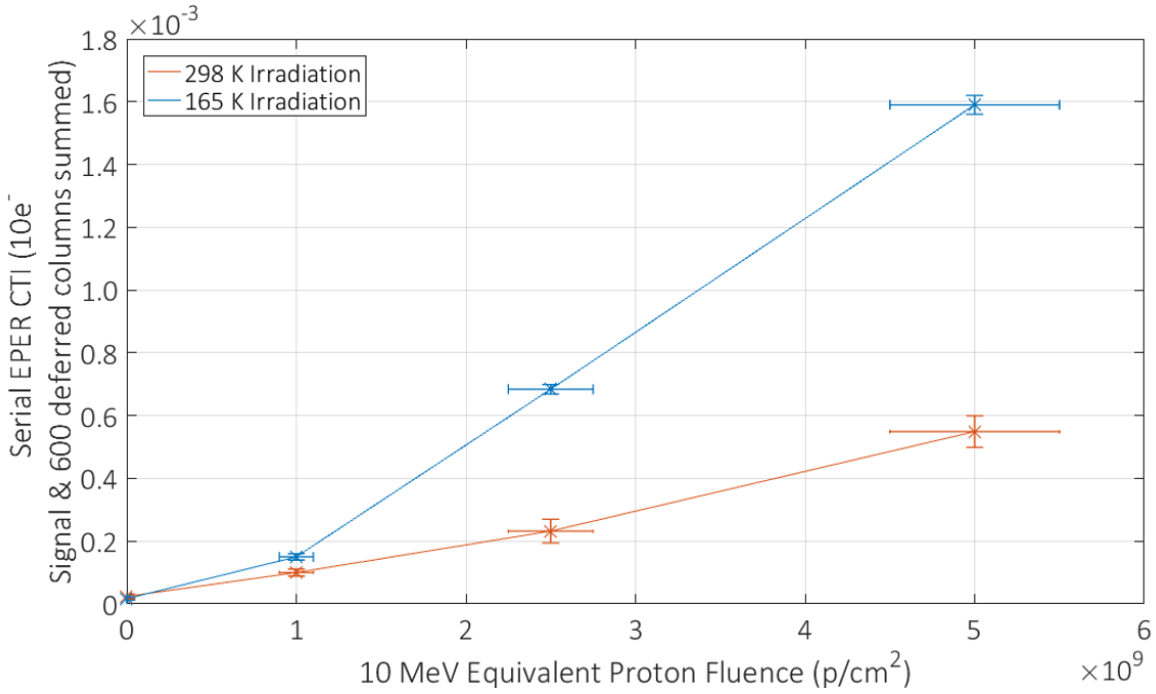

Figure 8.6: *Serial EPER results for devices irradiated at room temperature and under cryogenic conditions.*

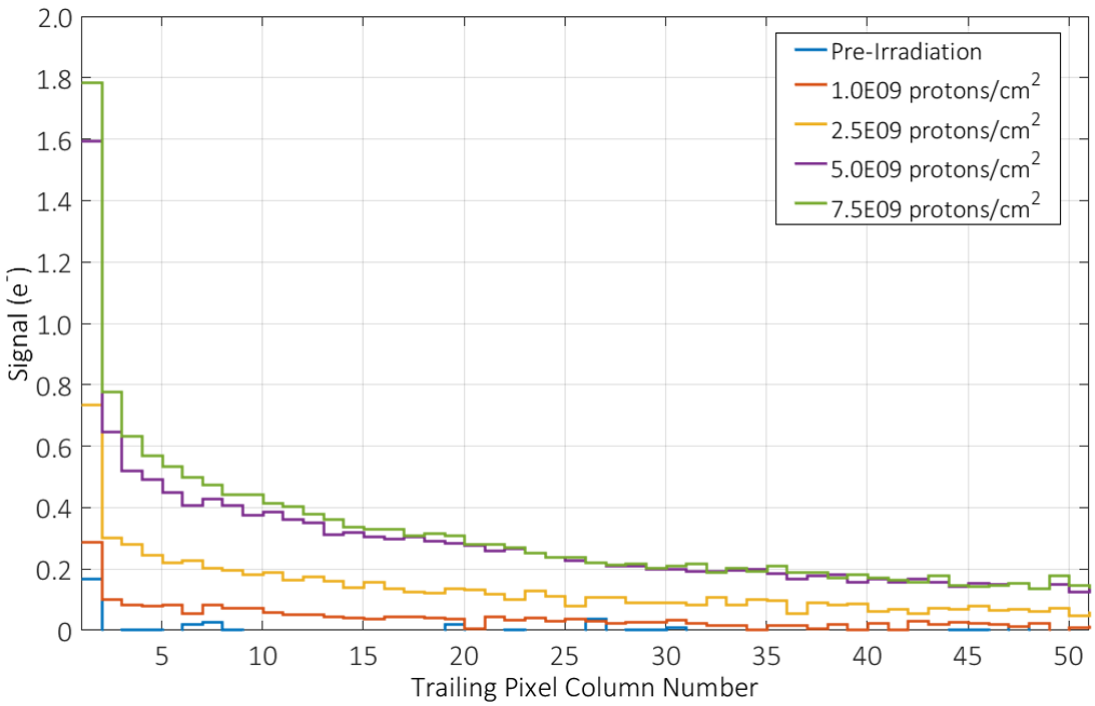

Figure 8.7: *The first 50 columns of the serial EPER tail for each fluence level. Pixel 1 is the first pixel after the flat field (approximately 10 electrons).*

8.2 First Pixel Response (FPR)

Measurement of CTI using First Pixel Response (FPR) probes the charge capture process and encompasses all trapping species relevant to CTI under the standard operating conditions of the measurement. The same parallel clocking scheme was used for the FPR measurement as described for the EPER measurement (see Figure 8.2) and the trapping species responsible for the measurement are similar to that ascribed to EPER with a few differences:

- The Si-A centre is not expected to contribute to the parallel FPR CTI measurement.
- Only charge trapped beneath $\phi 2$ due to the VV^{--} is expected to contribute to CTI.
- The VV^{-} is expected to contribute to the CTI measurement due to traps beneath $\phi 2$ and $\phi 4$.
- Approximately 50% of Si-E centres will contribute to the measurement since a fraction will remain filled between successive frames.

CTI exhibited an approximately linear relationship with proton fluence for both the room temperature and cryogenic irradiated device, as shown by Figure 8.8. The charge lost from the leading row for the cryogenic irradiated device is shown by Figure 8.9. Once again, the cryogenic case was seen to be worse by an approximate factor ×2. The potential explanations for the differences observed for parallel EPER also apply for this measurement, particularly an increase

in the number of defects with emission time constants similar to the VV^{--} at this temperature. An interesting observation is that the factor difference between the room temperature and cryogenic case is approximately the same as that seen for parallel EPER, despite the sensitivity of FPR to traps with longer emission time constants. The measurement process for FPR means that an LED frame of signal is read through the device every 100 s. Traps with an emission time constant longer than 100 s will therefore mostly remain filled throughout successive frames and not contribute to the FPR measurement. These traps are therefore not encompassed in the difference between FPR at the room temperature and cryogenic case. The Si-E centre, however, does contribute, and the consistent factor difference between room temperature and cryogenic for parallel EPER and FPR implies that the concentration of the Si-E centre may be consistent between each case. This is a reasonable expectation as it is well established that the Si-E centre is stable, once formed, up to temperatures of approximately 373 K (Holland, 1993).

Figure 8.9 shows the average value of charge lost from the leading row of the flat field when read through the irradiated device. Since the CGI is observing at low signal levels some columns may perform significantly worse than others in the presence of radiation damage. At such low signal levels, the presence of a single trap that is consistently in the path of the signal could effectively render it useless since the single photo electron could be repeatedly captured and deferred. To investigate this, the charge lost from each column was binned in units of 0.1 e^- and plotted as a histogram for each fluence, as shown by Figure 8.10. It can be seen that the distribution of charge lost is very well modelled by a Gaussian distribution for each case. The standard deviation for each measurement varied from 0.7 to 0.9 e^-. The implication of this result is that the damage is distributed uniformly and randomly across the device, however, some columns contain a higher number of defects than others, giving rise to higher charge loss. The measurement shows that the knowledge of columns with a low density of traps (e.g. through the trap pumping technique) could help improve performance, as the PSF could be steered away from this area (within limits) into a region of better cosmetic quality.

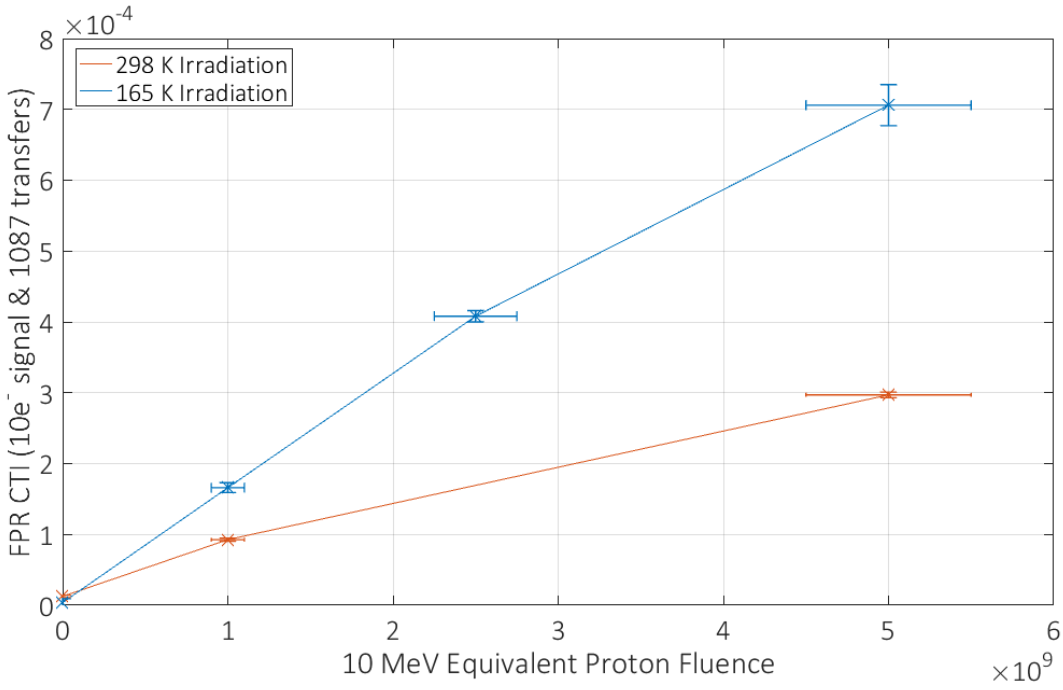

Figure 8.8: *CTI as measured using the FPR technique as a function of proton fluence for both the room temperature and cryogenic irradiations.*

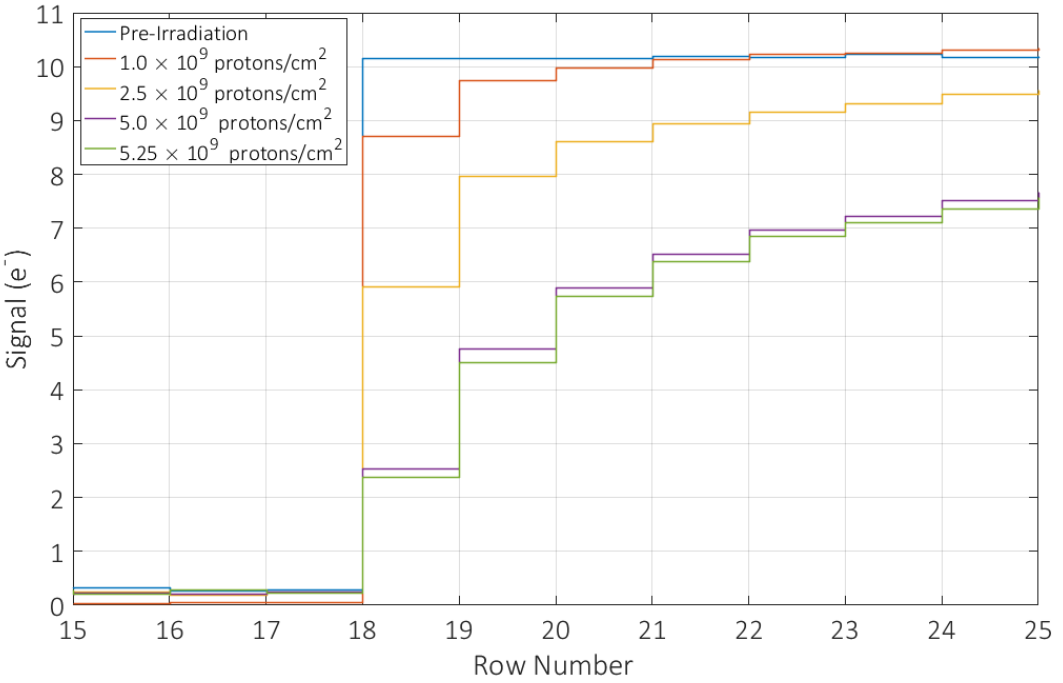

Figure 8.9: *The leading edge of the flat field illumination used to make the FPR measurement. The charge lost from row 18 was used to calculate the CTI. An increase in charge loss as a function of proton fluence was observed, as expected.*

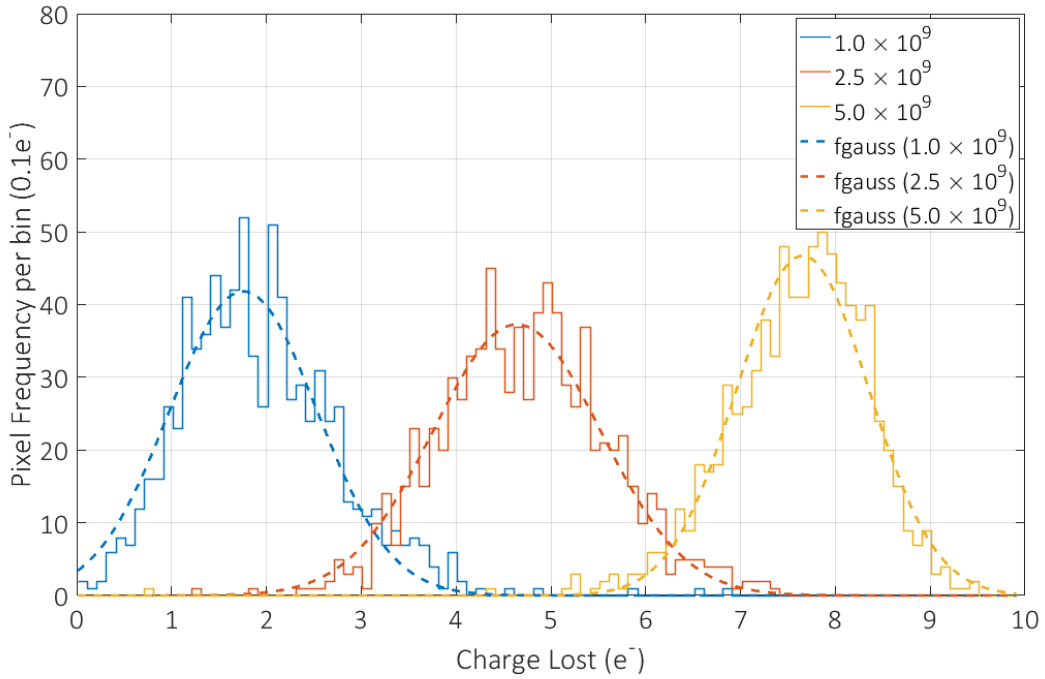

Figure 8.10: *Charge lost from the leading FPR row binned as a histogram for each fluence. The charge lost per column exhibits high variance for each fluence.*

8.3 Fe^{55} CTI

Measurement of CTI using Fe^{55} is similar to FPR in that it probes the charge capture process. Since the signal can be confined to a single pixel, the trailing pixels in the parallel and serial direction can also be used to probe immediate charge emission. The trap species shown by Figure 8.1 are expected to contribute to the measurement as follows:

- The Si-A centre is not expected to contribute to the parallel Fe^{55} CTI measurement. The majority of Si-A centres will not contribute to serial CTI however a small fraction will emit charge within the first trailing serial pixel.
- The VV^{--} is expected to contribute to the parallel Fe^{55} CTI measurement. Only charge trapped beneath $\phi 2$ due to the VV^{--} will contribute to CTI. The majority of the charge will be emitted in the first trailing parallel pixel. The VV^{--} will contribute to the serial Fe^{55} CTI measurement
- The VV^{-} is expected to contribute to the CTI measurement for both parallel and serial CTI.
- The Si-E centre will contribute to the measurement since a fraction remain filled, dependant on the average time taken for an X-ray to pass through a pixel (not necessarily equal to the frame integration time).

Figure 8.11 shows an example measurement for a device irradiated at room temperature to 5.0×10^9 protons/cm^2. The background of the plot shows the single X-ray events selected for analysis in grey. These events are selected by first imposing a signal threshold appropriate to the

calibration of the system and locating a candidate event. The pixels surrounding the candidate event are then checked to see if they contain any significant amount of signal charge (typically using a 5σ threshold). If charge is contained with the surrounding pixels, then the event is considered a "split", meaning charge from the packet is contained within 2 or more pixels. If no charge is found, the event is considered a "single" and deemed suitable for analysis. Figure 8.11 shows how there is a clear trend of decreasing signal with row number as charge is lost to trapping sites. The 'x' markers show the peak locations of gaussian fits to these events within specified row bins (typically 100 pixels in width). The error bar is the standard deviation of the fitted gaussian. A straight line is fitted to these points from which the CTI is calculated.

The linear CTI relation was once again observed as a function of fluence and the cryogenic case was once again observed to be worse than the room temperature case, as shown by Figure 8.12 and Figure 8.13. The factor difference is larger than observed for FPR, a factor of ×3 for parallel CTI and a factor of ×5 for serial CTI (summarised in Table 8.1).

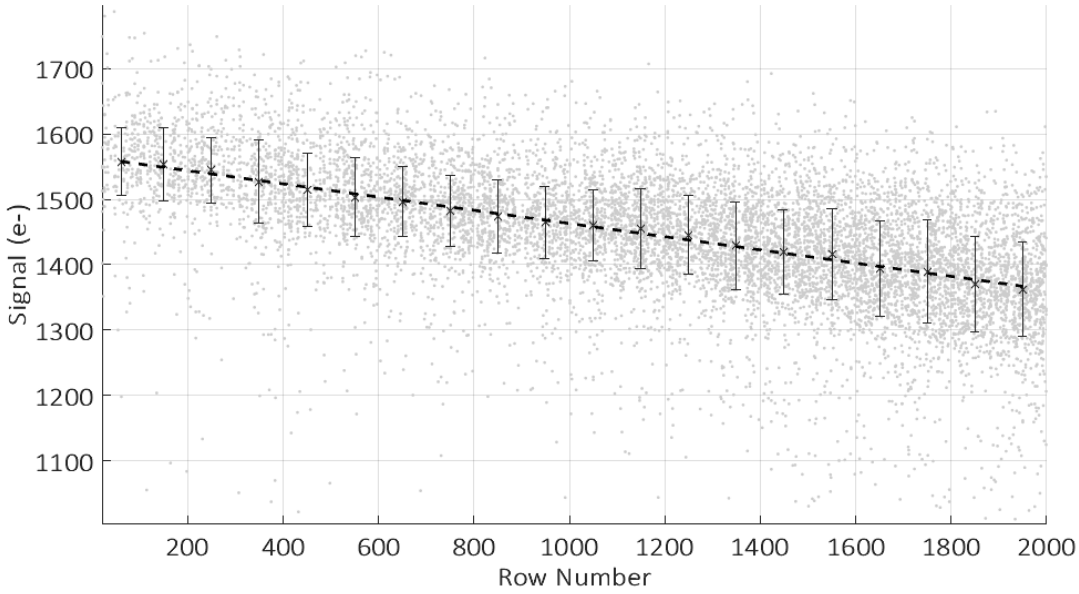

Figure 8.11*: Example CTI plot for a device irradiated at room temperature to 5.0 × 10^9 protons/cm^2. The grey background points are single events identified during processing. The 'x' markers show the peak locations of gaussian fits to these events within specified row bins (typically 100 pixels in width). The error bar is the standard deviation of the fitted gaussian. A straight line is fitted to these points from which the CTI is calculated.*

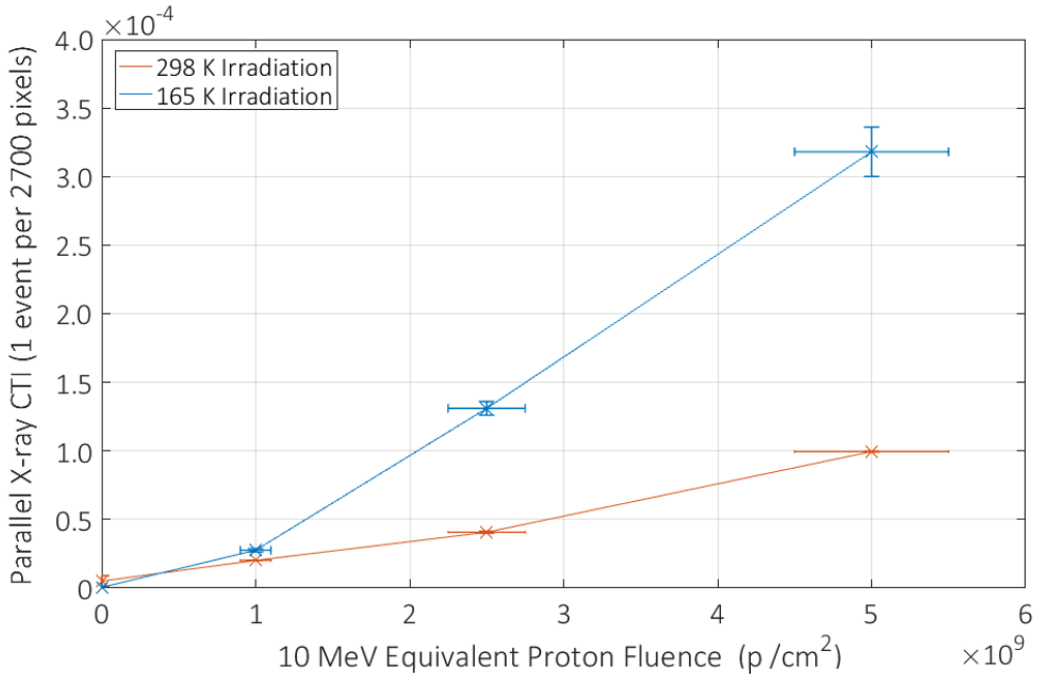

Figure 8.12: *Parallel X-ray CTI results for devices irradiated at room temperature and under cryogenic conditions.*

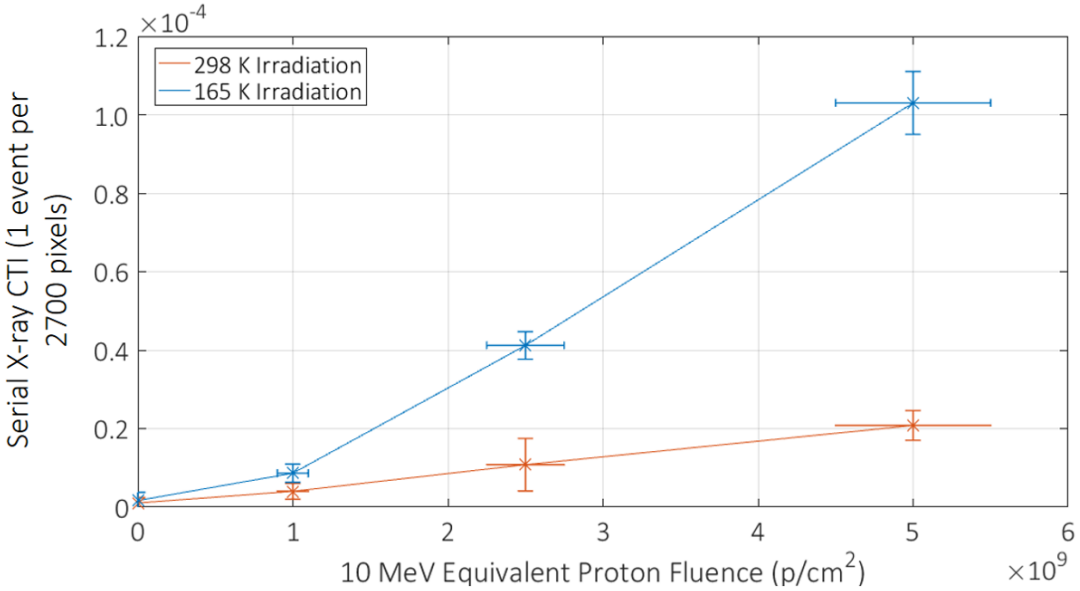

Figure 8.13: *Serial X-ray CTI results for devices irradiated at room temperature and under cryogenic conditions.*

Both FPR and X-ray CTI probe charge capture and so one might expect the differences between the room temperature and cryogenic case to be equal. In truth, the exact reason is not known, however, differences in the measurement technique may have contributed to this observation. To begin, the X-ray density for measurements was approximately 1 event per 2700 pixels (with an approximate 10% uncertainty). This density was observed over a 100 s integration time and

the distribution was random yet isotropic. A Monte Carlo simulation highlighted that the predicted time taken for a row to have an X-ray transferred through it increases exponentially as you move further from the output node (shown by Figure 8.14). Taking the limit of the furthest row from the serial register, an X-ray must interact within the pixel for the trap to become filled, since now no rows are above it to pass charge into it. The average time for a pixel to experience an X-ray under these conditions was found to be approximately 1100 s, however, this value was skewed heavily by the exponential nature of the distribution. The median value is more suitable and was found to be 200 s for the array. The key point here is that the time taken for a pixel to have charge pass through and fill a proportion of traps is longer than the nominal frame-integration time of 100 s. This calculation ignores split events; however, it should be noted that the charge packet size for a split event (a few hundred electrons) is smaller than the full packet size by an approximate factor of 2 (discussed in Chapter 11) and so a fraction of the total trapping sites remains unfilled when a single event (used in analysis) is transferred through.

The FPR method makes use of an LED flash every 100 s, and so all traps within the frame store region will experience a signal packet and have the opportunity to become filled within each frame. For the conditions of this study, the X-ray CTI technique is therefore more susceptible to traps that have an emission time constant longer than the frame integration time of 100 s. If more of these defects are created at cryogenic temperatures, it would explain the discrepancy in the factor difference between the two measurements. The implication is that the cryogenic irradiation may have resulted in a larger population of defects with τ_e > 100 s than the room temperature case.

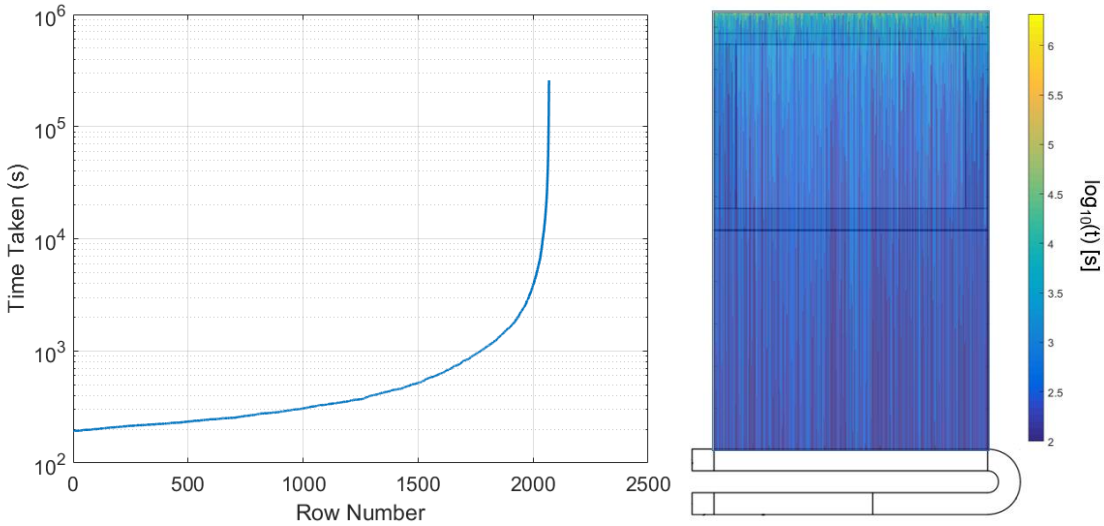

Figure 8.14: *Monte Carlo simulation of the average time taken for a pixel to have an X-Ray transferred through it. The relevant operating conditions for the study were used as an input, namely an X-ray density of 1 event per 2700 pixels and an integration time of 100 s.*

To provide more information on the dominant trap species that affected CTI for this measurement, the "average" X-ray event was calculated following each cryogenic irradiation by summing all of the events selected for analysis, including the surrounding pixels. The result is illustrated by Figure 8.15, where the parallel and serial deferred charge tails can be seen to increase in intensity and length as a function of fluence. Summing the charge in all of the deferred pixels for a given fluence (Table 8.5) shows that the majority of the lost charge is not emitted in the first few trailing pixels, indicating that slow traps such as the VV^- and Si-E dominate the measurement.

Following a room temperature anneal, the CTI was not seen to change significantly for either the parallel or serial measurement. The results are summarised by Table 8.6. Since slower traps dominate the measurement, the conclusion is that the number density of these species has not changed significantly following a room temperature anneal.

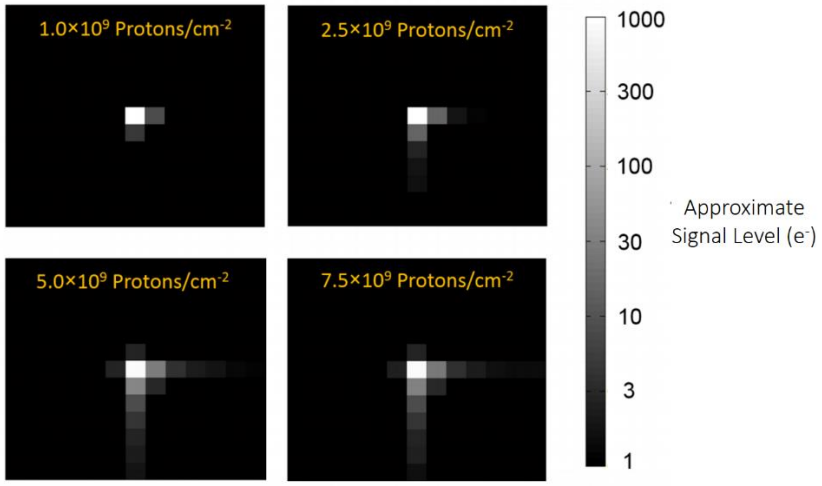

Figure 8.15: *Illustration of the "average" X-ray event from all events chosen for CTI analysis with logarithmic colour scale. The deferred charge tails can be seen in both the parallel and serial direction.*

Table 8.5: *Summary of charge distribution from 'average' X-ray event from the cryogenic 5.0×10⁹ protons/cm² fluence. Summing the deferred charge in the parallel and serial tails shows not all of the captured charge is emitted in the first trailing pixels. The majority is lost to "slow" traps, thought to be the VV^- and Si-E.*

Original Charge Packet	1616 e^-
Measured Charge at Output (average)	817 e^-
Charge in parallel tail (6 pixels)	54 e^-
Charge in serial tail (6 pixels)	39 e^-
Not emitted in first 6 pixels	706 e^-

Table 8.6: *Summary of X-ray CTI results prior to and following a room temperature anneal. The results from a room temperature irradiated device are also included for comparison.*

	Parallel X-ray CTI	Serial X-ray CTI
Sustained at 165 K (5.25×10^9 p/cm^2)	$(3.46 \pm 0.23) \times 10^{-4}$	$(9.65 \pm 0.82) \times 10^{-5}$
1 week at 298 K (5.25×10^9 p/cm^2)	$(3.77 \pm 0.24) \times 10^{-4}$	$(8.57 \pm 0.68) \times 10^{-5}$
2 week at 298 K (5.25×10^9 p/cm^2)	$(3.77 \pm 0.23) \times 10^{-4}$	$(8.50 \pm 0.64) \times 10^{-4}$
Room Temperature Irradiated Device (5.00×10^9 p/cm^2)	$(9.95 \pm 0.04) \times 10^{-5}$	$(2.08 \pm 0.38) \times 10^{-5}$

8.4 Conclusions from CTI measurements and impact on the CGI

CTI measurements from both the room temperature and cryogenically irradiated devices have revealed a significant disparity in the landscape of silicon defects present following each irradiation. While CTI was observed to increase linearly in each case, the cryogenically irradiated device exhibited significantly worse degradation that ranged between a factor of ×2 and ×4 depending on the measurement. Many hypotheses have been provided for the difference in CTI, with evidence that some defects were present following a cryogenic irradiation that were not necessarily present following a room temperature irradiation. Surprisingly, however, CTI measured following a room temperature anneal was found to be consistent with the cryogenic case, despite evidence that the defect landscape had changed following the anneal. From this observation, it was concluded that either:

1. A defect(s) was present within cryogenically irradiated devices that is not present following room temperature irradiation. This defect(s) act to significantly increase CTI for the operating conditions of this study.
2. The defect landscape between room temperature and cryogenically irradiated devices is similar, however irradiation under cryogenic conditions gives rise to *more* of one or more defect species, thus increasing CTI.

The observation that EPER, FPR and X-ray CTI measurements exhibit higher degradation following cryogenic irradiation highlights that if the first hypothesis is correct, more than one additional defect species is responsible. This is rooted in the fact that EPER probed defects with $\tau_e < 4$ s where X-ray CTI probed defects with $\tau_e < 200$ s. There is no clear way to eliminate either hypothesis without additional information from in-situ trap parameter studies through trap pumping.

With respect to the WFIRST CGI, CTI is likely to be the primary concern with respect to degradation due to radiation damage. An order of magnitude degradation is observed even for the lowest fluence levels which will equate to a longer integration time per planet in order to reach an adequate S/N ratio. FPR is the most representative measurement for the CGI since it probes all relevant defects that may capture charge following a 100 s cadence. At the lowest fluence level, approximately 1.2 e^- was lost from the leading edge of a 10 e^- following 1087 parallel transfers. How this result directly translates to the CGI is dependent on the volume difference between a 10 e^- and 1 e^- packet. This result is calculated in Chapter 11, and is at best 50 % smaller and at worst 20 %. Radiation damage therefore has the potential to seriously limit the signal throughput of the device.

CTI mitigation is therefore a priority to maximise the science performance of the CGI. These measurements have highlighted many possible mitigation strategies. Changes in temperature and clocking speed that are appropriate to the trapping species responsible for the majority of charge loss. For the parallel section, the VV^{--} is responsible for immediate charge trailing and a large fraction of the Si-E centre population is expected to emit within successive frames. The recommendation is that the integration time is reduced so as to keep a larger proportion of Si-E centres filled and the parallel clocking frequency is altered so as to allow the majority of charge captured by the VV^{--} to emit into the original charge packet. Mitigation of trap species using these methods will rely on in-depth characterisation of the defect landscape so that clocking schemes can be properly optimised.

An interesting conclusion from results presented within this chapter is that the instrument detectors may benefit from being stored at room temperature while not in use. The CGI is expected to have approximately 1 year of observation time within the nominal 6 year mission duration and this is unlikely to be a single continuous segment. While not in use, the detectors could be stored unbiased at ambient temperature which in principle could result in a significant reduction in CTI degradation due to radiation damage. This conclusion remains tentative however, since much more information is required to explain fully the differences between a cryogenic and room temperature irradiation. Nonetheless, this is a promising result for instruments such as the CGI that do not have the luxury of 100% telescope observation time while still having to compete with the demands presented by operation in a radiation environment.

The increase in CTI is only one of the effects of radiation damage that will impact CGI performance. With CTI analysis complete, discussion turns to the dark signal results from the irradiation campaign and the impact on science performance compared to the CTI results presented in this chapter.

9 The impact of dark signal on CGI performance

Dark signal will accumulate within successive frames in the WFIRST CGI imager and IFS that may act to generate "false positive" events in photon counting mode. In analogue mode, the dark signal adds additional shot noise to the expected spectra and planet PSF in each camera system. Displacement damage can also give rise to hot pixels that act as significant dark signal generation sites, sometimes in excess of 1 e^-/pix/s. These sites not only impact the primary pixel but can create tails of charge in both parallel and serial directions due to CTI. Clock Induced Charge (CIC) is included under the generic description of "dark signal" within this section since it is not an optically generated photon source, however, there remains a clear distinction; while dark signal is integration time dependant, CIC is only added once per frame. Prior to this study, the impact of radiation on CIC was thought to be unknown and so it required investigation to understand the full impact on CGI detector noise throughout the mission. This chapter discusses the results from dark signal testing on the CCD201-20 prior to and following irradiation unbiased at room temperature and biased at the nominal operating temperature of the mission. Additional performance measurements are included that describe the complex physical mechanisms behind CIC generation and how it can be minimised through clock optimisation. The chapter concludes with a discussion of the potential impact of each noise source on CGI science performance alongside mitigation strategies.

9.1 Thermal dark signal

9.1.1 Pre-irradiation measurements

The pre-irradiation dark signal was seen to exhibit a small degree of variance across devices measured throughout the study (Table 9.1). At 165 K in IMO, the values were constrained between 10^{-5}-10^{-4} e^-/pix/s. The mode value was observed as approximately 3.0×10^{-5} e^-/pix/s at 165 K in IMO. A consistent difference was noted for dark signal measured in the store section of the device as opposed to the image section (summarised in Table 9.2). Since the image area is photo-sensitive, an obvious explanation was that some stray light was impacting the result, however, additional measurements showed a temperature dependence of the difference that eliminated this as a possibility. Both the image and the store section are back-thinned and so have back-surface traps that contribute an additional component to the total dark signal. The contribution is a diffusion component since any generated dark signal must thermally diffuse towards the depletion region before it recombines to be collected as signal. The shorter the diffusion path and higher the temperature, the higher the collected signal. Since the image section is thinner than the store section (12 µm compared to 20 µm respectively), this is a possible

reason for the observed difference. Supporting evidence includes the observed temperature dependence and the lack of a dependence on radiation dose. An alternate hypothesis was that the deposited aluminium was providing an additional degree of passivation to the back-surface traps, however, this was concluded to be unlikely since the aluminium coated pixels surrounding the image area exhibited higher dark signal than those in the store; leaving the silicon thickness as the only remaining free variable.

For all cases, the pre-irradiation dark signal is lower than the CGI requirement of 1×10^{-4} e^-/pix/s (Harding *et al.*, 2016). The conclusion is that device-device variation in dark signal does not represent a significant risk for the CGI not meeting the dark signal requirement at BOL.

Table 9.1: *Summary of pre-irradiation dark signal measurements from a selection of CCD201-20 devices used in the WFIRST radiation campaigns. Each measurement was taken at 165 K in IMO. Measurements where the effect of hot pixels are excluded are also presented to illustrate the variation was not due to a few hot pixels skewing the mean value.*

Device serial number	Notes	Pre-irradiation dark signal (hot pixels included)	Pre-Irradiation dark signal (hot pixels excluded)
14222-11-02	Engineering grade trap at FWC	$(3.11\pm0.43)\times10^{-5}$	$(3.35\pm0.44)\times10^{-5}$
10091-16-09	Engineering grade high dark signal	$(7.13\pm0.49)\times10^{-5}$	$(7.25\pm0.49)\times10^{-5}$
11153-13-14	Engineering grade hot pixels	$(3.20\pm0.50)\times10^{-5}$	$(3.25\pm0.78)\times10^{-5}$
12231-13-14	Science Grade	$(4.89\pm0.42)\times10^{-5}$	$(3.62\pm0.32)\times10^{-5}$
14222-11-6	Engineering grade trap at FWC	$(5.63\pm0.47)\times10^{-5}$	$(5.87\pm0.49)\times10^{-5}$

Table 9.2: *Pre-irradiation dark signal measured in the image and store sections of the device. Higher dark signal was measured in the image section for each device studied. The difference was also observed to have temperature dependance.*

Device serial number	Notes	Pre-irradiation dark signal image section (hot pixels included) (e^-/pix/s)	Pre-irradiation dark signal store section (hot pixels included) (e^-/pix/s)
14222-11-02	Engineering grade Trap at FWC	$(3.11\pm0.43)\times10^{-5}$	$(1.50\pm0.36)\times10^{-5}$
12231-13-14	Science Grade	$(4.89\pm0.42)\times10^{-5}$	$(1.45\pm0.14)\times10^{-5}$
14222-11-6	Engineering grade Trap at FWC	$(5.63\pm0.47)\times10^{-5}$	$(1.17\pm0.28)\times10^{-5}$

9.1.2 Post-irradiation measurements

The well-established trend of a linear increase in thermal dark signal with proton fluence was observed throughout the study (Table 9.3, Figure 9.1). The devices were operated in IMO throughout the campaign and so the observed increase must be due to radiation induced bulk traps. A higher increase in dark signal as a function of fluence was observed for the cryogenic case; an approximate factor of ×6-×8 difference depending on whether hot pixels are included in the measurement (Table 9.3, Figure 9.1). Following a room temperature anneal, the dark signal of the cryogenically irradiated device was observed to return to levels expected from a room temperature irradiation (Figure 9.1).

The implication is that a trap species was present at cryogenic temperatures that has annealed at room temperature to form another species that contributes significantly less to the bulk dark current but can still contribute to CTI. Through SRH statistics, it can be shown that the closer a defect energy level is to midband, the greater the contribution to the bulk dark current. In the previous section, evidence was presented for carbon complexes that were present during the cryogenic stage of the campaign but annealed to divacancy sites following a room temperature anneal. The concentration of carbon complexes was estimated to be approximately equal to Divacancies through trap pumping analysis performed at 165 K at a constant phase time. The same argument can be present to explain the change in dark current; some carbon complexes are closer to midband and so would contribute a greater amount to the bulk dark current than the VV^{--} despite being approximately equal in concentration while the device is maintained at cryogenic temperatures. Following a room temperature anneal, a fall in carbon complexes and rise in VV^{-} would explain a reduction in dark current while keeping CTI constant. It seems unlikely, however, that this species alone is responsible for the entire difference in measured dark current values. The Si-E centre, for example is much closer to midband and known to be present in a higher concentration than both the VV and C_i for room temperature irradiated devices. Raising the device to room temperature is unlikely to cause a significant change in the population of Si-E centres, since this site has a known annealing temperature of around 373 K (Holland, 1993). The implication is that there is another species contributing to the dark current with as yet unknown origin that can anneal within the temperature range of 165 K to 298 K.

Table 9.3: *Summary of pre- and -post irradiation measurements of thermal dark signal for the CCD201s used in this study. Irradiation under cryogenic conditions gave rise to a substantially increased dark signal, even with hot pixels excluded from the measurement.*

10 MeV equivalent cumulative proton fluence (p/cm^2)	Conditions of irradiation	Thermal dark signal (including hot pixels) (e$^-$/pix/s)	Thermal dark signal (excluding hot pixels) (e$^-$/pix/s)
Pre-Irradiation	Irradiated at 165 K	$(4.89\pm0.42)\times10^{-5}$	$(3.62\pm0.32)\times10^{-5}$
	Irradiated at 298 K	$(3.20\pm0.50)\times10^{-5}$	$(3.25\pm0.78)\times10^{-5}$
1.0×10^9	Irradiated at 165 K	$(2.01\pm0.13)\times10^{-4}$	$(1.41\pm0.05)\times10^{-4}$
	Irradiated at 298 K	$(4.11\pm0.42)\times10^{-5}$	$(3.88\pm0.52)\times10^{-5}$
2.5×10^9	Irradiated at 165 K	$(5.01\pm0.48)\times10^{-4}$	$(3.10\pm0.20)\times10^{-4}$
	Irradiated at 298 K	$(5.75\pm0.44)\times10^{-5}$	$(4.37\pm0.71)\times10^{-5}$
5.0×10^9	Irradiated at 165 K	$(8.06\pm0.52)\times10^{-4}$	$(5.80\pm0.43)\times10^{-4}$
	Irradiated at 298 K	$(1.04\pm0.10)\times10^{-4}$	$(8.82\pm0.10)\times10^{-5}$
5.25×10^9	Irradiated at 165 K & 2 week 298 K anneal	$(9.39\pm0.81)\times10^{-5}$	$(6.60\pm0.81)\times10^{-5}$

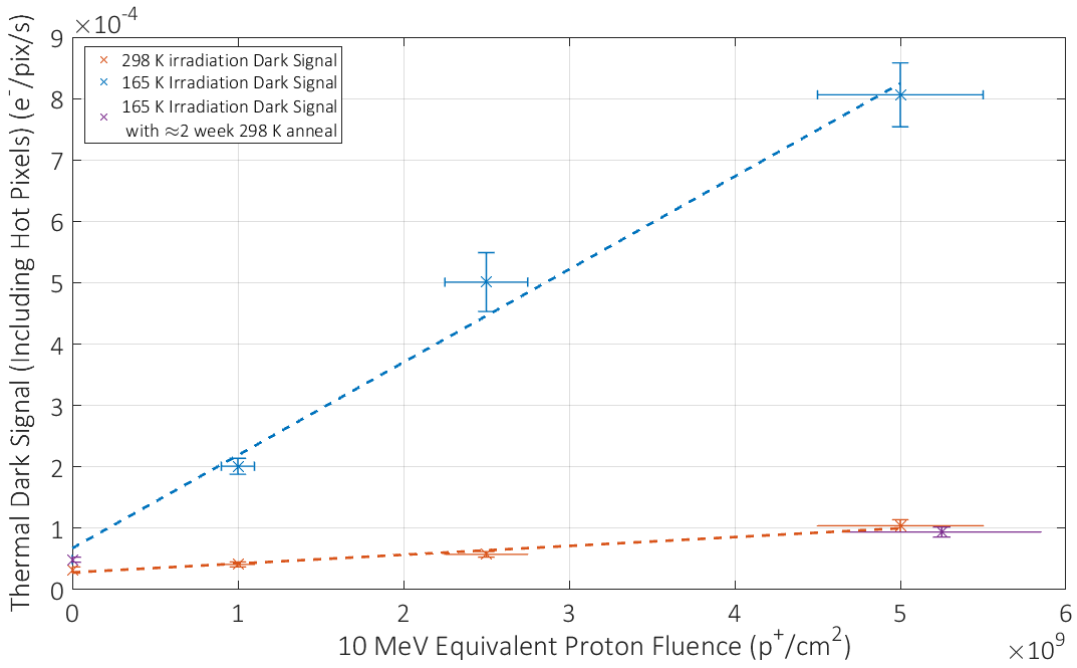

Figure 9.1: *Summary of thermal dark signal results pre- and post-irradiation for devices irradiated at room temperature and under cryogenic conditions. A consistent factor ×8 difference was observed across the fluence range for this study. Following a room temperature anneal, dark signal reduced to a level one may expect from the comparative room temperature irradiation.*

9.1.3 Hot pixels

The total number of hot pixels was observed to increase as a function of the irradiation fluence in the same manner as the mean dark current described within the previous section. The distribution of signal generation showed that most of the hot pixels had a generation rate of 0.05 e^-/pix/s or lower, some however, had a substantially higher generation rate (> 10 e^-/pix/s) and also suffered significant smearing due to CTI within the image section and serial register. Following a room temperature anneal, both the total number and mean generation rate of the dark signal fell substantially (Figure 9.2).

The exact explanation for this behaviour is currently unclear. Hot pixels are believed to be midband state traps or clusters of defects that have a dark signal generation rate significantly enhanced by barrier lowering effects due to the local electric field (Sirianni *et al.*, 2006). Defects that are closest to the midband exhibit the highest generation rate, and so the electric field is assumed to act in such a way as to bring the energy level closer to mid-band in each case. The findings from this investigation imply that hot pixels created under cryogenic temperatures in general exhibit an energy close to mid-band, since the generation rate is much higher than that seen following the room temperature anneal period. The reduction in the mean generation rate, and indeed reduction in number of hot pixels in general, implies that some of the defects are thermally stable at cryogenic temperatures but re-orient into a more stable configuration following a room temperature anneal. With respect to WFIRST, most of these defects act to degrade science performance as they have a distinct possibility of generating a signal spike within the nominal 100 s integration time. The significant reduction following a room temperature anneal suggests this is a viable solution to control the hot pixel population on orbit since there, at present, appears to be no degradation in CTI but significant reductions in dark current and the number of hot pixels.

It is worth commenting on the difference in the total number of hot pixels identified from devices irradiated at room temperature using 74 MeV protons and the device irradiated cryogenically using 5 MeV protons. The high-energy protons appear to give rise to a similar number of hot pixels with a generation rate above 0.05 e^-/pix/s (Figure 9.3) when compared to the cryogenic case. This difference is believed to be due to the difference in maximum possible energy that a primary knock-on atom can have between the two beam energies, with the higher energy protons having a greater probability of forming defect clusters within a pixel.

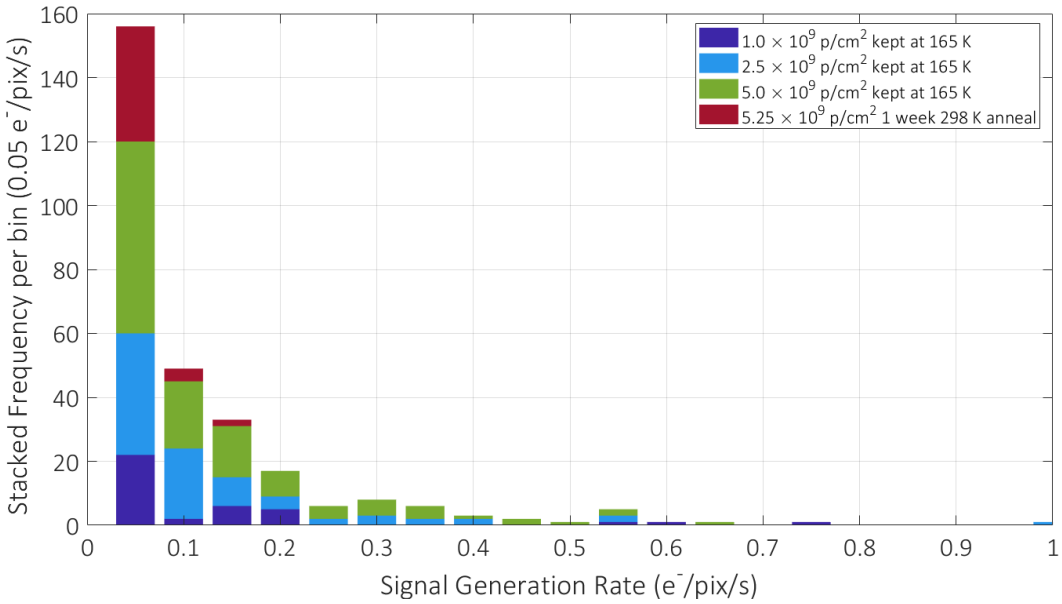

Figure 9.2: *Hot pixels measured on a science grade device 12231-13-14 throughout the cryogenic irradiation campaign. The defects were binned according to the estimated generation rate (assumed linear in time). Some defects with a substantially higher generation rate (> 10 e⁻/pix/s) were also identified but are not shown here. Following a room temperature anneal, both the total number of defects and the mean generation rate fall substantially.*

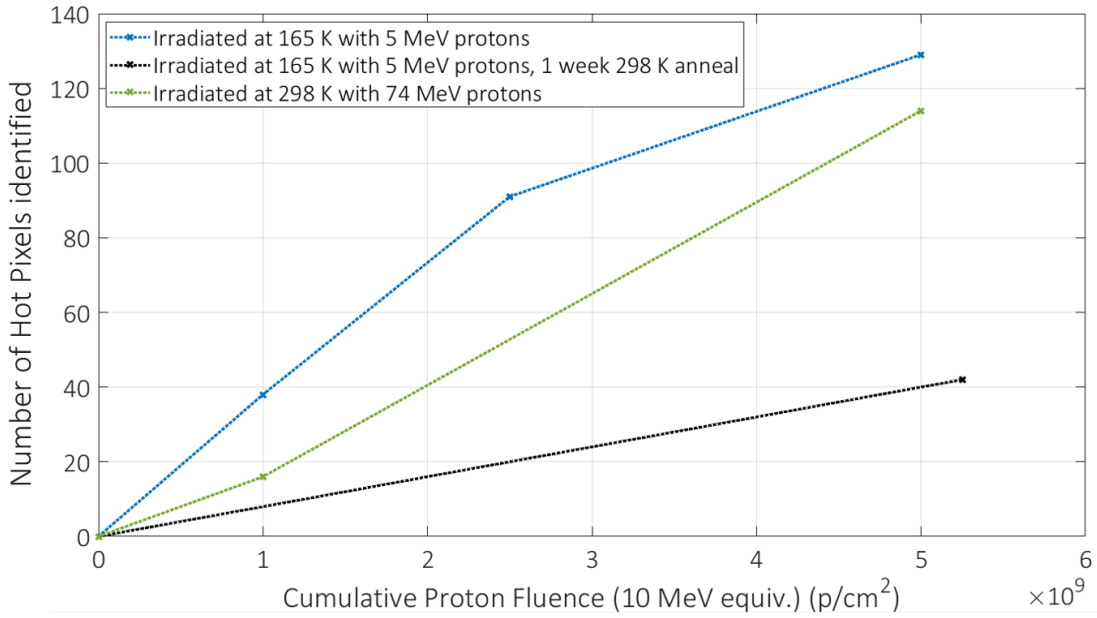

Figure 9.3: *Total number of hot pixels identified for cryogenic and room temperature irradiated devices using a threshold of 0.05 e⁻/pix/s. An interesting observation is that the room temperature irradiated devices that used a higher energy primary proton beam produced a number of hot pixels that was comparable in number to the cryogenic irradiation case.*

9.2 Parallel Clock Induced Charge (CIC)

Clock Induced Charge (CIC) is one of the primary concerns with respect to noise performance for an EM-CCD based instrument such as the WFIRST CGI since any spuriously generated electrons are indistinguishable from a signal electron within a photon counted image. Parallel CIC was measured on a variety of devices throughout the testing campaign and as a function of various parameters in order to conclude whether it posed a significant risk to science performance following irradiation and to determine how a device can be appropriately optimised to reduce CIC throughout the mission lifetime.

9.2.1 Simulation of CIC generation

To better understand the CIC generation process, a CCD201-20 image pixel moving from the inverted to the non-inverted state was simulated with the goal of confirming the key CIC generation sites. Figure 9.4 shows a cross section of the pixel mid-way through clocking. The highest electric field is present at the dielectric interface, reaching 10^7 Vm^{-1} towards the centre of the pixel. Electric fields in excess of 10^7 Vm^{-1} are sufficient to accelerate holes to the saturation velocity (≈ 9 ×10^6 cms^{-1} in Si) where they have kinetic energy in excess of the impact ionisation threshold (5.0 eV for holes). The regions of highest electric field correlate with the regions of highest recorded impact ionisation as one may expect. CIC is known to be exponentially dependant on clock amplitude since this directly results in an increase in the electric field at the interface and hence the population of holes with energy in excess of the ionisation threshold.

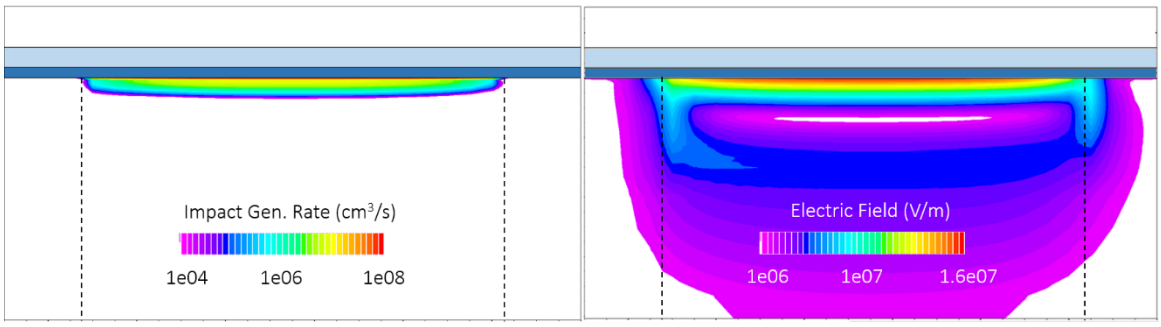

Figure 9.4: *Cut from a 3D TCAD simulation of a CCD201 image pixel moving from the inverted to non-inverted state. The high electric fields present at the dielectric interface correlate with the regions of high impact ionisation.*

9.2.2 Device-device variation

While only a small degree of variation in thermal dark signal was noted, pre-irradiation CIC measurements highlighted a significant variation across devices from different batches operated under the same conditions. Table 9.4 summarises the results from the devices used in this study, where there is up to a factor ×5 variation. The CIC was also seen to vary as a function of column number. Figure 9.5 shows a cut of the column profile of CIC measured from 3 devices prior to irradiation. Each device shows a similar trend of increasing CIC towards the centre of the device. This trend may be linked to the propagation of the clock edge from each side of the chip (the CCD201 is dual side driven) to the centre, or due to a manufacturing effect whereby the centre of the chip exhibits more interface states due to uneven passivation.

The difference in magnitude is possibly due to batch to batch variation within the devices giving rise to a difference in either interface state density or pinning voltage. A difference in the pinning voltage due to batch to batch variation could give rise to the same effect seen here, as the default substrate operating voltage of V_{SS} = 4.5 V (e2v Technologies, 2015) is unlikely to be optimal for each device. In the pinning regime, the voltage at the interface becomes "pinned" to the substrate voltage so long as it is above the potential at the interface when the clock phase is low. The typical range for pinning voltage is between 7 and 9 V for an e2v device (e2v Technologies, 2015) and so for the operating conditions of this study, the effective voltage applied to the substrate for an image low level of -5.0 V was 9.5 V, well above the typical pinning requirement. Once above the pinning threshold, raising V_{SS} increases the hole concentration further still so as to maintain the equality between interface potential and substrate voltage. This was confirmed through 3D TCAD simulation of a CCD201-20 image pixel within the pinning regime (shown by Figure 9.6). The higher population of holes at the interface is likely linked to higher CIC. Thus, optimum operation of a device for low CIC and low dark current will occur when the substrate voltage is approximately equal to the pinning voltage. For operation within a radiation environment in the presence of ionising damage, V_{ss} should perhaps be raised a small amount above the pinning voltage so that any possible flat-band voltage shift does not push the device out of the pinning regime. These results therefore show that V_{ss} should be appropriately optimised for flight devices to ensure the device operates in IMO while minimising CIC as much as possible.

Table 9.4: *Summary of parallel CIC measured in IMO at standard datasheet voltages at 165 K for all devices used in the WFIRST radiation damage study. An approximate factor of ×5 variation was observed across these devices.*

Device Serial Number	Notes	Pre-Irradiation Parallel CIC 12 V swing measured in IMO (e^-/pix/frame)
14222-11-02	Engineering grade Trap at FWC	$(3.65\pm0.04) \times 10^{-2}$
10091-16-09	Engineering grade high dark signal	$(4.47\pm0.24) \times 10^{-2}$
11153-13-14	Engineering grade hot pixels	$(8.80\pm0.38) \times 10^{-3}$
12231-13-14	Science Grade	$(4.38\pm0.15) \times 10^{-2}$
14222-11-6	Engineering grade Trap at FWC	$(2.42\pm0.14) \times 10^{-2}$

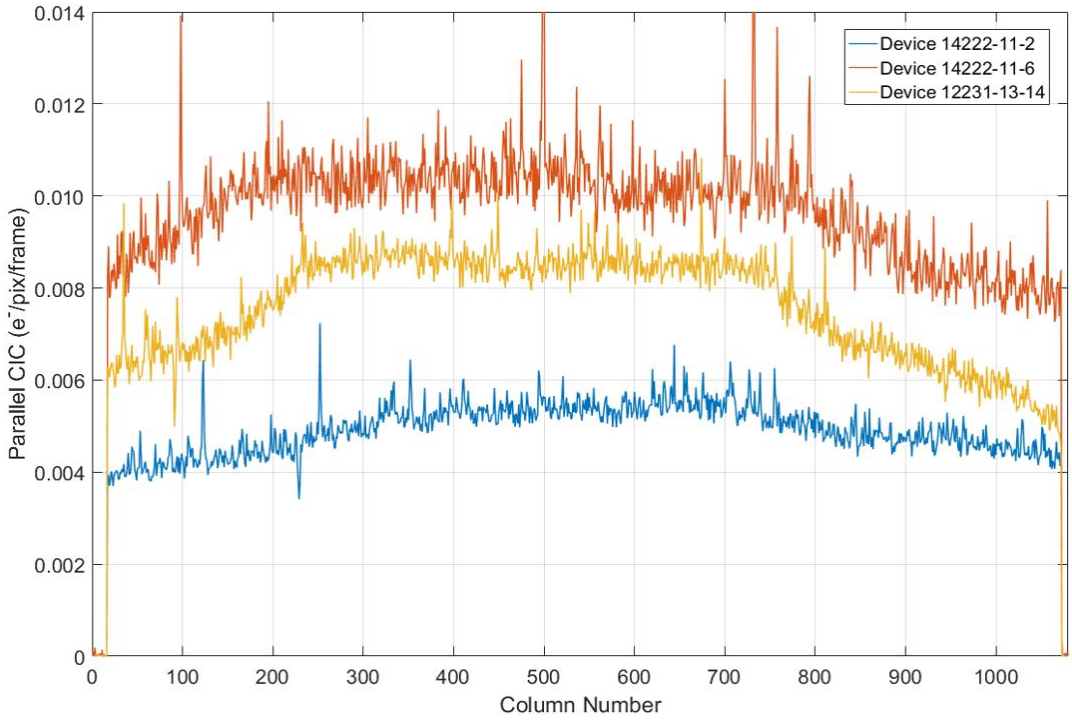

Figure 9.5: *Column profile of CIC measured in various CCD201 devices at 165 K in IMO at datasheet voltages. The pixel "spikes" were observed to be real and not due to measurement noise. Spatial variation in CIC generation can also be seen for each device, with CIC within the central columns appearing higher than at the edges of the device.*

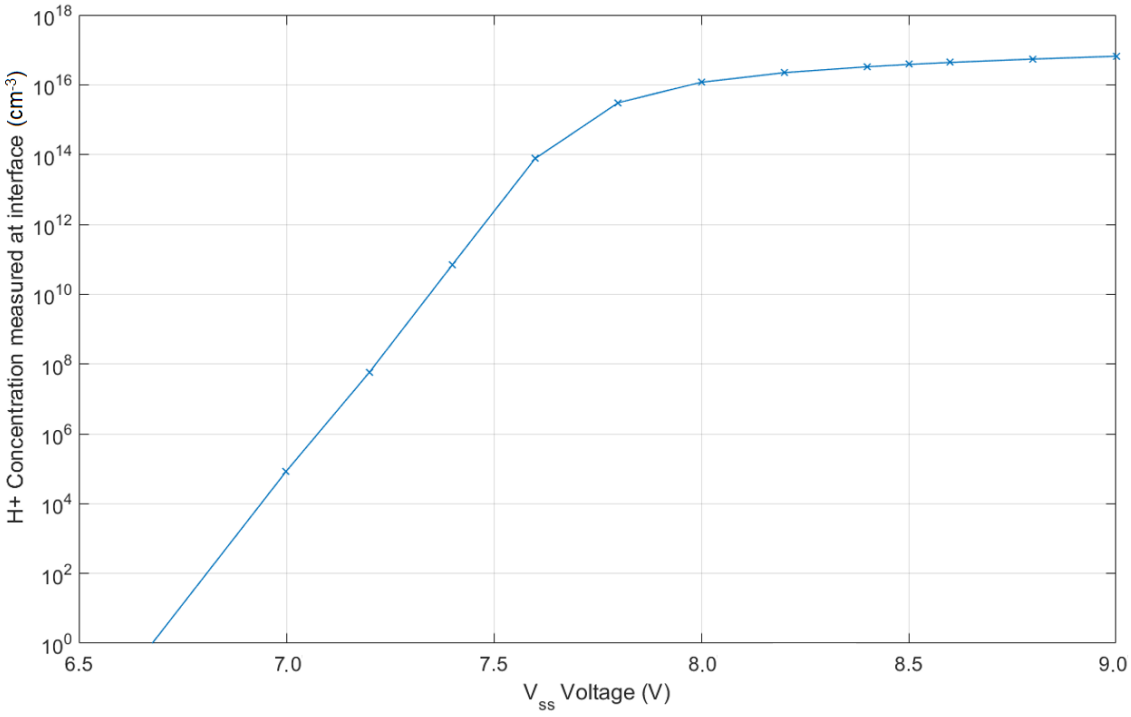

Figure 9.6: *Concentration of holes measured at the semiconductor-insulator interface beneath the centre of Iϕ2 as a function of substrate voltage. The hole concentration saturates at approximately V_{SS} = 8 V, indicating that the surface has become pinned, however, the hole concentration continues to increase from this point onwards to keep the interface potential equal to the substrate voltage.*

9.2.3 Impact of clock voltage and operating mode

For all devices tested throughout the study, an approximately exponential dependence of CIC on clock amplitude was observed under operation in IMO, where clock amplitude is defined as the voltage difference between the image high and low level. The electric field beneath the gate increases linearly with the applied gate voltage, however, impact ionisation is exponentially dependent on the applied electric field. For operation in NIMO, the population of holes at the interface is orders of magnitude lower than operation in IMO hence explaining the significant reduction in CIC. A comparison between the two modes for multiple voltage swings is shown by Figure 9.7 and is consistent with expectations.

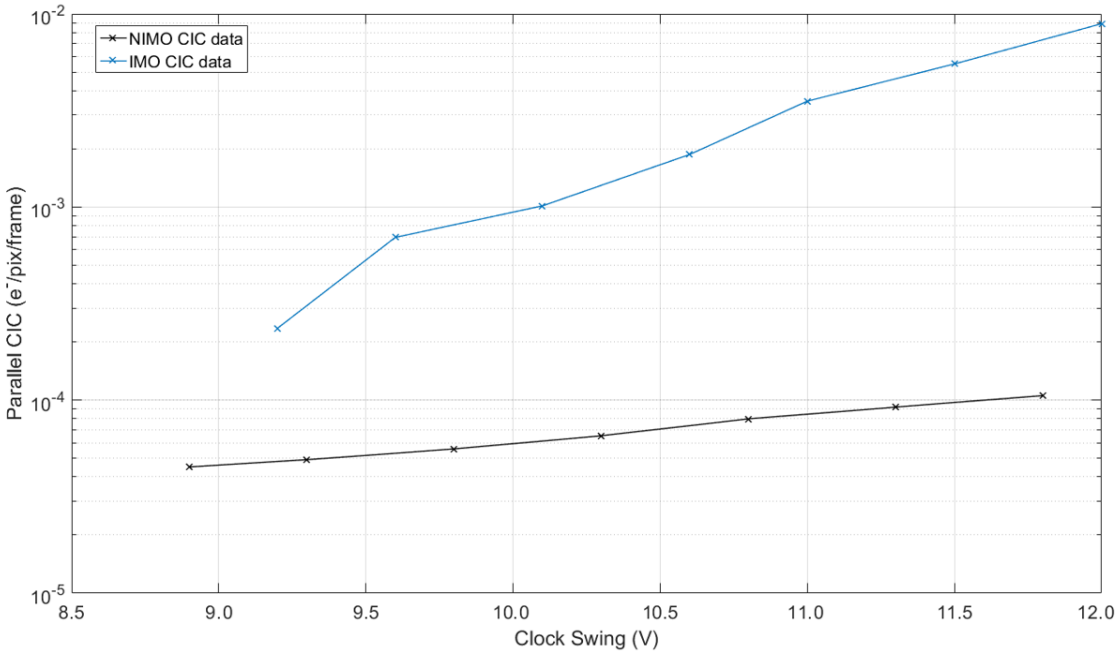

Figure 9.7: *CIC measured as a function of clock amplitude in both IMO and NIMO for device 11153-13-14. An approximately exponential dependence on clock amplitude was observed under each operating mode, with operation in IMO coinciding with an approximate order of magnitude increase in CIC across all voltages.*

9.2.4 Impact of clock delay

Charge acceptor states at the interface exhibit a broad density of states that is effectively continuous within the upper half of the band gap (Bush *et al.*, 2014). The longer a phase is held in the high state, the longer the possibility that a trap will accept an electron (and hence, donate a hole) that can generate CIC. Faster clocking speeds therefore mitigate CIC since they limit the time available for hole emission and hence the number of traps that can contribute to CIC. Figure 9.8 shows the density of states for interface state defects, taken from Bush *et al.* (2014) where the advantages of faster clocking can be seen.

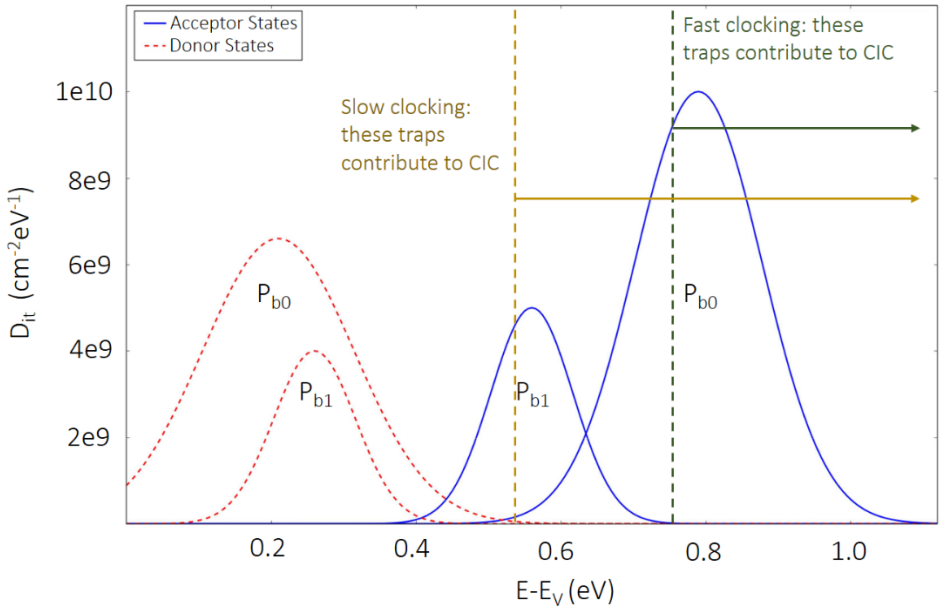

Figure 9.8: *Density of states for the interface traps known as P_{b1} and P_{b0} centres and their relationship to CIC generation.*

Measurements of parallel CIC as a function of clock delay (Figure 9.9) confirmed this expectation showed an approximately logarithmic relationship whereby higher CIC was associated with a longer phase delay. This measurement correlates with observations in other studies that have focused on faster clocking speeds for CIC mitigation (Daigle *et al.*, 2008, Harding *et al.*, 2016).

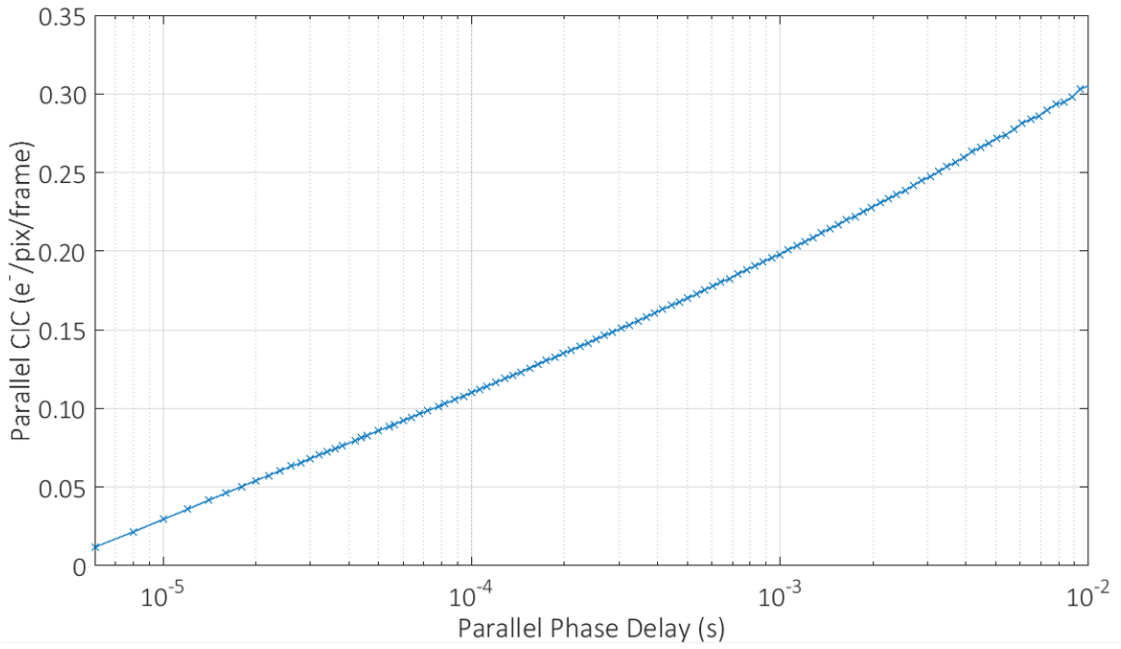

Figure 9.9: *Measurement of parallel CIC vs parallel phase delay for device 14222-11-6. A logarithmic dependence on phase time was observed.*

9.2.5 Impact of temperature

Hole mobility increases with decreasing temperature (Sze & Ng, 2006), and so one may expect an increase in CIC generation as the temperature of the device is decreased. However, as the temperature is lowered, the fraction of traps available to emit within a given phase time will decrease, leading to a potential reduction in CIC. The dependence observed in this study was weak, with only a small change noted in the measurement range of 153 to 203 K for a given phase time (Figure 9.10). For phase times extending past the ms regime, the dependence on temperature is more pronounced, shown by Figure 9.11. In these measurements, higher temperatures correspond to greater CIC, likely as more interface traps can emit within a fixed phase time. The conclusion is that it is unlikely CIC can be optimised through a change in operating temperature to the device, since the dependencies on clock amplitude and phase time are much more pronounced.

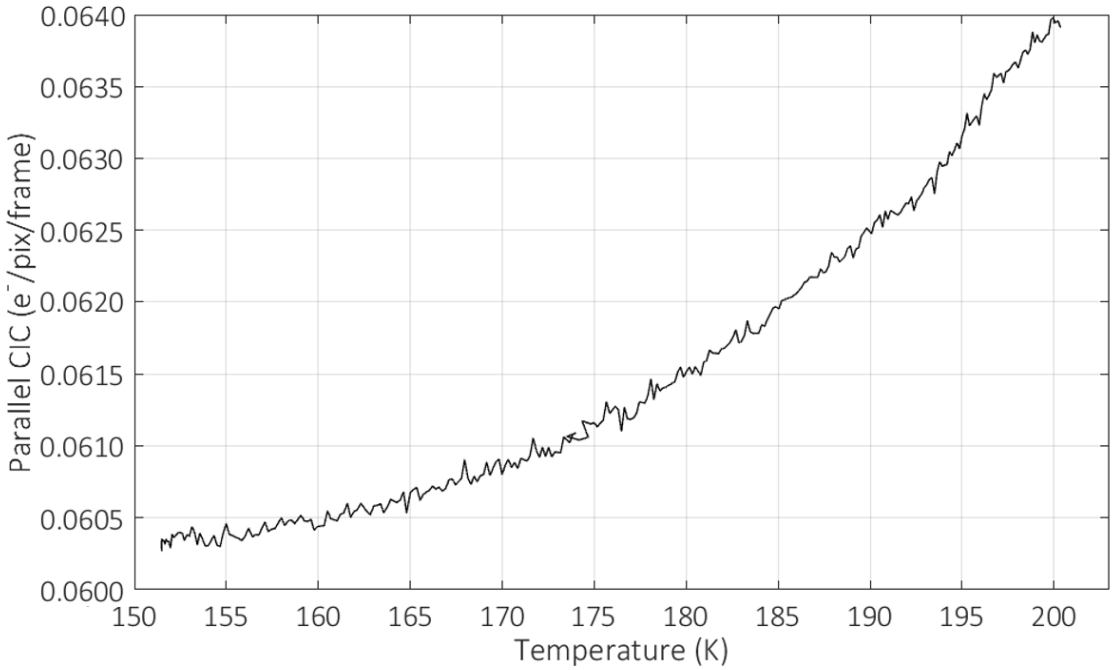

Figure 9.10: *The impact of temperature on parallel CIC for one phase time (12 µs) for an unirradiated CCD201 operated in IMO with a 12 V clock swing. Only a 5% change in CIC was measured over a 50 K range.*

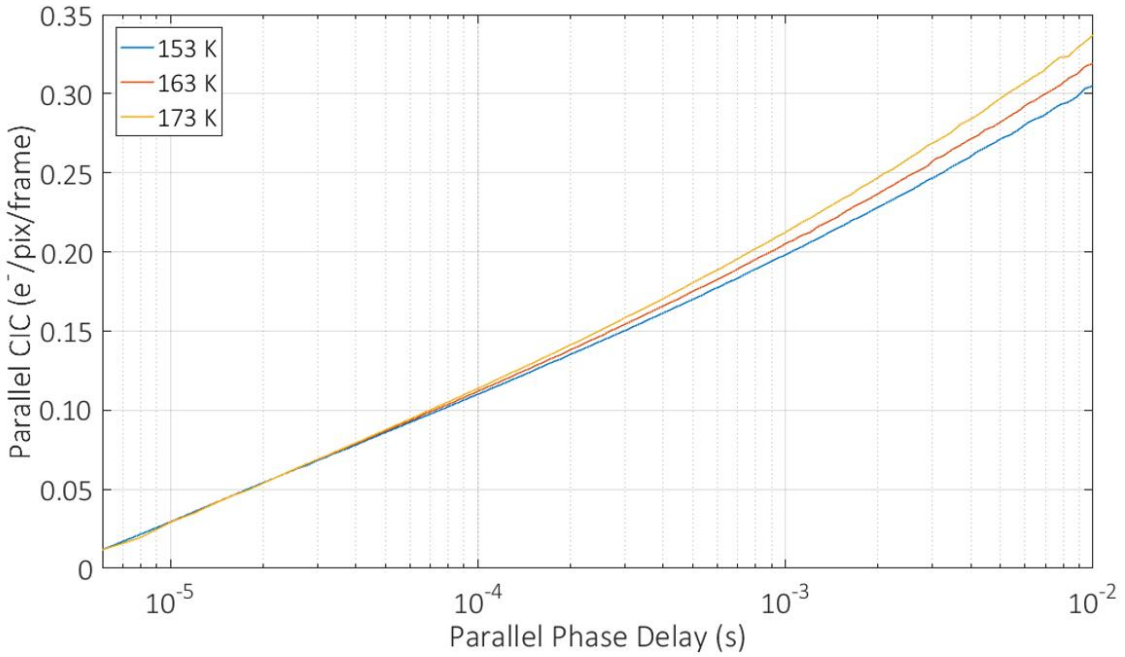

Figure 9.11*: Temperature dependence of parallel CIC as a function of phase time for an unirradiated CCD201 operating in IMO with a 12 V clock swing. A larger difference as a function of temperature is visible for the longer phase times.*

9.2.6 Impact of irradiation

The impact of radiation damage on CIC was measured for devices irradiated unbiased at room temperature and biased at 165 K. For the unbiased room temperature irradiations, little to no increase in parallel CIC was expected since the ionising component of damage was expected to be small and hence correspond to a negligible flat-band voltage shift and/or change in interface trap density (Hopkinson *et al.*, 1996). For the devices irradiated to 2.5×10^{9} protons·cm^{-2}, a very small change in CIC was observed but discounted because of the irradiation since the deviation was small with respect to the error on the measurement. For the other room temperature irradiated devices, post-irradiation characterisation occurred with a longer interval at room temperature following the irradiation. For these devices, an increase in parallel CIC was observed in the irradiated region. An additional measurement of device 11153-13-14 (2.5×10^{9}) confirmed an increase following a month and an additional year at 298 K, as shown by Figure 9.12 and Figure 9.13. A similar result was obtained for device 14222-11-6, with the results summarised within Table 9.5. This behaviour is similar to that observed by other authors for room temperature annealing of surface dark signal (Hopkinson, 1993). This increase was correlated with the movement of hydrogen species to form stable interface traps over time scales up to or exceeding a year. The implication is that the ionising component of the irradiation caused an increase in CIC over time due to increase in the number of traps at the interface.

Additional measurements of CIC vs phase delay and temperature for device 14222-11-6 showed that the increase due to irradiation was dependant on each variable, with the largest factor increase seen for fast clocking speeds and lower temperatures (Figure 9.14). The dependence of temperature shown in Figure 9.14 implies that a new interface trap has formed that was not present prior to the irradiation.

Table 9.5: *Summary of parallel CIC values measured at 12 V in IMO at 165 K for devices irradiated at room temperature throughout the irradiation campaign.*

Device	Proton Fluence	Pre-irradiation Parallel CIC (IMO at 165 K, 12 V swing)	Post-Irradiation Parallel CIC	Time at room temperature since the irradiation	Factor Change
10091-16-09	2.5×10^{9}	$(4.47\pm0.24)\times10^{-2}$	$(4.86\pm0.26)\times10^{-2}$	4 days	1.09
11153-13-14	2.5×10^{9}	$(8.80\pm0.38)\times10^{-3}$	$(9.90\pm0.10)\times10^{-3}$	12 days	1.13
14222-11-6	5.0×10^{9}	$(2.68\pm0.27)\times10^{-2}$	$(2.97\pm0.30)\times10^{-2}$	1 month	1.11
14222-11-2	1.0×10^{9}	$(2.29\pm0.23)\times10^{-2}$	$(2.84\pm0.28)\times10^{-2}$	5 months	1.24
14222-11-6	5.0×10^{9}	$(2.68\pm0.27)\times10^{-2}$	$(4.00\pm0.27)\times10^{-2}$	1 year	1.49

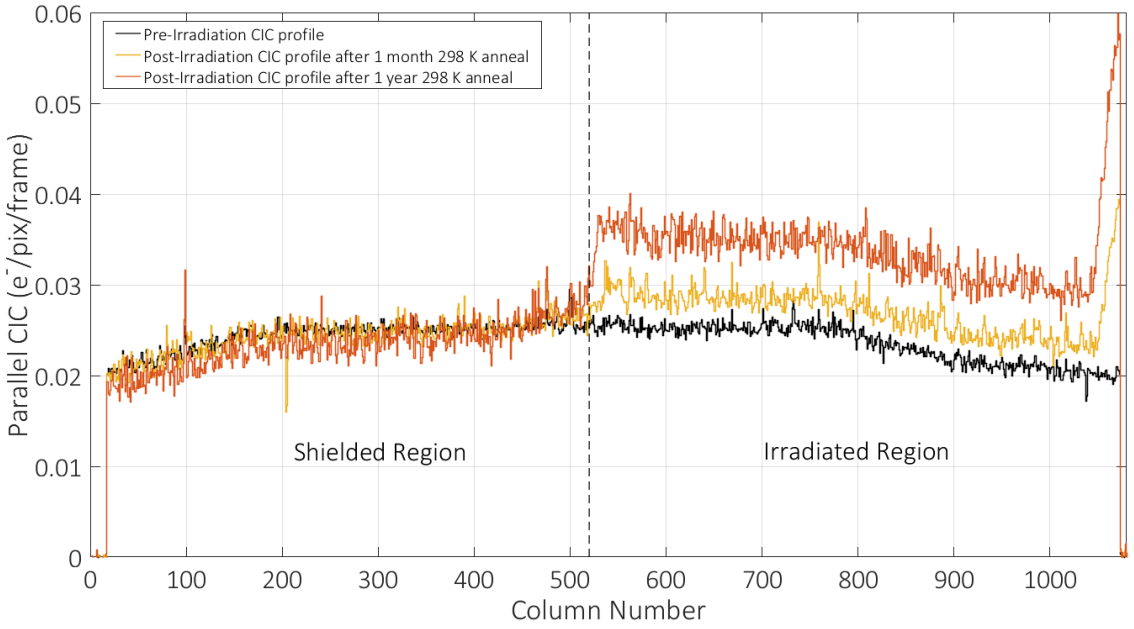

Figure 9.12: *Parallel CIC profile for device 14222-11-6 measured following a month and year at 298 K following the irradiation.*

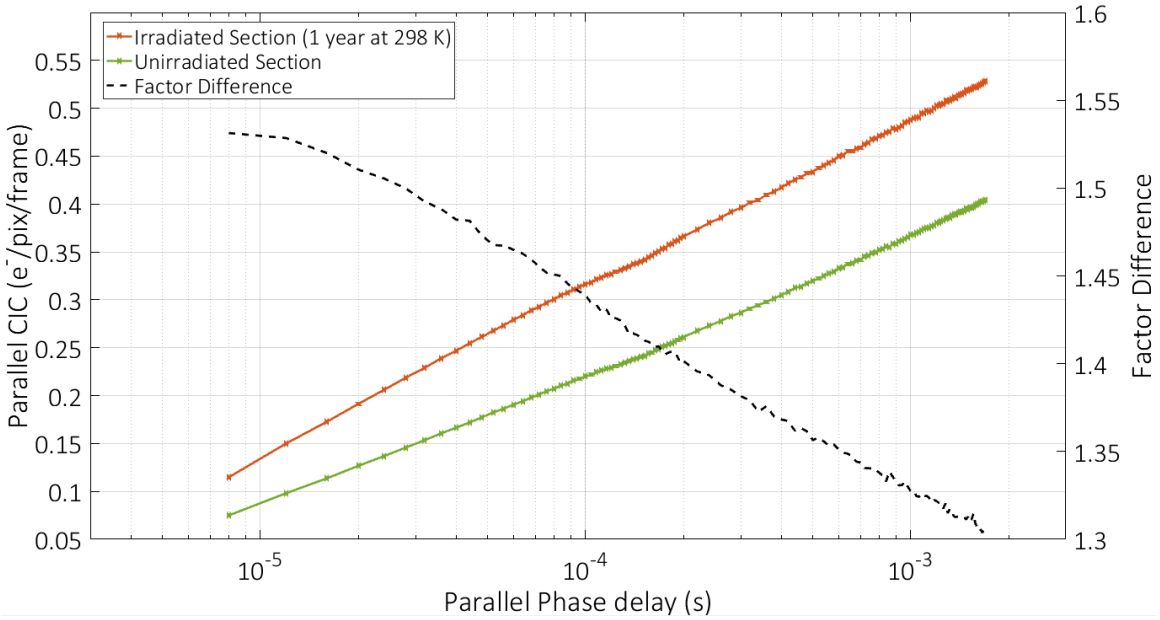

Figure 9.13: *Parallel CIC vs phase delay for device 14222-11-6 measured following a year at 298 K following a room temperature irradiation. The factor difference between irradiated and control regions is dependent on the phase delay.*

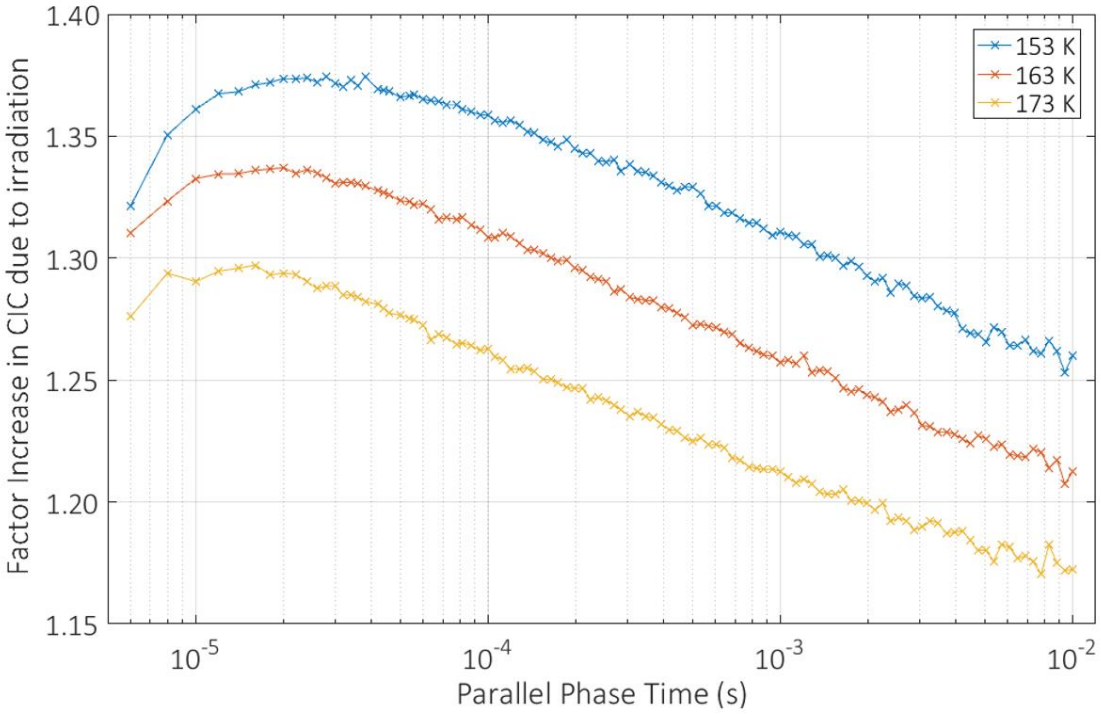

Figure 9.14: *Factor difference in parallel CIC as a function of both temperature and phase delay for device 14222-11-6 (irradiated to 5.0 × 10^9 p·cm^{-2} and following a 1 year 298 K anneal). The highest factor difference is seen for lower temperature and fast clocking speeds. Note the maximum moves with temperature, indicating a new interface trap has formed with temperature dependant emission that was not present prior to the irradiation.*

For the device irradiated under biased, cryogenic conditions, a measurable increase in parallel CIC was observed following each irradiation (Figure 9.15). The increase was observed across multiple clock swing values, except for the case of a 9 V swing whereby a decrease in CIC was observed for the final proton fluence (Figure 9.16). Irradiation under biased conditions gives rise to a flat-band voltage shift, since the electric field within the gate oxide forces electrons to move from the generation site relatively quickly, while the relatively immobile holes remain trapped and lead to charge build-up. The flat-band shift would have caused an increase in parallel CIC for a given input voltage, since the effective clock swing is now equal to the applied swing plus any flat-band shift due to irradiation. For the 9 V clock swing, the observed decrease is thought to be due to the fact that the flat-band shift has raised the low-level clock to a point where it is no longer fully inverted.

The cumulative total ionising dose experienced by the device was estimated using the NIST PSTAR framework, from which it was calculated the device was expected to have experienced an ionising

dose of order 2 krad (Table 9.6). An investigation into the effects of ionising damage on EM-CCD was performed by Hadwen *et al.* (2004) where a flat-band voltage shift of 0.1-0.2 V/krad was observed following a gamma irradiation of a CCD87. The flat-band shift experienced by the cryogenically irradiated device was estimated by fitting the CIC data for each clock swing value following each proton fluence to an exponential dependence on clock swing and calculating the flat-band shift responsible for the best fit to the data. From this, a shift of 0.06 V/krad was calculated, a value significantly lower than that estimated by Hadwen *et al.* Since this is not a standard method for calculating the voltage shift, it is entirely possible an additional mechanism is present that gives rise to an underestimated voltage shift. In addition, the measurement conditions for this study differ greatly from those used by Hadwen *et al.* in their investigation. Nonetheless, the fit showed that the increase in parallel CIC is near negligible in the sense that a 0.15 V reduction in parallel clock swing would reduce the parallel CIC to pre-irradiation values for the operating conditions of this study.

The increase in CIC due to radiation damage therefore appears to be a minor concern with respect to other factors such as dark current and CTI. While an increase was observed for both room temperature and cryogenic irradiations, the increase was small and was consistently below a factor of ×1.5. Mitigation appears rooted in operating the device with a V_{ss} value that is slightly above the pinning potential of the device and reducing the clock amplitude in the presence of a flat-band voltage shift so as to regain pre-irradiation performance.

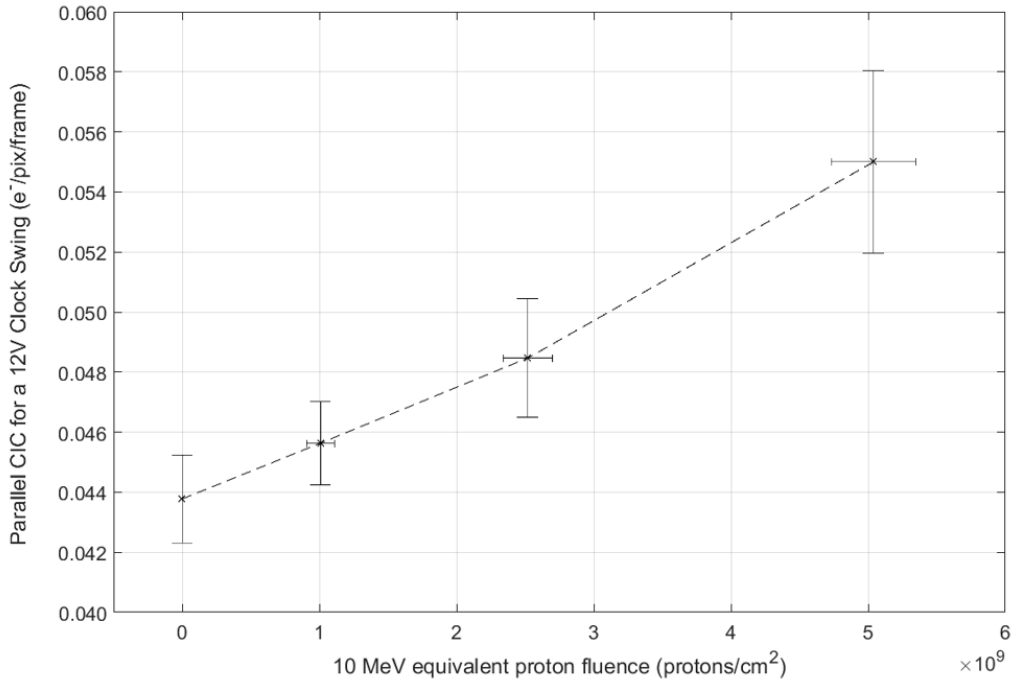

Figure 9.15: *Parallel CIC measured in IMO at 165 K using a 12 V clock swing following biased, cryogenic irradiation.*

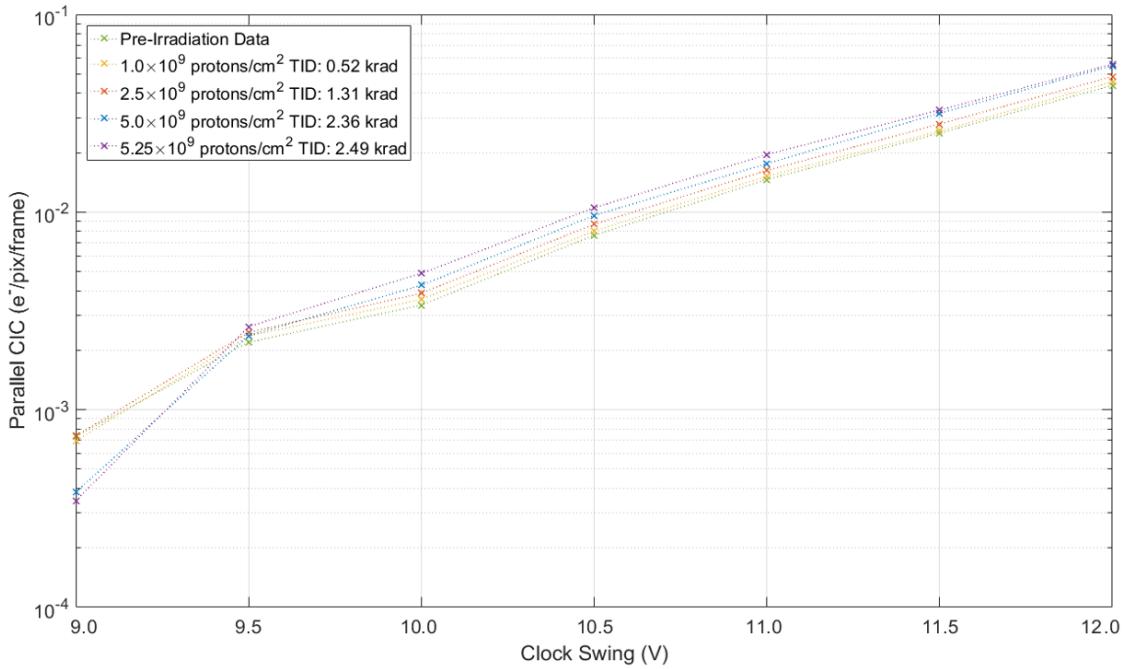

Figure 9.16: *Parallel CIC measured a function of clock swing following each successive proton fluence. An increase is seen for the majority of the clock swing values, except for 9 V where a decrease is observed. This decrease is thought to be due to the fact the device is on the edge of inversion for this particular clock low level and voltage shift configuration.*

Table 9.6: *Total ionising dose (TID) estimated using the NIST PSTAR stopping tables for energy deposition of a 5 MeV proton beam into silicon dioxide. Data for the final fluence is included, however, since this irradiation was not successful it should be ignored.*

Date of irradiation	10 MeV target fluence (protons/cm^2)	5 MeV target proton fluence (protons/cm^2) (equation 6.2)	Estimated Cumulative total ionising dose (krad)
19/06/15	1.0×10^9	5.32×10^8	0.52
26/06/15	1.5×10^9	8.00×10^8	1.31
03/07/15	2.5×10^9	1.33×10^9	2.36
10/07/15	2.5×10^9	1.33×10^9	3.93

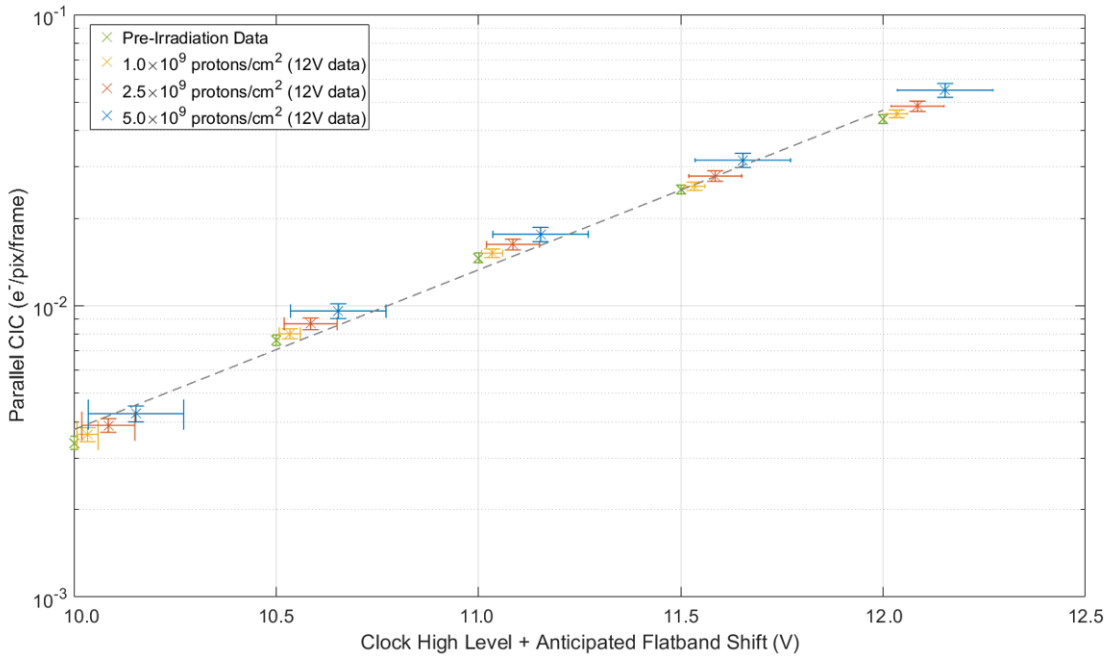

Figure 9.17: *Fit of parallel CIC data and estimated flat-band voltage shift to an exponential function that describes the CIC per frame as a function of clock amplitude. The best fit was observed for a flat band shift of 0.06 V/krad.*

9.3 Summary of radiation study results

The study presented within this chapter has shown the potential for large disparity in the estimated performance degradation of CCDs for the WFIRST CGI depending on whether the device is irradiated at room temperature or at the nominal operating temperature of the mission. The difference is believed to be due to variation within the landscape of silicon defects created through irradiation at different temperatures. For this study, the degree of degradation per proton was observed to be worse for irradiation at the cryogenic temperature of 165 K for every single performance metric measured. Following a room temperature anneal, dark current returned to levels one may expect for a typical room temperature irradiation however CTI remained unchanged within experimental error. Evidence was presented for a change in the defect landscape following a room temperature anneal, however the changes appear to have had a negligible impact on the measured CTI for the operating conditions of this study.

CIC, dark current and CTI remain the key performance metrics of concern with respect to radiation damage for the CGI. The increase in dark current is manageable and below the quoted EOL threshold value of 10^{-3} e^-/pixel/s for adequate S/N performance (Harding *et al.*, 2016). A room temperature anneal has also been shown to reduce the dark current value measured at cryogenic temperatures by an order of magnitude, as well as eliminate a significant proportion of hot pixels. CIC was seen to increase when the detector was irradiated biased due to the increased ionising component of the proton damage, however the increase was small and could easily be accounted

for through alteration to the image clock voltage amplitudes. CTI remains the largest concern and science return of the instrument could be greatly enhanced if it is mitigated through appropriate variation to clock timings and the operating temperature of the instrument during its lifetime. A possible mitigation strategy already highlighted at this point is the potential of significant reduction in CTI degradation if the device is stored at ambient temperature (298 K) when not in operation. To further understand this conclusion and the differences in the room temperature and cryogenic irradiation of the device a more in-depth study of the defect landscape is required. The “trap pumping” technique has the potential to answer some of these key questions and provide more information as to how CTI can be optimised for the specific case of the WFIRST instrument and will be investigated in the next chapter.

10 Defect identification in the CCD201-20

The results presented thus far have highlighted how charge transfer performance is intrinsically linked to the landscape of silicon defects following irradiation. At this point many questions remain open; why is CTI performance at cryogenic temperatures significantly worse than the room temperature equivalent? When warmed to room temperature, why did CTI not return to the room temperature equivalent case? What are the dominant defects responsible for CTI degradation for the WFIRST CGI and can they be mitigated?

More detailed information concerning the defect landscape of the CCD201-20 is required to answer these questions. The properties of individual traps must be probed and compared with one another to evaluate the respective performance impact. The trap pumping technique can provide this information, but prior to the work for this thesis had not been implemented on the CCD201-20 due to the complexity introduced by the 2-phase barrier implants.

Within this chapter, the trap pumping technique is revisited (see section 6.8) and, for the first time, applied to the case of the 2-phase CCD201-20. Example trap pumping schemes are presented that are, in principle, valid for any 2-phase device. The schemes are verified through TCAD and laboratory measurements and found to be able to probe the location of defects to sub-micron precision, with the potential for finer resolution if needed.

An extensive experimental trap pumping investigation is presented whereby some of the dominant defects responsible for CTI within CCD based imagers are probed to a new level of precision. The properties of each defect, including energy level, cross section and density, are provided through correlation with results from TCAD simulations of charge cloud volumes. Finally, the implication of these results for future CTI mitigation techniques and CGI performance is discussed.

10.1 Implementing trap pumping for the CCD201-20

The theory of trap pumping had been presented within Section 6.8, however, it was only described for the case of a standard 3-phase pixel, with phases of equal size and no additional implants that deform the electronic potential. The CCD201-20 image area is designed for 2-phase operation and has barrier implants located beneath two of the image phases that make the potential asymmetric for standard clocking conditions (a schematic is shown by Figure 10.1). The barrier phases are also physically smaller than the storage phases which must be considered when attempting to calculate the effective volume of the pixel probed by pumping. The application of the theory presented within Chapter 6 to the CCD201 therefore required more detailed consideration of the potential profile within the image area so that the movement of

charge during the trap pumping process could be accurately predicted. TCAD simulations of the CCD201-20 had the ability to produce an accurate representation of the pixel potential and so became the starting point for devising the CCD201-20 trap pumping technique.

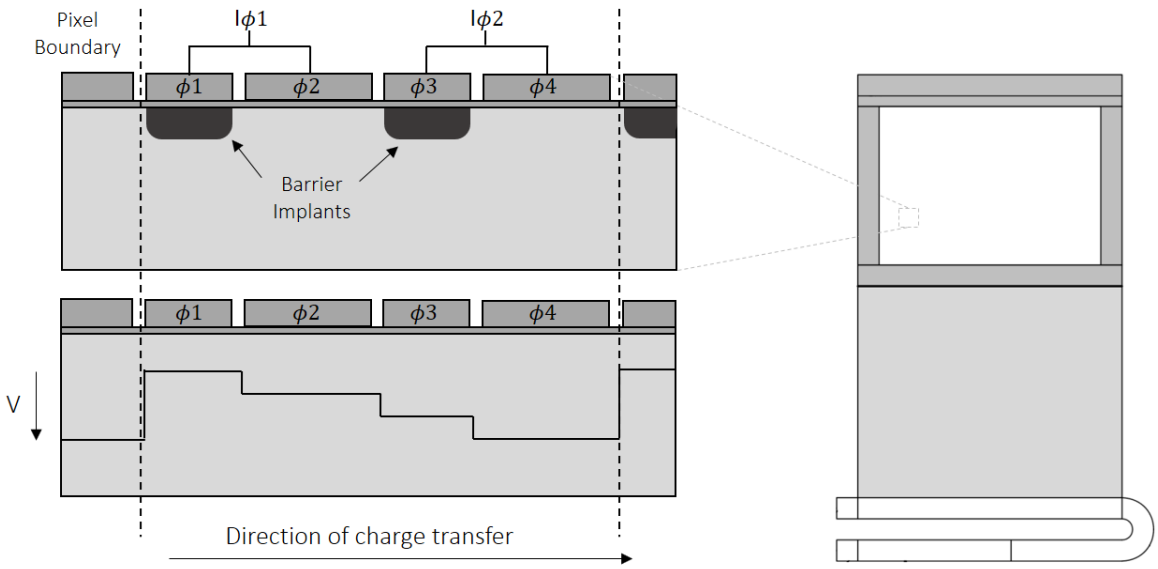

Figure 10.1: *Schematic of a CCD201-20 image pixel, showing the asymmetric phase structure and the positioning of barrier implants that allow 2-phase clocking. The potential structure shown on the bottom panel is only indicative; TCAD simulations were required to provide the true structure.*

The CCD201-20 image area and standard register pixels were constructed within a commercial TCAD software package (SILVACO©) with the aim of measuring the potential profiles throughout each pixel at various stages of clocking. The models were 2D in nature, with a nominal dimension of 1 µm perpendicular to the direction of charge transfer. Measurement of the electronic potential perpendicular to the direction of transfer, incorporating the channel stops of the pixel, showed that the profile was symmetric and approximately flat towards the centre of the pixel. The functional form of the profiles presented within this section therefore apply across the whole pixel. However, the exact magnitude of the potential at a given co-ordinate is expected to decrease approaching the channel stops, illustrated by Figure 10.2.

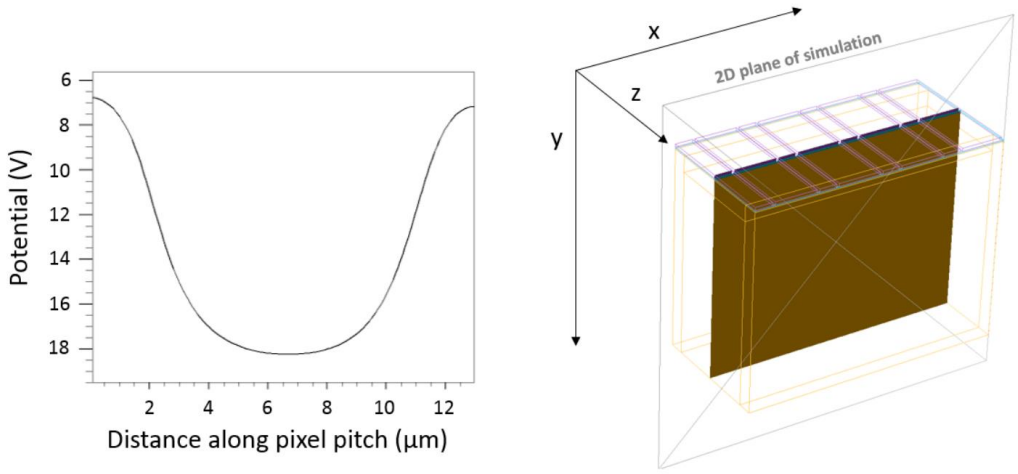

Figure 10.2: *Simulation of the potential profile in the Z direction for a CCD201 image pixel. The 2D plane of simulation is located at the centre of the pixel.*

All parameters relating to the manufacturing of the pixel were accurately simulated, including ion implantation, fully-coupled dopant diffusion and polysilicon deposition processes. The geometry of the pixels was set to standard e2v design parameters, including phase dimensions and the width of dielectric layers. Implantation doses were set such that each pixel had performance characteristics in-line with e2v specifications, including the channel parameter (ϕ_{CH}) and the "barrier potential" for the barrier phases of the image pixel. The voltages applied to each pixel were set to e2v CCD201 datasheet voltages and are summarised by Table 10.1 (e2v Technologies, 2015). The clocking conditions for each of the simulated results corresponded to standard e2v datasheet clocking and are summarised by Figure 10.3.

Table 10.1: *Voltage values for each of the potential profile simulations.*

Bias Line	Voltage Value (V)
ϕ_1,ϕ_2,ϕ_3,ϕ_4 High	7.0
ϕ_1,ϕ_2,ϕ_3,ϕ_4 Low	-5.0
V_{SS}	4.5

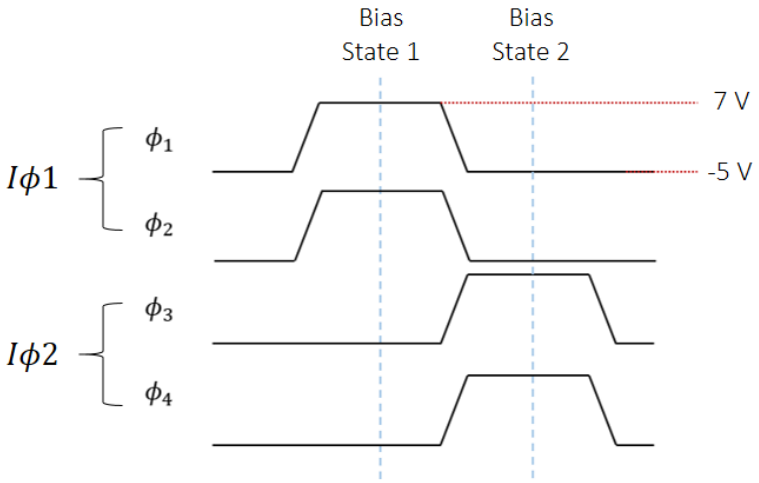

Figure 10.3*: Summary of the clocking conditions that were simulated.*

During operation, the pixel is clocked from bias state 1 to bias state 2 periodically to move charge from one pixel to the next. Figure 10.4 shows the result of the simulation for Iϕ_2 high, where the advantages of the 2-phase potential structure are clear; the profile is such that any captured charge is promoted to re-join the original signal packet so long as it emits within the same clocking cycle. The point at which charge will be deferred to the first trailing pixel is given by the local potential minima within the pixel, at which point $\frac{dV}{dx} = 0$. Charge captured and then released between this point and the pixel boundary will emit to the neighbouring pixel, contributing to CTI. The location of the minima was required for the construction of the TCAD pumping schemes, as successful trap pumping relies on charge being preferentially emitted to a pixel neighbour within a given timeframe. Measurement of the location where $\frac{dV}{dx} = 0$ for each bias state shows that the peak was 1.2 µm from the left-hand edge of ϕ_3 for bias state 1 and approximately 1.2 µm from the right-hand edge of ϕ_1 for bias state 2. In other words, the potential minima beneath each barrier phase is symmetric with respect to how the adjacent phases are biased - an important conclusion for the design of the pumping schemes.

The potential maxima dictate the charge storage location and is important for the design of trap pumping schemes since it determines the charge storage location. For standard bias conditions, the potential maximum was found to shift by approximately 0.5 µm depending upon the adjacent barrier phase that was held high. Figure 10.5 shows this for the case of either ϕ_1 or ϕ_3 being held high with ϕ_2. The exact location of the maximum could be moved by changing the bias to these adjacent storage phases from the nominal value (+12 V relative to low level) to lower values (+10 V, +9 V etc.). Thus, careful adjustment of the bias to an adjacent barrier phase allows one to

"scan" the charge packet through this portion of the silicon to provide high resolution location information for trapping sites beneath the charge storage phases. With this information to-hand, the movement of charge as a function of displacement throughout the pixel could be accurately predicted and thus allowed the design of the CCD201 trap pumping schemes.

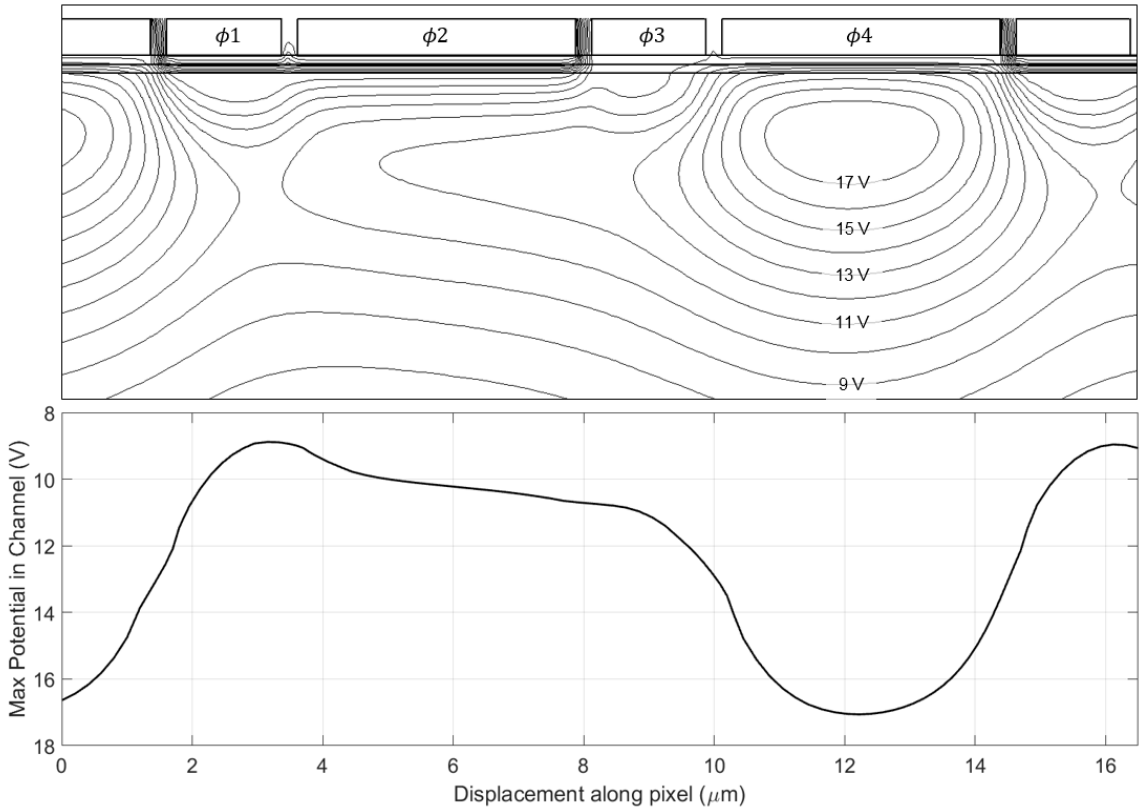

Figure 10.4*: TCAD simulation of a CCD201 image bias in bias state 2.*

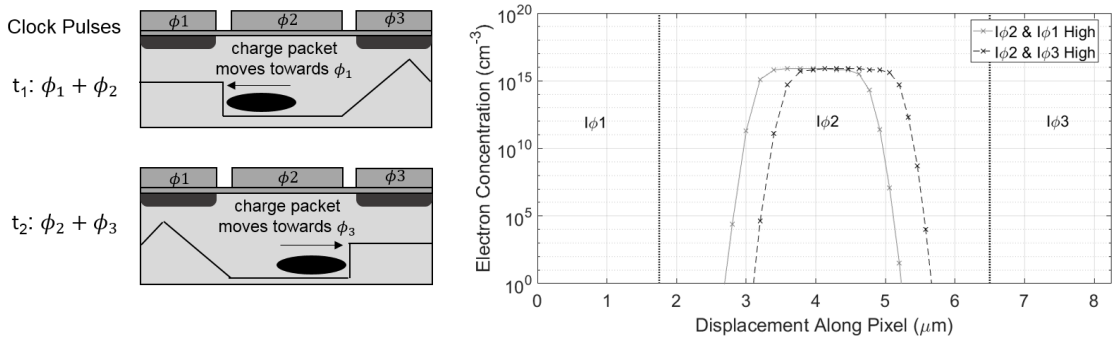

Figure 10.5*: Left: movement of charge depending upon how the adjacent barrier phase is biased. Right: TCAD simulation of a 10,000 e^- packet in the presence of the two bias configurations shown on the left panel.*

10.2 CCD201 trap pumping schemes

The simulations presented in the previous section provided the potential profiles needed to predict the movement of charge under arbitrary clocking conditions. This allowed trap pumping schemes to be designed and implemented for the 2-phase CCD201-20. An example trap pumping scheme is presented by Figure 10.6. A total of four separate clock pulses are required for a complete cycle before the process repeats. Note how the conditions for successful trap pumping are satisfied; trapping sites can be filled beneath either of the storage phases that can then emit charge to the neighbouring pixel. Over multiple cycles, the signal level within the primary pixel will decrease while the signal in the neighbouring pixel will increase. Also note how the direction of transfer for the captured signal is dependent on the phase location of the defect; charge captured beneath ϕ_4 will pump along the direction of transfer, while charge captured beneath ϕ_2 will pump against the direction of transfer. For brevity, we will now refer to each of these configurations as "positive" and "negative" orientations, respectively. So, for this particular scheme, a positively orientated dipole indicates a trapping defect beneath ϕ_4 while a negatively orientated dipole indicates a trap beneath ϕ_2.

An additional subtlety is present where between clock pulses 1 and 2, and then between 3 and 4, the barrier phase that is biased high is switched. This gives rise to the phenomenon illustrated by Figure 10.5, whereby the charge storage location shifts by a small amount between each pulse. Taking the example of the transition between pulse 1 and 2; within pulse 1, charge trapping sites beneath the centre and right-hand side of ϕ_2 become filled in this time, while within pulse 2 charge trapping sites beneath the centre and left-hand side of ϕ_2 become filled. During pulse 2, charge trapping sites beneath the left-hand side of ϕ_2 are no longer in the presence of the charge cloud and so can emit. The result is a different phase time relationship for trapping sites in this location than the rest of the phase. The same logic applies to ϕ_4, however in this instance trapping sites beneath the right-hand side of ϕ_4 exhibit the difference. Of course, the designation of "left-hand side" and "right-hand side" is dependent upon the signal size and biases used during the trap pumping scheme. For standard bias conditions and a signal level of approximately 10,000 e^-, the difference was measured to be ≈ 0.5 µm. Thus, following the same analysis presented in Section 6.8, for this scheme there are two phase relationships for defects depending upon their location. In addition to these phase relationships, the polarity of the dipole allows one to distinguish traps beneath ϕ_2 and ϕ_4.

For defects located beneath the centre and left-hand side of ϕ_2 and the centre and right-hand side of ϕ_4 :

$$I = NP_C(e^{-\frac{t_{ph}}{\tau_e}} - e^{-\frac{2t_{ph}}{\tau_e}}) \qquad \textit{Equation 10.1}$$

Whereas defects on the right-hand side of ϕ_2 and the left-hand side of ϕ_4 will follow:

$$I = NP_C(e^{-\frac{2t_{ph}}{\tau_e}} - e^{-\frac{3t_{ph}}{\tau_e}}) \qquad \textit{Equation 10.2}$$

As a reminder, I is the intensity of the dipole, *N* is the number of pumping cycles, P_C is the capture probability of the defect, t_{ph} is the phase delay between clock pulses and τ_e is the emission time constant of the defect.

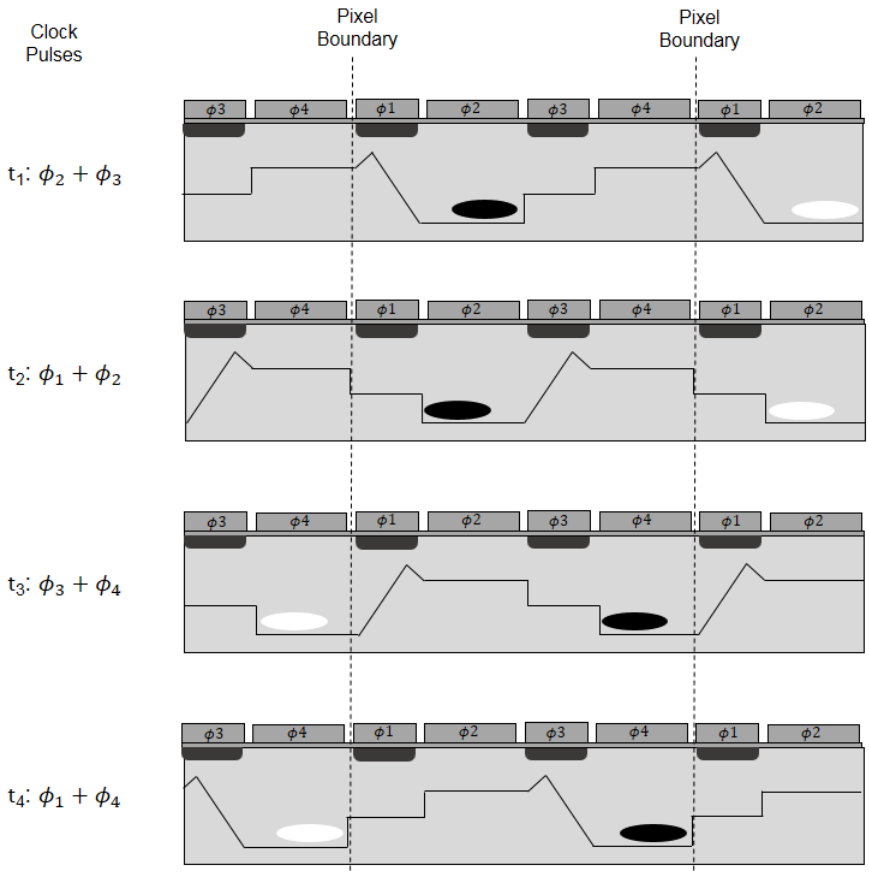

Figure 10.6: *Example trap pumping scheme for the 2-phase CCD201-20. The primary signal packet is shown in black, neighbouring signal packets are shown in white.*

The example presented here is just one of many trap pumping schemes possible with this architecture of device. A total of four schemes were implemented in this study that probed 100%

of the pixel area relevant to CTI. In the above analysis, charge capture beneath the barrier phases was ignored. This was because 2D simulations of charge transfer had highlighted that the probability of capture beneath these regions was very low, since the transfer of signal took place within a short time frame (of order 10 ns, as shown by Figure 10.7). However, in the limit of long rise times, 3D simulations with a fixed trap background highlighted some defects beneath the barrier phases could become filled, as the charge packet moves slightly between the boundary before the actual transfer. This is shown by Figure 10.8 where an isosurface of filled traps can be seen following a transfer of 10,000 e^- from ϕ_2 to ϕ_4. Based on this result, analysis for capture beneath barrier phases was also performed but is rarely expected to be needed.

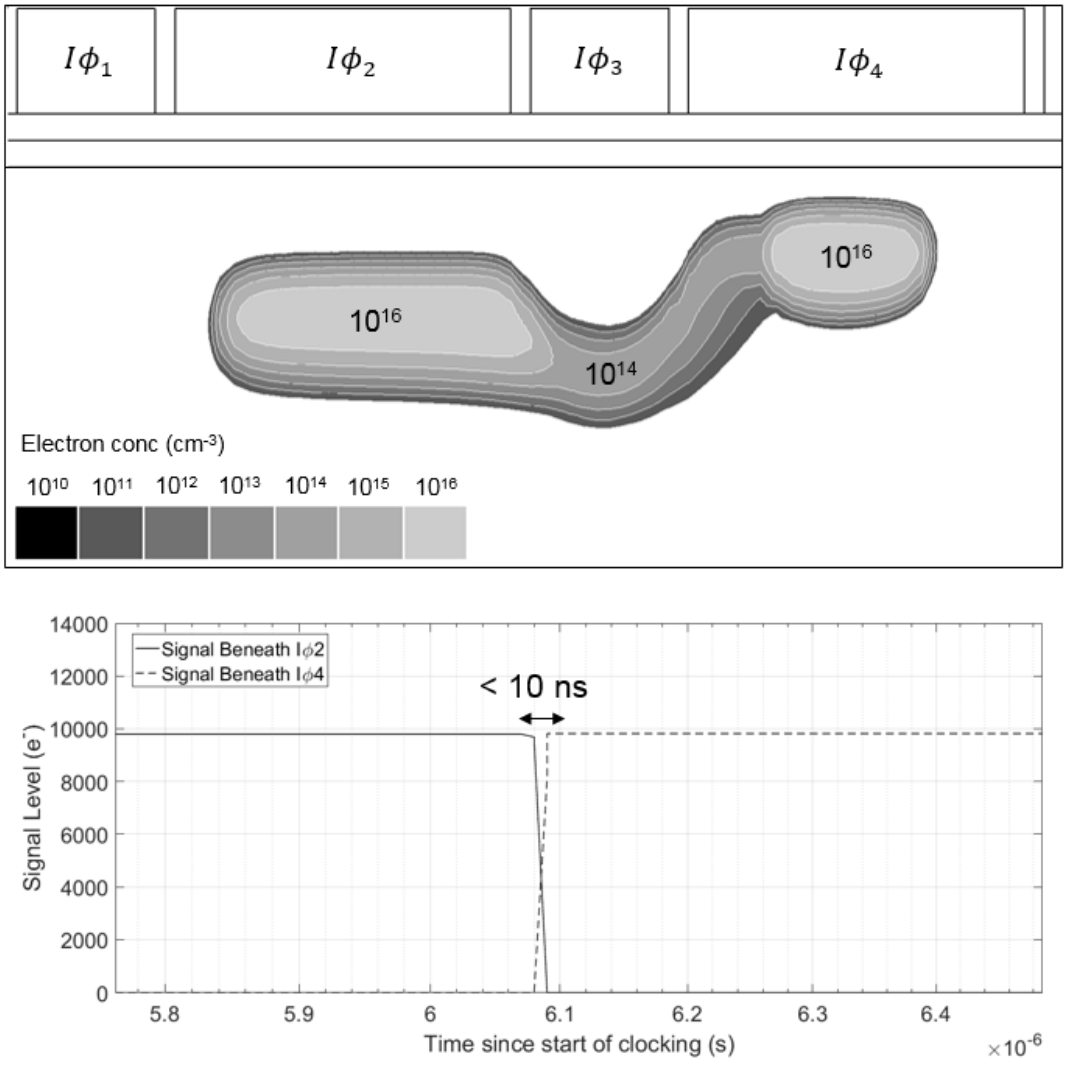

Figure 10.7*: 2D simulation of charge transfer between ϕ_2 and ϕ_4. The signal size was 10,000 e^-, clock amplitudes were 12 V and the rise/fall time was 100 ns. The majority of the transfer takes place within 10 ns, corresponding to a negligible probability of capture beneath the barrier phases.*

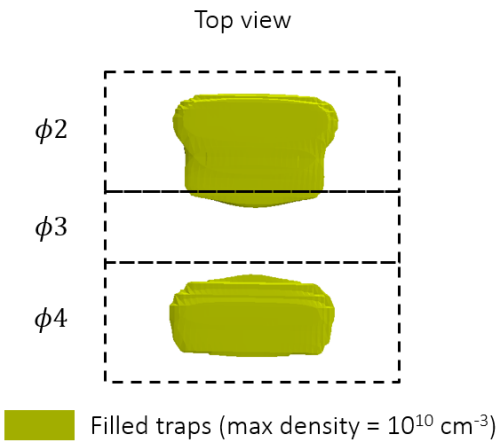

Figure 10.8: *Result from a 3D TCAD charge transfer simulation whereby a 10,000 e^- charge cloud was transferred from ϕ_2 to ϕ_4. The rise time was 10 µs for this simulation. As a result, the charge packet moved beneath the edge of the barrier phase ϕ_3 and filled a small portion of traps in this region.*

Figure 10.9 and Figure 10.10 summarise the analysis for each of the four pumping schemes used in this study. The discussion of these schemes should provide the reader with the impression that the trap pumping process is intrinsically related to the device structure and so, even for simple pumping schemes, knowledge of the exact pixel structure and TCAD simulations of said structures are invaluable for explaining some of the more complicated phenomena one may expect to observe. With the schemes designed, discussion moves to experimental measurement of trap properties within the CCD201-20.

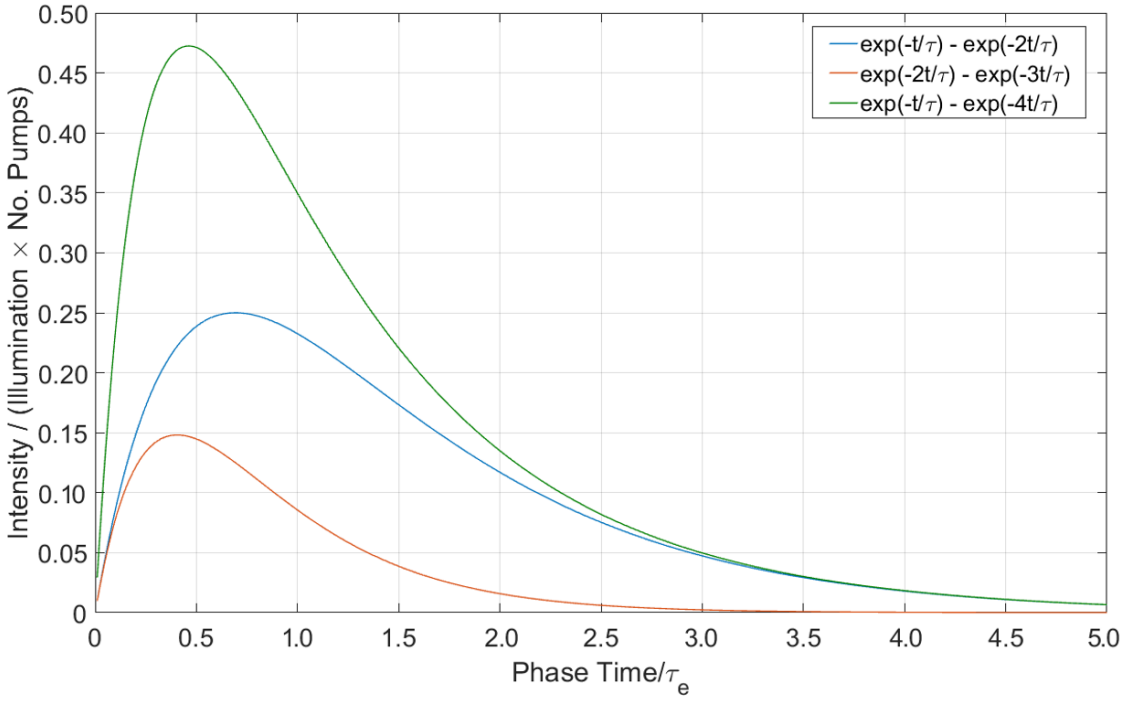

Figure 10.9: *Plot of the three different intensity curves expected when using the four schemes designed for trap pumping within the CCD201. Unitless axes are used to highlight the functional form of each curve irrespective of temperature or trap species.*

	$\phi 1$			$\phi 2$			$\phi 3$			$\phi 4$		
	LHS	Centre	RHS	LHS	Centre	RHS	LHS	Centre	RHS	LHS	Centre	RHS
Scheme 1												
Scheme 2												
Scheme 3												
Scheme 4												

Figure 10.10: *Summary of the appearance of dipoles within an image based upon the scheme used and phase location of the trap. The colour of the dipole represents the expected intensity curve that the trap will follow based upon Figure 10.9.*

10.3 Experimental implementation

As explained in Chapter 6, the identification of trapping sites using the "trap pumping" technique has typically required measurements of dipole amplitude as a function of phase time at a given temperature. Intensity curves are then fitted to these data that return the emission time constant for each defect. Measurements of the emission time constant over a range of temperatures allows estimation of the defect energy level and cross section, from which the physical nature of the defect can be inferred.

This theory was implemented through use of each of the trap pumping schemes summarised in the previous section on irradiated CCD201-20s. Three devices were used for this study. Most of the data was collected using an engineering grade CCD201-20 irradiated unbiased, at room temperature to 1.0×10^9 protons/cm^2 during May 2016 (see Section 6.2). Additional testing and consistency checks were performed using engineering grade CCD201-20s that were irradiated unbiased at room temperature to 2.5×10^9 protons/cm^2 and 5.0×10^9 protons/cm^2 respectively. A summary of the devices used for this study is presented in Table 10.2.

Table 10.2*: Summary of devices used for this study and the irradiation conditions.*

Serial Number	Device grade and reason	Proton Fluence (p/cm^2) (10 MeV equiv.)	Irradiation Condition	Irradiation Pattern
14222-11-2	Engineering grade Trap at FWC	1.0×10^9	298 K unbiased 74 MeV protons	Serial and parallel regions, with parallel control region
11153-13-14	Engineering grade hot pixels	2.5×10^9	298 K unbiased 74 MeV protons	Serial and parallel regions, with parallel control region
14222-11-6	Engineering grade Trap at FWC	5.0×10^9	298 K unbiased 74 MeV protons	Serial and parallel regions, with parallel control region

Trap pumped images were obtained using customised CCD drive sequences that replicated the pumping schemes. In the majority of cases, Scheme 1 was used for measurement purposes due to its simplicity and the fact it probes defects beneath each of the storage phases of the device. This scheme alone therefore probes the vast majority of the pixel area relevant to standard operation and allows calculation of both emission time constant and defect density with supporting information from TCAD simulations. Where possible, additional data was obtained using schemes 2, 3 and 4 in order to check the consistency of results (see Figure 10.10).

Illumination was provided by a pair of LEDs (peak wavelength ≈750 nm) directed towards the back of the cryostat such that the reflected light would provide uniform illumination across the device. In practise, the uniformity was measured to be > 90% (peak to trough) across the image area. The target illumination level was approximately 10000 e^- for trap pumping analysis except for cases whereby the effect of illumination level was being investigated. This illumination level provided a balance whereby P_C=1 for the vast majority of the charge packet and the maximum dipole intensity remained beneath both the image and register full well capacity.

Some data was obtained through the Large Signal (LS) output of the device thereby utilising the EM gain mechanism (see Figure 4.1). The gain used varied according to the measurement temperature, however was typically within the range of ×10-20. Degradation in data quality was noticed at higher multiplication gains (where peak signals exceeded approximately 400,000 e^-) whereby the benefit of reduced read noise was negated by increased CTI on the bright pixel of the dipole. An Fe^{55} source was pointed at the device at all times throughout data collection, which provided a means to carry out real-time calibration for each set of images. This was deemed necessary since the nature of the investigation required frequent changes in temperature which in turn affected the multiplication gain and QE of the device. The large signals also meant a degree of device ageing was experienced that needed to be calibrated against so that the illumination was not underestimated.

These complications meant that the equipment was soon modified to connect the High Responsivity (HR) standard CCD output for the remainder of data collection (see Figure 4.1). In general, the data from the HR output was of much higher quality (as one should expect, see Chapter 3) and its use is recommended where possible when this technique is implemented on EM-CCDs.

10.4 Results from trap pumping

A summary of the parameter space probed within this investigation overlaid on the "trap diagram" (Figure 5.14) is given by Figure 10.11. Each of the major (known) defect species known to affect CTI within CCDs was probed in this study. Discussion now turns to the results of the investigation, beginning with some general trends observed for all datasets.

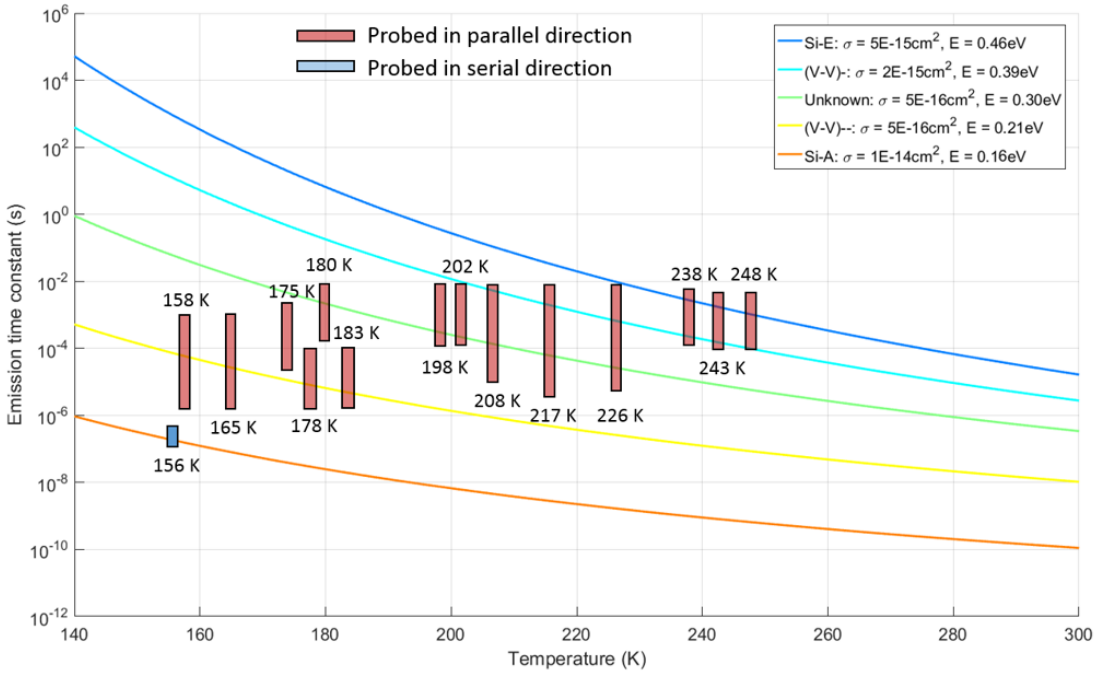

Figure 10.11: *Summary of parameter space probed using the trap pumping technique.*

10.4.1 General trends

Many trends were noted in the trap pumping data that were present for all identified defect species that are worthy of discussion since they provide important information about how the trap pumping technique should be implemented and how the results should be interpreted. The discussion of these trends is focused primarily around data obtained in the parameter space of the defect nominally known as the VV^{--}, since other investigations had been performed on this defect that could act as a basis of comparison (e.g. Wood *et al.*, 2016).

The first observation was a "split peak" phenomenon that was noted when any data from a single trap pumping scheme was analysed. Figure 10.12 shows an energy level histogram obtained at 165 K in the parameter space of the VV^{--} with many interesting features worthy of further discussion.

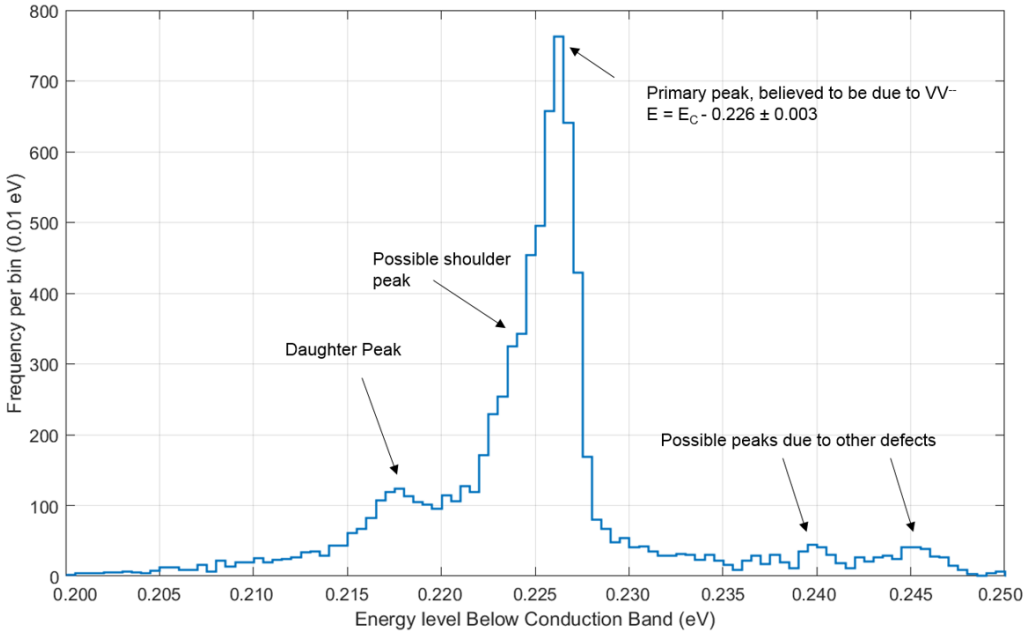

Figure 10.12: *Histogram of defect energy levels obtained by probing the VV^{--} parameter space at 165 K. The literature cross section of 5×10^{16} cm^2 was assumed for the calculation (D J Hall et al., 2014).*

First, two distinct peaks can be seen within the histogram. A primary peak exists with mode energy level $E = E_C - (0.226 \pm 0.003)$ eV. This value is in good agreement with the literature value of the VV^{--} as measured with the DLTS technique and a previous trap pumping study performed on an N-channel CCD47-10 (Pichler, 2004, Wood *et al.*, 2016). There is also a secondary peak with significantly lower intensity and mode energy level 0.218 eV. At first glance, the conclusion would be that there are either two separate defects being probed within this parameter space or perhaps some physical effect is causing the effective energy level of the VV^{--} to be split (for example lattice strain or field enhanced emission). For this study and this dataset, it is currently believed that neither of these are the case. Scheme 1 was used to generate this histogram which is known to probe defects beneath each of the storage phases. Two intensity curves are expected to be present depending upon the physical location of the defect (Equation 10.1 and Equation 10.2).

Although each functional form was built into the analysis code, it was discovered that it was difficult to distinguish between the two curves based upon the quality of the fit alone. It was often the case that a trap that would exhibit the relationship described by Equation 10.1 would in fact be better represented by Equation 10.2 with a slightly lower value of P_C to account for the lower peak dipole intensity. Placing limits on the possible allowable values of P_C did not ameliorate the

issue, since in practise a variety of values ranging from 0-2 is possible depending on the trap density and location of the charge cloud with respect to the trap.

Fitting a function of the form of Equation 10.1 to a dipole that is in fact described by Equation 10.2 results in a distortion in the calculated value of τ_e equal to $\ln(2)/\ln(3/2) \approx 1.7$. Inspection of the histogram of the calculated emission time constants from this particular dataset reveals that the location of the daughter peak closely matches this expectation (Figure 10.13). Converting into energy, the location of the daughter peak is expected to lie at $E \approx E_C - 0.218$ eV which is in close agreement with that observed within this dataset (Figure 10.12).

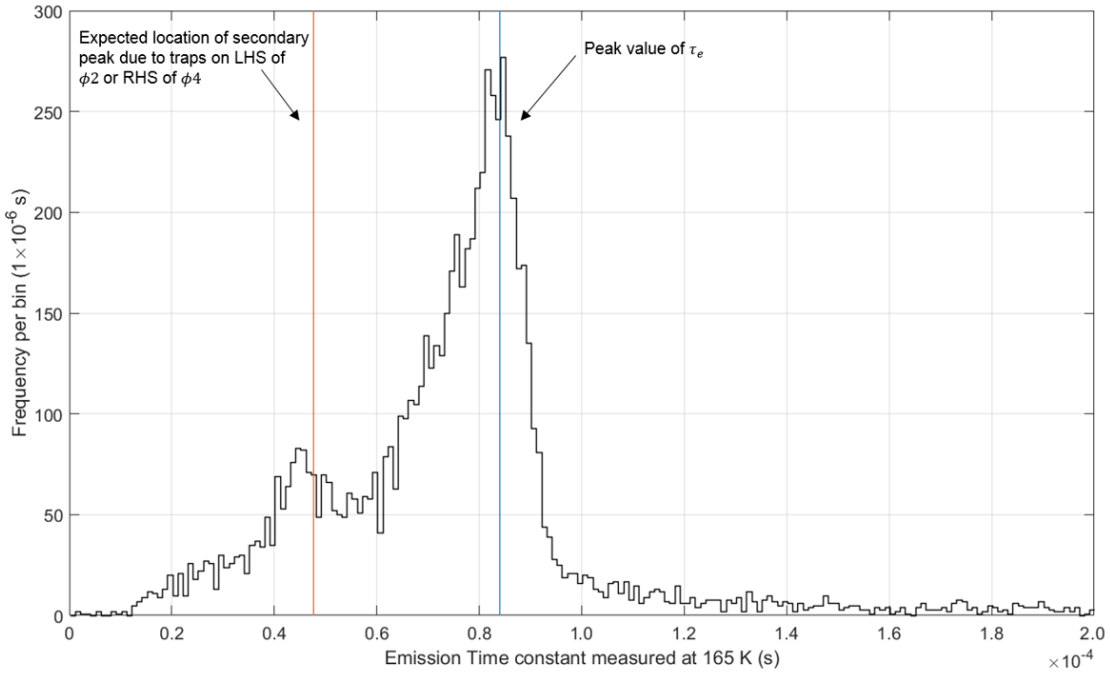

Figure 10.13 *: Emission time constant histogram for the VV^{--} parameter space measured at 165 K. Two distinct peaks are present. The daughter peak is still believed to be due to the VV^{--} however lies away from the primary peak due to limitations of curve fitting to each of the expected functions. The location of the secondary peak coincides with the expected location based upon the expected error from fitting the incorrect curve to a trap that is present either under the LHS of $\phi 2$ or the RHS of $\phi 4$.*

Further evidence is available in the form of the fitted values of P_C for each particular dipole (Figure 10.14). For the majority of the traps, the returned probability of capture is approximately equal to 1, corresponding to the location of the trap being within the central region of the charge cloud. The frequency then drops dramatically with P_C, corresponding to traps that are located in regions where the charge density is lower or dipoles that have lost signal through radiation induced CTI. There is a daughter peak located at $P_C \approx 0.6$ that has a similar intensity ratio with respect to the primary peak to that observed in the energy level histogram.

The peak intensity for each of the dipole relationships differs by approximately (0.15/0.25) = 0.6, meaning that if a trap had a P_C = 1 but was fitted with Equation Equation 10.1 instead of Equation 10.2, the result would be a fitted value of P_C = 0.6. The location of the secondary peak closely matches this expectation (Figure 10.14), providing further evidence that the daughter peak illustrated in Figure 10.12 is an artefact of analysis as opposed to a separate defect species to the VV^{--}.

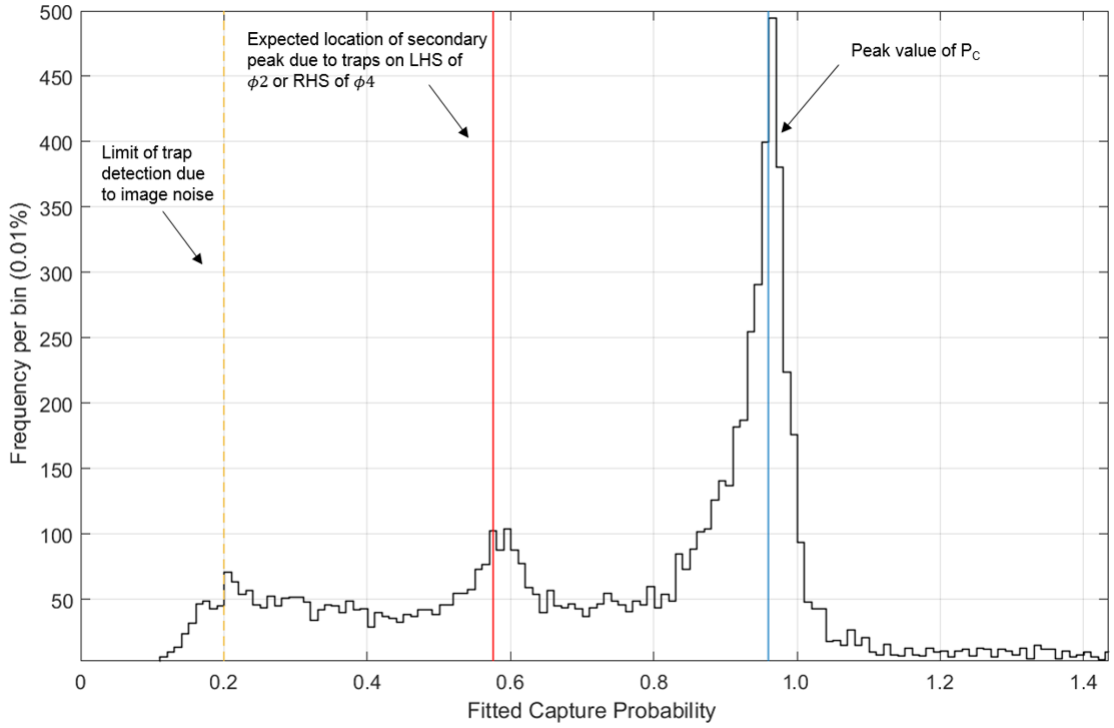

Figure 10.14: *Histogram of the fitted capture probability for each of the VV^{--} defects identified within a dataset at 165 K. The location of the secondary peak matches the expectation based on traps located under the LHS of $\phi 2$ or the RHS of $\phi 4$ being erroneously fitted.*

To confirm this theory, additional data was obtained for the VV^{--} using device 14222-11-2 (Irradiated to 1.0×10^9 protons/cm^2) using all four of the pumping schemes. The combination of all four schemes gave the ability to spatially resolve the defects at the sub-phase level, and remove those identified to lie at either the RHS or LHS of each of the storage phases from the emission time constant histogram. The result is that the daughter peak has been removed (Figure 10.15), providing the final evidence that the formation of this peak is due to a data analysis effect as opposed to a separate defect species.

It is entirely likely that a similar explanation is responsible for the split dipole peaks observed in the works of Wood *et al.*, (2016). Investigation into the architecture of the CCD47-10 revealed it has asymmetric phase widths which would give rise to multiple intensity relations using the clocking schemes described in this work.

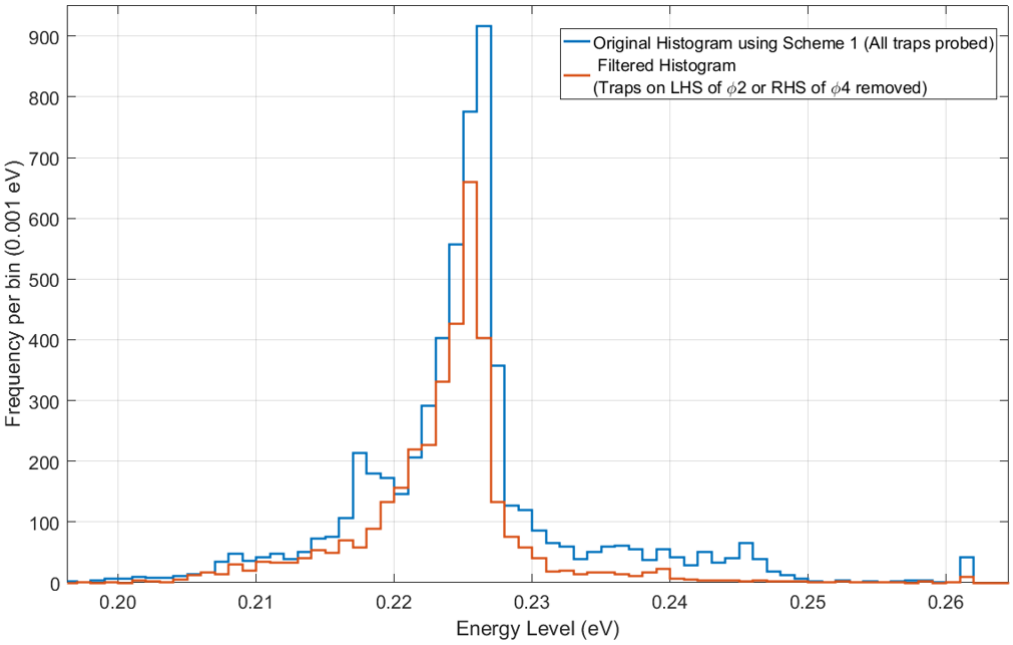

Figure 10.15*: Energy level histogram for the VV^{--} for the case where traps to the LHS of $\phi 2$ and RHS of $\phi 4$ are included (blue) and when they are not included (red). The removal of the daughter peak confirms that its presence is due to a fitting artefact.*

Once these defects are removed it is interesting that the primary peak retains the same asymmetry shown in Figure 10.12 with a greater weighting towards the conduction band edge. There are many possibilities for this observation:

1. The VV^{--} remains the primary defect responsible for the peak, however, internal device effects (e.g. field enhanced emission, lattice strain) distort the energy level preferentially towards the conduction band edge.
2. An additional defect species with energy level very close to the VV^{--} has been located during analysis. The resulting primary peak is actually the super-position of two very closely spaced peaks, giving rise to the asymmetric form seen in Figure 10.15.
3. The VV^{--} remains the primary defect responsible for the peak, however, additional processes are affecting the fitting process (e.g. radiation induced CTI) causing an artificial distortion in the peak towards the conduction band edge.

Each of these possibilities was investigated and found to give rise to asymmetry towards the conduction band edge, but not in a way that could fully explain the observed distribution. Further

work is required to fully understand why the defect energy levels are spread over such a large range and exhibit an asymmetric energy level distribution.

In summary, the use of a single scheme to analyse the trap data can give rise to a secondary daughter peak due to the inability to distinguish the physical location of the defect and hence fit the correct curve. For the remainder of the results presented in this Chapter, a single scheme was used for analysis due to simplicity and speed of data collection, however the knowledge of the expected location of the secondary peak allowed it to be ignored when considering the intrinsic properties of each defect.

10.4.2 The double acceptor state of the silicon divacancy (VV^{--})

The silicon divacancy is one of the best studied defects within silicon and is formed of two silicon vacancies that have combined to form a single complex. The defect has a total of four known electronic states, three of which correspond to energy levels in the band gap. The single and double acceptor states (VV^{-}, VV^{--}) can impact N-Channel device performance whereas the donor state (VV^{+}) is relevant for P-Channel devices (Table 10.3).

For the CGI, the VV^{--} was thought to impact both parallel and serial CTI (Chapter 8) and determination of the properties of this defect will allow optimisation of clocking schemes to reduce its impact on science performance following irradiation.

Table 10.3: *Summary of charge states of the divacancy relevant to CCD operation (Pichler, 2004).*

Charge State	Literature Energy Level (eV)	Notes
VV^{+}	E_v + (0.23-0.28)	Primarily relevant for P-channel devices.
VV^{-}	E_C - (0.39-0.42)	Relevant for N-channel devices (such as that used in this study)
VV^{--}	E_c - (0.21-0.23)	Relevant for N-channel devices (such as that used in this study)

The VV^{--} was probed at multiple temperatures to ensure that the behaviour of the mode emission time constant as a function of temperature was as expected. The results of four separate measurements are shown by Figure 10.16. The calculated mode energy level (assuming $\sigma = 5\times10^{-16}$ cm^{-2}, a literature value that may have large error was consistent for each measurement and is summarised within Table 10.4.

Table 10.4: *Summary of measurements of the mode VV^{--} emission time constant and corresponding energy level for a variety of temperatures.*

Temperature (K)	Mode Emission Time constant (s)	Corresponding Mode Energy Level (assuming $\sigma = 5\times10^{-16}$ cm^{-2}) (eV)
158 ± 1	$(1.65\pm0.13)\times10^{-4}$	0.226 ± 0.004
165 ± 1	$(8.41\pm0.13)\times10^{-5}$	0.226 ± 0.003
178 ± 1	$(2.10\pm0.13)\times10^{-5}$	0.226 ± 0.005
183 ± 1	$(9.55\pm0.13)\times10^{-6}$	0.224 ± 0.005

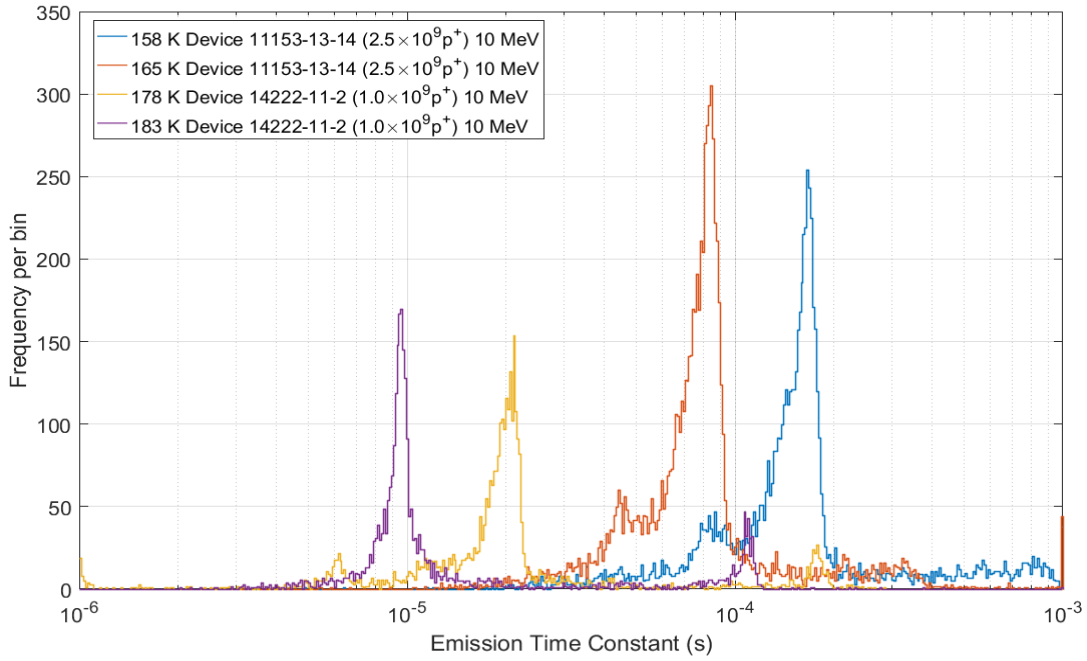

Figure 10.16: *Emission time constant histograms for the VV^{--} at multiple temperatures. Note two different devices were used for these measurements, and the factor difference in traps between each device is consistent with the difference in proton fluence.*

Detailed error analysis was performed on the fitted emission time constants and calculated energy levels for each defect to ensure that fitting routines were behaving as expected and not producing unwanted artefacts in the final data. Figure 10.17 shows the energy level of defects identified from a dataset at 165 K with their respective error. There is a large cluster of points at $E \approx E_C$ - 0.225 eV with error $\Delta E < 8\times10^{-4}$ eV that is consistent with the expected location of the VV^{--} There is a spread of points that have a similar energy level but exhibit higher error. The spread on the energy level of VV^{--} is much larger than the estimated error for any given single calculation - the cluster of defects extends across range of almost 10^{-2} eV in a region where the mean estimated error is almost an order of magnitude lower. This is strong evidence that the

distribution of energy levels of these defects is intrinsic and not an artefact of measurement noise.

The clustering of other defects with different energy levels around 0.240 eV and 0.245 eV can be seen, which also have an error of order 10^{-3} eV. The error increases as the energy level moves further from the conduction band edge due to the maximum phase time used for the dataset (around 2.6×10^{-4} s in this case) which in turn places a limit on the maximum energy level that can be probed at this temperature using the available data.

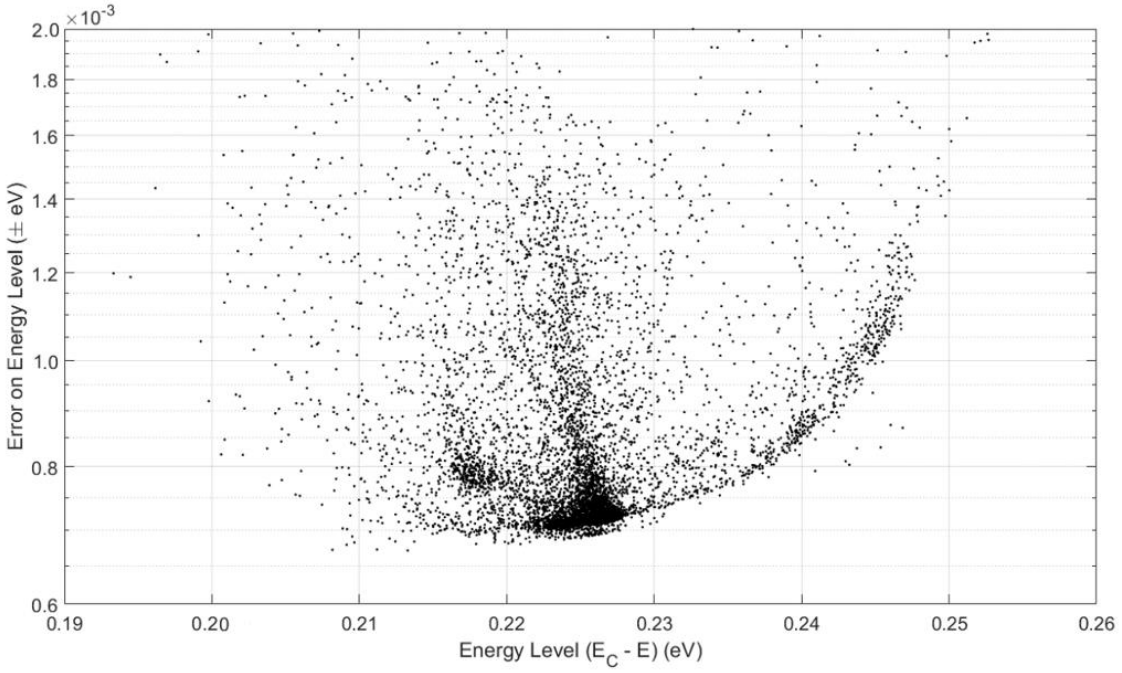

Figure 10.17: *Plot of energy level vs error on energy level for each defect identified in a dataset at 165 K. The clustering of points around 0.225 eV is thought to be due to the VV^{--}.*

The VV^{--} was probed at a variety of signal levels in order to provide multiple references points for a density calculation and to observe any possible effect of signal size on the distribution of the emission time constants. As the signal level is decreased the total number of identified defects also decreases owing to the shrinking physical size of the charge cloud (Figure 10.18). The general form of the histogram remains consistent, including the expected daughter peak and a possible shoulder peak (Figure 10.19).

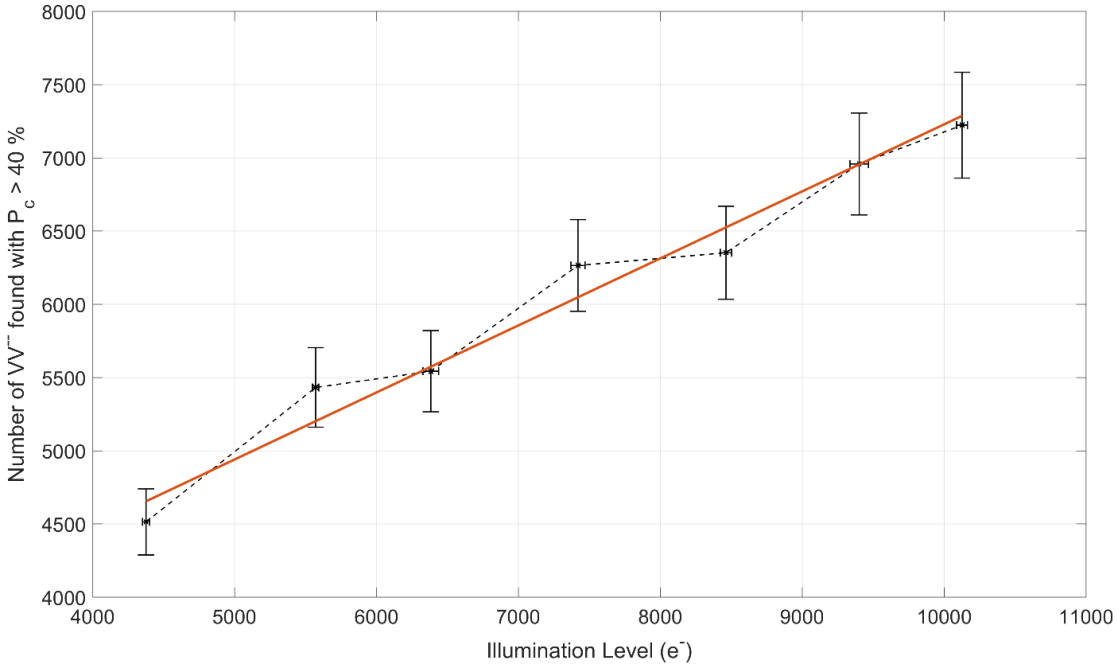

Figure 10.18: *Number of VV^{--} found with P_C > 40% as a function of signal level. The functional form is expected to be logarithmic but was approximated to be linear over this signal range. (Measurements of the TCAD signal volume in the CCD201 over the same range showed that the data was well represented by either a linear or logarithmic function over this signal range).*

The post-irradiation trap density was calculated by finding the number of VV^{--} present at a given signal level and dividing by the volume probed by the trap pumping technique at that particular signal level, given by TCAD. The volume probed was found by multiplying the volume probed per pixel by the number of pixels analysed during trap pumping analysis (in this case, an 800 x 300 pixel grid).

The results for the device irradiated to 2.5×10^9 protons/cm^2 are consistent across the range of signal levels that were tested (Table 10.5). The uncertainty in the calculated value begins to increase as the signal level is lowered since the signal level that is pumped (maximum of 2000 e$^-$ for P_C =1) is becoming comparable to the background signal level. The effective volume available for pumping therefore starts to decrease significantly as a result.

The calculation was also performed on a device irradiated to 1.0×10^9 protons/cm^2 (Table 10.6) and on the control regions of each device (Table 10.7) to observe the dependence on fluence level. It should be noted that the control regions would have experienced a small degree of radiation damage due to secondary neutrons during the irradiation, and so may exhibit a slightly higher density than an un-irradiated device. The density of defects as a function of irradiation fluence was found to be linear, as expected (Figure 10.20).

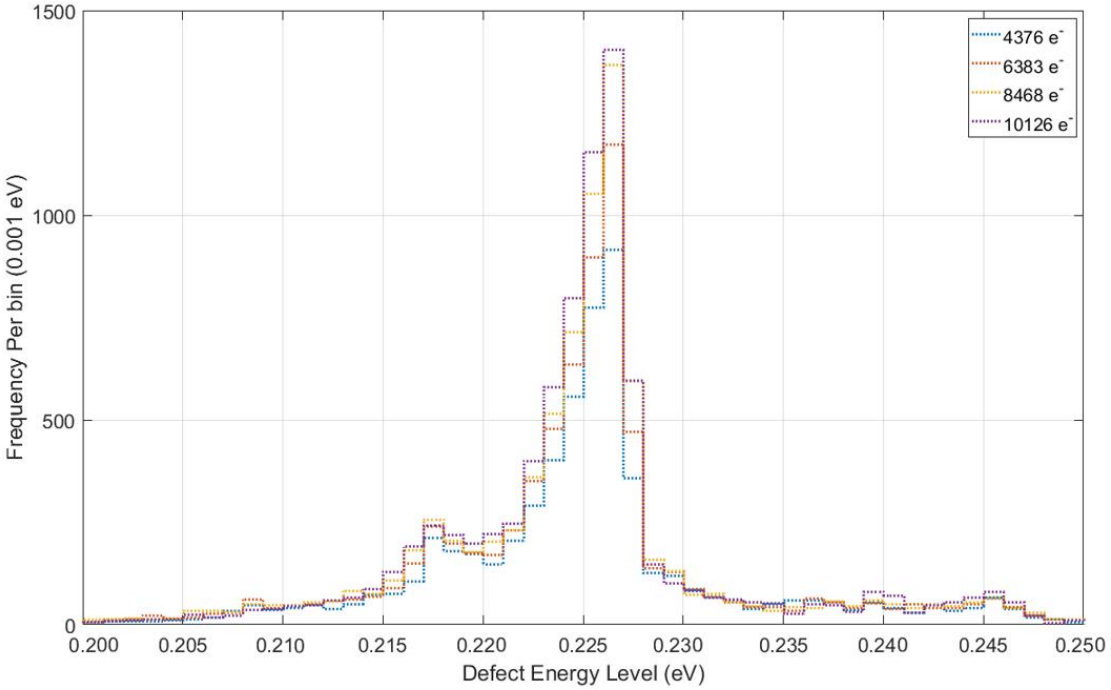

Figure 10.19: *Histogram of VV^- energy levels as a function of illumination level. The histogram retains the same functional form as a function of illumination level, as expected.*

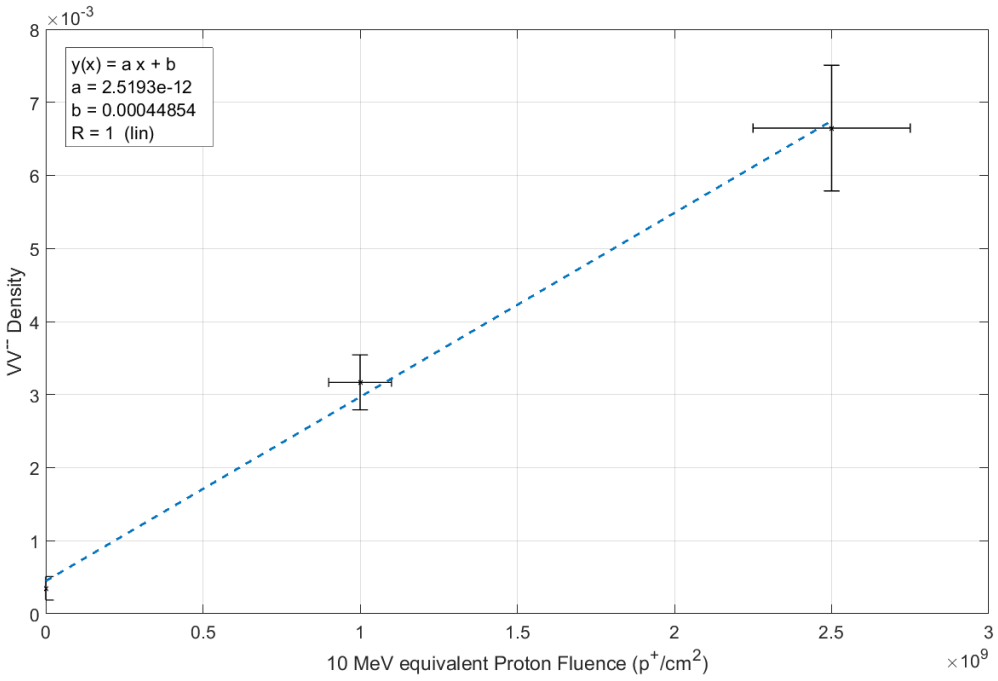

Figure 10.20: *Plot of the density of VV^- defects as a function of proton fluence. The data illustrated here is from devices that were irradiated at room temperature.*

Table 10.5: *Summary of calculated density values of the VV^{--} for a device irradiated to 2.5×10^9 p/cm^2 at room temperature using 74 MeV protons normalised to a 10 MeV equivalent fluence.*

Illumination Level (e^-)	Number of VV^{--} identified corresponding to $P_C >$ 0.40 (800 × 300 pixel ROI)	Density of VV^{--} (μm^{-3}) for a device irradiated to 2.5×10^9 p/cm^2
10127±38	7222	$(6.89 \pm 0.78) \times 10^{-3}$
9402±65	6957	$(6.88 \pm 0.80) \times 10^{-3}$
8463±40	6351	$(6.61 \pm 0.81) \times 10^{-3}$
7420±50	6264	$(6.92 \pm 0.89) \times 10^{-3}$
6383±55	5542	$(6.52 \pm 0.88) \times 10^{-3}$
5571±22	5431	$(6.62 \pm 0.94) \times 10^{-3}$
4376±25	4513	$(6.08 \pm 0.92) \times 10^{-3}$

Table 10.6: *Summary of calculated density values of the VV^{--} for a device irradiated to 1.0×10^9 p/cm^2 at room temperature using 74 MeV protons normalised to a 10 MeV equivalent fluence.*

Illumination Level (e^-)	Number of VV^{--} identified corresponding to $P_C >$ 0.40 (800 × 300 pixel ROI)	Density of VV^{--} (μm^{-3}) for a device irradiated to 1.0×10^9 p/cm^2
8484±46	2808	$(2.92 \pm 0.35) \times 10^{-3}$
9503±44	3468	$(3.41 \pm 0.40) \times 10^{-3}$

Table 10.7: *Summary of calculated density values of the VV^{--} for the control regions of devices irradiated at room temperature using 74 MeV protons normalised to a 10 MeV equivalent fluence.*

Device	Illumination Level (e^-)	Number of VV^{--} identified corresponding to $P_C >$ 0.40 (800 × 300 pixel ROI)	Density of VV^{--} (μm^{-3}) for control regions of un-irradiated devices
14222-11-2	8562±47	358	$(3.72 \pm 1.50) \times 10^{-4}$
11153-13-14	10745±41	331	$(3.26 \pm 1.70) \times 10^{-4}$

10.4.3 The "unknown" trap species

Initially, two datasets were obtained to search for the "unknown" trap, one at 175 K and another 180 K. Some defects were found within this parameter space, but none with a density sufficient to contribute to CTI. The results from these datasets strongly suggested that either the "Unknown" trap as seen by Holland (1993) was not present in this device, or that it is present but within a different region of the trap parameter space. Further datasets were obtained at successively higher temperatures until the concentration of defects located in the analysis became significant. A total of 5 datasets were obtained that contained evidence of a trap within the target parameter space consistent with the unknown defect in this study. Table 10.8 summarises the results for the mode emission time constant, while Figure 10.21 shows the trend of emission time constant vs temperature for device 11153-13-14.

The calculated mode energy level, assuming $\sigma = 5\times10^{-16}$ cm^{-2}, for this defect appears to be centred around 0.34-0.35 eV (Table 10.8) and was consistent for datasets over a wide range of temperatures (Figure 10.22). The error on the energy level, using the assumed cross section, is also small as shown by Figure 10.23. The defect energy level differs considerably from the originally ascribed value of 0.30 eV (Holland, 1993) and is also significantly different from that of the VV^- for the assumed cross section value. For each of the emission time constant histograms, a daughter peak can be seen that was also noted during analysis of the VV^{--} (Figure 10.21). The origin of this daughter peak is believed to be the same as that seen for the VV^{--} whereby traps on the LHS of $\phi 2$ and RHS of $\phi 4$ are being probed that obey a different intensity curve.

The density of the defect was calculated for the device irradiated at room temperature to 2.5×10^9 protons/cm^2 and found to agree, within error, with the density for the VV^{--} for this fluence (Table 10.9). The density of traps within the control region also agrees with the VV^{--} within error (Table 10.10).

It is unclear whether the trap identified in this study at this position is the same as that seen by Holland, whether this is a new defect entirely, or whether this is in fact the VV^- albeit in an unexpected position. The possibility of this trap being the VV^- is discussed in more detail in the next section. Regardless of its structural identity, a key conclusion is that this defect is present at a density that will contribute to CTI under certain temperature and clocking scheme configurations and has not been seen before within this section of the trap parameter space in other studies.

Table 10.8: *Summary of emission time constant values as a function of temperature and the corresponding mode energy level for the Unknown trap.*

Temperature (K)	Mode Emission Time constant (s)	Corresponding Mode Energy Level (assuming $\sigma = 5\times10^{-16}$ cm^{-2}) (eV)
198 ± 1	$(4.04\pm0.10)\times10^{-3}$	(0.344±0.003)
203 ± 1	$(2.50\pm0.10)\times10^{-3}$	(0.345±0.003)
210 ± 1	$(1.25\pm0.05)\times10^{-3}$	(0.343±0.003)
217 ± 1	$(6.40\pm0.17)\times10^{-4}$	(0.345±0.003)
226 ± 1	$(2.90\pm0.17)\times10^{-4}$	(0.346±0.003)

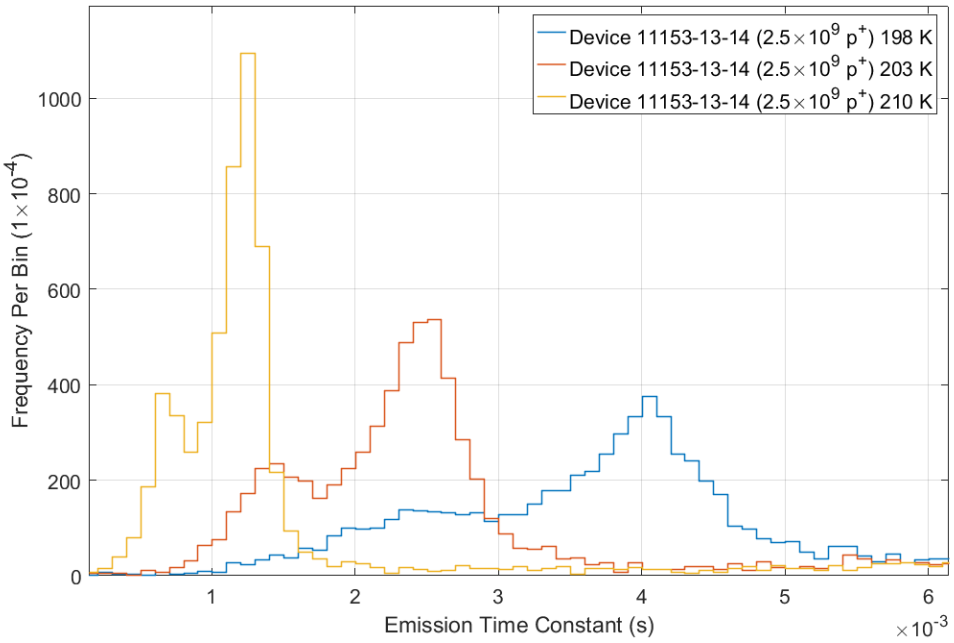

Figure 10.21: *Emission time constant histograms for what may be the "unknown" defect obtained at three separate temperatures.*

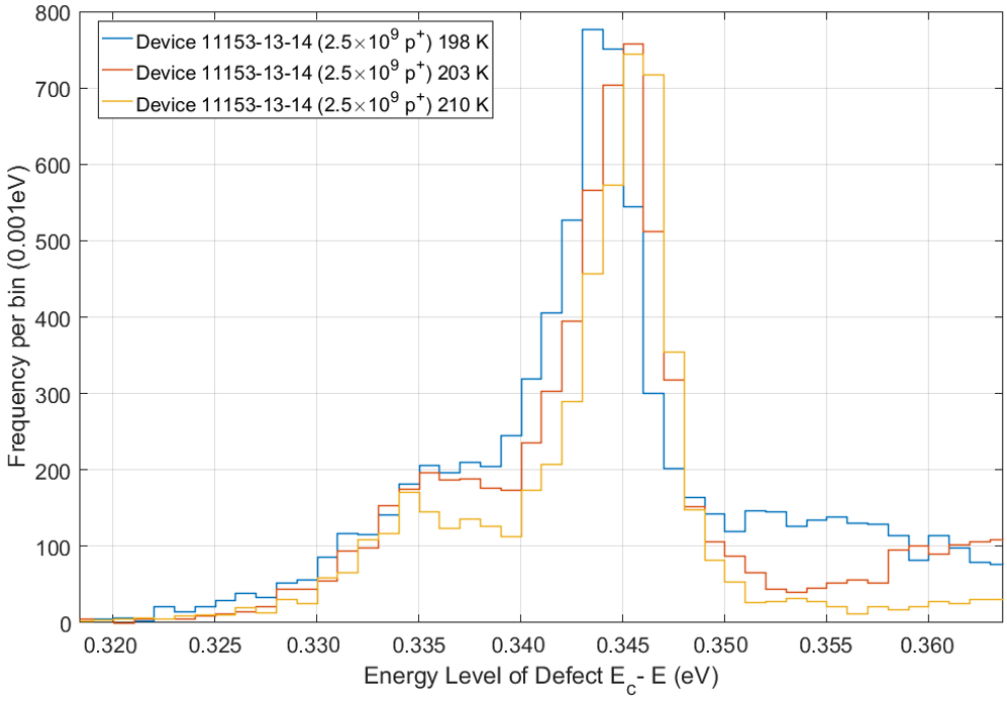

Figure 10.22: *Energy level histograms for each of the datasets shown in Figure 10.21 assuming a cross section of σ=5×10^{-15} cm^{-2}. The mode value agrees within error for each of the datasets.*

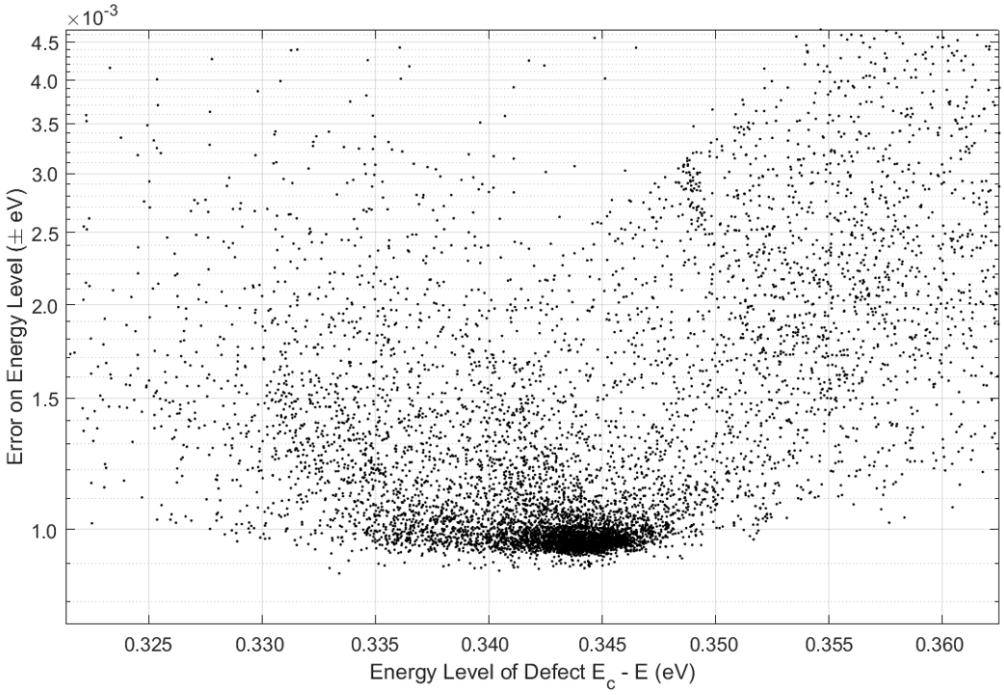

Figure 10.23: *Energy level error diagram for the what may be the "unknown" defect or the VV-. The error on the calculated energy level (assuming a cross section of σ=5×10^{-16} cm^{-2}) is of order 10^{-3} eV.*

Table 10.9: *Summary of density results for what may be the unknown trap or the VV^- for a device irradiated to 2.5×10^9 protons/cm^2 (10 MeV) at room temperature.*

Illumination Level (e^-)	Number of "Unknown" identified corresponding to $P_C > 0.40$ (800 × 300 pixel ROI)	Corresponding density of traps (μm^{-3})
10959±210	9592	$(7.55\pm0.76)\times10^{-3}$
10015±316	8988	$(7.38\pm0.77)\times10^{-3}$
8627±105	7899	$(6.92\pm0.76)\times10^{-3}$

Table 10.10: *Summary of density results for what may be the unknown trap or the VV^- for the **control region** of a device irradiated to 2.5×10^9 protons/cm^2 (10 MeV) at room temperature.*

Illumination Level (e^-)	Number of "Unknown" identified corresponding to $P_C > 0.40$ (800 × 300 pixel ROI)	Corresponding density of traps (μm^{-3})
11620±305	277	$(2.12\pm0.28)\times10^{-4}$

10.4.4 The single acceptor state of the silicon divacancy (VV^-)

It is generally accepted that the double and single acceptor states of the silicon divacancy are ascribed to the same silicon defect under different charge states. The association of the two energy levels to the same defect was corroborated by the observation that both levels have perfectly correlated introduction rates during irradiation with electrons and γ rays (Pichler, 2004). This one-to-one proportionality was not observed in irradiation studies with protons and alpha particles, nor when neutrons or ions in the MeV range were implanted. In these investigations, the concentration associated with the single acceptor level at $E \approx E_C - 0.40$ eV was found to exceed that of the concentration associated with the double acceptor level at $E \approx E_C - 0.23$ eV significantly around the maximum of the damage (Pichler, 2004). This was explained by Vasil'ev *et al.* (1989) by a bending of the energy bands near disordered regions resulting from the collision cascade which inhibits the observation of the $E \approx E_C - 0.23$ eV level here. The conclusion was that the $E \approx E_C - 0.23$ eV level corresponds to the divacancies in the undisturbed matrix remote from the cores of the disordered regions while the level at $E \approx E_C - 0.40$ eV accounts for the total concentration.

This is one explanation for the observed difference in concentration, however, others include the postulation that other defects are present that are erroneously ascribed as VV^- when they are in fact due to an additional defect with very similar energy level.

Preliminary evidence for what appeared to be the VV^- was seen in the dataset obtained at 208 K (Figure 10.11) which was primary intended to identify the "unknown" defect. Defects were seen that were consistent with the energy level of the VV^-, however, the error on the energy level of these defects was large and, in many cases, comparable to the energy level itself and so the results could not be trusted. Datasets were obtained at 217 K and 226 K with the purpose of identifying the VV^-, however, the calculated energy level and density was consistent with that of the Si-E centre and no defects with the expected properties of the VV^- could be located (Figure 10.24).

This finding raised the question as to whether what was previously identified as the "unknown" was in fact the VV^-. Since the VV^- (single acceptor) and the VV^{--} (double acceptor) are ascribed to the same physical defect, location analysis was performed whereby a map of "unknown" defects across the CCD201 was correlated with a map of the VV^{--} for approximately equal signal levels (≈ 10,000 e^-).

The result is shown by Figure 10.25 and no correlation was seen, which implied that what has been observed here is not the VV^-. That being said, other physical mechanisms may be at play that mask the observation of one charge state under certain conditions. Further investigation into defect dynamics is required to fully understand these observations.

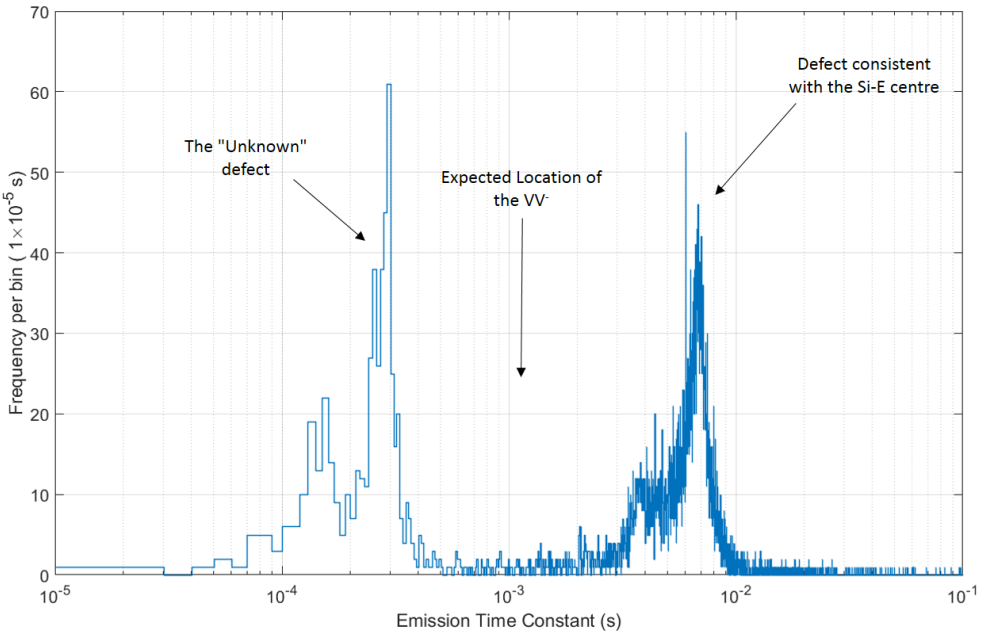

Figure 10.24: *Histogram of emission time constants for a dataset obtained at 226 K that shows the distinct peaks due to what may be the "unknown" and a defect that is consistent with the Si-E centre. No peak was identified in the expected location of the VV$^-$. Note that the integrated counts under the supposed Si-E centre peak are much higher than that of the "unknown" defect (about 4× higher). The linear binwidth on the logarithmic scale does not make this readily apparent.*

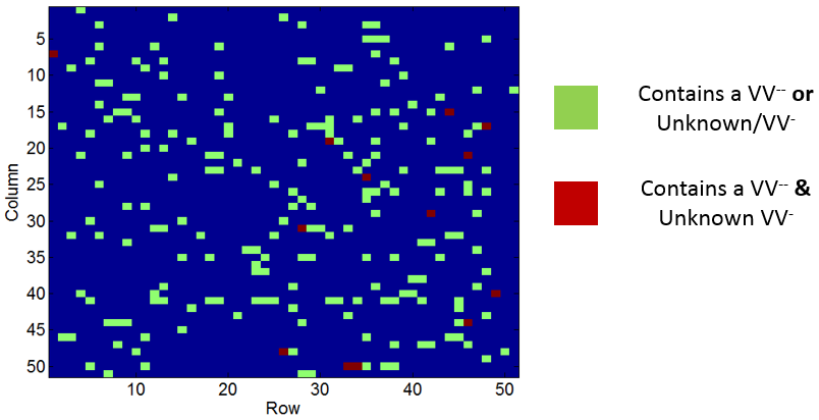

Figure 10.25: *50×50 pixel map of the irradiated region of a CCD201-20 where the locations of the VV^{--} and unknown defect have been correlated. If the unknown defect was in fact the VV$^-$ then one may expect the locations to correlate strongly since they are different states of the same defect. Other physical effects may be present that explain a lack of correlation.*

The energy level of the VV$^-$ is reasonably well defined as E =E_C - (0.39-0.42) eV, however literature values for the cross section vary considerably. There is a degeneracy between the value for the cross section and energy level such that different combinations of these values may result in a very similar emission time constant at a given temperature, shown by Equation 10.3.

$$\tau_e = \frac{1}{\sigma N_c v_{th}} \cdot e^{\left(\frac{E}{k_B T}\right)}$$ Equation 10.3

There is therefore potential that the unknown was in fact the VV^- but not seen in the expected location due to an inaccurate literature value for the cross section. The cross section was set as a free parameter, while keeping the energy level at the lowest literature value of 0.39 eV and was fitted to the available data. The best fit value was approximately $\sigma = 7\times10^{-15}$ cm^{-2}. The data is still better represented by a defect with energy $E = E_C - 0.34$ eV and $\sigma = 5\times10^{-16}$ cm^{-2} (i.e. a different defect to the VV^-). The result of the two fits is shown by Figure 10.26.

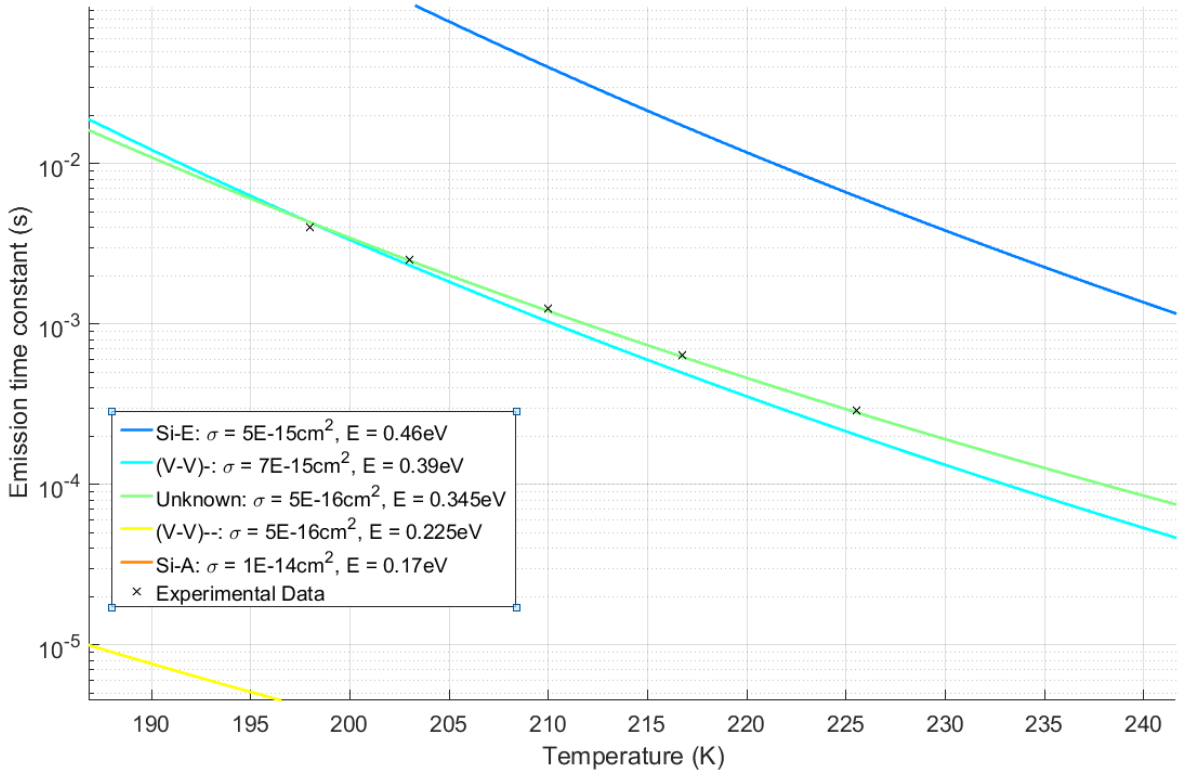

Figure 10.26: *Illustration of Equation 10.3 for values of energy and cross section that allow the VV^- to closely match what was observed for the unknown defect. Although the fit result is close, the data is still better represented by a different defect to the VV^-.*

In summary, the supporting evidence for the defect identified in the previous section being the "unknown" defect is that the locations do not appear to correlate between itself and the VV^{--} and the unaltered energy and cross section do not agree with the literature values of the VV^-. Evidence for the defect identified in the previous section being the VV^- is that the density is close to that of the VV^{--}, implying a 1:1 introduction rate. The presence of the VV^- has also been inferred in previous investigations through CTI measurements. Alteration of the cross section while keeping

the energy in-line with literature values also produces emission time constants that are consistent with what was measured in the previous section, however, the data is still better fitted by the "unknown" defect with E = E_C - 0.34 eV.

10.4.5 The phosphorus vacancy complex (Si-E/PV)

The Si-E centre is formed from a phosphorus vacancy pair and has literature values for the energy ranging from E = E_C - 0.43-0.47 eV (Pichler, 2004). Its presence has been noted in many past investigations of CCD performance following irradiation (for example see the works of Holland, 1993 and Hardy *et al.*, 1998). Phosphorus is commonly said to be responsible for the defects noted around this energy level as the defect is not found to be present in P-channel devices where boron is the buried channel dopant. In addition, annealing studies have found a defect with energy level consistent with the Si-E centre to disappear following extended annealing in the range 353-373 K, consistent with the annealing temperature of the phosphorus vacancy complex (Moll, 1999).

Three datasets were obtained that were deemed suitable for detailed analysis of the Si-E centre, one at 238 K using the device irradiated to 2.5×10^9 protons/cm^2, and two others at 243 K and 248 K using the device irradiated to 1.0×10^9 protons/cm^2. The mode emission time constants and energy levels (assuming a literature cross section of $\sigma = 2\times10^{-15}$ cm^{-2}) are in good agreement with the literature range of E = E_C - 0.43-0.47 eV for each of the datasets and are summarised within Table 10.11.

Figure 10.27 shows a histogram of the calculated energy levels assuing a literature cross section of $\sigma = 2\times10^{-15}$ cm^{-2}) for the dataset obtained at 238 K. The width of the primary peak is very large and spreads approximately 0.2 eV before falling below 10% intensity either side of the peak. The error on the calculated energy levels is shown by Figure 10.28 and is once again of order 10^{-3}, indicating the spread is not due to measurement error. The implications of such a large spread are large, since at very low temperatures even a small variation in the defect energy level can cause a large variation in the emission time constant. Translating this result to the CGI operating temperature of 165 K, emission time constants for this trap can vary between 30 s and 120 s.

Table 10.11: *Summary of measured emission time constants for the Si-E centre and corresponding mode energy levels assuming $\sigma = 5\times10^{-15}$ cm^{-2}.*

Temperature (K)	Mode Emission Time constant (s)	Corresponding Mode Energy Level (assuming $\sigma = 2\times10^{-15}$ cm^{-2}) (eV)
238 ± 1	(1.60±0.08) × 10^{-3}	(0.450±0.005)
243 ± 1	(9.90±0.23) × 10^{-4}	(0.450±0.005)
248 ± 2	(5.90±0.19) × 10^{-4}	(0.449±0.005)

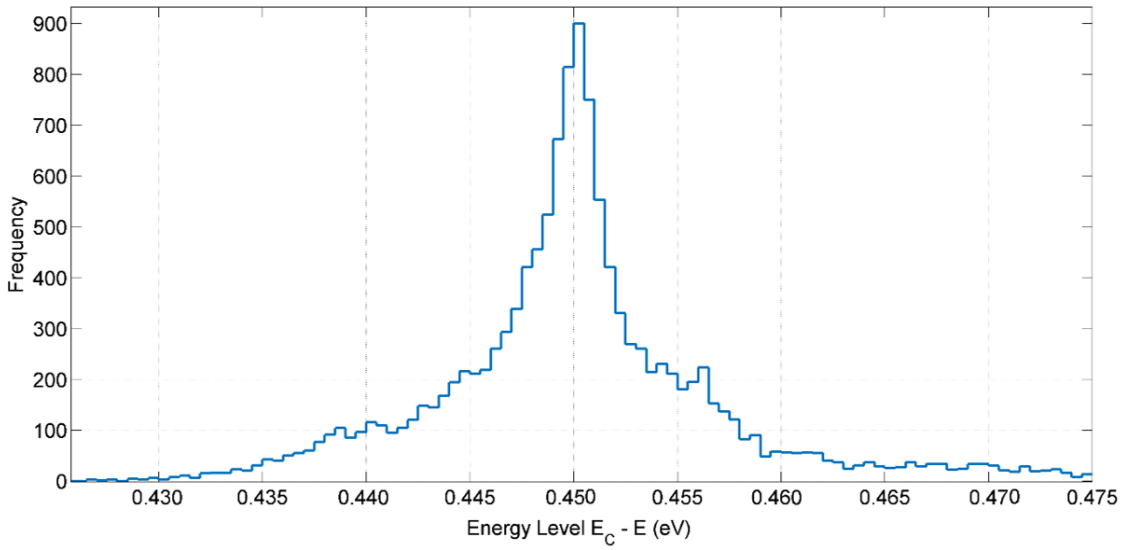

Figure 10.27: *Energy level histogram for the Si-E centre assuming $\sigma = 5\times10^{-15}$ cm^{-2}. Dataset was obtained at 238 K.*

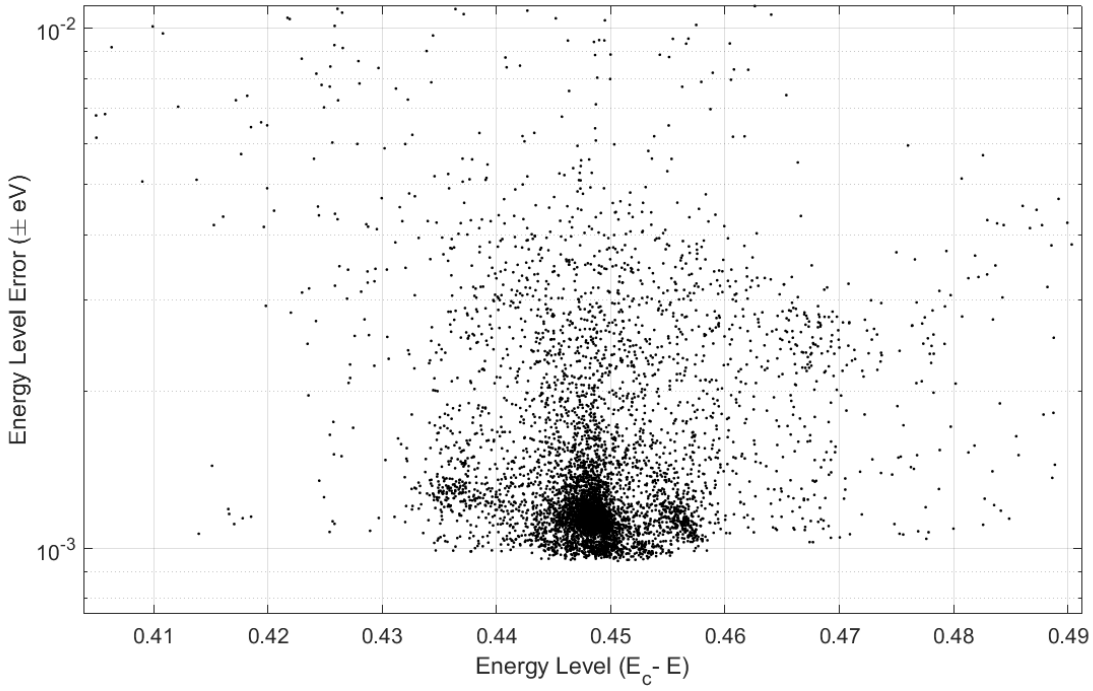

Figure 10.28: *Energy level error diagram for the Si-E. The error on the calculated energy level (assuming a cross section of σ=5×10^{-15} cm^{-2}) is of order 10^{-3} eV.*

The calculated density of the Si-E was found to be linear with fluence and approximately 4-5× larger than that of the VV^{--} and unknown defect (Table 10.12 and Figure 10.29). The control region density was found to be similar to that seen for the other defects in this study. Figure 10.29 shows a comparison of a 50 x 50 pixel grid from a CCD201 irradiated to 1.0 × 10^9 protons/cm^2 for both the VV^{--} and the Si-E where the difference in density is very clear to see. This result is consistent with the observations made during the room temperature and cryogenic irradiation campaign, where X-ray CTI results showed that "slow" traps (the VV^-/unknown) dominate the measurement compared to the faster traps (VV^{--}/Si-A) that have little/no impact. This was shown in Section 8.3 through comparison of charge in the tail of the X-ray to the total charge lost. The table is included again for clarity (Table 10.14). Chapter 8 discussed how:

- CTI in the parallel direction is impacted by the VV^{--} ,VV^-/Unknown, Si-E.
- CTI in the serial direction is impacted by the VV^{--}.

The analysis showed that only half the VV^{--} contributes to parallel CTI, and so the remaining 54 e^- in the parallel tail are due to effectively half of the total density of this defect. It is therefore expected that a factor ×10 greater charge loss will occur due to the combined effect of the VV^- /unknown and the Si-E due to the density difference, equating to approximately 540 e^- not emitted in the first few pixels. This rough calculation accounts for approximately 85% of the total charge loss and so the densities presented here are fairly consistent with the CTI results presented earlier for Fe^{55} X-ray CTI.

Table 10.12: *Summary of measured density values for the Si-E centre for each device in the irradiated regions.*

Device	Illumination Level (e^-)	Number of "Si-E" identified corresponding to $P_C > 0.40$ (800 × 300 pixel ROI)	Corresponding density of traps (μm^{-3})
11153-13-14	10841±104	47548	$(3.10\pm0.40) \times 10^{-2}$
14222-11-2	15629±179	23190	$(1.28\pm0.30) \times 10^{-2}$
14222-11-2	15275±85	19533	$(1.09\pm0.25) \times 10^{-2}$

Table 10.13: *Summary of density values for the Si-E centre for each device measured in the control region.*

Device	Illumination Level (e^-)	Number of "Si-E" identified corresponding to $P_C > 0.40$ (800 × 300 pixel ROI)	Corresponding density of traps (μm^{-3})
11153-13-14	10942±60	706	$(4.59\pm0.59) \times 10^{-4}$
14222-11-2	15135±164	576	$(3.22\pm0.39) \times 10^{-4}$
14222-11-2	14801±86	511	$(2.89\pm0.35) \times 10^{-4}$

Table 10.14: *Summary of charge distribution from 'average' X-ray event from the cryogenic 5.0×10^9 protons/cm^2 fluence. Summing the deferred charge in the parallel and serial tails shows not all of the captured charge is emitted in the first trailing pixels. The majority is lost to "slow" traps, thought to be the VV$^-$ and Si-E.*

Original Charge Packet	1616 e^-
Measured Charge at Output (average)	817 e^-
Charge in parallel tail (6 pixels)	54 e^-
Charge in serial tail (6 pixels)	39 e^-
Not emitted in first 6 pixels	706 e^-

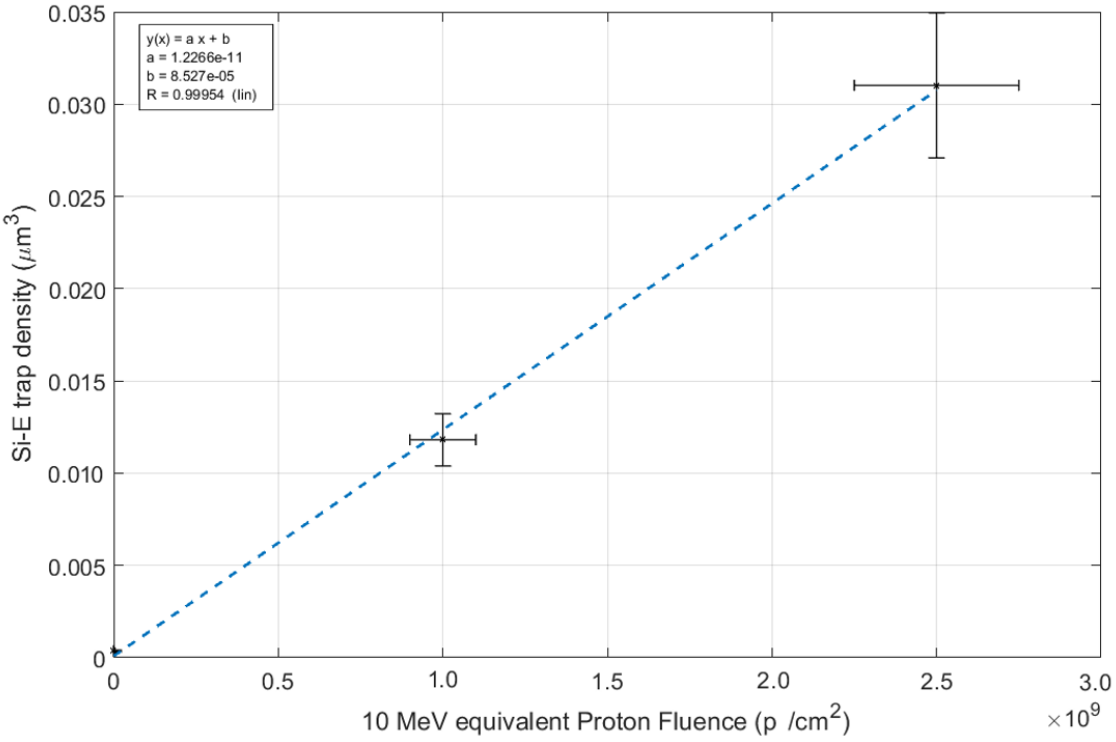

Figure 10.29: *Plot of trap density vs 10 MeV equivalent proton fluence. Applies to devices irradiated at room temperature.*

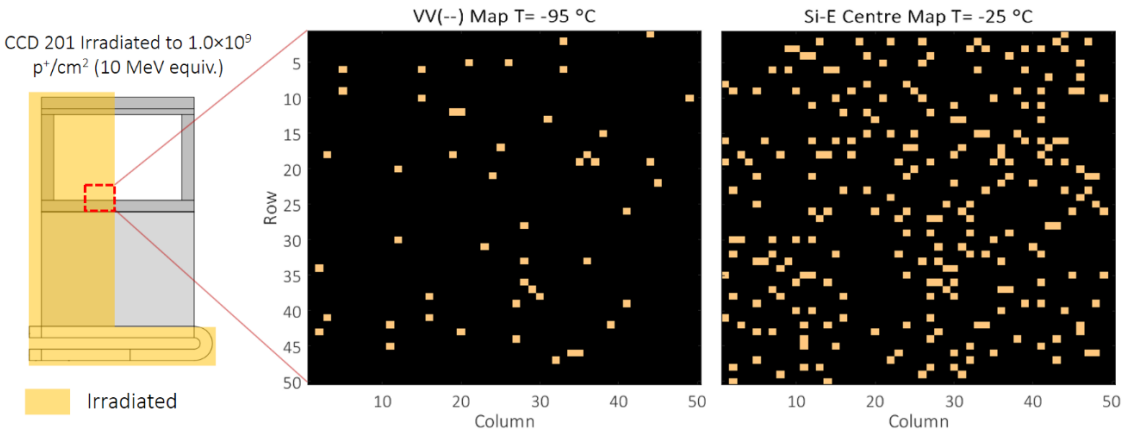

Figure 10.30: *50 x 50 pixel grid from a CCD201 irradiated to 1.0×10^9 protons/cm^2 for both the VV^{--} and the Si-E. The Si-E has an approximate ×4 higher density than the VV^{--}.*

10.4.6 The Si-A centre

The Si-A centre is formed from an oxygen atom occupying an off-centre position in a vacancy between two silicon atoms (Pichler, 2004). The background oxygen concentration in silicon used to fabricate e2v devices is high at $\approx 10^{18}$ cm^{-3}, compared to $\approx 10^{16}$ cm^{-3} for the dopant concentration. As a result, the Si-A centre is often assumed to be the most abundant silicon defect that can potentially impact CTI prior to and following irradiation. Its shallow energy level, however, typically means that it predominantly affects serial CTI when operating at fast scan rates. The emission time constant is typically much quicker than the majority of feasible parallel clocking speeds such that parallel CTI remains largely unaffected. For this very reason, it was not possible to probe the Si-A centre using the experimental setup used for this study. The maximum possible parallel clock speed was approximately 0.5 MHz, and the lowest possible temperature was approximately 150 K. Under these conditions, the Si-A centre could still not be probed.

Instead, an attempt was made to probe the Si-A centre in the serial register. Here, it was possible to trap pump with effective pixel rates of a few MHz which was within the parameter space of the Si-A centre at the lowest temperatures feasible with the experimental setup. Initial tests using the irradiated devices revealed an additional complication whereby the density of defects was too high for analysis. This was in-line with expectations based upon literature estimates of the density when compared to other defects analysed in this study. Reduction of signal size to reduce the density of defects probed did not ameliorate the issue and use of the device irradiated to 1.0×10^{9} protons/cm^{2} yielded similar results. Instead, an additional un-irradiated engineering grade device was analysed as this was found to have a sufficiently low density of traps.

Additional complications were found in that clock overshoots and ringing using the current setup may have interfered with the pumping process at the fastest speeds, adding additional noise to the data. Serial CIC was found to vary as a function of the pumping speed which also added additional noise to the data. One dataset was returned that was deemed useful for analysis. The results are summarised by Table 10.15, Figure 10.31 and Figure 10.32.

The energy level, assuming a cross section of $\sigma=1\times10^{-14}$ cm^{-2}, is in agreement with the values seen in the literature (Hall *et al.*, 2014 and Pichler, 2004), however the uncertainty is high and it is recommended that further work should be performed on probing the Si-A centre should it be found this is an important defect for mitigating serial CTI for the CGI.

Table 10.15: *Emission time constant and mode energy level for the Si-A centre assuming* $\sigma=1\times10^{-14}\ cm^{-2}$.

Temperature (K)	Mode Emission Time constant (s)	Corresponding Mode Energy Level (assuming $\sigma = 1\times10^{-14}\ cm^{-2}$) (eV)
152 ± 1	$(1.21\pm2.0)\times10^{-7}$	(0.16±0.01)

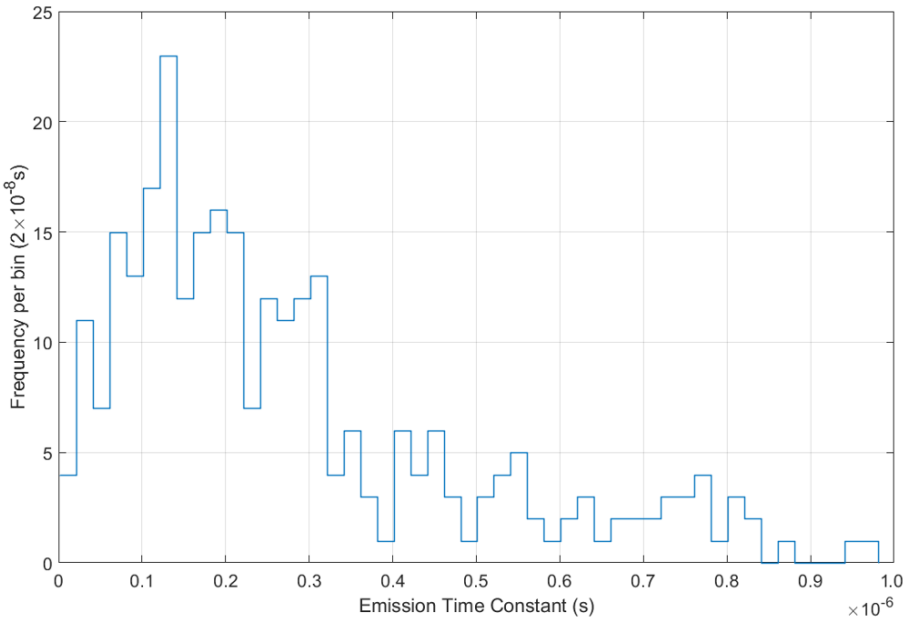

Figure 10.31: *Histogram of emission time constants for the Si-A centre probed at 152 K.*

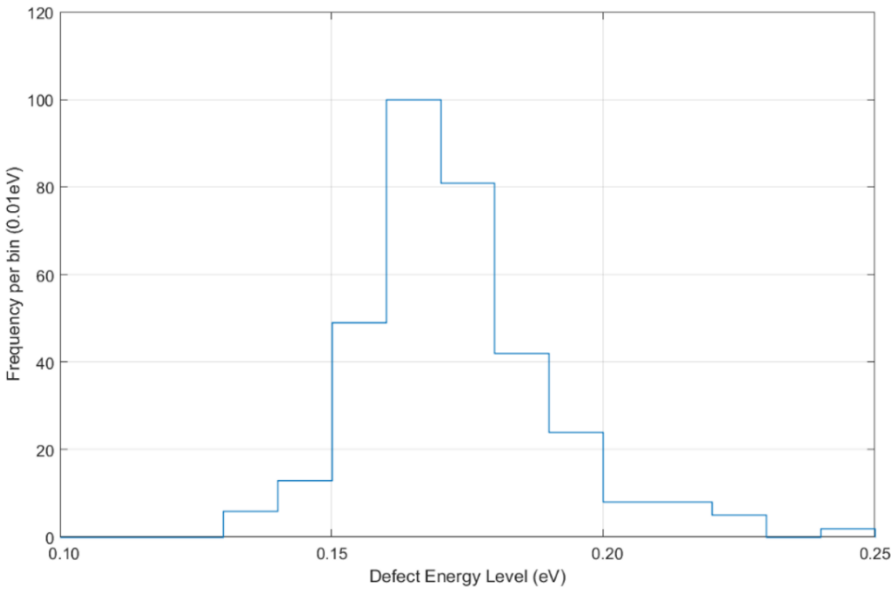

Figure 10.32: *Histogram of energy levels for the Si-A centre probed at 152 K assuming* $\sigma=1\times10^{-14}\ cm^{-2}$.

10.4.7 Other defects

During the initial search for the "unknown" trap a small density of defects were found with energy levels that were in between the dominant literature defects thought to impact CTI. Analysis of the intensity as a function of phase time indicated that these defects followed the expected relationships very well indicating that these defects were genuine and not artefacts of fitting routines being applied to device effects (e.g. cosmic rays, bright pixels etc.). The density of these defects was low, and the emission time constants were found to span a large range with no clear defined peak. Calculation of the density returned a value of approximately $2.0\pm1.0 \times 10^{-4}$ μm^{-3} (i.e. significantly less than the dominant species). This analysis showed that there is perhaps a low density of defects across the entire parameter space with a variety of energy levels and emission time constants. These are thought to be due to trace impurities within the silicon introduced during manufacturing.

10.5 Summary of results and implications for the WFIRST CGI

This chapter has described a detailed investigation whereby the trap pumping technique was applied, for the first time, to a 2-phase EM-CCD. To the authors best knowledge, it is the largest trap pumping investigation performed on a CCD to date and has provided invaluable information regarding the key defects responsible for CTI within CCDs. Figure 10.33 shows the original "trap diagram" first introduced in section 5.7 and below it is the "revised" trap diagram (Figure 10.33) showing the mode emission time constants measured at each temperature during this study, with modifications to the defect energy levels to achieve the best fit. Note the literature values for the cross sections have remained the same. The change is dramatic, with only the Si-A and Si-E have retained approximately the same position. All four defect species identified in this study have the potential to impact CTI within the CGI. Table 10.16 summarises the defect properties and the emission time constant at 165 K (CGI nominal operating temperature).

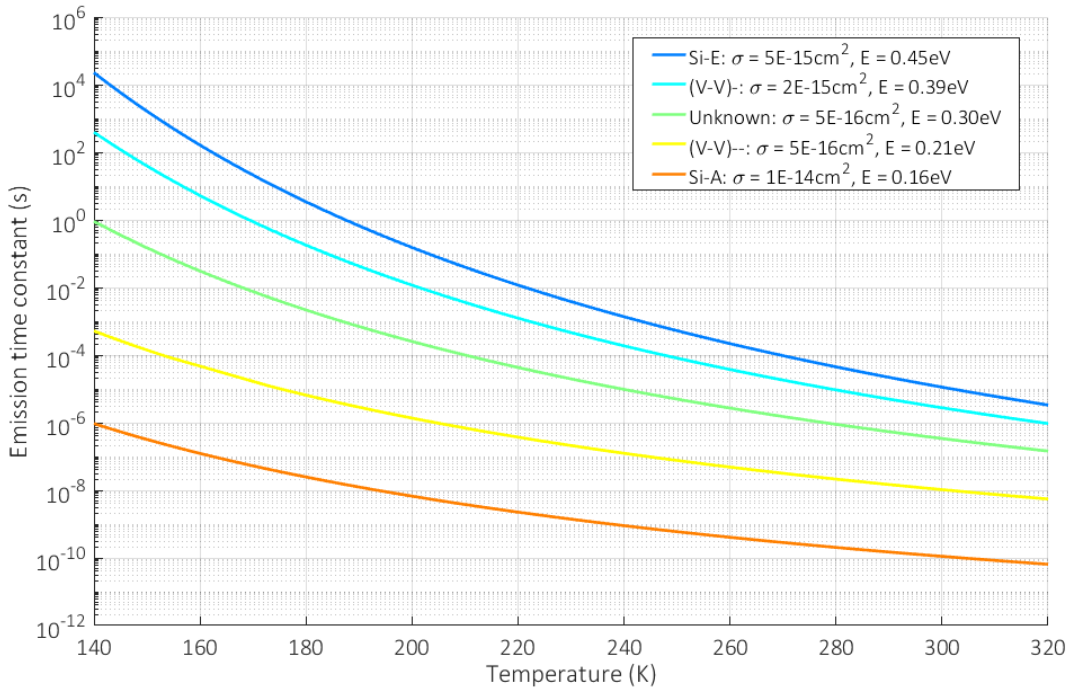

Figure 10.33: *"Trap diagram" using the literature values for defects taken prior to this study.*

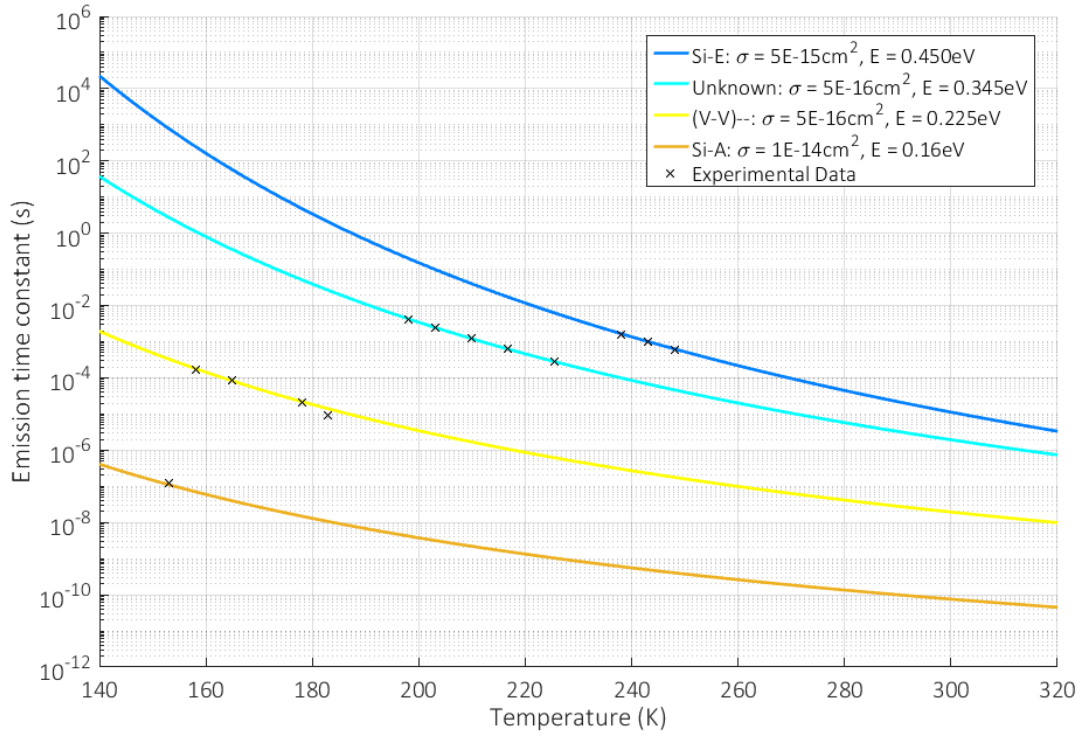

Figure 10.34: *Revised "trap diagram" based on the results of this study.*

The Si-E centre was the defect found to be measured with the highest density with an emission time constant of approximately 60 s at 165 K. Literature estimates place the density of the Si-A centre at double that of the Si-E centre, but this could not be measured in this study (Holland,

1993). The long emission time constant coupled with high density is problematic for CGI performance, since the baselined long integration times mean that a large fraction of these defects will empty between successive frames and capture signal charge. The probability that they will emit charge back into the original signal packet is near negligible. Mitigation against this particular species is therefore limited to either keeping trapping sites filled, preventing charge capture or thermal annealing. The first may be possible to an extent through reduction of the single frame integration time to the 10 s range as opposed to 100 s. A larger proportion of Si-E centres will then remain filled due to background cosmic ray flux than would be the case for a longer 100 s frame time. The penalty is the factor ×10 increase in CIC associated with the larger number of frame reads, and so the improvement in CTI will need to be balanced with this increase in noise. Preventing charge capture is possible to extent through faster operating speeds and shorter integration times, however even at the fastest baselined speed of 10 MHz the parallel delay is of order 1 ms and so charge capture is almost impossible to completely prevent. The effect of shorter integration time, faster operating speed and also the benefit of a narrow channel structure will be discussed in the next chapter and have the potential to provide a substantial reduction in CTI due to the Si-E centre.

Finally, a thermal anneal may significantly reduce the impact of the Si-E centre. Studies have shown that the Si-E centre undergoes significant thermal annealing in the temperature range of 353-373 K (Holland, 1993). The exact performance benefit appears to be dependent on the time that the device is annealed for, since the annealing process appears to have multiple stages, with Si-E centres annealing to be replaced with other vacancy complexes such as the V_2O centre. The impact on CTI following an anneal would therefore have to be measured experimentally to be sure of a benefit.

Although the Si-A centre is most populous, it is the defect of lowest concern for the CGI so long as the devices are appropriately optimised. Its shallow energy level means that it has a negligible impact on parallel CTI, thanks in part due to the 2-phase structure of the CCD201. In the serial section, clocking speeds greater than 1 MHz have the potential to allow Si-A induced CTI at 165 K however at fast speeds and low signal levels the capture probability is so small that it should not be much of a concern. There are therefore two mitigation strategies against the Si-A that can be employed, operation at slow scan rates so that any captured charge re-emits into the signal packet, or operating at fast scan rates to prevent the process of charge capture. The latter is more desirable since it has the added benefit of reducing the serial component of clock induced charge.

As will be shown in the next chapter, operation at 10 MHz reduces the capture probability to near negligible levels and so remains a viable mitigation strategy for the CGI to prevent the Si-A centre impacting the science objectives.

Finally, we are left with the divacancy centres which are predicted to predominantly affect the parallel CTI of the instrument. The densities of each of these defects are low compared to the Si-E and Si-A centres, however, they are harder to optimise against and have annealing temperatures higher than what would be considered practicable for a space mission (above 400 K (Pichler, 2004)). For the VV^{--}, the parallel delay times should be long enough such that any capture charge beneath the preceding phase will emit into the original packet. At 165 K this is a delay of approximately a 1 ms. Only charge beneath one half of the pixel will re-emit into the original packet, the remainder will be lost to a trailing pixel, and so a customised parallel clocking scheme whereby the total transfer is split into two ≈1 ms transfers should be considered. This operating mode would benefit from a slight increase in operating temperature (to approximately 160 K) to increase the fraction of charge that re-emits within this window. The impact of this temperature change on the Si-E centre CTI will be small so long as the frame integration time is reduced accordingly. The VV^{-} centre has a much longer emission time constant (a few seconds at 165 K) and so optimisation should be focused on keeping this defect filled. The entire frame readout should be performed within the space of a second to ensure that any filled VV^{-} remain filled throughout the entire frame read.

This stage of the investigation has therefore provided a wealth of useful results concerning the landscape of defects within the CCD201-20 and how they can potentially impact performance. With the properties of the four main defects known, attempts can be made to optimise CTI performance based upon their properties. Clock speed optimisations and narrow channel variants have been mentioned that can significantly improve performance in the presence of these defects, however, more understanding is required concerning the interaction of signal packets with trapping sites to be sure of the benefit. The next chapter discusses charge storage modelling within the CCD201-20 and builds upon some of the remarks in this summary with a focus on how CTI can be mitigated in the CCD201-20 through device modifications.

Table 10.16: *Summary of experimental results from trap pumping analysis. Literature values substituted where appropriate.*

Trap Species	Energy Level (eV)	Electron Capture Cross section (cm^{-2})	Mode emission time constant (s) (165 K) (3 s.f.)	Density following irradiation to 2.5×10^{9} p/cm^{2} (μm^{-3})	Notes
Si-A	(0.16±0.01)	1.0×10^{-14}	$(3.95\pm4.0)\times10^{-8}$	6.00×10^{-2}	Literature value for the density based upon it being twice the concentration of the Si-E centre. The Si-A centre could not be probed in the parallel section due to limitations of the experimental setup used in this study. A measurement was made in the serial direction at 152 K from which the emission time constant at 165 K was deduced.
VV^{--}	(0.226 ± 0.003)	5.0×10^{-16}	$(8.41\pm0.13)\times10^{-5}$	$(6.75\pm0.97)\times10^{-3}$	Emission time constant measured at 165 K. Energy level calculated using the literature value for the cross section and found to agree within error across multiple datasets. Values measured between two different devices were consistent.
Unknown/ VV^{-}	(0.345± 0.003)	5.0×10^{-16}	$(3.54\pm0.82)\times10^{-1}$	$(7.29\pm0.98)\times10^{-3}$	A trap was found with properties that were consistent with either the unknown trap or VV^{-} depending on the exact value for the cross section and energy used. Emission time constant at 165 K inferred from data measured at warmer temperatures.
Si-E	(0.450±0.005)	5.0×10^{-15}	(57.0 ± 24.0)	$(3.08\pm0.50)\times10^{-2}$	Emission time constant calculated for 165 K based on measurements at warmer temperatures. Values measured between two different devices were consistent.

11 Charge storage modelling in the CCD201-20

11.1 Introduction

The results from trap pumping presented in the previous chapter have helped highlight possible CTI mitigation strategies through the modification of parallel and serial clock timings to reduce the impact of bulk trapping sites. Although there may be a benefit, it is clear that regardless of the operating conditions, bulk trapping sites cannot be completely mitigated and so further understanding about the charge capture process in the presence of traps is required to inform optimum operating conditions. In addition, device modifications may be possible that reduce the volume of charge packet that is available due to capture by the bulk traps. A study as to whether such modifications can improve CGI science performance in radiation damage is presented.

11.2 Signal volume theory

An electron contained within the potential well of a CCD is not confined to a point but better represented as a charge density distribution whereby there is some volume within which the probability of the electron being captured by the trap is significant for a given dwell time, t_{dw}. The physical interpretation of this effect is that the signal charge has kinetic energy provided by scattering processes on interaction with lattice and impurity atoms. Although the favourable position of the electron is at the potential maximum of the potential well, it can be imagined as constantly oscillating around this point due to successive scattering with lattice phonons. The phonons follow an energy distribution for a given temperature T, which can be assumed to be approximately Maxwellian. There is therefore a mean energy provided by a scattering event (giving rise to the average thermal energy of $\frac{3}{2}k_bT$) however in practise the supplied thermal energy follows the Maxwellian distribution, with high energy events rarer than low energy events. The potential well and associated electric field within the CCD pixel provide a restoring force directed towards the centre of the well at all times. The energy distribution for scattering, coupled with the potential profile of the pixel, results in a non-uniform density profile for the charge cloud when averaged over time, with a high density at the centre that exponentially tends to 0 at the edges according to the field structure and signal size.

The non-uniform density within the electron cloud means that the definition of a charge packet "volume" is non-trivial, since there is no clear defined edge to the charge packet. Nonetheless, the representation of the charge cloud having a fixed volume, *V*, is often useful for device modelling purposes where an entire device readout needs to be simulated for a variety of illumination patterns and clocking schemes. One approach to defining a charge packet volume is

to introduce the concept of a cut-off density ρ_{CUT} whereby the volume of the charge cloud that has a signal density greater than this value is considered significant (Short *et al.*, 2010). The choice of ρ_{CUT} is typically influenced through use of Equation 11.1 and Equation 11.2 whereby, a threshold value of P_c is selected (e.g. 10%) and the dwell time of the packet is used to infer the corresponding value for the signal density *n*, which is now equal to the cut off density ρ_{CUT}.

$$\tau_C = \frac{1}{\sigma n v_{th}} \qquad \text{Equation 11.1}$$

$$P_c = 1 - e^{-\frac{t_{dw}}{\tau_c}} \qquad \text{Equation 11.2}$$

This approach is complicated by the fact that different sections of the device have different dwell times and so will have different effective volumes despite the signal magnitude remaining constant. The capture cross section, σ, also varies according to the trap species under consideration. This can be accounted for by simply adopting the largest known capture cross section relevant to the application (e.g. the Si-A centre where σ=1×10^{-14} cm^{-2}) and using this as a "worst case scenario".

With an effective volume defined through the use of ρ_{CUT}, the non-uniform density information of the charge cloud is lost and instead the density is then assumed to be uniform and calculated using the expression:

$$n = \frac{N_e}{V} \qquad \text{Equation 11.3}$$

where N_e is the number of electrons within the charge packet and *V* is the volume using the value of ρ_{CUT}. As more signal is added to the charge packet, the effective volume increases and is typically modelled as follows:

$$\frac{V_C}{V_G} = \left(\frac{N_e}{FWC}\right)^{\beta} \qquad \text{Equation 11.4}$$

Where FWC is the pixel full well capacity and V_G is the assumed maximum geometrical volume that electrons can occupy within a pixel (i.e. the volume of the electron cloud when N_e = FWC). β is referred to as the electron cloud expansion coefficient and describes how the volume of the electron cloud changes as additional signal is added to the charge packet. Since β is intrinsically linked to the shape of the potential profile within the pixel, it is dependent upon the pixel geometry and applied electrode bias levels. For β = 1 the model is referred to as "volume driven"

since the charge confinement volume increases linearly with signal size. For β = 0 the model is referred to as density driven since the volume remains fixed for an increase in signal size (Short *et al.*, 2010).

Knowledge of the β parameter therefore allows simple yet effective modelling of how the volume of the charge cloud available for trapping changes as a function of signal size. β can in principle be inferred through laboratory measurements of CTI, however it is complicated by the statistical processes of capture and emission that can skew the result away from the true value. Device modelling allows accurate calculation of the β parameter so long as all relevant pixel features are simulated. The operating conditions of the device, including temperature, integration time and clock timings, must also be incorporated into the calculation.

11.2.1 CGI operating modes

To calculate appropriate values of β, the operating speeds of the CGI needed to be incorporated into Equation 11.1 and Equation 11.2 in order to select an appropriate value for the cut-off density ρ_{CUT}. At the time of writing, the operating speeds for the CGI were not finalised since they depend upon a non-trivial trade-off between competing noise sources such as CIC and CTI. Three modes of operation were considered that spanned the current range of possible operating speeds, presented in Table 11.1. The parallel wait times were calculated using the parallel speed, assuming standard 2-phase clocking (e.g. 100 kHz frequency gives 10 µs of time for a pixel-pixel transfer. Equal 2-phase clocking means that 5 µs is spent beneath each phase). An additional wait period is present under one of the storage phases while the serial register is read out, termed Parallel Wait 2. This delay consists of the standard wait period plus the time taken to readout a line which in turn depends on the serial readout speed. The line length was taken as 2160 serial transfers, which equates to the CCD201 full register readout. The serial wait times were calculated using the serial speed and assuming standard 3 phase clocking with equal wait times beneath phases, e.g. 100 kHz serial speed gives 10 µs of time for pixel to pixel transfer and hence 3.33 µs beneath each phase (assuming equal clocking). This ignores the overlap period where two phases are high for a short amount of time.

The cut-off densities were then chosen by incorporating the calculated dwell times under phases for a given operating mode into Equation 11.1 and Equation 11.2, and calculating the signal density required for a probability of capture equal to 10% for the case of the Si-A centre. The values are summarised by Table 11.2. The Si-A centre was chosen since this was the defect with the highest literature cross section. The 10% choice of threshold was arbitrary, however, it ensured that the volume of the cloud was not underestimated and allowed clear comparison between alternate operating modes and pixel geometries.

Figure 11.1 shows the probability of capture for each operating mode described within Table 11.2 as a function of charge density for the case of the Si-A centre. It can be seen that, depending upon the operating mode, different cut-off densities give rise to an equivalent probability of capture as a function of the pixel dwell time. The conclusion is that, while the charge packet technically has a finite volume, the *effective* volume of the packet available for trapping increases as a function of dwell time as traps in the presence of lower charge densities have more time available to capture signal.

Table 11.1: *Summary of example operating modes under consideration for the CGI and the respective dwell times.*

Description	Mode 1	Mode 2	Mode 3
Serial Frequency	100 kHz	1 MHz	10 MHz
Parallel Frequency	100 kHz	1 MHz	1 MHz
Parallel Wait 1	5 µs	0.5 µs	0.5 µs
Parallel Wait 2	21.6 ms	2.16 ms	0.216 ms
Serial Wait (per phase)	3.33 µs	333 ns	33.3 ns

Table 11.2: *Summary of calculated cut-off density values equivalent to a 10% probability of capture of the Si-A centre at 165 K for each of the operating modes and corresponding dwell times.*

Operating mode and clock designation	Dwell time (s)	Calculated cut-off density (e^-cm^{-3})
Parallel Integration Time	1	6.0×10^{5}
Parallel Integration Time	10	6.0×10^{4}
Parallel Integration Time	100	6.0×10^{3}
Mode 1: Parallel Wait 1	5.0×10^{-6}	1.2×10^{11}
Mode 2: Parallel Wait 1	5.0×10^{-7}	1.2×10^{12}
Mode 3: Parallel Wait 1	5.0×10^{-7}	1.2×10^{12}
Mode 1: Parallel Wait 2	2.16×10^{-2}	3.0×10^{7}
Mode 2: Parallel Wait 2	2.16×10^{-3}	3.0×10^{8}
Mode 3: Parallel Wait 2	2.16×10^{-4}	3.0×10^{9}
Mode 1: Serial Wait	3.33×10^{-6}	2.0×10^{11}
Mode 2: Serial Wait	3.33×10^{-7}	2.0×10^{12}
Mode 3: Serial Wait	3.33×10^{-8}	2.0×10^{13}

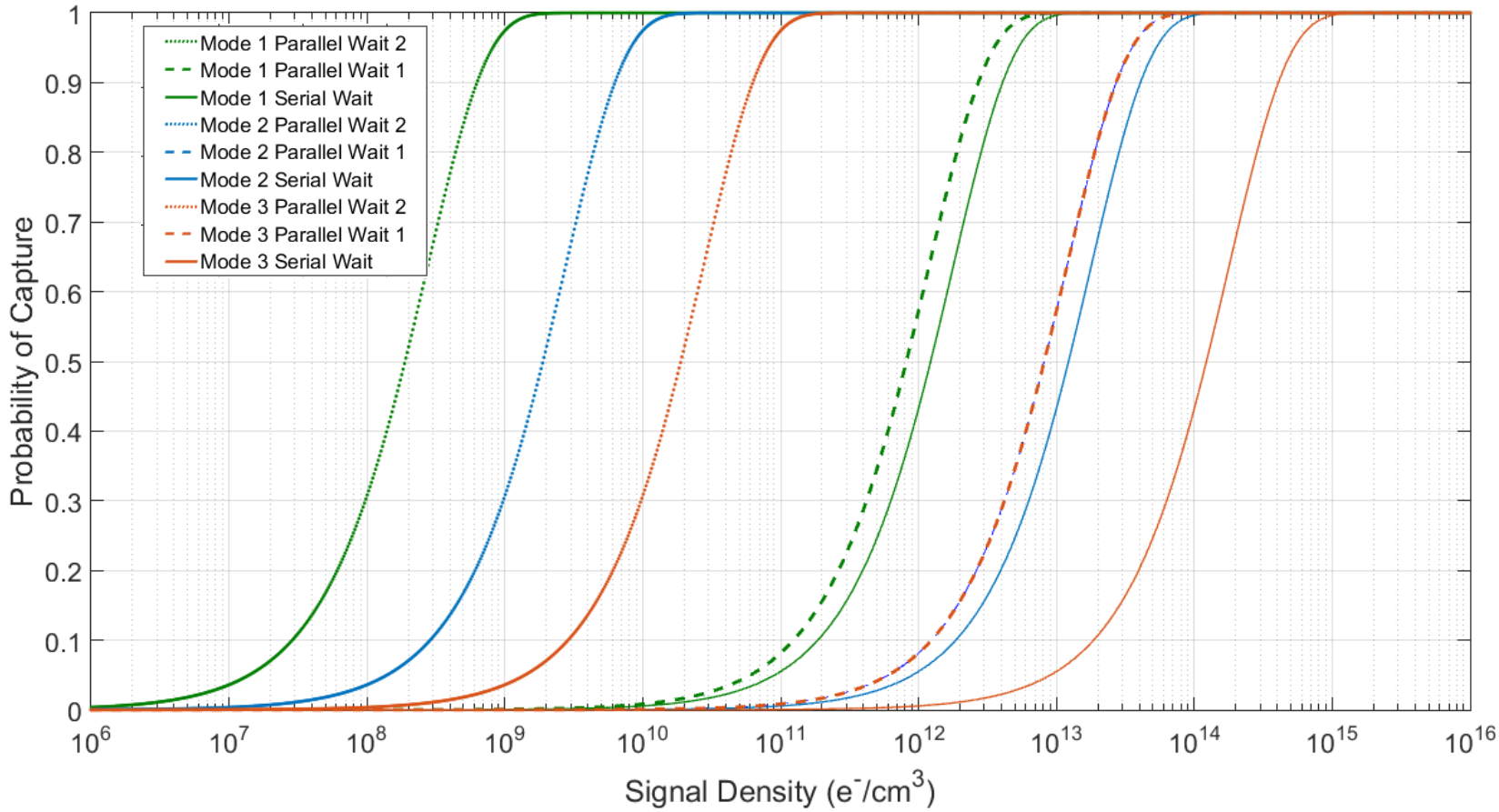

Figure 11.1: *Plot of probability of capture for each operating mode described within Table 11.2. The cross section of the Si-A centre (1×10^{-14} cm^2) was used for the calculation with a temperature of T = 165 K.*

11.3 Signal volume results for the CCD201

11.3.1 Models and experimental method

The measurement of the signal-volume characteristics of the CCD201 pixels required accurate TCAD models of each of the pixel structures. Four separate pixel structures were investigated in this study, based upon the principle pixel architectures of the CCD201-20. These included the image pixel (identical to the store pixel) and three types of register pixel; the register pixel adjacent to the image area, register pixel that leads to the EM register and the EM register pixel.

The CCD201-20 image pixel is 13 µm square with a 4-phase electrode structure with two pairs of phases of alternate widths. $\mathrm{I}\phi 2$ and $\mathrm{I}\phi 4$ are each 4.5 µm wide, including insulating oxide, and are where charge is stored $\mathrm{I}\phi 1$ and $\mathrm{I}\phi 3$ are each 2.0 µm wide, including insulating oxide, and have additional P implants that prevent the backflow of charge during clocking.

Adjacent to the CCD201-20 image area is a row of standard serial register elements. The pixels are 3-phase, with 13 µm pitch and 24 µm width. These register elements have a dump gate that runs parallel to the direction of transfer and can act to remove charge from the register when pulsed (a schematic of the pixel structure is shown within Figure 11.2). The dump gate replaces that location of what would otherwise be a channel stop. Its presence therefore influences the form of the potential within each of the register pixels and so needed to be included within the model to accurately represent charge storage characteristics.

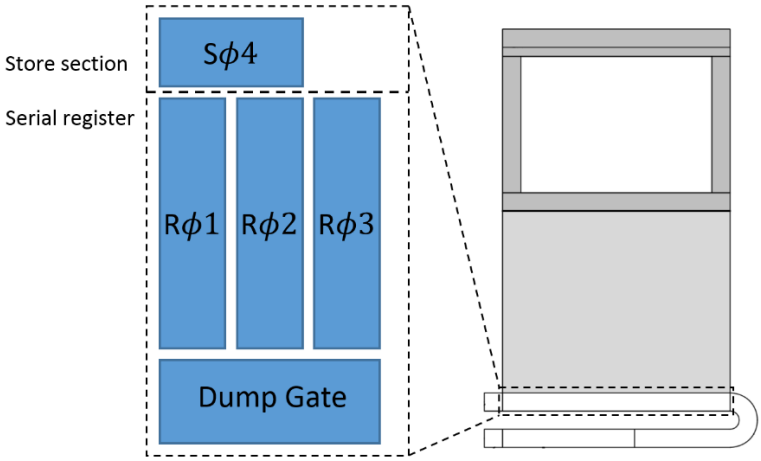

Figure 11.2*: Schematic of register pixel layout for the case where the dump gate runs parallel to the register. Approximate relative position on the CCD201 is also shown.*

Following the standard serial register elements adjacent to the image area, further serial register elements exist that are similar to those adjacent to the image area but do not have a dump gate that runs parallel to the direction of charge transfer. Instead, the pixel boundaries are defined by

channel stops, similar in structure to those within the image area. There are also corner elements that act to rotate the transfer direction by 180 degrees such that the remainder of the standard register and EM register run parallel to the image area. For this study, the corner elements were treated as standard serial register elements without the dump gate present. This approximation is thought to be appropriate for the case of device modelling since the corner elements are small in number compared to other elements (approximately 20 elements to complete the full bend) and so any net effect on CTI due to the effect of geometrical variation on the charge cloud within these pixels is expected to be small.

The final stage of the readout chain for the CCD201 is comprised of 604 multiplication elements whereby signal carriers are accelerated to energies sufficient for the generation of additional carrier pairs through impact ionisation. The EM register pixel within the CCD201 has a 40 µm channel width and 16 µm pitch to allow for high charge storage capacity.

Each pixel was constructed using TCAD by first simulating the manufacturing processes, including ion implantation and dopant diffusion and then passing the model onto a separate program that allowed simulation of the electrical properties consistent with standard operation. The models were constructed in a way as to make them as accurate as practically possible, including the construction of overlapping polysilicon gates (where possible) and accurate representation of all dopant profiles. This was particularly important for the case of the CCD201 image pixel where the additional 2-phase implants severely alter the potential structure and incorrect simulation of manufacture gives rise to potential pockets.

For simulation of standard operation, the pixels were biased according to standard e2v datasheet potentials consistent with IMO operation (Table 11.3). Illumination was injected through simulation of an optical light source that could have the intensity configured to provide any required level of illumination. The volume of each charge packet was measured through an automated Python script that examined the TCAD output and calculated the volume using the chosen cut-off density (ρ_{CUT}).

Table 11.3: *Summary of potentials simulated for the CCD201 pixels*

Pixel	Clock High Level (V)	Clock Low Level (V)	Substrate Voltage (V_{ss})
Image Pixel	0	0	4.5
Register Pixels	12	0	4.5

Each pixel was benchmarked against standard e2v performance specifications that included the channel parameter, FWC and pinning potential. The channel parameter was measured by depleting the device and measuring the maximum potential within the channel beneath an unbiased gate. The FWC of the pixel was measured by providing variable degrees of illumination to the pixel and measuring that signal level at which charge transfer efficiency decreased significantly, indicating that the practical charge storage limit of the pixel had been exceeded. Charge transfer efficiency was measured at a signal level of approximately 2000 e^- (close to the signal produced by an Fe^{55} X-ray) and was calculated by finding the fraction of charge successfully transferred from one pixel to another. The pinning potential was measured by measuring the concentration of holes at the semiconductor-insulator interface as a function of V_{SS}. The pinning potential was taken as the voltage whereby the concentration of holes at the interface began to saturate. All performance parameters for each pixel were in-line with expectations, with the detailed results of this benchmarking included within Table 11.4.

Table 11.4*: Comparison of benchmark results from SILVACO models when compared to e2v expectations for each of the CCD201 models used in this study. In each case, the modelled results agree well with expectations.*

	Test Parameters							
	Channel Parameter (V)		NIMO Full Well Capacity (e^-)		Charge Transfer Inefficiency		Pinning Potential (V)	
Pixel Design	e2v expectation	SILVACO model result	e2v expectation	SILVACO model result	e2v expectation	SILVACO model result	e2v expectation	SILVACO model result
Image/Store Pixel	11±1	10.78	80000	90000	$< 10^{-5}$	$< 10^{-7}$	7.0-9.0	8.0
Register Pixel with Dump Gate	11±1	11.2	N/A	≈450000	$< 10^{-5}$	$< 10^{-7}$	7.0-9.0	8.0
Register Pixel without Dump gate	11±1	11.2	N/A	≈450000	$< 10^{-5}$	$< 10^{-7}$	7.0-9.0	8.0
EM Register Pixel	11±1	11.2	740,000	800,000	$< 10^{-5}$	$< 10^{-7}$	7.0-9.0	8.0

11.3.2 Image pixel results

Figure 11.3 shows the volume of a charge packet as a function of signal size for the CCD201 for each of the proposed CGI operating modes. Regardless of operating mode, the effective volume of the signal packet increases as a function of signal size as one may expect. Operating modes with faster parallel clock rates give rise to a shorter dwell time and hence smaller volume of the packet available for capture due to traps. The impact of operating mode is clearly significant, with a factor ×2 increase in effective volume for Mode 1 (5 µs dwell) compared to Mode 2/3 (0.5 µs dwell) for example. For the case of charge capture alone, Modes 2/3 should give rise to improved CTE however one must remember that a shorter dwell time also reduces the probability that charge can re-join the original signal packet and so both processes must be considered.

The volume of the packet increases logarithmically as a function of signal size for small signal packets (< 1000 e^-). For charge packets in excess of 1000 e^-, the central storage density approaches 10^{16} e^-/cm^3 which corresponds to a short dwell time for P_C = 1. An increase in dwell time for these larger packets therefore corresponds to a smaller increase in the volume available for trapping, since it is only the outer edges of the packet with lower density that require a longer dwell time to reach non-negligible values of P_C.

Figure 11.4 shows that an increase in integration time has the same effect as an increase in dwell time as one might expect, however, the factor difference between 1 s and 100 s is less than ×2. Therefore, although shorter integration times reduce the volume of the charge packet available for trapping, the benefit may be small compared to that from clock timing optimisations.

Equation 11.4 was found to represent the data well for signal levels in excess of 100 e^- but showed significant deviation for signal levels smaller than 10 e^- and so an additional term was added to better represent the behaviour at lower signal levels:

$$V_C = \alpha {N_e}^{\beta_{LOW}} + V_G \left(\frac{N_e}{FWC}\right)^{\beta_{HIGH}} \qquad \text{Equation 11.5}$$

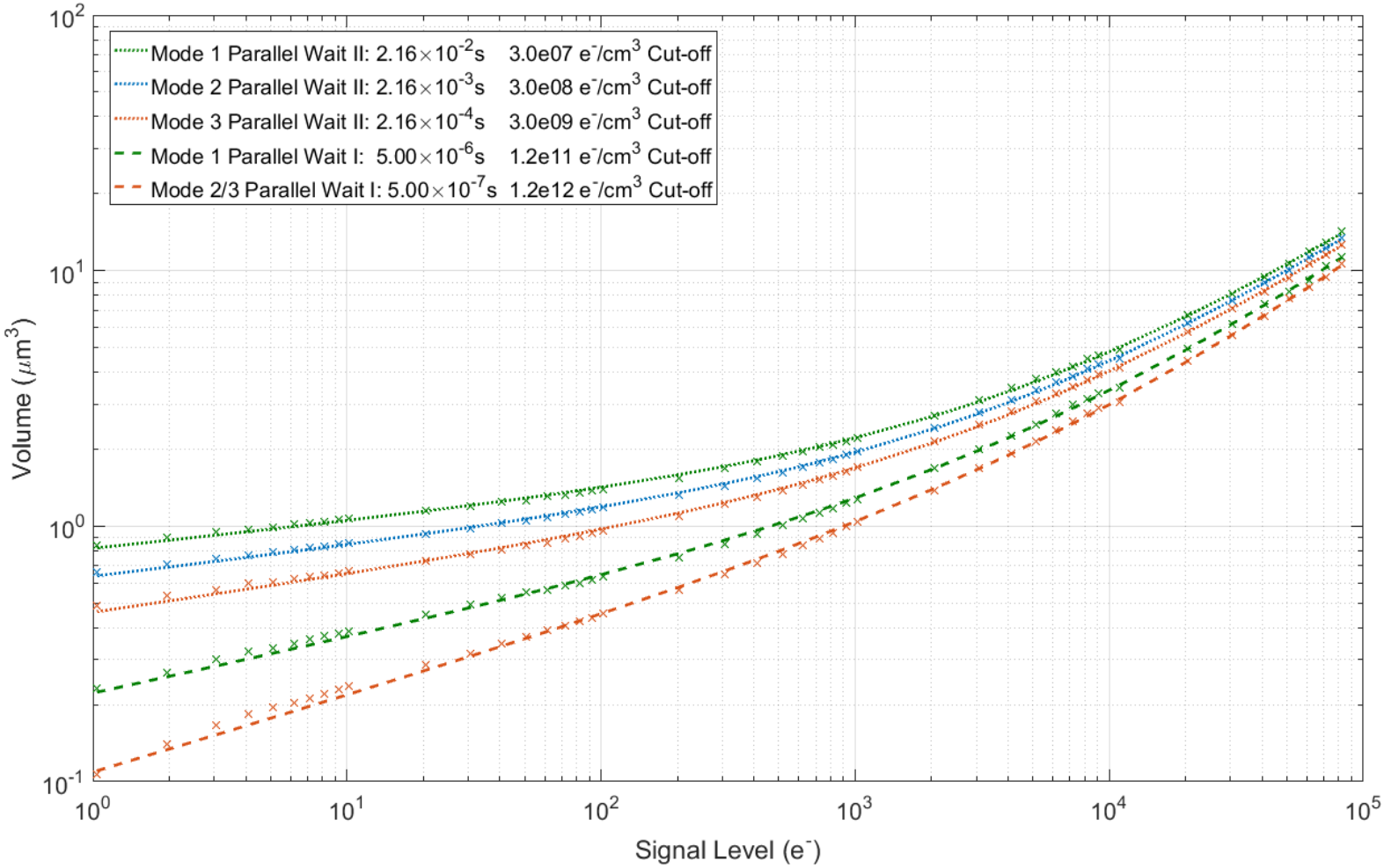

Figure 11.3: *Volume of charge packet as a function of signal level for each of the proposed CGI operating modes. The cut-off densities were selected based upon a 10% probability of capture for an Si-A centre with capture cross section $\sigma=1\times10^{-14}$ cm^{-2} at 165 K.*

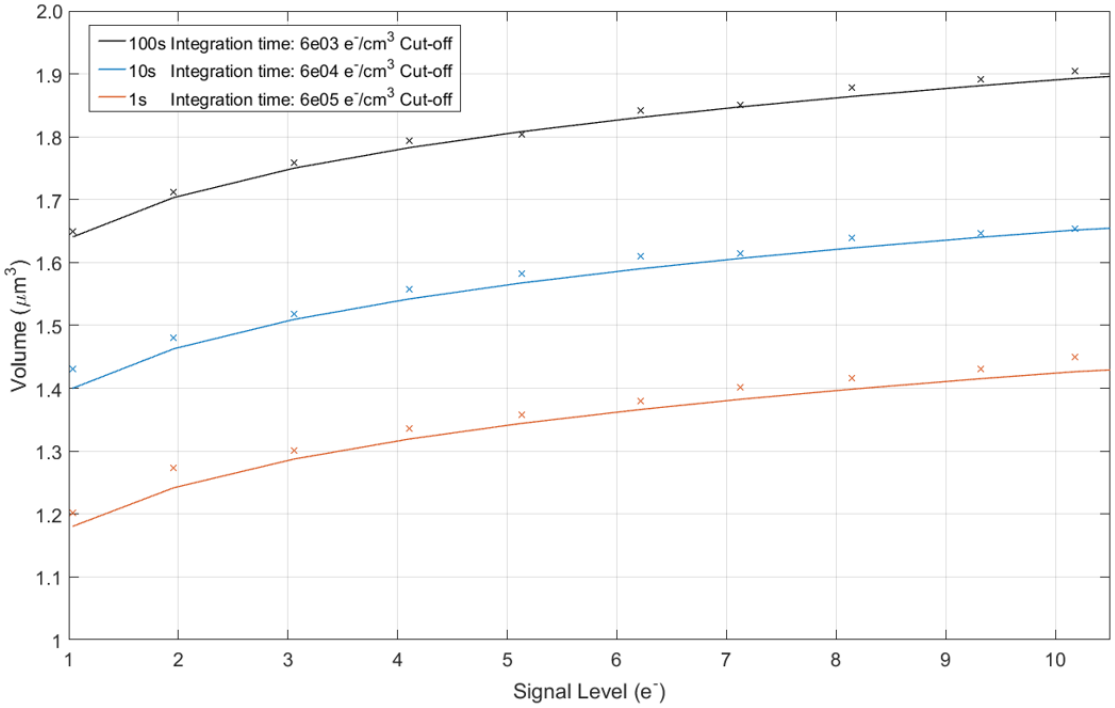

Figure 11.4: *Volume of charge packet as a function of signal level in the range of 1-10 e⁻ for three different pixel integration times.*

11.3.3 Register pixel results

The register pixels exhibited a similar trend of increasing volume with signal size, however the behaviour at the lowest signal levels is markedly different from that observed within the image pixel. Each of the register pixels have a larger channel width compared to the image area, with 24 µm for the standard register pixels and 40 µm for the EM register pixel, leading to a significantly more diffuse charge packet within these pixels when compared to the image/store pixel equivalent. The dwell times are also orders of magnitude smaller, typically within the ns regime compared to the µs and ms regime (Table 11.2). The result is that at small signal levels, the charge density within the central region of the packet is insufficient to give rise to a significant capture probability and so the ”effective” volume available for charge capture tends to 0 (Figure 11.5, Figure 11.6). Since the EM register pixel has a larger channel width (40 µm compared to 24 µm), this effect is significant for signal sizes as large as 20 e^-. Due to the behaviour at low signal levels, Equation 11.5 did not represent data below approximately 1000 e^-. For higher signal levels, the data was reasonably well represented by Equation 11.4.

Since WFIRST will primarily image small signals less than 10 e^-, the implication of these results is that, within the serial register pixels, utilising clock speeds of 10 MHz or more means that charge capture due to trapping sites is unlikely.

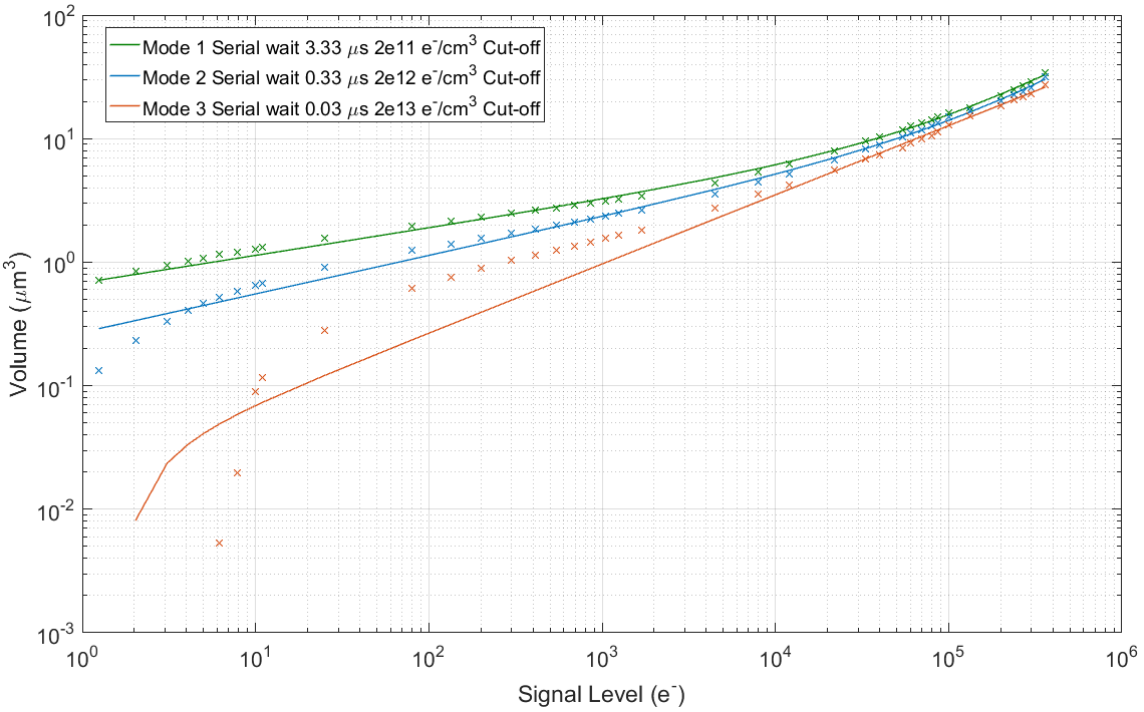

Figure 11.5: *Signal volume relationship for the standard register pixel for each operating mode. At smaller signal levels and shorter dwell times, the volume available for capture tends towards 0.*

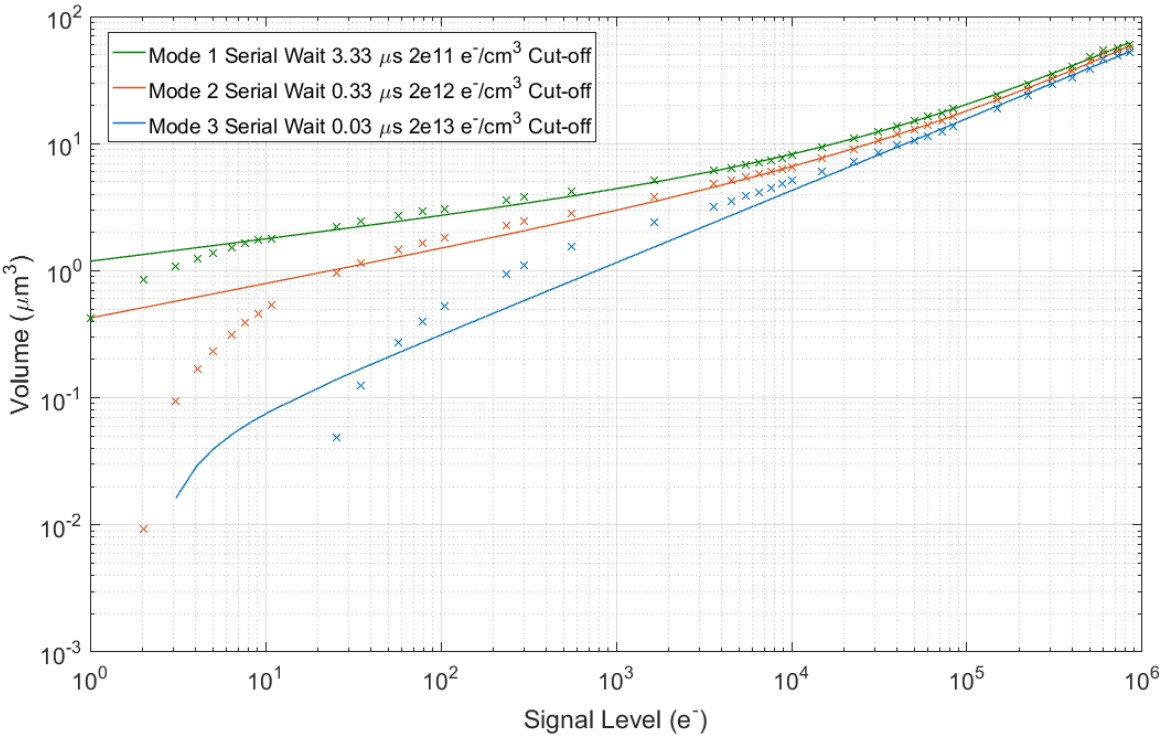

Figure 11.6: *Signal volume relationship for the EM register pixel for each operating mode. At smaller signal levels and shorter dwell times, the volume available for capture tends towards 0. The increased channel width compared to the standard register pixel (Figure 11.5) means this begins to occur at a higher signal.*

11.4 Implications for the CGI

The signal volume investigations for the CCD201-20 have highlighted that there are in fact two distinct regimes with respect to charge capture within the CCD201-20. Within the image pixel, the effective volume of the charge packet increases with increasing dwell/integration time. Operation at faster speeds reduces the volume available for trapping, but also reduces the probability that a captured electron can rejoin the signal packet. It is not currently thought to be possible to operate at a speed that fully eliminates the possibility of charge capture, and so some balance between minimising capture and maximising the fraction of charge that re-emits into the signal packet will give rise to the optimum CTE.

For the serial register, operation at speeds of approximately 10 MHz gives rise to a negligible capture probability for the CGI signal levels of interest. The implication of these findings is that operation at faster speeds will give rise to near negligible CTI due to radiation induced traps, however at these speeds other mechanisms that can induce CTI must also be considered. Here we refer back to the Chapter 2 where the CTI due to charge transport mechanism was first introduced. For small signal levels, field induced drift is the primary mechanism responsible for charge transfer and should not limit the CTI of the device at speeds of approximately 10 MHz, as the ≈0.2 ns required for adequate CTI (Figure 11.7) is easily accommodated within the total budget of a 100 ns pixel transfer time. The problem is instead for larger signal packets that, for example, may arise from cosmic ray interactions or hot pixels that have deposited a significant amount of charge within the frame integration time. Here, signal levels may easily reach in excess of 10^5 e^-, where field induced drift is no longer the primary interaction mechanism and thermal/self-induced drift are responsible for initiating the transfer process. The required wait time for adequate CTI is orders of magnitude longer, approximately 50 ns for a 13 µm pixel, and so there is a possibility that larger charge packets will exhibit CTI tails when the device is run at these speeds (Figure 11.8).

Operation at high speed within the serial register may therefore successfully mitigate radiation induced CTI by significantly reducing the probability for charge to be captured but comes with the caveat that larger signals may exhibit measurable CTI since the pixel to pixel transfer time is simply too short to adequately transfer such large signal packets.

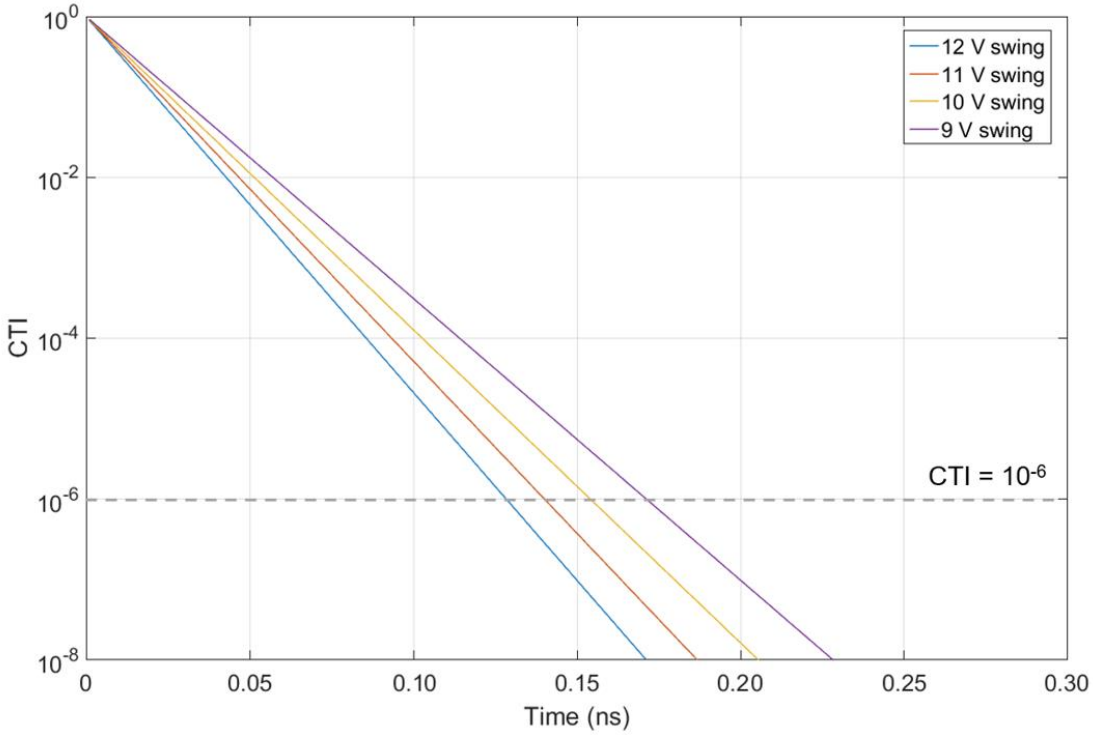

Figure 11.7: *The effect of clock swing on CTI for the field-induced drift transport mechanism, first introduced in Chapter 2. The time taken to achieve a given value of CTI from one phase to the next is significantly shorter than the total pixel transfer time (100 ns) for operation at 10 MHz.*

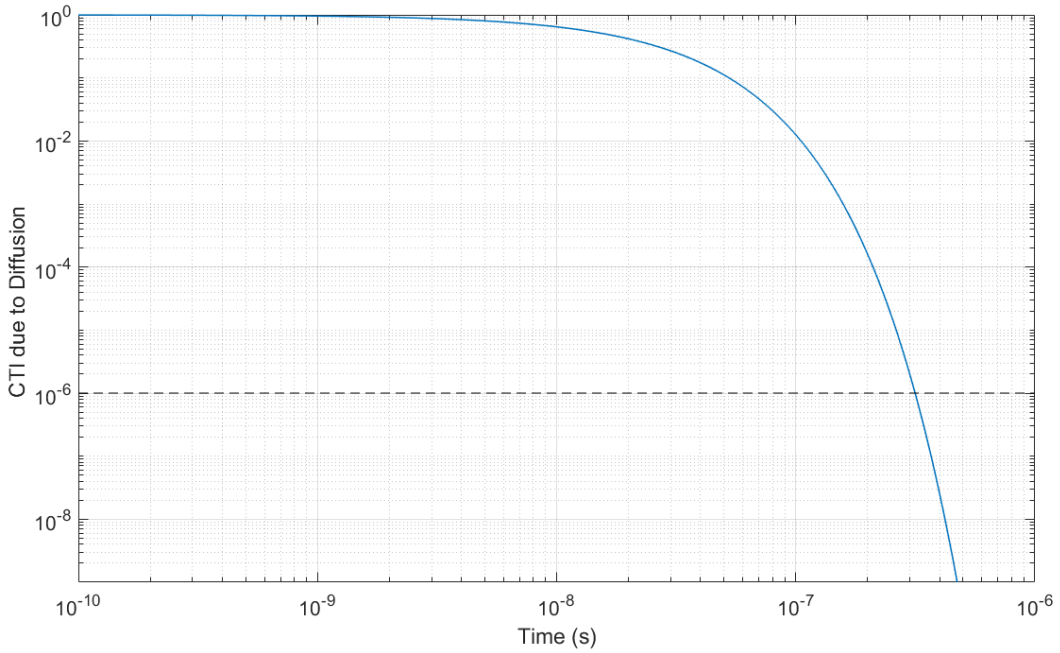

Figure 11.8: *Estimated CTI due to thermal drift across a 13 µm pixel for various "wait times". Thermal drift is the dominant transfer mechanism for larger signal packets. The wait time required for adequate CTI is approaching the total pixel transfer time (100 ns) for operation at 10 MHz.*

The signal volume results presented so far have been useful in highlighting the likelihood of charge capture with respect to the different operating modes of the CGI. A mitigation strategy was offered for the case of the serial register, where fast pixel rates have the potential to effectively stop the charge capture process. For the image and store section, however, a similar approach is not currently thought to be possible. Discussion now turns to another possible mitigation strategy whereby the volume of the charge is constricted in the direction perpendicular to transfer through reduction of the buried channel width. The reduction in volume is thought to be correlated with a reduction in the probability of trapping, however to fully calculate the factor improvement a new approach whereby the non-uniform nature of the charge density profile is fully accounted for is required as will now be discussed.

11.5 Narrow channel modelling

11.5.1 Non-uniform charge density profiles

While the standard model for the equivalent volume of a charge packet is useful, it does not account for the non-uniform charge density distribution within the signal packet. For large signal levels, the assumption of an approximately uniform density is valid since as the signal exceeds approximately 1000 e^- the mean density continues to approach the dopant density of the device. For small signal levels, such as those the CGI is expected to image, the peak signal density is orders of magnitude below the dopant density. The charge density is therefore non-uniform throughout the packet and the use of a cut-off density is less representative of the actual volume of the packet. Figure 11.9 illustrates this point clearly where a comparison between a 1 e^- packet and a 10,000 e^- packet shows the assumption of uniform charge density is not true for small signal levels.

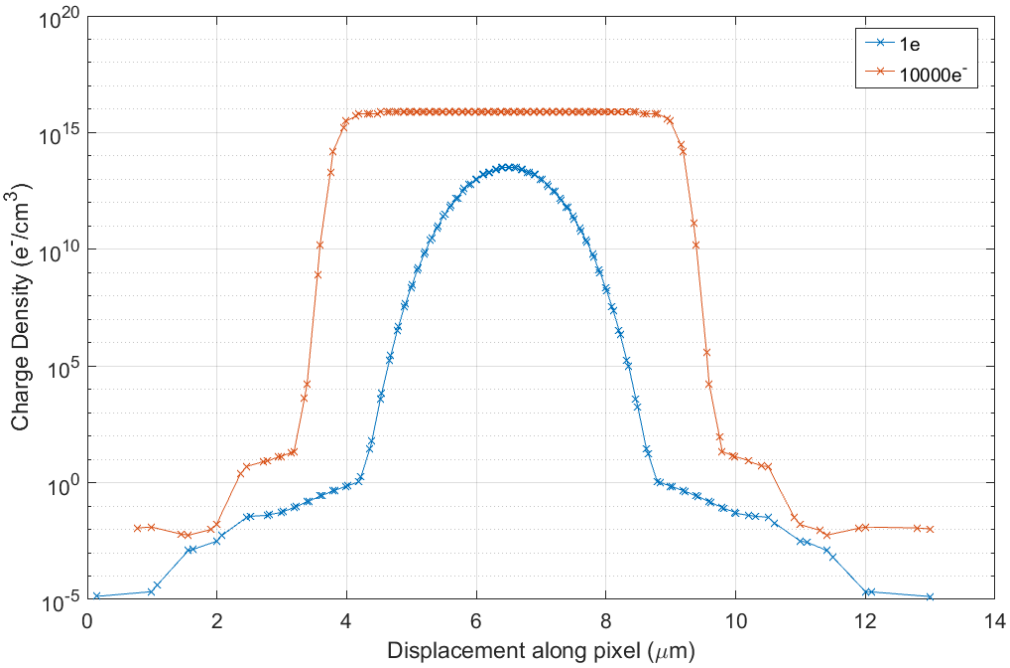

Figure 11.9: *Comparison of the charge density profile for a 1 e^- and 10000 e^- charge cloud in the CCD201-20 image pixel. The larger cloud cloud maintains a constant peak density throughout the majority of the packet. In this instance, the use of a cut-off density is appropriate since the loss of the non-uniform charge density profile is less significant with respect to the mean value of P_C. For the 1 e^- cloud, the charge density remains non-uniform throughout.*

Within the previous section, it was also shown that the standard method of volume calculation has the potential to return null values for the volume of the packet in the regime where the peak density within the cloud falls below the value of the cut-off density. Null values have the potential to severely underestimate CTI, as even a small capture probability has the potential to be significant to global CTI if the density of traps and number of transfers is large enough. For example, within the previous chapters, the Si-A centre was identified as a trap present in high density with the potential to impact horizontal CTE as sufficiently fast pixel rates (> 1 MHz at 165 K). The density of the defect means that there is at least 1 trap per pixel within the volume of a 1 e^- charge packet. The horizontal register of the CCD201-20 consisted of 2160 transfers, and so for a capture probability of 0.01%, the total probability of the charge *not* being captured at any point is given by the binomial distribution with random variable *X* with a probability of exactly *k* successes in *n* trials:

$$\Pr(X = k) = \binom{n}{k} p^k (1-p)^{n-k} \qquad \text{Equation 11.6}$$

For transferring a single electron through the Si-A centres in the serial register of the CCD201-20 this reduces to:

$$\Pr(X = 2160) = \binom{2160}{2160} 0.9999^{2160}(1 - 0.9999)^{2160-2160} \quad \text{Equation 11.7}$$

$$\Pr(X = 2160) = 0.81$$

Approximately 80% of the charge is predicted to transfer successfully under these simplifying assumptions, indicating how even a small capture probability can still impact the total charge that is successfully transferred.

11.5.2 Narrow channel structures

The concept of a narrow channel or "notch" as a means to improve the bulk radiation hardness of devices is not a new one. Sensors aboard HST made use of a notch to improve parallel CTE, and more recently the ESA Gaia satellite used a customised CCD91 with a small supplementary buried channel to improve charge transfer performance at small signal levels. The basic underlying principle is that if the charge packet is confined to a smaller volume then it encounters fewer trapping sites along its path to the output node. While this is certainly true for larger signals, the situation is more complex for smaller signal levels where the charge density profile is non-uniform. In this regime, a change in the volume of the packet also corresponds to a change in the central charge density of the packet, which can in turn increase the net probability of capture. Prediction of a factor improvement through volume reduction is therefore less reliable at smaller signal levels, and the entire probability of capture of the packet must be taken into consideration to ascertain whether there is any potential benefit in parallel/serial CTE.

For the WFIRST CGI, the signal levels are unity and so the volume of the charge packet within the pixel is already small. It was therefore unclear whether confining the packet further would result in a benefit to predicted CTE. For the serial register, the channel width is large, resulting in a large yet diffuse charge packet. It was also unclear whether a narrow serial register would provide a benefit to CTE, since the reduction in volume would correspond to an increase in the net probability of capture. Narrow channel variants of each pixel were modelled and the net probability of capture per unit volume was calculated for each case in order to predict the factor improvement in CTE such a modification could provide if implemented on the CCD201-20.

11.5.3 Narrow channel image pixel

The standard CCD201-20 image pixel structure used for the signal-volume modelling in the previous section was duplicated with different channel widths in order to estimate the impact of a narrow channel structure. The nominal channel with of the pixel is approximately 9 µm, and so additional models with a 4 µm and 2 µm channel width were also constructed. A 2 µm channel is believed to be the practical limit of manufacturing, whereby if the channel is made any smaller the variations due to geometrical misalignment could give rise to potential pockets that significantly degrade performance. A 4 µm channel is comfortably within the limit of manufacturing tolerances, and so this represented a balance between the best benefit to CTI while keeping manufacturing risks low.

The reduction in channel width of the pixel significantly alters some of its key characteristics, including FWC, Channel Parameter and the pinning potential. In general, as the channel width is reduced, each of these values decreases since the effect of fringing fields from the un-implanted silicon begins to increase. The reduction in channel parameter and pinning potential can be recovered through an increase in the ion-implanted buried channel dose, however unless the reduction in channel potential is significant then this is not always necessary. For this study, the channel parameter was reduced to approximately 9 V for a 2 µm channel which is still conducive to good CTE. The reduction in pinning potential may mean that clock high and low-levels have to be optimised to ensure the device moves in and out of inversion as required. Particular attention should be paid to the case of the serial register to ensure it does not become inverted at any stage and thus increase CIC. Even with the smallest channel width, the pinning potential is still +5 V greater than the nominal low level of the register and so the risk remains low.

Table 11.5: *Summary of performance parameters measured for the narrow channel variants of the CCD201-20 image pixel.*

Channel Width (µm)	Channel Parameter (V)	Pinning Potential (V)
9	12	8.0
4	11	6.7
2	9	5.6

The charge storage characteristics of the narrow channel image pixels were measured through inputting fixed levels of signal charge into each of the pixels and calculating the average probability of capture per unit volume for each packet using Equation 11.8 and Equation 11.9, assuming a dwell time of 1 ms, a temperature of 165 K and a capture cross section of 1×10^{-14} cm^2 (consistent with the Si-A centre):

$$\tau_C = \frac{1}{\sigma n v_{th}} \qquad \text{Equation 11.8}$$

$$P_c = 1 - e^{-\frac{t_{dw}}{\tau_c}} \qquad \text{Equation 11.9}$$

For small signal levels, there is significant reduction in the average probability of capture per unit volume for the narrow channel variants, with an approximate factor ×2 difference for a 4 µm channel and a factor ×3 difference for a 2 µm channel (Figure 11.10). A benefit is still seen for large signal levels but begins to reduce significantly beyond the 1000 e^- mark. This is mainly because beyond this signal level size, the peak charge storage density is equal to the dopant density within the buried channel. The factor reduction in volume from narrowing the channel is therefore smaller at these signal sizes, since the charge storage density can no longer increase within the central region. For the smaller signal levels, the reduction in channel width acts to increase the central charge storage density (Figure 11.11). For the dwell times under consideration for WFIRST (≈ 1 ms), the central probability of capture is already equal to 1. An increase in the charge density within this region therefore cannot increase the capture probability further (Figure 11.12, Figure 11.13). The average probability of capture per unit volume therefore decreases, giving a predicted benefit with respect to the susceptibility to charge capture.

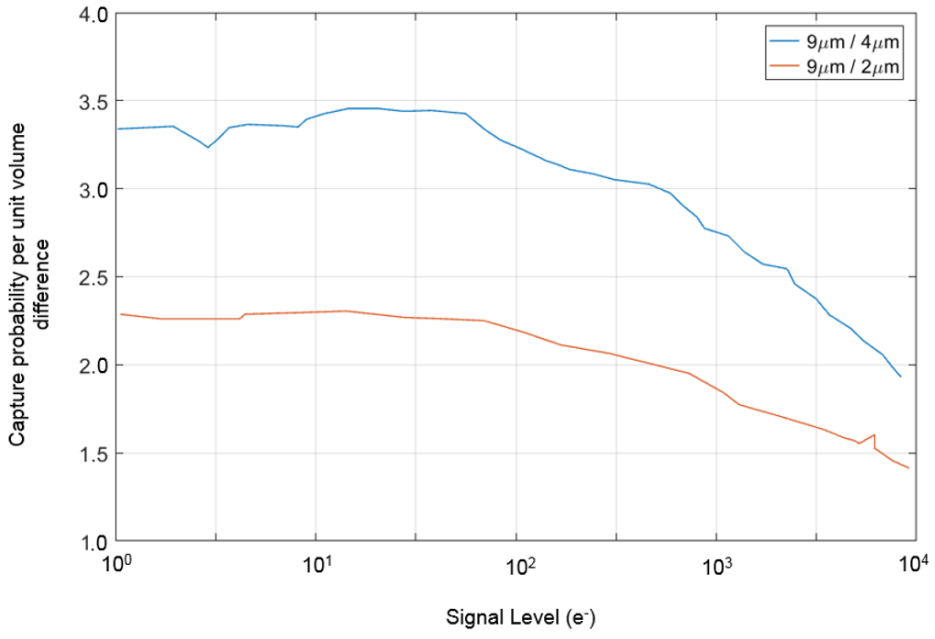

Figure 11.10: *The factor change in average capture probability between the 9 µm and 4 µm, and the 9 µm and 2 µm buried channels.*

The benefit in the image section is therefore largely afforded by the longer dwell times that ensure the central capture probability is equal to 1. As the dwell time decreases, the value of P_C within the central region falls below 1 and so then can increase as the channel width is shortened. For short dwell times, the reduction in volume is therefore accounted for by the increase in charge density at the centre of the charge packet. For dwell times of order of a ns, there is no perceived benefit from use of a narrow channel (Table 11.6).

For the CGI, even at serial speeds of 10 MHz, the parallel dwell time will remain within the ms regime and so the results presented in this section make a strong case for the implementation of a narrow channel image pixel as a means to mitigate radiation induced CTI.

Table 11.6: *Average probability of capture per unit volume as a function of dwell time for the image pixel for three different channel widths.*

Dwell Time (s)	Image Section Average Probability of Capture per unit volume			Maximum Factor Improvement
	9 µm	4 µm	2 µm	
10^{-3}	1.73×10^{-2}	7.50×10^{-3}	5.20×10^{-3}	3.32
10^{-4}	1.16×10^{-2}	5.30×10^{-3}	3.60×10^{-3}	3.22
10^{-5}	6.70×10^{-3}	3.20×10^{-3}	2.30×10^{-3}	2.91
10^{-6}	2.70×10^{-3}	1.60×10^{-3}	1.20×10^{-3}	2.25
10^{-7}	4.99×10^{-4}	4.17×10^{-4}	3.69×10^{-4}	1.35
10^{-8}	5.50×10^{-5}	5.25×10^{-5}	5.18×10^{-5}	1.06
10^{-9}	5.56×10^{-6}	5.39×10^{-6}	5.41×10^{-6}	1.03

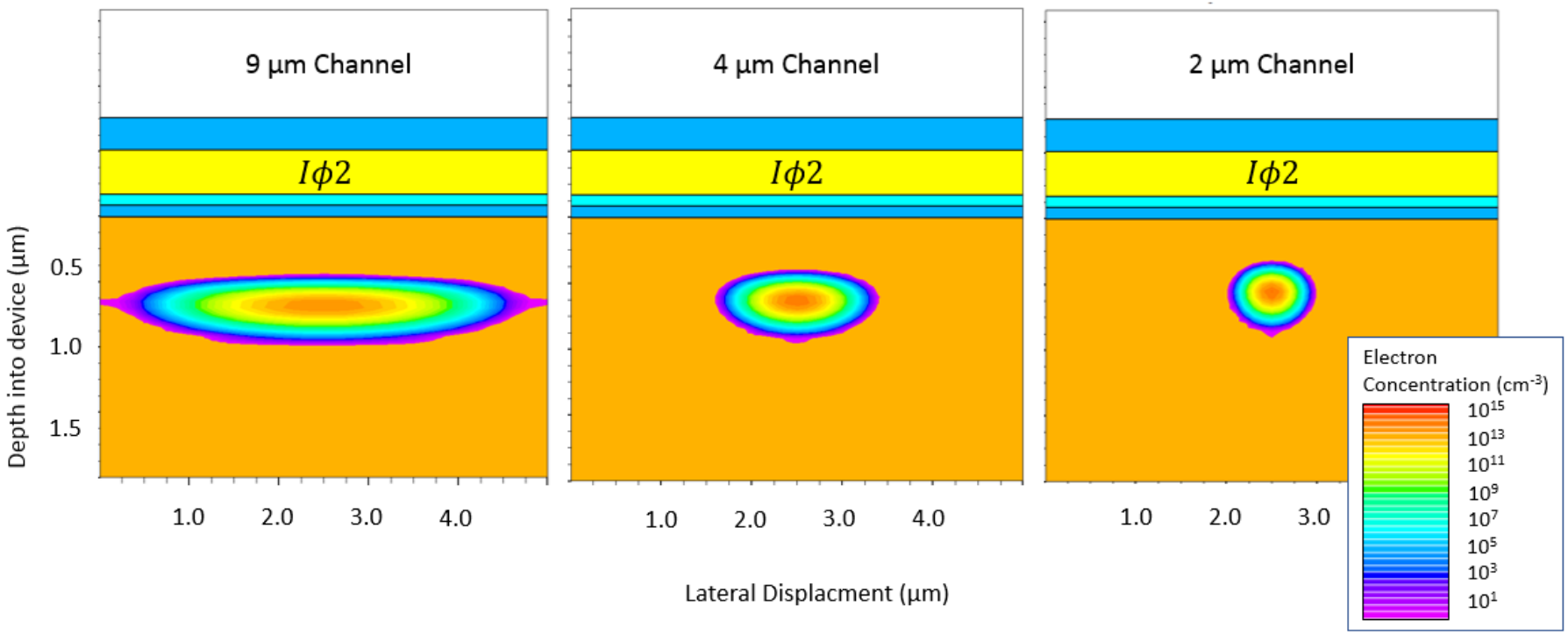

Figure 11.11: *A 1 e^- charge packet within the CCD201-20 for the three channel widths that were modelled. The volume decreases with channel width and the average charge density of the packet increases as a result. The reduction in channel width causes a reduction in the channel parameter and so the charge storage location also moves closer to the interface.*

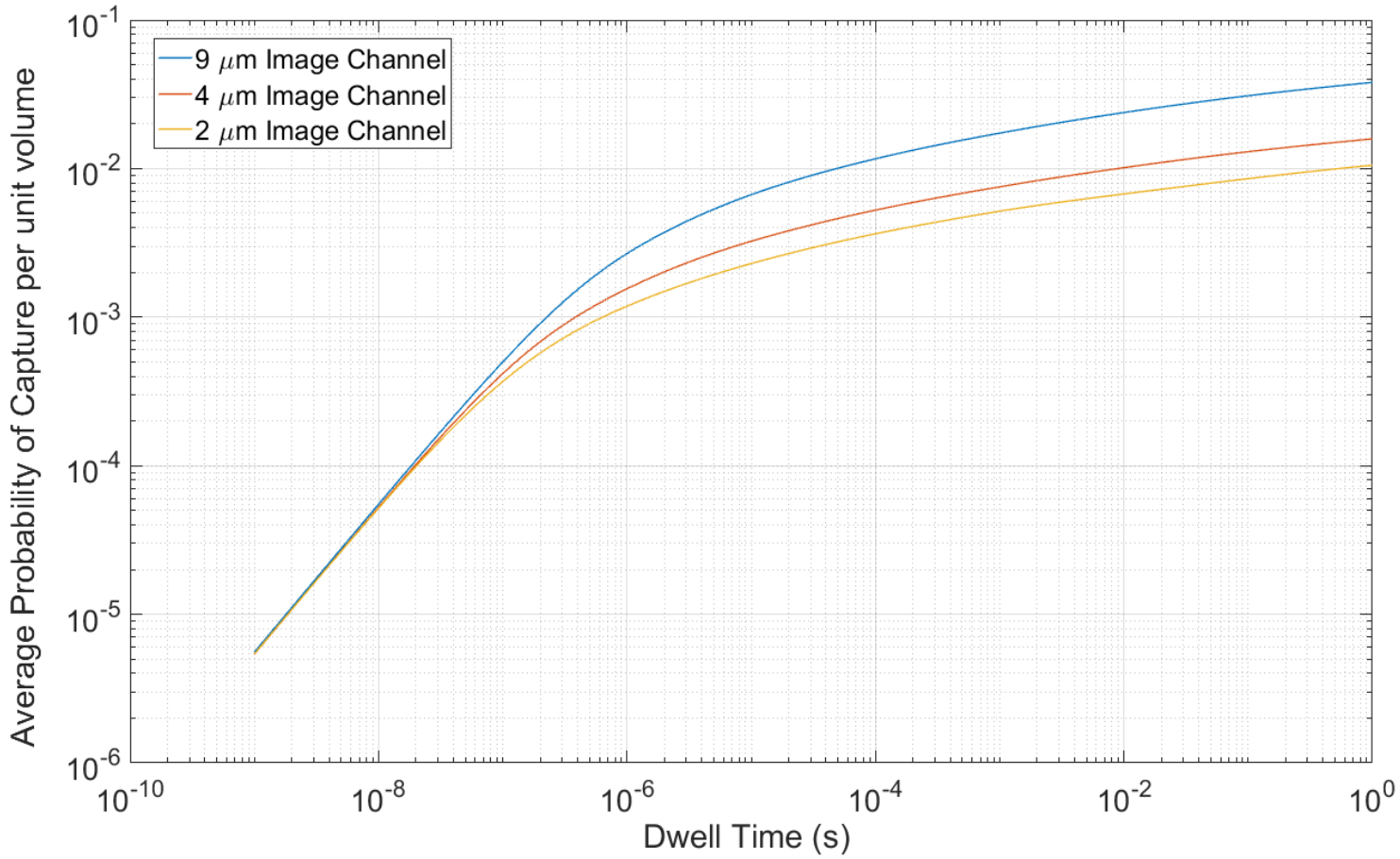

Figure 11.12: *Average probability of capture per unit volume as a function of dwell time for the image pixel for three different channel widths for a 1 e^- charge packet. In the ns regime, there is no benefit from a narrow channel since the peak P_C is significantly less than 1 for the unmodified pixel. For typical parallel dwell times (ms) there is a noticeable benefit from narrowing the channel.*

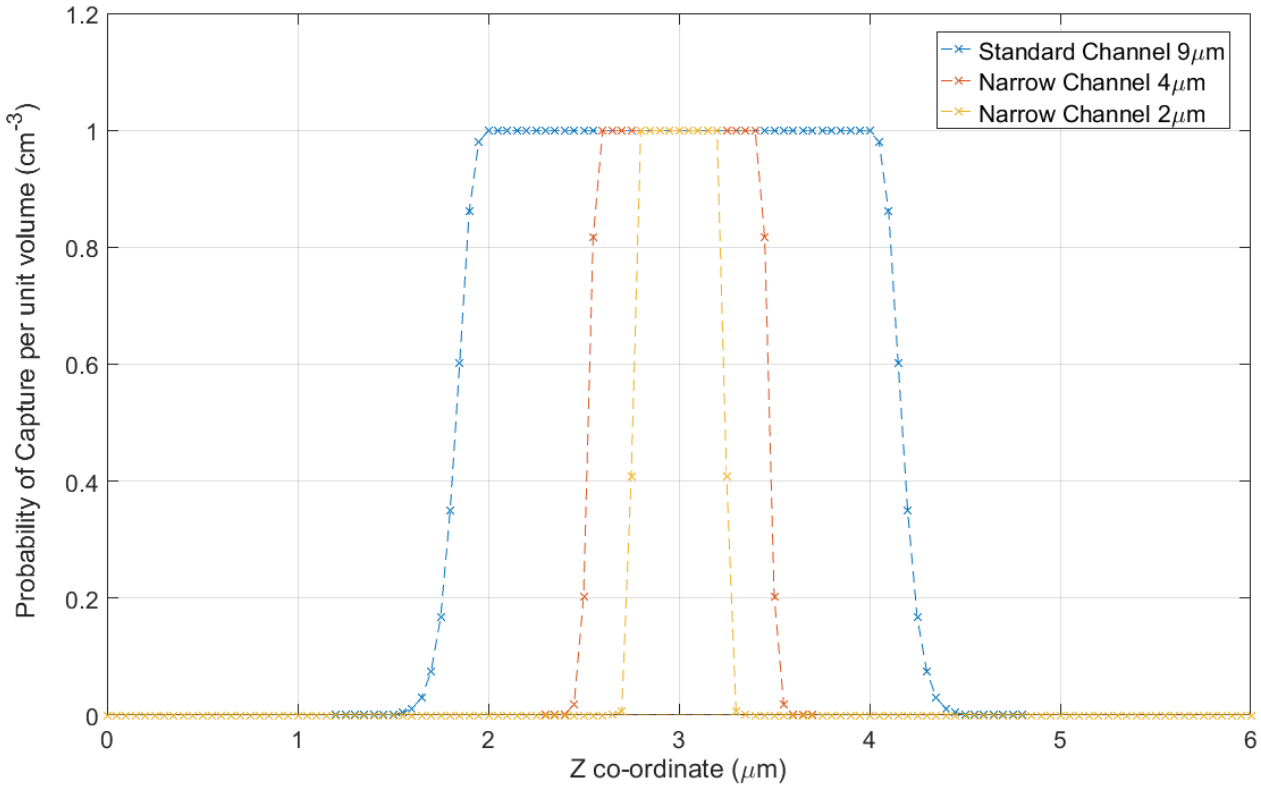

Figure 11.13: *Plot of capture probability as a function of Z co-ordinate (a cut taken perpendicular to the direction of transfer, across the central region of the charge packet) for both the original and narrow channel variants of the image pixel model. The probability of capture within the central region of the charge packet is equal to 1 for the sufficiently long dwell times (the ms regime). Reduction of the packet volume increases the central density further, however the capture probability cannot increase, leading to a reduction in the total volume available for trapping. If the dwell time is reduced, the benefit is lost (Figure 11.12).*

11.5.4 Narrow channel serial pixel

A narrow channel variant of the CCD201-20 serial pixel was modelled in a similar method to that used for the image pixel with a few subtle differences. For the image pixel, narrowing the channel width consisted of increasing the size of the channel stop region (or rather, reducing the fraction of the pixel that is ion implanted with phosphorus). For the serial pixel, a different method was used due to the more complicated pixel structure. The standard register pixel borders the image area and also has a dump gate that runs parallel to the direction of charge transfer. Between the image and serial register regions, there is a small (≈ 2 µm) region that more lightly doped than the buried channel, resulting in a barrier potential that prevents backflow of charge from the serial register into the image region during clocking. This "door-stop" implant (Figure 11.14) can be extended in size to confine the charge packet volume further within the serial register, however there is a risk that a door step that is too large will impede the transfer of charge from the image to the register region. An alternative method of signal confinement is to increase the width of the dump gate that runs parallel to the register. This method does not confine the packet as much as an ordinary channel stop would, since the area beneath the dump gate is also implanted with buried channel dopant, however it was the method associated with the lowest risk should devices be manufactured and so was chosen for analysis within this study. The standard 24 µm channel variant was modelled and compared with a 12 µm variant to ascertain if there was any predicted benefit for the imaging of small signals using a CCD201 with a narrow serial register.

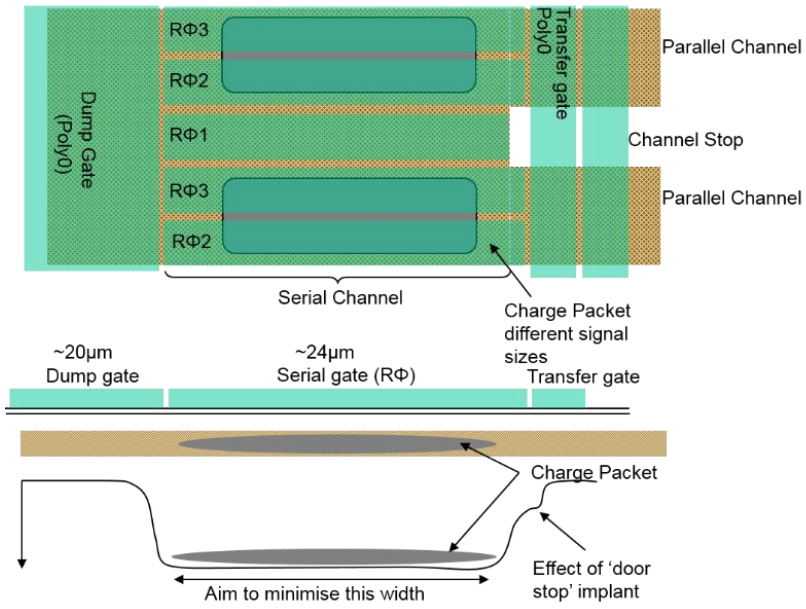

Figure 11.14: *Schematic of the CCD201-20 register pixel model, including the last parallel phase, door-stop implant, channel area and dump gate.*

Reduction of the channel width within the serial register decreased the charge packet volume by a factor approximately equal to the difference in channel width (shown by Figure 11.15). The central charge density of the packet increased as a result, corresponding to an increase in the capture probability within this region (Figure 11.16). For dwell times consistent with operation at 1-10 MHz, this increase in capture probability was found to compensate for the reduction in volume, leading to the prediction of no net improvement in CTE (Table 11.7, Figure 11.17). As the dwell time is increased to times consistent with parallel clocking, a factor improvement approximately equal to the geometrical reduction in channel width becomes apparent. The conclusion is that for the case of CGI, narrowing the serial register appears to provide no predicted benefit and so is not a recommended device modification.

Table 11.7: *Average probability of capture per unit volume as a function of dwell time for the serial register pixel for two different channel widths.*

Dwell Time (s)	Serial Register Average Probability of Capture per unit volume		Maximum Factor Improvement
	24 µm	12 µm	
10^{-3}	2.47×10^{-2}	1.02×10^{-2}	2.42
10^{-4}	1.62×10^{-2}	6.66×10^{-3}	2.43
10^{-5}	7.22×10^{-3}	3.71×10^{-3}	1.95
10^{-6}	1.47×10^{-3}	1.15×10^{-3}	1.28
10^{-7}	1.65×10^{-4}	1.58×10^{-4}	1.04
10^{-8}	1.67×10^{-5}	1.65×10^{-5}	1.01
10^{-9}	1.67×10^{-6}	1.66×10^{-6}	1.01

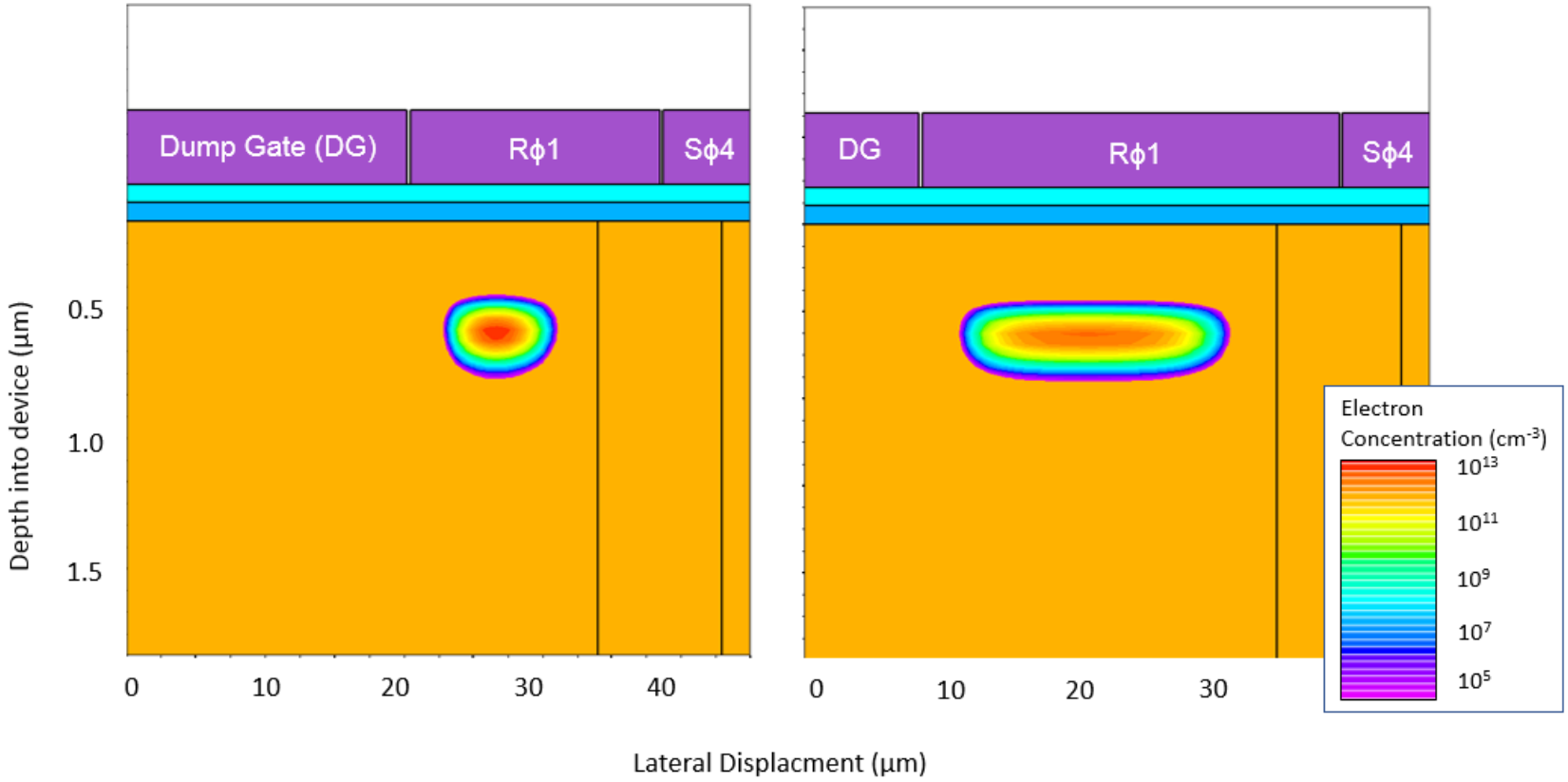

Figure 11.15: *A 1 e^- charge packet within the CCD201-20 for the two channel widths that were modelled in the serial pixel. The volume decreases with channel width and the average charge density of the packet increases as a result.*

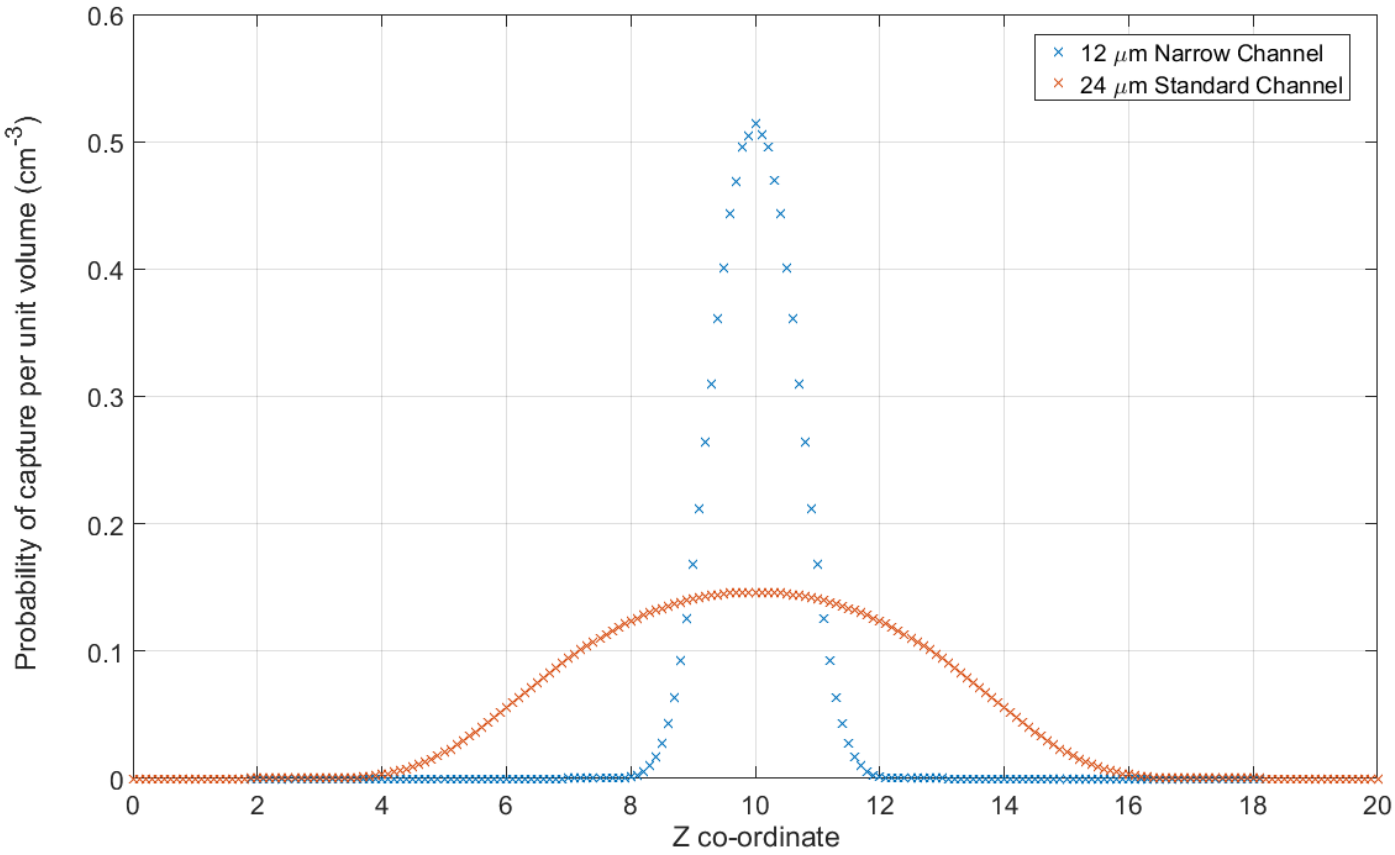

Figure 11.16: *Plot of capture probability as a function of Z co-ordinate (a cut taken perpendicular to the direction of transfer across the central region of the charge packet) for both the original and narrow channel variants of the serial register model. While the charge packet is confined to a smaller volume, the capture probability increases within the central region such that there is no predicted improvement for the operating conditions of this study (1 e^- at 1-10 MHz).*

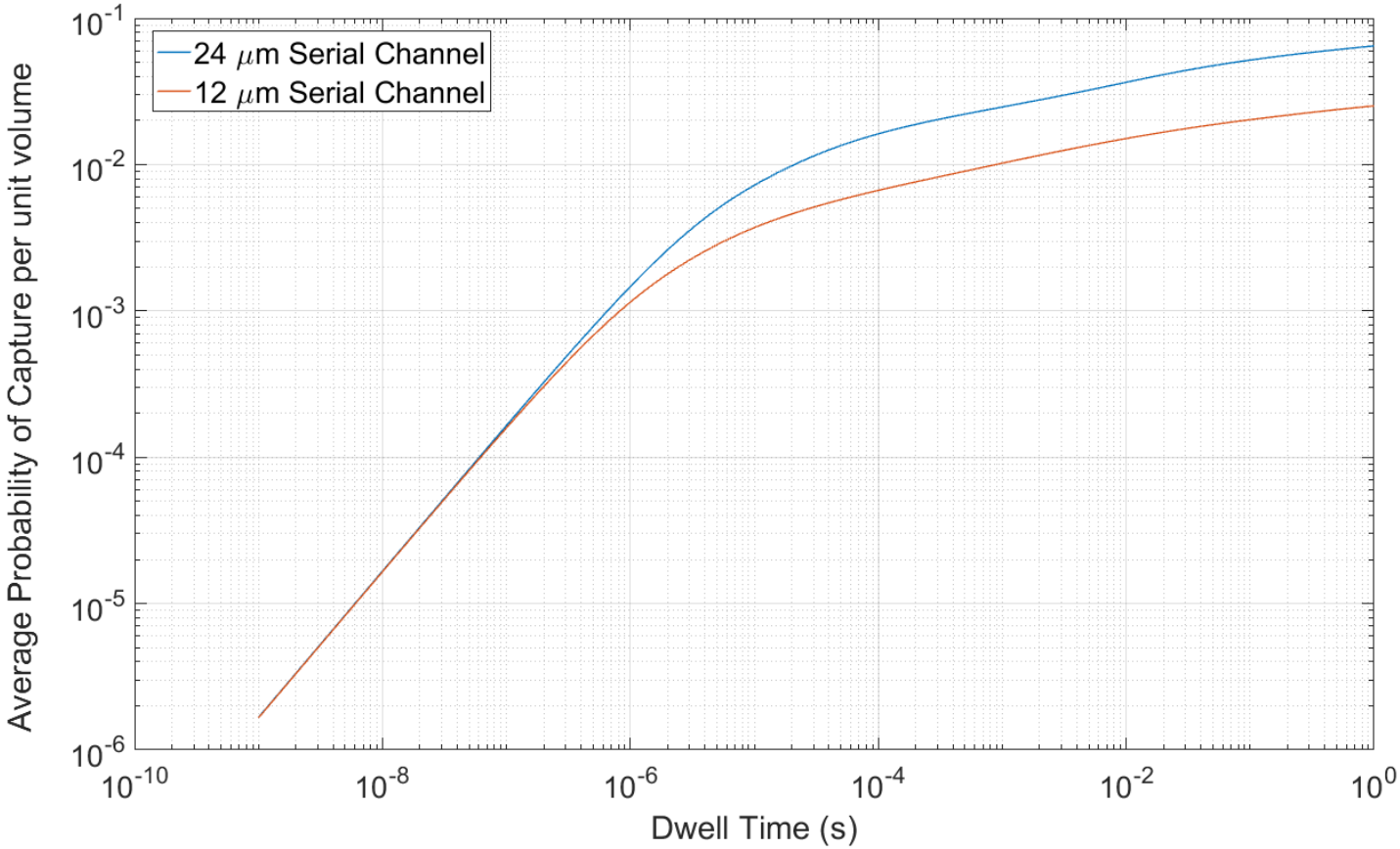

Figure 11.17: *Average probability of capture per unit volume as a function of dwell time for the serial register pixel for two different channel widths and a 1 e^- charge packet. In the µs to ns regime there is no benefit from reducing the channel from 24 µm to 12 µm as the peak probability of capture is below 1 for the unmodified pixel and so a reduction in volume is compensated by an increase in P_C within the central regions. Above the µs regime a benefit becomes apparent since the increase dwell times correspond to increase values for P_C within the unmodified pixel.*

11.6 Conclusions from charge storage modelling for the CGI

The study of charge storage modelling for the CCD201-20 has both built upon existing knowledge of the behaviour of charge packet volume as a function of signal level as well as providing new insight into the interaction between small signal levels and trapping sites. For large signal levels and/or long dwell times, whereby the probability of capture is uniform throughout the charge packet, the established Signal-Volume relationships are accurate at predicting the effective volume of the charge packet. As the dwell time and or signal levels reduce, the capture probability distribution becomes non-uniform throughout the packet and this relationship is no longer adequate to describe the interaction of the charge packet with trapping sites. In this regime, the capture probability per unit volume is a better metric to describe the likelihood of charge capture since it retains the non-uniform charge density profile of the signal packet.

For the parallel section of the CCD201-20, the dwell time is sufficiently long for charge capture to take place even at the fastest operating speeds of 10 MHz. The optimum dwell time for CTI mitigation will therefore be a balance between reducing capture and promoting previously captured charge to emit back into the signal packet. Narrow channel modelling has shown a predicted reduction in average charge capture probability of approximately ×3 for the 2 µm channel structure, a significant factor improvement. The use of a narrow channel parallel section is therefore a viable CTI mitigation strategy for the CGI that is predicted to provide a substantial benefit.

For the serial section of the CCD201-20, the dwell time is too short at the fastest speeds for a significant amount of charge capture to take place. CTI mitigation for the serial section is therefore thought to be primarily rooted in preventing charge capture from taking place as opposed to allowing captured charge to re-emit into the parent packet. Narrow channel serial structures are not predicted to provide a significant improvement in CTE. As the packet is made smaller, the charge density within the central region of the packet is increased and so there is no net reduction in the capture probability per unit volume. If the dwell time of the serial section is increased to a point comparable with the parallel section, or the signal level is increased significantly, a benefit becomes apparent. However, since the CGI will primarily image signal levels in the range of 1 to 10 e^-, a modification to this section of the device is not recommended.

12 Conclusions and future work

Through investigating the impact of radiation damage on the WFIRST CGI, this thesis has presented detailed findings into the manifestation of radiation induced damage in CCD based detectors and how this damage impacts performance. The EM-CCD was introduced and presented as the ideal detector candidate for the WFIRST CGI, owing to the inbuilt multiplication gain mechanism that provides single photon sensitivity. Performance considerations for operation with high multiplication gain in photon counting mode were presented, as well as a discussion concerning the optimum operating mode for the conditions of the CGI.

The role of radiation induced damage was introduced through first discussing the orbital selection for the mission based upon competing science arguments and then discussing the impact of radiation damage on the detector properties. Regardless of the choice of orbit, solar proton induced damage was found to dominate the damage delivered to the device so long as modest shielding was employed. The primary performance concern due to proton damage was the generation of radiation induced trapping sites that act to increase dark current, form hot pixels and increase CTI. The degree of damage was investigated by measuring performance degradation of the CCD201-20 following irradiation to proton fluence levels representative of different levels of shielding, both at room temperature and at the nominal operating temperature of the mission (165 K). Through this investigation, and the subsequent investigations into CTI mitigation strategies, there are three key conclusions from this thesis that are valuable to the WFIRST mission and the wider scientific community as a whole:

1. **For the operating conditions of this study, irradiation at the nominal operating temperature of the WFIRST CGI (165 K) leads to significantly worse performance degradation compared to the room temperature irradiation (298 K) equivalent.**

The mobility of defects is known to be temperature dependant and so it follows that the defect-limited performance degradation observed within CCD based image sensors is dependent upon the temperature at which the device is irradiated. For the operating conditions of this study, performance degradation was consistently worse for irradiation at the nominal operating temperature. CTI was worse for the cryogenic case by between a factor of ×2-×4, depending upon the measurement technique. Dark current was found to be almost an order of magnitude higher for the device irradiated under cryogenic conditions. Following the room temperature anneal, dark current returned to levels expected from the equivalent room temperature irradiation, however **CTI did not**. A thorough description of the lattice mechanics behind this observation was beyond the scope of this thesis, however evidence for significant a change in the defect landscape following a room temperature anneal was presented through results using the trap pumping

technique. For missions such as WFIRST where the impact of radiation damage is severe, minor changes to the defect landscape have the potential to significantly change the predicted science performance. Irradiation at the nominal operating temperature of the mission is necessary to accurately predict EOL performance for CCD based instruments.

The CGI is in a unique position whereby results from the room temperature and cryogenic irradiations are applicable, since the instrument will spend a large proportion of its time idle while the WFI maps the sky. The devices can therefore be actively cooled to 165 K, or stored at 298 K alongside other components of the CGI optics. Based on the results of this investigation, storage at 298 K with the detector unbiased is recommended as the detectors will potentially experience significantly reduced damage compared to the cryogenic equivalent. However, should this prove impractical for the mission, the results presented in this thesis showed that a room temperature anneal from cryogenic storage provided no disadvantages. Dark signal was shown to be reduced by an order of magnitude, and CTI remained consistent with the cryogenic results for each measurement technique. Therefore, a room temperature anneal is recommended following prolonged periods of either storage or operation at 165 K in order to reduce thermal dark signal.

Even at cryogenic temperatures, the increase in dark signal was shown to be manageable and below the science requirement of the mission for modest fluence levels. CIC increases, but by a small factor that is easily mitigated through modification of the image clock amplitudes of the device. The conclusion of the radiation damage study was that CTI due to bulk traps was found to be the limiting factor for science performance of the CGI for both irradiation at room temperature or under cryogenic conditions. This was based upon measurements of low signal CTI using the FPR technique, whereby even irradiation to the lowest fluence level (1.0×10^9) demonstrated significant charge loss (> 1 e^-) from the leading edge of a small signal packet (10 e^-). The signal-volume results presented in chapter 11 showed how the volume of a 1 e^- packet is at most 50% smaller than a 10 e^- packet, and so the implication of this result is that the impact of CTI on single photon imaging will be severe.

Attention therefore turned to the defects responsible for CTI within the CCD201 through development of customised trap pumping schemes that could probe defects in the presence of barrier implants. Within this thesis, for the first time on an EM-CCD, trap pumping schemes were designed, tested and validated that accurately probed defects down to sub-phase resolution. The trap landscape was then extensively probed on devices irradiated at room temperature to

provide more information on the trap species properties including emission time constant and density. This investigation lead to the second main conclusion of this thesis:

2. **For devices irradiated at room temperature, there are four main defect species that can impact CTI for the case of the CGI.**

These species are believed to be the Si-E centre, Si-A centre the double acceptor state of the divacancy (VV^{--}) and either the single acceptor state of the divacancy or another species entirely. The study presented in this thesis was the most extensive trap pumping investigation performed on a EM-CCD to-date and has led to a significant revision of the "trap diagram" for the case of CCDs similar to the CCD201 (Figure 12.1 Figure 12.2).

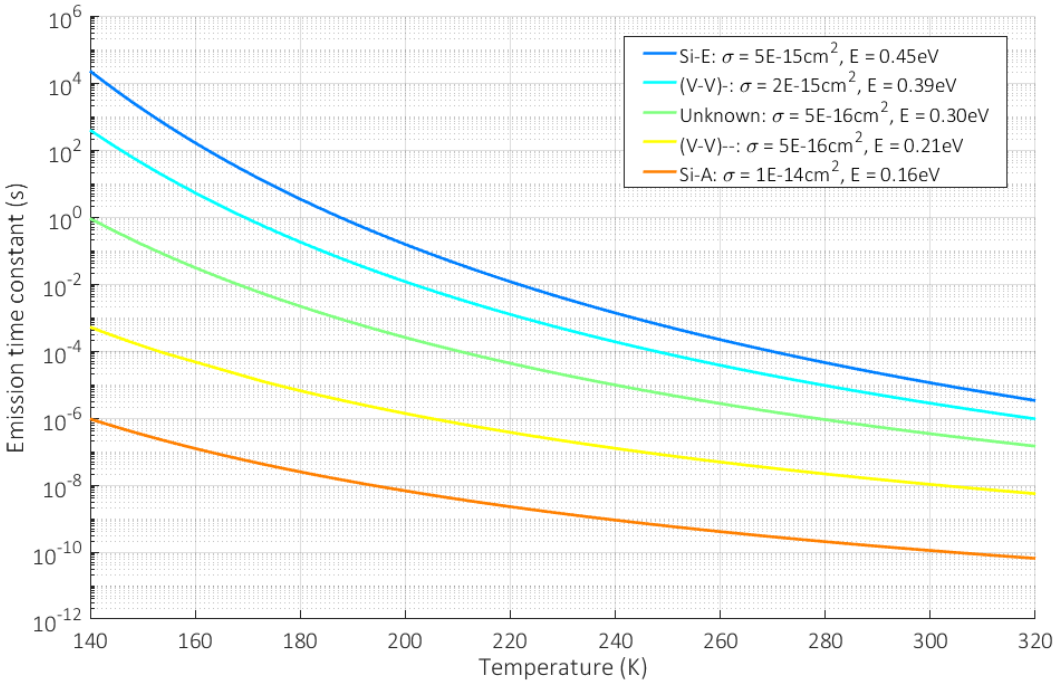

Figure 12.1: *"Trap diagram" using the literature values for defects taken prior to this study.*

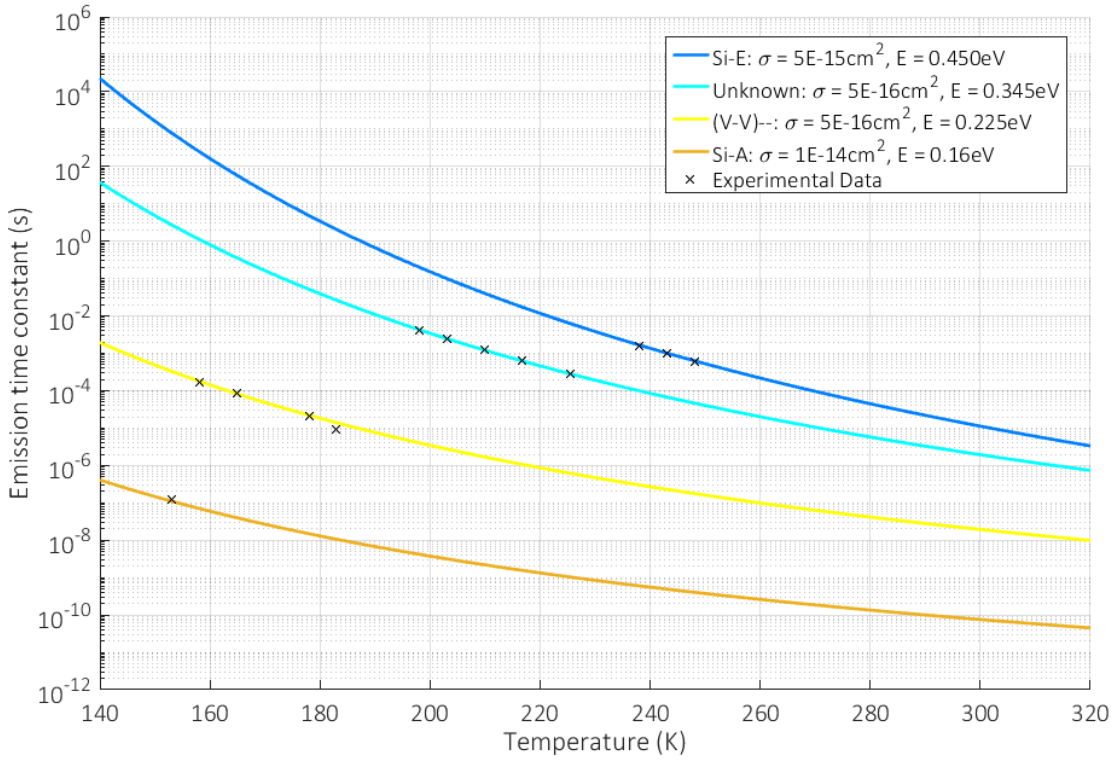

Figure 12.2*: Revised "trap diagram" based on the results of this study.*

The implications of each of these trap species on CGI performance were discussed. The Si-A centre is believed to have the highest density, but also has the shallowest energy level and so should not significantly impact CTI as long as the device is appropriately optimised. The Si-E centre exhibits a high density and a long emission time constant at the nominal operating temperature and so is the primary concern for the performance of the CGI. The Si-E is known to experience annealing at temperatures in excess of 373 K and so the impact of a thermal anneal on CGI performance should be investigated as further work. Each of the acceptor states of the divacancy (VV^{--}, VV^{-}) and/or the "unknown" trap affect CTI in different ways. It is thought to be possible to optimise against the VV^{--} through a change in operating temperature and a customised parallel clocking scheme that promotes charge emission into the original signal packet. The benefit of these changes should be investigated further. For the VV^{-}, the focus of the optimisation is to keep these sites filled for the frame readout process so that they affect as few signal packets as possible. Even with these mitigation strategies employed, trapping sites can seriously limit performance of single photon imaging and so an investigation was performed whereby narrow channel structures of the CCD201 were benchmarked against the standard variant to investigate any predicted improvement. This investigation lead to the final main conclusion of this thesis:

3. A Narrow Channel variant of the CCD201-20 image pixel has the potential to significantly improve performance in the presence of radiation induced damage.

Reduction of the channel width of the image pixel from 9 µm to 4 µm lead to an approximate factor ×2 reduction in the trapping probability per unit volume for a single electron charge packet. A further reduction to a width of 2 µm gave a predicted ×3 reduction in the trapping probability per unit volume compared to the standard design. The reduction in FWC and channel parameter is not perceived to have a detrimental impact on the CGI application and so it was strongly recommended that this modification was incorporated into a revised design of the CCD201. Simulations of the CCD201 serial register pixels at high speed and low signal levels showed that the traditional method for calculating the volume of a signal packet was inadequate. Instead, the probability of capture per unit volume is needed to accurately predict the benefit. A key result was that at fast speeds and low signal levels, narrow channel variants do not provide a benefit, as the total trapping probability in the pixel is conserved. Modification to the serial register was therefore not recommended. As a result of this work, test devices incorporating the narrow channel modification are being manufactured by e2v as part of a technology development program of the WFIRST CGI. These devices should be thoroughly characterised in order to conclude whether the measured benefit in CTI is close to the theoretical prediction provided by TCAD. The narrow channel modelling also helped drive the development of a new technique for estimating the predicted performance benefit from such device modifications.

The work in this thesis contributed significantly to the adoption of EM-CCD for the WFIRST CGI through the in-depth investigation into the effects of radiation on the detector, and has informed a detailed technology development programme at JPL where radiation-hard variants of the device are under development. The WFIRST CGI was introduced in the first chapter as perhaps the most demanding optical application for CCD-based technologies to-date, imaging extremely low flux in the presence of radiation induced damage. This thesis has presented the key issues associated with such an endeavour and the results have been extremely positive, with many mitigation strategies presented that can significantly improve the science performance of the instrument. The CGI is likely the first of many future missions that will utilise EM-CCD technology within the space environment, and so it is the hope of the author that the results presented in this thesis will help continue to further the development and research into the use of this technology for future space applications.

13 Bibliography

1. Alig, R. C., Bloom, S., & Struck, C. W. (1980). Scattering by ionization and phonon emission in semiconductors. Phys. Rev. B, 22(12), 5565–5582. https://doi.org/10.1103/PhysRevB.22.5565
2. Basilevsky, A. T., Mall, U., Keller, H. U., & Skorov, Y. V. (2015). NavCam Observations of the Hathor Cliff and Hapi Area on the Nucleus of Comet 67p/Churyumov-Gerasimenko. In Lunar and Planetary Science Conference (Vol. 46, p. 1152).
3. Batalha, N. M., Rowe, J. F., Bryson, S. T., Barclay, T., Burke, C. J., Caldwell, D. A., … Welsh, W. F. (2013). Planetary Candidates Observed by Kepler. III. Analysis of the First 16 Months of Data. The Astrophysical Journal Supplement Series, 204(2), 24. Retrieved from http://stacks.iop.org/0067-0049/204/i=2/a=24
4. Bautz, M., Prigozhin, G., Kissel, S., LaMarr, B., Grant, C., & Brown, S. (2005). Anomalous annealing of a high-resistivity CCD irradiated at low temperature. IEEE Transactions on Nuclear Science, 52(2), 519–526.
5. Beaudoin, L., Parent, M.-A., & Vroomen, L. C. (1996). Cheops: A compact explorer for complex hierarchies. In Visualization'96. Proceedings. (pp. 87–92).
6. Bonamente, M., Joy, M. K., LaRoque, S. J., Carlstrom, J. E., Reese, E. D., & Dawson, K. S. (2006). Determination of the cosmic distance scale from Sunyaev-Zel'dovich effect and chandra X-ray measurements of high-redshift galaxy clusters. The Astrophysical Journal, 647(1), 25.
7. Boyle, W. S., & Smith, G. E. (1970). Charge coupled semiconductor devices. Bell Labs Technical Journal, 49(4), 587–593.
8. Brau, J. E., & Sinev, N. (2000). Operation of a CCD particle detector in the presence of bulk neutron damage. IEEE Transactions on Nuclear Science, 47(6), 1898–1901.
9. Brueckner, G. E., Howard, R. A., Koomen, M. J., Korendyke, C. M., Michels, D. J., Moses, J. D., *et al*. (1995). The large angle spectroscopic coronagraph (LASCO). Solar Physics, 162(1–2), 357–402.
10. Bush, N., Hall, D., Holland, A., Burgon, R., Murray, N., Gow, J., *et al.* (2016). Cryogenic irradiation of an EM-CCD for the WFIRST-AFTA coronagraph: preliminary performance analysis. In SPIE Astronomical Telescopes+ Instrumentation (p. 99150A--99150A).

11. Bush, N., Stefanov, K., Hall, D., Jordan, D., & Holland, A. (2014). Simulations of charge transfer in electron multiplying charge coupled devices. Journal of Instrumentation, 9(12), C12042.
12. Catala, C., Consortium, P., *et al*. (2009). PLATO: PLAnetary Transits and Oscillations of stars. Experimental Astronomy, 23(1), 329–356.
13. Caughey, D. M., & Thomas, R. E. (1967). Carrier mobilities in silicon empirically related to doping and field. Proceedings of the IEEE, 55(12), 2192–2193.
14. Chen, Y., Xu, Y., Chae, Y., Mierop, A., Wang, X., & Theuwissen, A. (2012). A 0.7 e- rms-temporal-readout-noise CMOS image sensor for low-light-level imaging. In Solid-State Circuits Conference Digest of Technical Papers (ISSCC), 2012 IEEE International (pp. 384–386).
15. Daigle, O., Carignan, C., Gach, J.-L., Guillaume, C., Lessard, S., Fortin, C.-A., & Blais-Ouellette, S. (2009). Extreme faint flux imaging with an EMCCD. Publications of the Astronomical Society of the Pacific, 121(882), 866.
16. Daigle, O., Gach, J.-L., Guillaume, C., Lessard, S., Carignan, C., & Blais-Ouellette, S. (2008). CCCP: a CCD controller for counting photons. In SPIE Astronomical Telescopes+ Instrumentation (p. 70146L--70146L).
17. Dryer, B., Smith, P., Nuns, T., Murray, N., Stefanov, K. D., Gow, J. P. D., Holland, A. D. (2016). Validation of NIEL for> 1MeV electrons in silicon using the CCD47-20.
18. e2v technologies. (2006). Low Light Technical Note 5: An Overview of the Ageing Characteristics of L3Vision(TM) Sensors.
19. e2v technologies. (2015). e2v Low-Light Technical Note 4. Retrieved from http://www.e2v.com/content/uploads/2015/04/a1a-low-light_tn4_3_v1.pdf
20. e2v technologies. (2016). CCD42-40 Datasheet. Retrieved from http://www.e2v.com/resources/account/download-datasheet/1208
21. Evagora, A. M., Murray, N. J., Holland, A. D., & Burt, D. (2012). Single event gate rupture in emccd technology. Journal of Instrumentation, 7(12), C12002.
22. Evagora, A. M., Murray, N. J., Holland, A. D., Burt, D., & Endicott, J. (2012). Novel method for identifying the cause of inherent ageing in Electron Multiplying Charge Coupled Devices. Journal of Instrumentation, 7(1), C01023.
23. Fano, U. (1947). Ionization yield of radiations. II. The fluctuations of the number of ions. Physical Review, 72(1), 26.
24. Freedman, W. L., Madore, B. F., Gibson, B. K., Ferrarese, L., Kelson, D. D., Sakai, S., *et al.* (2001). Final Results from the Hubble Space Telescope Key Project to Measure the Hubble Constant. \apj, 553, 47–72. https://doi.org/10.1086/320638

25. Fröhlich, eg H. (1947). On the theory of dielectric breakdown in solids. Proc. R. Soc. Lond. A, 188(1015), 521–532.
26. Garmire, G. P., Bautz, M. W., Ford, P. G., Nousek, J. A., & Ricker Jr., G. R. (2003). Advanced CCD imaging spectrometer (ACIS) instrument on the Chandra X-ray Observatory. Proc. SPIE. https://doi.org/10.1117/12.461599
27. Gow, J. P. D., Murray, N. J., Wood, D., Burt, D., Hall, D. J., Dryer, B., & Holland, A. D. (2016). Charge transfer efficiency in a p-channel CCD irradiated cryogenically and the impact of room temperature annealing. In High Energy, Optical, and Infrared Detectors for Astronomy VII (Vol. 9915). Retrieved from http://oro.open.ac.uk/47005/
28. Hall, D. J., Holland, A., Murray, N., Gow, J., & Clarke, A. (2012). Modelling charge transfer in a radiation damaged charge coupled device for Euclid. In SPIE Astronomical Telescopes and Instrumentation (Vol. 8453).
29. Hall, D. J., Murray, N., Gow, J., Wood, D., & Holland, A. (2014). In situ trap parameter studies in CCDs for space applications. In Proceedings of SPIE (Vol. 9154). Retrieved from http://oro.open.ac.uk/40941/
30. Hall, D. J., Murray, N. J., Gow, J. P. D., Wood, D., & Holland, A. (2014). Studying defects in the silicon lattice using CCDs. Journal of Instrumentation, 9(12). Retrieved from http://oro.open.ac.uk/41458/
31. Hall, R. N. (1952). Electron-hole recombination in germanium. Physical Review, 87(2), 387.
32. Harding, L. K., Demers, R. T., Hoenk, M., Peddada, P., Nemati, B., Cherng, M., *et al.* (2016). Technology advancement of the CCD201-20 EMCCD for the WFIRST coronagraph instrument: sensor characterization and radiation damage. Journal of Astronomical Telescopes, Instruments, and Systems, 2(1), 11007.
33. Hardy, T., Murowinski, R., & Deen, M. J. (1998). Charge transfer efficiency in proton damaged CCD's. IEEE Transactions on Nuclear Science, 45(2), 154–163.
34. Heim, G. B., Biesterfeld, B., Burkepile, J., Frame, W. W., Harding, T., Harris, J., *et al*. (2009). A 5.5 megapixel high-performance low-light military video camera. In SPIE Defense, Security, and Sensing (p. 730703).
35. Holland, A. D. (1993). The effect of bulk traps in proton irradiated EEV CCDs. Nuclear Instruments and Methods in Physics Research A, 326, 335–343. https://doi.org/10.1016/0168-9002(93)90374-Q

36. Hopkinson, G. R. (1993). Radiation-induced dark current increases in CCDs. In Radiation and its Effects on Components and Systems, 1993., RADECS 93., Second European Conference on (pp. 401–408).
37. Hopkinson, G. R., Dale, C. J., & Marshall, P. W. (1996). Proton effects in charge-coupled devices. IEEE Transactions on Nuclear Science, 43(2), 614–627.
38. Hopkinson, G. R., & Mohammadzadeh, A. (2003). Comparison of CCD damage due to 10-and 60-MeV protons. IEEE Transactions on Nuclear Science, 50(6), 1960–1967.
39. Hublitz, K., & Lyon, S. A. (1992). Light emission from hot carriers in Si MOSFETS. Semiconductor Science and Technology, 7(3B), B567.
40. Ivezic, Z., Tyson, J. A., Abel, B., Acosta, E., Allsman, R., AlSayyad, Y., *et al*. (2008). LSST: from science drivers to reference design and anticipated data products. arXiv Preprint arXiv:0805.2366.
41. Janesick, J. R. (2001). Scientific charge-coupled devices. Scientific charge-coupled devices, Bellingham, WA: SPIE Optical Engineering Press, 2001, xvi, 906 p.~SPIE Press monograph, PM 83. ISBN 0819436984.
42. Janesick, J., Elliott, T., & Pool, F. (1989). Radiation damage in scientific charge-coupled devices. IEEE Transactions on Nuclear Science, 36(1), 572–578.
43. Jenkner, H. (1990). The Hubble Space Telescope Before Launch: A Personal Perspective. In G. Klare (Ed.), Accretion and Winds (pp. 297–312). Berlin, Heidelberg: Springer Berlin Heidelberg. https://doi.org/10.1007/978-3-642-76238-3_20
44. Jerram, P., Pool, P., Bell, R., Burt, D., Bowring, S., Spencer, S., *et al*. The LLLCCD : Low Light Imaging without the need for an intensifier. Proc. SPIE 4306, Sensors and Camera Systems for Scientific, Industrial, and Digital Photography Applications II, (15 May 2001); doi: 10.1117/12.426953.
45. Jorden, P. R., Pool, P., & Tulloch, S. M. (2002). Secrets of e2v technologies ccds (ex marconi ccds). Experimental Astronomy, 14(2), 69–75.
46. Kinchin, G. H., & Pease, R. S. (1955). The Displacement of Atoms in Solids by Radiation. Reports on Progress in Physics, 18(1), 1. Retrieved from http://stacks.iop.org/0034-4885/18/i=1/a=301
47. Kittel, C., & Holcomb, D. F. (1967). Introduction to solid state physics. American Journal of Physics, 35(6), 547–548.
48. Klein, H. P. (1977). The Viking biological investigation: general aspects. Journal of Geophysical Research, 82(28), 4677–4680.
49. Koch, D. G., Borucki, W. J., Basri, G., Batalha, N. M., Brown, T. M., Caldwell, D., *et al*. (2010). Kepler mission design, realized photometric performance, and early science. The Astrophysical Journal Letters, 713(2), L79.

50. Krist, J., Nemati, B., & Mennesson, B. (2016). Numerical modeling of the proposed WFIRST-AFTA coronagraphs and their predicted performances. Journal of Astronomical Telescopes, Instruments, and Systems, 2(1), Vol. 11003.
51. Laborie, A., Davancens, R., Pouny, P., Vétel, C., Chassat, F., Charvet, P., *et al.* (2007). The Gaia focal plane. In Optical Engineering and Applications (Vol. 6690)
52. Laureijs, R. J., Duvet, L., Sanz, I. E., Gondoin, P., Lumb, D. H., Oosterbroek, T., & Criado, G. S. (2010). The Euclid Mission. In SPIE Astronomical Telescopes and Instrumentation (Vol. 7731).
53. Macchetto, F., Marconi, A., Axon, D. J., Capetti, A., Sparks, W., & Crane, P. (1997). The Supermassive Black Hole of M87 and the Kinematics of Its Associated Gaseous Disk. The Astrophysical Journal, 489(2), 579. Retrieved from http://stacks.iop.org/0004-637X/489/i=2/a=579
54. Macintosh, B., Graham, J. R., Ingraham, P., Konopacky, Q., Marois, C., Perrin, M., … others. (2014). First light of the gemini planet imager. Proceedings of the National Academy of Sciences, 111(35), 12661–12666.
55. Marshall, H. L., Tennant, A., Grant, C. E., Hitchcock, A. P., O'Dell, S., & Plucinsky, P. P. (2003). Composition of the Chandra ACIS contaminant. arXiv Preprint Astro-ph/0308332.
56. Massey, R., Stoughton, C., Leauthaud, A., Rhodes, J., Koekemoer, A., Ellis, R., & Shaghoulian, E. (2010). Pixel-based correction for charge transfer inefficiency in the Hubble Space Telescope advanced camera for surveys. Monthly Notices of the Royal Astronomical Society, 401(1), 371–384.
57. Murray, N. J., Burt, D. J., Holland, A. D., Stefanov, K. D., Gow, J. P. D., MacCormick, C., Allanwood, E. A. H. (2013). Multi-level parallel clocking of CCDs for: improving charge transfer efficiency, clearing persistence, clocked anti-blooming, and generating low-noise backgrounds for pumping.
58. Murray, N. J., Holland, A. D., Gow, J. P. D., Hall, D. J., Stefanov, K. D., Dryer, B. J., Burt, D. J. (2014). Assessment of the performance and radiation damage effects under cryogenic temperatures of a P-channel CCD204s. In Proc. SPIE (Vol. 9154, p. 91540P).
59. Noecker, M. C., Zhao, F., Demers, R., Trauger, J., Guyon, O., & Kasdin, N. J. (2016). Coronagraph instrument for WFIRST-AFTA. Journal of Astronomical Telescopes, Instruments, and Systems, 2(1), 11001.

60. Pasquale, B., Content, D., Kruk, J., Vaughn, D., Gong, Q., Howard, J., Kuan, G. (2014). Optical Design of WFIRST-AFTA Wide-Field Instrument. Proc. SPIE 9293, International Optical Design Conference 2014, 929305 (17 December 2014); doi: 10.1117/12.2177847
61. Peale, S. J. (1993). On the verification of the planetary system around PSR 1257+ 12. The Astronomical Journal, 105, 1562–1570.
62. Pesnell, W. D. (2015). Solar Dynamics Observatory (SDO). Springer.
63. Pichler, P., (2004). Intrinsic Point Defects. Intrinsic Point Defects, Impurities, and Their Diffusion in Silicon, 77–227.
64. Pollacco, D. L., Skillen, I., Cameron, A. C., Christian, D. J., Hellier, C., Irwin, J. *et al.* (2006). The WASP project and the SuperWASP cameras. Publications of the Astronomical Society of the Pacific, 118(848), 1407.
65. Rauscher, E. (2015). 20 Years of Exoplanets: From Surveys Towards Characterization. In AAS/Division for Planetary Sciences Meeting Abstracts (Vol. 47).
66. Riess, A. G., Nugent, P. E., Gilliland, R. L., Schmidt, B. P., Tonry, J., Dickinson, M., Veilleux, S. (2001). The Farthest Known Supernova: Support for an Accelerating Universe and a Glimpse of the Epoch of Deceleration. The Astrophysical Journal, 560(1), 49. Retrieved from http://stacks.iop.org/0004-637X/560/i=1/a=49
67. Robbins, M. S., Member, S., & Hadwen, B. J. (2003). The Noise Performance of Electron Multiplying Charge-Coupled Devices, 50(5), 1227–1232.
68. Shockley, W., & Read Jr, W. T. (1952). Statistics of the recombinations of holes and electrons. Physical Review, 87(5), 835.
69. Short, A., Prod'homme, T., Weiler, M., Brown, S., & Brown, A. (2010). A fast model of radiation-induced electron trapping in CCDs for implementation in the Gaia data processing. Proc. SPIE. https://doi.org/10.1117/12.856386
70. Simms, L. M., Figer, D. F., Hanold, B. J., Kerr, D. J., Gilmore, D. K., Kahn, S. M., & Tyson, J. A. (2007). First use of a HyViSI H4RG for astronomical observations. In Proc SPIE (Vol. 6690)
71. Sirianni, M., Mutchler, M., & Lucas, R. A. (2006). Hot pixels growth in ACS CCDs. In The 2005 HST Calibration Workshop: Hubble After the Transition to Two-Gyro Mode (p. 45).
72. Smith, B. A., Soderblom, L., Beebe, R., Boyce, J., Briggs, G., Bunker, A., Suomi, V. E. (1981). Encounter with Saturn: Voyager 1 Imaging Science Results. Science, 212(4491), 163–191. https://doi.org/10.1126/science.212.4491.163
73. Smith, D. R., Ingley, R., & Holland, a. D. (2006). Proton irradiation of EMCCDs. IEEE Transactions on Electron Devices, 53(2), 205–210. https://doi.org/10.1109/TED.2005.861730

74. Smith, D. R., Walton, D. M., Ingley, R., Holland, A. D., Cropper, M., & Pool, P. (2006). EMCCDs for space applications. Proc. SPIE. https://doi.org/10.1117/12.671368
75. Spergel, D., Gehrels, N., Baltay, C., Bennett, D., Breckinridge, J., Donahue, M., *et al.* (2015). Wide-Field InfrarRed survey telescope-astrophysics focused telescope assets WFIRST-AFTA 2015 report. arXiv Preprint arXiv:1503.03757.
76. Spergel, D., Gehrels, N., Breckinridge, J., Donahue, M., Dressler, A., Gaudi, B. S., *et al.* (2013). Wide-field infrared survey telescope-astrophysics focused telescope assets WFIRST-AFTA final report. arXiv Preprint arXiv:1305.5422.
77. Srour, J. R., Marshall, C. J., & Marshall, P. W. (2003). Review of displacement damage effects in silicon devices. IEEE Transactions on Nuclear Science, 50(3), 653–670.
78. Sze, S. M., & Ng, K. K. (2006). Physics of semiconductor devices. John Wiley & Sons.
79. e2v Technologies (2015). CCD201-20 datasheet. Retrieved from http://www.e2v.com/resources/account/download-datasheet/1491
80. Tutt, J. H., Holland, A. D., Hall, D. J., Harriss, R. D., & Murray, N. J. (2012). The Noise Performance of Electron-Multiplying Charge-Coupled Devices at X-ray Energies. IEEE Transactions on Electron Devices, 59(1), 167–175. https://doi.org/10.1109/TED.2011.2172611
81. Tutt, J. H., McEntaffer, R. L., DeRoo, C., Schultz, T., Miles, D. M., Zhang, W., *et al,* (2014). Developments in the EM-CCD camera for OGRE. In SPIE Astronomical Telescopes+ Instrumentation (Vol. 9154).
82. Tylka, A. J., Adams, J. H., Boberg, P. R., Brownstein, B., Dietrich, W. F., Flueckiger, E. O., Smith, E. C. (1997). CREME96: A revision of the cosmic ray effects on micro-electronics code. IEEE Transactions on Nuclear Science, 44(6), 2150–2160.
83. Vago, J., Gardini, B., Kminek, G., Baglioni, P., Gianfiglio, G., Santovincenzo, A., *et al.* (2006). ExoMars-searching for life on the Red Planet. ESA Bulletin, 126, 16–23.
84. Vision, C. (2005). Space Science for Europe 2015-2025. ESA Brochure, 247, 1–111.
85. Wood, D., Hall, D., Gow, J. P. D., & Holland, A. (2016). A study of the double-acceptor level of the silicon divacancy in a proton irradiated n-channel CCD. In SPIE Astronomical Telescopes and Instrumentation (Vol. 9915).